Structural explorations of fabrication-aware design spaces for non-standard architecture

Romain Mesnil

UNIVERSITÉ PARIS-EST

UNIVERSITE PARIS-EST

École doctorale Science, Ingénierie et Environnement

Thèse de doctorat

Spécialité: Structures et Matériaux

présentée par

Romain Mesnil

Structural explorations of fabrication-aware design spaces for non-standard architecture

---

Soutenue à l'École Nationale des Ponts et Chaussées
le 3 février 2017 devant le jury constitué de:

Président	Maurizio Brocato	École d'architecture de Paris-Malaquais
Rapporteurs	Bernard Maurin	Université de Montpellier
	Chris Williams	University of Bath
Examinateurs	Christoph Gengnagel	Universität der Künste Berlin
	Laurent Hauswirth	Université de Marne-La-Vallée
	Nicolas Pauli	École d'architecture de Montpellier
Directeur de Thèse	Olivier Baverel	École des Ponts ParisTech
Co-encadrant	Cyril Douthe	École des Ponts ParisTech

Résumé

Les dernières décennies ont vu l'émergence de formes architecturales non standard. Les concepteurs se retrouvent généralement démunis face à la complexité géométrique de ces objets, dont la fabrication rime souvent avec complication. De plus, les outils utilisés dissocient forme et fonctionnement structurel, ce qui complexifie le processus de décision pour ingénieurs et architectes. Ce mémoire prend un point de vue fondé sur la notion d'invariance par transformation géométrique et étudie plusieurs stratégies de génération de formes satisfaisant des contraintes constructives usuelles pour remédier à ces manques. Trois contraintes constructives ont été identifiées et correspondent à trois contributions indépendantes de cette thèse.

La répétition des nœuds d'assemblage est étudiée via les transformations par maillages parallèles. Ces dernières sont utilisées pour créer une généralisation des surfaces de révolution. On retrouve par là un paramétrage particulier des surfaces moulures de Monge avec une grande répétition d'éléments, et notamment de nœuds d'assemblage.

Les réseaux de cyclides sont ensuite utilisés pour dessiner des formes parametrées par leurs lignes de courbures. Cela permet la couverture par panneaux plans ainsi que l'offset des éléments structurels sans excentricité. L'apport de cette thèse est l'implémentation de plusieurs améliorations, notamment l'introduction de plis à double courbure, un algorithme permettant de généraliser les réseaux de cyclides à des topologies quelconques, et la génération de surfaces généralisant les surfaces canal à partir de deux courbes rail et une courbe profil.

Finalement, une méthode innovante inspirée de la géométrie descriptive permettant la génération de formes courbes couvertes par des quadrangles plans est proposée. La méthode, baptisée méthode marionnette, réduit ce problème à un système linéaire, ce qui permet une manipulation de ces formes constructibles en temps réel. Une étude comparative montre que cette technique peut être utilisée pour paramétrer des problèmes d'optimisation de forme de coques sans perte de performance par rapport aux paramétrages utilisés de façon classique. L'intégration des contraintes de fabrication dans le processus d'optimisation structurelle ouvre de nouvelles possibilités d'applications, comme des coques réticulées et des coques discrètes. La pertinence de ces nouvelles solutions est démontrée par de multiples études de cas.

Mots clés : morphologie structurale, outil de génération, processus de conception, géométrie descriptive, optimisation structurelle, gridshell, maillage marionnette, coque mince.

Abstract

The last decades have seen the emergence of non-standard architectural shapes. Designers find often themselves helpless with the geometrical complexity of these objects. Furthermore, the available tools dissociate shape and structural behaviour, which adds another complication. This dissertation takes the point of view based on invariance under geometrical transformations, and studies several strategies for fabrication-aware shape modelling. Three technological constraints have been identified and correspond to three independent contributions of this thesis.

The repetition of nodes is studied via transformations by parallelism. They are used to generalise surfaces of revolution. A special parametrisation of moulding surfaces is found with this method. The resulting structure has a high node congruence.

Cyclidic nets are then used to model shapes parametrised by their lines of curvature. This guarantees meshing by planar panels and torsion-free beam layout. The contribution of this dissertation is the implementation of several improvements, like doubly-curved creases, a hole-filling strategy that allows the extension of cyclidic nets to complex topologies, and the generation of a generalisation of canal surfaces from two rail curves and one profile curves.

Finally, an innovative method inspired by descriptive geometry is proposed to generate doubly-curved shapes covered with planar facets. The method, called marionette technique, reduces the problem to a linear problem, which can be solved in real-time. A comparative study shows that this technique can be used to parametrise shape optimisation of shell structures without loss of performance compared to usual modelling technique. The handling of fabrication constraints in shape optimisation opens new possibilities for its practical application, like gridshells or plated shell structures. The relevance of those solutions is demonstrated through multiple case-studies.

Keywords : structural morphology, generative tool, design process, descriptive geometry, structural optimisation, gridshell, marionette mesh, thin shell.

Acknowledgment

Il faut une ouverture d'esprit certaine pour lancer des ponts entre différentes disciplines. J'ai eu la chance d'avoir des encadrants ayant cette qualité. Ce travail doit autant à leur rigueur scientifique qu'à cette ouverture.

Merci à Olivier, mon directeur de thèse, pour son enthousiasme, pour la confiance qu'il a placée en moi dès le début de ce travail et pour le plaisir d'enseigner qu'il m'a communiqué. Merci pour ses conseils et tout ce qu'il a pu m'apprendre, sur les structures complexes, mais bien plus en encore.

Merci à Cyril, conseiller scientifique, d'avoir su trouver les mots pour me faire revenir de ce côté de l'Atlantique, et sans qui je n'aurai surement jamais fait de thèse. Ce travail s'est nourri de nos discussions qui ont donné naissance à de multiples idées, dont certaines se sont concretisées dans ce document. Merci aussi pour avoir relu ce long mémoire ainsi que les quelques articles qui en sont issus, et d'avoir notoirement amélioré la clarté du propos. Merci enfin de m'avoir invité à prendre part à l'enseignement de Construire le Courbe et d'avoir pu me permettre de confronter la géométrie à la matière.

Je remercie Bruno Léger pour ses conseils et pour l'orientation de ce travail vers les structures. Merci à Bouygues Construction d'avoir financé ce projet de thèse, qui portait une ambition forte. Merci à Marc Blondeau et son équipe d'avoir pris le temps d'échanger sur des problématiques de la vraie vie d'une entreprise de construction.

Je tiens à remercier Bernard Maurin et Chris Williams, rapporteurs de ce mémoire, pour leurs conseils précis et avisés. Je remercie également tous les membres de mon jury pour leur écoute attentive. Merci à Maurizio Brocato, son président, pour ses remarques judicieuses lors de ma soutenance. Merci à Christoph Gengnagel, Nicolas Pauli et Laurent Hauswirth pour leur relecture du manuscrit et leurs commentaires pertinents qui continueront à nourrir ce travail.

Mes remerciements vont aussi à Karam Sab, directeur du laboratoire Navier, et à Jean-François Caron, qui a suivi mon travail et qui a porté le projet du Build'In Lab avec Françoise Préteux. Je suis heureux que nous puissions écrire les pages de cette nouvelle aventure ensemble.

Un mémoire ne constitue qu'une partie d'une vie de thésard. Je tiens à remercier toutes les personnes que j'ai eu le plaisir de cotoyer au quotidien et qui en rendu les bons moments meilleurs et m'ont soutenu durant les moments plus difficiles. A mes co-bureaux: Achille, Bachar, Grégoire, Michele, Philippe, Rawad, Stefania. A toute l'équipe de Thinkshell, une histoire encore en construction: Arthur, Frederic, Lionel. Aux copains avec qui j'ai partagé les pauses café: Lorenzo, Marie, Pierre, Nicolas, Robin, Romain B. et Romain D., Vianney. Aux étudiants de l'Ecole à qui j'ai eu le plaisir d'enseigner, et plus particulièrement ceux que j'ai encadrés plus longuement: Christiane, Hugo et Yann. Un grand merci enfin à Marie Françoise pour son aide et sa gentillesse.

Il y a la joie de terminer cette étape, mais je n'oublie pas les moments difficiles passés au cours de ces trois années. A mes amis et ma famille qui m'ont soutenu pendant ces périodes: mes parents, ma grand-mère, Pascale et Francis qui m'ont accueilli dans leur famille, ma sœur Amélie et son mari Raphaël,

ma chère nièce et mes chers neveux. J'ai eu à l'esprit mon neveu Charlie tout au long de ce travail. Il y a aussi ces destins croisés le 13 novembre 2015, et toute la Belle Equipe. Je pense enfin à ma sœur Hélène avec qui j'aurais été si heureux de partager ces moments.

Enfin, je remercie Marion d'être restée à mes côtés durant ces trois annés (et un peu plus) et pour celles qui viennent. Notre famille s'est agrandie et je remercie Marcus qui m'a fait la plus grande des joies en venant au monde.

Contents

List of Figures

List of Tables

Part I

Problem statement

'La faculté qui nous apprend à voir, c'est l'intuition. Sans elle, le géomètre serait comme un écrivain qui serait ferré sur la grammaire, mais qui n'aurait pas d'idée. '

Henri Poincaré

Chapter 1

Opportunities of free-form structures

Geometry lies at the core of structural design, it is a science used both by architects and engineers to generate harmonious and efficient structural configurations. The construction of curvilinear structures remains however a challenge for designers and builders. This dissertation presents new computational strategies for the fabrication-aware design of doubly-curved structures and envelopes. This first chapter proposes a quick and critical overview of the existing literature on the rationalisation of complexly-shaped buildings.

1.1 On curvature in architecture

1.1.1 What is free-form architecture?

The last three decades have seen the emergence of complexly shaped buildings, modelled with contemporary computer-aided design tools. Moving away from modernism, architects explore new formal possibilities offered by the computer. Some spectacular realisations focused the attention of the media and have often associated so-called *free-form architecture* with the idea of limitless creativity, but also of high budget and delay. There is no consensus on a precise definition for the term *'free-form architecture'*. In the following of this dissertation, the expressions *'free-form architecture'* and *'non-standard architecture'* will be employed to describe all doubly-curved architectural shapes.

The use of doubly-curved shapes in architecture is actually not new. Among the first buildings built by men, surfaces of revolutions are well represented, as it is easy to draw a circle from a simple rope and a fixed point. Curved shapes were therefore seen as a way to solve construction and representation problems. Some curved shapes are also known to be structurally efficient, and are found in nature, which has been a source of inspiration for a long time.

1.1.2 Potential of complex shapes

For Democritus, the existence of natural objects is the fruit of *'chance and necessity'*. It is commonly admitted that natural shape can be attributed to functional imperatives, like structural reliability or maximisation of energy input. The shapes arising in nature are curvilinear, far from the variations on cubes built in the western countries. This is the meaning of the famous quote by catalan architect Antoni Gaudi *'The straight line belongs to men, the curve one to God'*.

Structural engineers know that doubly-curved shells can be much more efficient than planar slabs, because of their geometrical stiffness. The potential of shapes to create efficient structures is well illustrated by realisation of structural artists in the twentieth century. Figure 1.1 shows two high performance structures that withstand loads due to their shapes. The Mannheim Multihalle, shown in Figure 1.1a, is a double layer gridshell designed by Frei Otto with the engineers of Ove Arup and partners. It has a maximum span of 60 meters for a structural depth of 15 centimetres, and a self-weight of only 20 kilograms per square meter. The Sicli Pavilion, shown in Figure 1.1b, is one of the 1850 shells designed

by the Swiss engineer Heinz Isler. This reinforced concrete shell is remarkably thin, its slenderness is higher than the one of an eggshell.

(a) Manneim Multihalle (archive Frei Otto)

(b) Sicli Pavilion (distributed under Creative Commons License)

Figure 1.1 – Shape as a way to withstand loads: two iconic structures.

Structure is only one aspect of building engineering. The potential of form for other performance criteria, like energy consumption, remains largely unexplored. Shape optimisation of buildings for solar energy collection was performed with promising results in [134]. Figure 1.2a illustrates one typical result of such optimisation: different colours represent different cladding materials. The mastering of geometry can also allow the architect to control the shadows cast by a structural layout, like shown in Figure 1.2b [259]. These examples illustrates that comfort in buildings could benefit from geometrical optimisation.

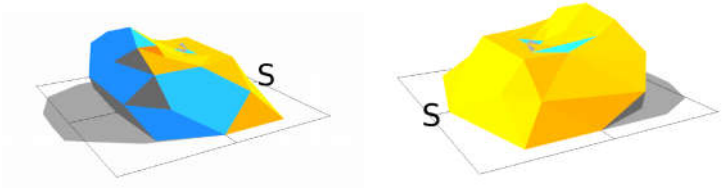

(a) Shape for solar energy collection (picture: [134])

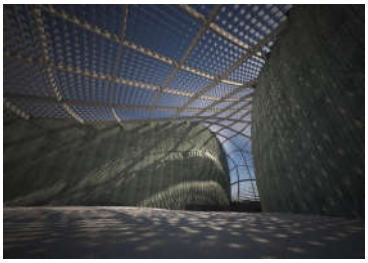

(b) Optimisation of shadows (picture: [259])

Figure 1.2 – Complex geometries optimised for non-structural purpose.

1.1.3 Challenges for the construction industry

The promise of structural efficiency is not always satisfied by free-form architecture. The performance of contemporary construction materials, of structural analysis tools and of computer-assisted fabrication allowed the construction of numerous structures that are rather inefficient, see Figure 1.3. Some structures become paradoxically praised as feats of engineering because of the efforts employed to make the inefficient work.

The complexity of the structural design of doubly-curved shapes should not however be understated. Ekkehard Ramm, one of the pioneers of computational mechanics, called thin shells the *Prima Donna* of structures: they can be in a *'good mood'* and have the efficiency of the structures presented in Figure 1.1, and they can be in *'bad mood'* and be subject to catastrophic failures. Shells are indeed sensitive to imperfections, so that imprecisions during construction or design based on simple mechanical models can lead to collapse. We can refer to many roof collapses during the twentieth century, even for structures designed by prominent structural engineers. For example, the shell roof of the Cuernavaca Chapel (designed by Felix Candela) collapsed during decentering. Several gridshells designed in the early 1990's

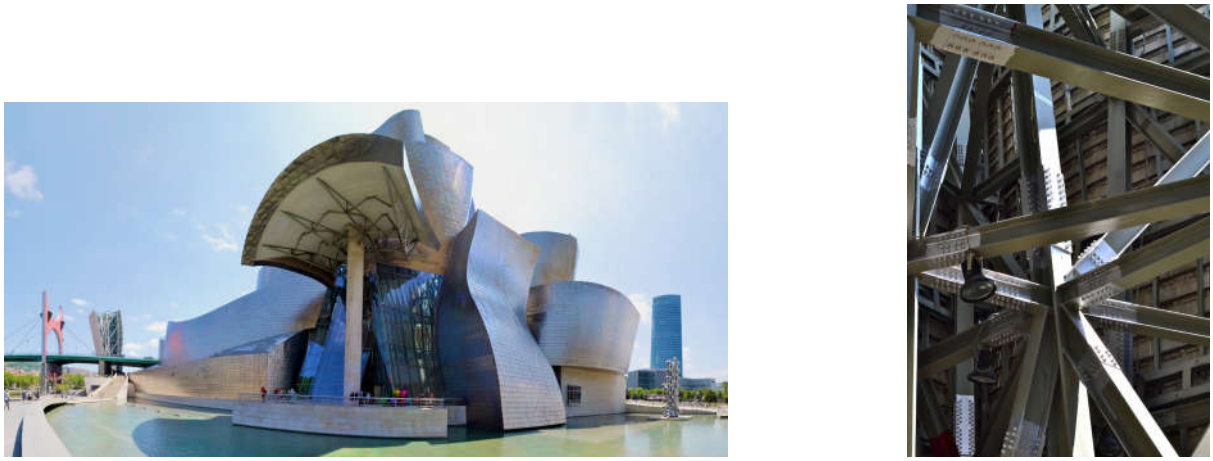

Figure 1.3 – A complex shape can hide an inefficient structure (picture: Romain Mesnil)

collapsed because of the connections used [226]. Such events lead to the assessment of the influence of the nodal stiffness in the stability of gridshells, which have demonstrated that doubly-curved structures are highly sensitive to small imperfection that can arise from manufacturing imprecisions. The interrelation between shape and structure is not considered by most of the computer-aided design tools, so that without guidance during early stages of design, such disorder can potentially be detected much later in the project timeline, with implication on the total cost.

In addition to these properties of shell structures, the new paradigm of *'free-form'* architecture challenges fabricators and builders by the complexity of their forms. In the building industry, the fabrication of elements relies on mass production and standardisation. When building free-form structures, the repetition of elements is no longer guaranteed as the number of polyhedra with extreme repetition of elements is limited and often restricted to spherical shapes. The five platonic polyhedra represented in Figure 1.4 are indeed the only polyhedra to have a unique vertex, face and edge. Beyond these shapes, the designer has to make compromise between repetition of elements and formal freedom.

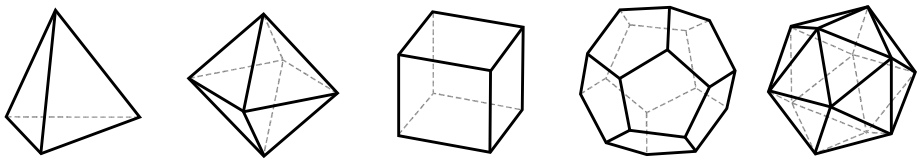

Figure 1.4 – The five platonic polyhedra: tetrahedron, octahedron, cube, dodecahedron and icosahedron

Repetition is not the only factor affecting the economy of free-form structures. The manufacturing of the different elements constituting the structure or the envelope is indeed often challenging. The most studied example is the planarity of quadrangular panels. Flat or singly-curved elements can easily be fabricated from extruded glass or metal sheets. Doubly-curved panels however require the fabrication of a mould, which is extremely expensive. Therefore, designs with planar facets are generally considerably less expensive than doubly-curved facets. This topic is reviewed in detail in Section 2.3.3.

The combination of these two factors - loss of repetition and difficulty of manufacturing - makes the design of free-form architecture tedious and fundamentally different from the design of conventional structures. In standard projects, fabrication is often thought independently from structural design and is only considered in preliminary or detailed design, whereas in non-standard architecture, fabrication should be considered from the conceptual design stage, as technological constraints might affect the final shape. Several strategies have been developed in order to cope with these difficulties. The next section presents a short overview of the different design methodologies employed in practice.

1.2 Limits of current design approaches and need for integrated design tools

Two opposing design approaches are commonly used in free-form architectural design. The first approach is a geometrically-constrained design strategy. It considers restricted families of shapes that are known to be constructible. The second approach propose to generate shapes with arbitrary methods and to consider fabrication constraints later on. We propose to illustrate the limitations of both approaches with two examples of built projects.

1.2.1 Limitations of geometrically-constrained methods

The engineering firm Schlaich Bergermann und Partner was the first to use geometrically-constrained strategies to generate free-form gridshells covered with planar facets. One of the most popular techniques developed in the office are the so-called *scale-trans surfaces*. They tried to apply this method for the shape generation of the roof of the Palacio de Comunicaciones in Madrid. Despite their efforts to rationalise the geometry, the engineers did not manage to fit the complex boundary shown in Figure 1.5 and finally used then a pneumatic surface covered with a triangular mesh [225]. Geometrically-constrained design methods lack of tools for shape modelling. The growing demand on complex shapes and the success of NURBS-based modelling in architecture has forced the engineers to use post-rationalisation techniques.

Figure 1.5 – The gridshell covering the courtyard of the Palacio de Comunicaciones *(picture distributed under Creative Commons licence)*

1.2.2 Limitations of post-rationalisation techniques

One of the first project using the most recent post-rationalisation techniques is the structure covering the department of islamic art in Le Louvre, shown in Figure 1.6. In the conceptual design stage, the shape was not covered with planar panels and a large room for the rationalisation was left to geometry experts *Evolute*. The reference geometry was parametrised by its lines of curvatures, because such parametrisation yields both planar panels and optimal offset properties, as we will see in Chapter 2. According to Wallner and Pottmann: *unfortunately this surface geometry does not leave us sufficient degrees of freedom to achieve a satisfactory quad mesh* [258]. The result of post rationalisation was indeed not satisfactory, both from æsthetical and structural perspectives. Another solution was to be found, and *Evolute* proposed an alternation of triangles and planar quadrilaterals, which is less costly than a triangular grid and was finally built [258].

This example shows that a post-rationalisation during late stages of the design is potentially very difficult. The most sophisticated algorithms can fail to find elegant discretisations satisfying manufacturing

(a) Overview *(picture distributed under Creative Commons licence)*

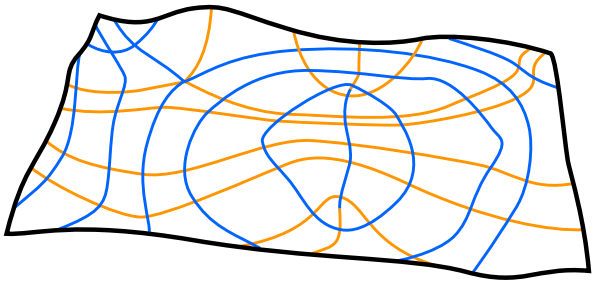

(b) Lines of curvature *(image inspired by [258])*

Figure 1.6 – Roof spanning over the Visconti court in Le Louvre museum (architect: Rudy Ricciotti and Mario Bellini).

constraints on some surfaces because of inherent surface properties. In other terms, the shape imposes the topology of the parametrisation, and the objectives of post-rationalisation might be changed in order to accommodate an otherwise infeasible design. An undeniable ingenuity for solving construction problems during post-rationalisation has to be recognised, but it does not mean that this is the best way forward.

1.2.3 Workflow in free-form architectural projects

The two design strategies currently used by engineers and architects suffer from different limitations. Geometrically-constrained approaches suffer from a lack of diversity, and are often not suited for highly-constrained projects. Besides, no new shapes for fabrication-aware design have been introduced since the 1990's. The limitations of post-rationalisation techniques do not lay within the mathematical methods, but rather on the workflow that they induce in free-form projects. Bagneris [15] denotes that post-rationalisation techniques *singularise* the shape in the design process, as its generation principle becomes irrelevant once set as an input in an optimisation procedure. Still, the form remains in interoperability with many factors, that would have to be solved during construction . Perhaps the most insidious flaw of post-rationalisation strategies is that the average user is unaware of the intrinsic limitations of the modelling technique he or she is using in the first place.

1.3 Existing tools for the rationalisation of fabrication

To better understand the specificity of free-form design, let us go back to organisation of the structural design process.

1.3.1 Conceptual structural design

The design of a building is generally divided in four stages: conceptual design, preliminary design, detailed design and production planning. In the conceptual design stage, the architects have an open range of possibilities, but little knowledge of their design. Engineers are typically involved in latter stage of design, when the structural form has already been defined, as illustrated in Figure 1.7 [176]. With time, the design knowledge increases whereas the design freedom decreases. In standard projects, fabrication is often considered in the latest design stages, as it requires a high level of knowledge on the design. This gap between the knowledge on the constructibility and the form-finding process has an impact on the overall cost of a complexly shaped envelope.

1.3.2 Classification of design tools

A parallel can be made between the project timeline and the tools used by architects and engineers. Three families of tools can be identified in structural morphogenesis: form-finding tools, analysis tools

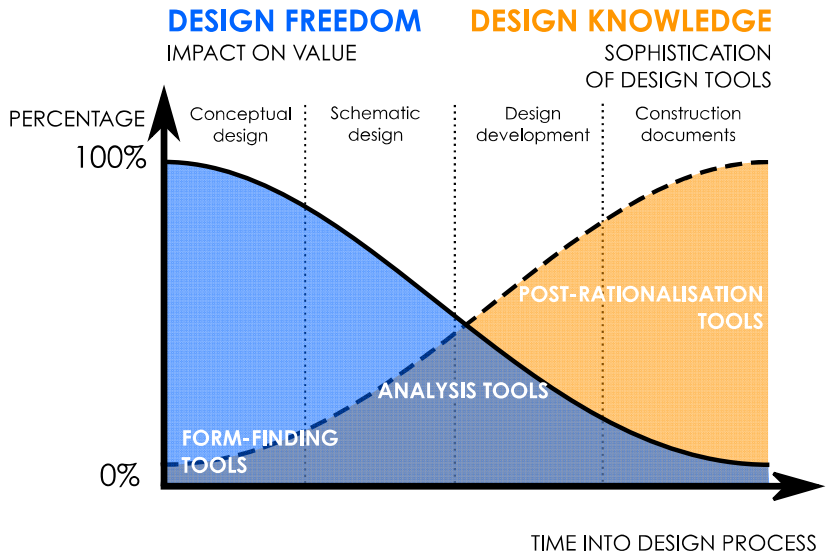

Figure 1.7 – Evolution of design freedom and design knowledge over the course of a project and corresponding tools. After [176].

and post-rationalisation tools.

Form-finding tools are used in early design stages and aim at generating a form. Although structural engineers usually identify the term *form-finding* to mechanical form-finding, we use it in a more general sense. The medium of the form-finding process can either be physical (like Frei Otto's soap film experiments) or Frank Gehry's models [230] or numerical.

Analysis tools are used from schematic design and aim at evaluating the performance of the generated shape or structural system. They are typically used by engineers, although some architecture offices make use of analysis tools in particular contexts. Frank Gehry's models are 3D-scanned and transformed as valid CAD information, which makes the analysis tools at the core of his design process. An ubiquitous example of analysis tools in the construction industry is the finite element analysis.

Post-rationalisation tools aim at improving some properties of the design: they are used in design development stage, once the shape and structural systems have been determined. They are often based on analysis tool and use optimisation techniques. We can cite various examples, like panel nesting (based on combinatorial optimisation), cross-section optimisation, mesh relaxation, etc.

1.3.3 How form is parametrised

Independently of the kind of design tool used, the shape parametrisation is a central issue in free-form architecture. Different tools are offered to the designers for that purpose. Two concurrent philosophies exist:the surface-based modelling strategy, and the mesh-based modelling strategy.

Surface-based modelling considers smooth surfaces that are later discretised. The most popular tools used are Non-Uniform Rational Basic Splines (NURBS) which were developed independently by two French engineers: Pierre Bézier and Paul de Casteljau [63, 24]. NURBS represent a surface by the means of control points and bases functions, namely Bernstein polynomials. NURBS have interesting mathematical properties, but do not provide the end-user with information on their constructibility or mechanical behaviour. They also encounter some limitations for the modelling of complex topologies.

NURBS patches have indeed a genus[1] of 0 or 1, so that parametrisation of shapes with complex topologies is difficult and requires many control points. Shepherd proposed surfaces of subdivisions for the modelling of complex shapes in architecture [231] because of the flexibility they offer in the generation of complex topologies and patterns (hexagonal, quadrilateral, etc.). A similar approach was proposed by Gebreiter [93].

Meshed-based modelling considers the generation of shapes as discrete surfaces. They can thus incorporate information about their potential fabrication, and also structural behaviour (for example through finite element analysis). It is a rich field of study, whose applications to architecture have emerged in the last decade. The drawback of those methods is the high memory usage and difficulty to reconstruct equivalents of smooth notions, like curvature for example. This specific topic is studied in a field of mathematics called discrete differential geometry.

1.4 Opportunities for structural design and problem statement

1.4.1 Need for guidance in conceptual design

Discrete differential geometry is constructed from the notion of invariance under certain transformations, and comes directly from the idea developed by Felix Klein [40]. These notions require a high level of mathematical abstraction, which lacks to most architects and engineers. Geometry is perhaps the most intuitive field of mathematics, as difficult problems can simply be drawn with rudimentary tools. The importance of intuitive reasoning in mathematics and geometry is brilliantly exposed by David Hilbert in his book *Geometry and the Imagination*.

> *As to geometry, in particular, the abstract tendency has here led to the magnificent systematic theories of Algebraic Geometry, of Riemannian Geometry, and of Topology; these theories make extensive use of abstract reasoning and symbolic calculation in the sense of algebra. Notwithstanding this, it is still as true today as it ever was that intuitive[2] understanding plays a major role in geometry. And such concrete intuition is of great value not only for the research worker, but also for anyone who wishes to study and appreciate the results of research in geometry.*
>
> David Hilbert [108]

One of the great challenges of architectural geometry is to provide the end-user with intuition on deep notions of geometry. The tools of architectural geometry should provide insight to the people who build. The most recent geometrical modelling tools are however used as black-boxes by the end-users and disconnect them from the comprehensions of the possibilities and limitations of the model they are creating. The question of intuitive steering of form is rarely assessed in existing literature, and some paradigms of computer graphics (like control points based deformation of meshes) are transposed to 'architectural geometry'. Modelling an architectural shape directly from a NURBS patch and the manipulation of its control points is rarely used in practice. Even in general free-form design, it is much more common to use some geometrical primitives, like lofting of curves or sweeping surfaces. Providing architects with intuitive ways of understanding complex geometrical notions is thus key for the development of new structural and architectural concepts. Combining intuitive shape generation and respect of fabrication constraints is one of the challenges offered to researchers and practitioners.

1.4.2 Design constraints as opportunity

The term constraint refers to a limitation and can thus be perceived with a bad connotation when associated to design. Some artists, architects or engineers used nonetheless constraints as a way to create

[1] The genus is a topological invariant which corresponds to the number of handles of a shape. Two shapes with the same genus can be mapped by a homotopy. A sphere (genus 0) and a torus (genus 1) are two different topological objects.

[2] highlighted by Hilbert

new pieces of art. Classical theater was based on rules of classical unities defined by Aristotle. In poetry, *l'ouvroir de littérature potentielle (OULIPO)* was founded to discuss the role of constraint in artistic creation. Constraint is viewed by the members of l'OULIPO as a potential for new literary material. Other related artistic movements appeared in the second half of the twentieth century.

Parce que la forme est contrainte, l'idée jaillit plus intense!

Charles Baudelaire

Architectural projects are obviously subject to cultural constraints linked to the site, so that architectural shape often emerges from the surrounding context. Technological constraints are however not considered with the same attention. In the present dissertation, we propose to follow this principle of constraint as design opportunity. Rather than rationalising a given shape, this dissertation explores the possibilities of generating shapes with a pre-defined set of fabrication constraints. Starting from construction constraints, we will show that it is possible to generate new design spaces that can be explored independently.

1.4.3 Fabrication-aware structural optimisation

The proposed methodology provides several method to generate economically-viable solutions in terms of fabrication. The richness of the available design space must then be evaluated in order to provide design guidelines for engineers and architects. The nature of the design space can be determined mathematically (e.g.: the space of feasible solutions is a vector space of dimension N), but also with more practical considerations (e.g.: it is possible to model easily a dome or a peanut-shaped structure).

Our approach follows guiding principles based on geometry. The mechanical reliability of the proposed structural configurations must therefore be assessed in order to provide the end-user with a complete overview of its design. To do so, this work proposes to explore space of feasible solutions by the mean of structural and multi-disciplinary optimization. The methods for shape generation developed in the present work create parametrised design spaces and can be compared to usual shape modelling frameworks, like NURBS.

1.4.4 Organisation of the dissertation

This dissertation is hence organised in three parts. The first part introduces the appropriate literature review on architectural geometry. The second part presents three different methods for fabrication-aware shape generation. The methods consider different constraints and yield different design spaces. The third part proposes an exploration of the design spaces generated in the second part from the point of view of a structural engineer. A particular emphasis on structural performance and on potential for the developments of innovative structural systems is made.

Hence, more precisely this chapter presented a brief and critical overview of the context of the design of complexly shaped structures and envelopes. The need for bottom-up design strategy for free-form architecture has been identified.

Chapter 2 reviews the main bibliographical references related to the design of doubly-curved shapes. A brief summary on existing literature is made and specific research questions addressed in the following of this dissertation are raised.

Chapter 3 introduces a new methodology for the generation of shapes with high node congruence. Mesh transformation by edge parallelism are used in an innovative way to yield repetition of elements. A new class of meshes derived from this methodology is then presented and its formal possibilities are explored. A link with smooth geometry is proposed, and it is demonstrated that the integral of gaussian curvature is the key parameter governing the repetition of elements in free-form structures.

Chapter 4 presents the application of the geometry of circles in space to the modelling of structures covered with planar facets. The potential offered by the parametrisation of complex shapes by portions of Dupin cyclides is discussed. A new family of shapes generated from three curves and called *super-canal surfaces* is derived from the proposed framework.

In Chapter 5, an innovative design strategy for the design of shapes with planar facets is developed. The method is a reinterpretation of descriptive geometry, which was invented in the eighteenth century. The reference to this ancient representation technique makes the method highly intuitive.

Chapter 6 explores the potential offered by the marionette method for the design and optimisation of shell structures. The relative performances of different optimisation algorithms are proposed for problems described with the marionette technique or with the ubiquitous NURBS modelling framework.

In Chapter 7, applications of the marionette method for the structural design of gridshells are discussed. The structural performance of non-regular grid pattern is assessed and compared to more conventional patterns.

The last chapter recalls the main results of this work, and concludes on their potential for practical application in free-form architectural design. Possible applications and improvements of the proposed methods will also briefly be exposed.

Chapter 2

Challenges of structural morphology

This chapter presents a critical literature review on different disciplines that deal with the rationalisation of free-form architecture. The review includes both structural and geometrical considerations and identifies potential areas of development that are studied in the next chapters of this dissertation.

2.1 Structural morphology

The term *structural morphology* is employed to describe the process that leads to the design of a structure, and deals more specifically with the interaction between form, structure and technology [263]. A working group (WG15) of the International Association for Shells and Spatial Structures was created in 1991 to face the challenge created by the use of new computer-aided design tools. This working group deals with the design process itself, and not just geometry. Keeping the same philosophy, the present section discusses the design process itself, whereas the next sections review specific technical aspects of free-form structures.

2.1.1 Representation in structural morphology

The question of representation is essential to the practice of architecture: Hanif Kara defines architecture as a *visual discipline*[1]. The visual representation of complex shapes but also of the design process is thus of high importance.

Descriptive geometry

Nowadays, representing a building with sections, plane view and elevation seems natural. Sakarovitch shows however that such representation is the result of a long evolution and that several competing techniques were discarded along the centuries [214]. Descriptive geometry was introduced by Gaspard Monge as a synthesis of different techniques used to describe complexly shaped blocks. This discipline is based on the representation of three dimensional objects in two dimensions, and the fundamental mathematical tools used are planar projections. This point of view is fundamentally the one of affine geometry. The representation of free-form structures with plans or cross section is however not sufficient anymore, and full 3D models are required to represent consistently and accurately curved shapes.

Descriptive geometry can be considered as a simple example of *dimensionality reduction*: it represents a three dimensional shape in two dimensions. It is interesting to notice that the topic of dimensionality reduction raises the interest of engineers and architects: the visualisation of a parameter space requires often to perform projections or classification, like proposed in [104]. The representation of shapes in two dimensions is an important aspect of the construction of an understanding of complex structures, because the brain reconstructs naturally three-dimensional objects from projections on the retina [175].

[1] Lecture *In Search of Design Through Engineers* at Harvard University, 2013.

Surfaces from two curves

The next section presents some families of shapes commonly used in architectural modelling. Those shapes are usually generated from two curves and a simple rule of transformation, like translation, scaling, rotation, etc. This point of view has several advantages. First, the properties of the discretisation can easily be controlled (facet planarity, repetition of elements, etc.). Second, it simplifies the representation and comprehension of the shape for the designer. The process is abstract (the designer has to manipulate transformations), but not computational (the designer cannot be substituted by a computer, which remains merely a way to speed up the shape generation). Third, it simplifies the exchange of information across different actors of a project, since one can share not only a geometry, but also the process that led to this geometry. In that manner, modifications to a design can be adapted in a coherent framework.

NURBS modelling

One of the most popular modelling software used by architects for free-form architecture is RHINOCEROS which describes surfaces as NURBS [2]. A comment has been made on NURBS modelling in the first chapter of this dissertation. By doing an analogy with computer programming language, we could say that shapes constructed from two or three curves are high level language, whereas NURBS modelling are lower level language, closer to computation and further away from intuition. Despite undeniable advantages for shape representation (efficient memory consumption, compact support), we can doubt that architects and engineers have an intuitive understanding of Bernstein polynomials. NURBS modelling is therefore a tool of representation, but unlike surfaces from two curves or descriptive geometry, it cannot be classified as a tool for comprehension [16].

2.1.2 Formex algebra and configuration processing

In this dissertation, the word complexity describes the behaviour of a system or model whose components interact in multiple ways. As an example: the panels of a free-form envelope can be considered to be in interaction with each other, as the modification of one panel affects automatically its neighbours. The discipline called nowadays *architectural geometry* deals with these interactions, as buildings are constituted of thousands of different components (panel, beam, node, etc.).

This definition of complexity was adopted by professor Hoshyar NOOSHIN, who describes the question of structural morphology as *configuration processing* [183]. NOOSHIN proposed an algebraic formalism to deal with configurations, called *formex algebra* [181]. Starting from elementary rules of tranformations, formex algebra generates a vast variety of structural configurations, like gridshells, space trusses or nexorades. An example of geometrical transformation used in formex algebra is the concept of *pellevation* which considers a fixed planar projection and different lifting strategies [182]. Formex algebra deals with the relations between components, and as such, is suited for parametric problem representation. Rather than solving one problem, formex algebra aims at solving a family of problems. A programming language, called Formian was developed for that purpose [184].

The work on formex algebra is a pioneering work that triggered reflections on parametric design in structural engineering and architecture. Many followed this path, as the use of parametric design gained popularity in the late 2000's with the use of GRASSHOPPER™, a visual scripting tool thought as a plug-in for the NURBS modelling software RHINOCEROS™.

2.1.3 Structural morphology and Motro's diagram

The spectrum of all possible interactions between architectural components goes beyond geometrical considerations. Buildings have indeed to withstand loads, either induced by their own weight or by external actions, like wind or snow. MOTRO identified five aspects that can be treated by structural engineers [1] (see Figure 2.1):

- Form: this term can refer to the form of the whole structure, or to the form on individual components;

[2] Other examples of software implementing NURBS are CATIA, SOLIDWORKS, etc.

- Force: which encapsulates the external forces, pre-stress, and structural response (displacement, stress);
- Structure: which describes the arrangement of components (grid pattern, hierarchy, etc.), this notion is related to *configuration processing*;
- Material: the term deals here with the mechanical properties of material: stiffness, brittleness, etc.;
- Technology is the term that focuses on fabrication and construction processes.

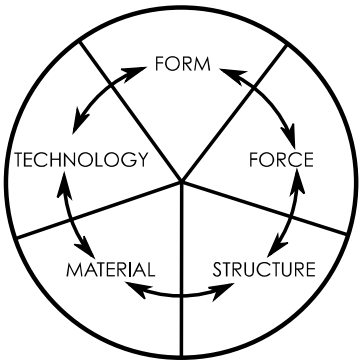

Figure 2.1 – The form-force diagram [15].

Bagneris *et al.* identified three main design strategies for free-form structures based on the intepretation of the form-force diagram [16, 15]. We use this approach to present the literature review in the following of this chapter.

Geometrically-constrained design approach

The first design approach considered by Bagneris *et al.* considers shapes which have well-known properties. The composition and intersection of such shapes provides a design-space where the technological aspects are understood and taken into account throughout the whole process, from design to fabrication. The most commonly used analytical shapes are reviewed in Section 2.2.

Mechanically-constrained design approach

The second design approach considers shapes that solve a mechanical problem. The most common example is when the shape is the result of a form-finding process, either from physical or numerical modelling. Generally, the mechanical problem to solve is related to the properties of the structural material. Mechanically constrained approach often consider technology implicitly. For example, masonry structures cannot withstand tensile stress and need to follow funicular shapes. Tensile structures (polymer-coated membranes) cannot withstand compression and need to be pre-stressed.

Flexible design approach

In the last design approach identified by Bagneris *et al.*, the shape is determined by considerations that are not directly related to the last four items listed previously: the parameter 'form' stands out and is treated separately from constructional or mechanical aspects. This makes the communication with engineers and contractors more difficult than with the two previous design approaches. For the engineer, the challenge becomes to *'make it work'* rather than questioning the structural rationality [17]. The choice of material and structural system is then a matter value engineering and is done *a posteriori*. Steel structures are prominently used in flexible design approaches, because steel can withstand equally tension or compression.

2.1.4 Comment on structural morphology approaches

The design of complex geometries in architecture requires a thorough knowledge of different disciplines. Configuration processing studies the relations between different components of an envelope or structure. Its development gave birth to a parametric modelling approach that is now ubiquitous. A more general reading grid for design strategies was proposed by contributors of the structural morphology working group of the International Association for Shells and Spatial Structures. Three design approaches can be identified, whether they start from fabrication constraints, construction constraints, or other constraints. Some buildings appear to merge fabrication and structural performance altogether, making a classification in one category difficult. This is often the case for masterpieces of structural artists: like Felix Candela's shells, which are based on geometrical principles, but are remarkably thin. Nicolas Esquillan or Eugène Freyssinet shells are also based on construction principles and yet have a high structural efficiency. The design process of such projects could equally be qualified as a structurally-informed 'geometrically-constrained design approach' or fabrication-aware 'mechanically-constrained design approach'. A more recent example is the Dutch Maritime Museum, which is based on a form-found shape derived from an Airy stress function covered with with planar facets [6].

In the followings of this literature review, we adopt the reading grid proposed by Bagneris *et al.*. We should however recall that, like all classifications, the form-force diagram has some limitations. Since Motro's first work, the notions of comfort and use of the building have become an important component of building engineering, and are not unquantified concepts anymore. Among the many fields of building physics, we can list acoustics, light, energy consumption, etc. We should point out the fact that structural masterpieces can also have poor architectural quality because of bad thermal performance or noise insulation. The form-force diagram could be improved by taking into account the notion of usage, but this issue goes beyond the scope of this dissertation. This remark illustrates the complexity of the design process in architecture, even if restricted to engineering considerations. Facing this complexity, the designer needs to build an intuition of the geometry he or she is drawing, and of the consequences on the technological application. Most of the representation tools used in the history of architecture were aiming in that direction. Computer oriented applications should provide guidance to the designers, much remains to be done on this issue.

2.2 Analytical geometry and the rise of non-standard architecture

This section presents the main geometrically-constrained design approaches. Some families of shapes with interesting properties have been well-identified by builders and used in different technological contexts. Individually, each family of shape is restricted, but the mastery of ancient builders was based upon the composition of such shapes. In the following of works on stereotomy, designers developed analytical methods to generate shapes satisfying fabrication constraints. As new materials and structural systems emerged, the technical requirements of building envelopes evolved. Different families of shapes have been used in accordance to specific construction methods, from stone assemblies to thin reinforced concrete shells of the twentieth century or contemporary glazed steel gridshells.

2.2.1 Surfaces of revolution

One of the most common and ancient shape used in architecture is the surface of revolution,which is generated as the envelope of the rotations of a planar curve, called meridian, along an axis. The curves perpendicular to the meridians are called parallels. The first examples of circular housing can be found during the Neolithic. Domes are considered to have been invented by Assyrians, however they truly developed under the Roman Empire. A famous design from roman antiquity is the Pantheon in Rome, built around 125 AC, it is a spherical cupola spanning 43.3 meters. It was the largest span for a concrete shell structure up to the turn of the twentieth century: its design and structural behaviour is commented in [156, 155]. Figure 2.2 shows the cupola covering the Pantheon, the coffering follows the meridians and parallels of the surface of revolution, which are also lines of curvature.

Figure 2.2 – The pantheon in Rome, a concrete shell as a surface of revolution *(picture: Romain Mesnil)*

In a remarkable treaty[3], CHOISY explored the geometry and statics of Byzantine vaults, which are compositions of surfaces of revolution [54, 113]. He attributed this choice to the ease of fabrication, because a simple rope and one fixed point are sufficient to generate those surfaces: *'Furthermore, it would be illusory to attribute a rigorously defined geometrical drawing to Bizantine vaults. In more than one case, the irregularity of form of the vault panels shows that the Byzantines contended themselves with a compass to draw the profile.'*[4] [54].

More recently, surfaces of revolution have played a crucial role in the birth of reinforced concrete shells. The use of surfaces of revolution is indeed ubiquitous in early reinforced concrete shells realisations. It should be linked with the developments of shell theory, that was first formulated for shells with a symmetry of revolution [25]. For example, the German engineer Franz DISCHINGER masterfully designed thin concrete shells while deriving analytical formulæ on the buckling of shells of revolution [68].

Surfaces of revolution are still commonly used in many architectural applications for different structural systems. Their inherent properties make them economical: their lines of curvature (the meridians and parallels) are known by construction, and the symmetry of revolution yields high repetition of elements.

2.2.2 Constant slope surfaces

The development of timber frames and the separation between the structural behaviour of walls and roofs led to a new definition of shapes. Consider a roof spanning over a closed planar contour, like shown in Figure 2.3: a simple way to cover this is to generate a surface with constant slope. Such surface are generated by sweeping a line along a rail curve. The construction of such surfaces is thus eased by the fact that only straight elements are used, and the orientation of the beams is controlled by one unique angle. Constant slope surfaces are used in vernacular architecture in western Europe, and still used today, as illustrated by the San Benedegt Chapel designed by architect Peter ZUMTHOR.

For closed contours, the constant slope surface intersect itself and a crease appears at the apex of the shape, as seen in ZUMTHOR's design. This can be illustrated simply by considering a mechanical interpretation of constant slope surfaces. Considering a pile of sand, the stability is given by Coulomb's law. The critical shear stress τ is given as a function of the normal stress σ, cohesion c and friction angle ϕ.

$$\tau = c + \sigma \tan \phi \tag{2.1}$$

In sand, there is no cohesion, and the stability of piles imposes thus the slope to be equal to ϕ (a common value for ϕ is 35°). One can think of experiments by Frei OTTO and his team with sand piles published in IL25 and based on following remark: *'Any granular material falling from a fixed point forms a cone on the surface below and a funnel within the granulate mass with the same angle of inclination, the natural*

[3]The book can freely be consulted on the INHA website.

[4]Translated by us from the citation: *'Au surplus, il serait illusoire d'attribuer à toutes les voûtes byzantines un tracé géométrique rigoureusement défini, et dans plus d'un cas l'irrégularité de forme que présentent les panneaux des voûtes montre que les Byzantins se sont contentés d'un cimbelot pour tracer l'arêtier, se fiant pour régler la courbure des surfaces.'*

(a) (Picture: Leo Thomas Naegele) (b) (Picture: Felipe Camus)

Figure 2.3 – St. Benedetg Chapel: an example of constant slope surface (arch. Peter Zumthor)

angle of repose, 35 degree.'[92]. Therefore, sand piles or dunes are constant slope surfaces: the normal discontinuity at the apex of dunes is an illustration of the shapes taken by constant slope surfaces.

The example of a rectangular planar view gives four planes, and constitute a classical roof shape in western housing. For planar contours, the sharp features of constant slopes surfaces can be computed using the medial axis of the contour curve. A point is on the medial axis of a curve if it is the center of a circle which is tangential to the contour curve in two distinct points at least. Different computational method for the determination of the medial axis of a shape have been proposed, a survey of which is proposed in [13]. Recently, constant slope surfaces were revisited with robotic fabrication in order to create complex compositions with sand piles [114] in Figure 2.4.

Figure 2.4 – Sand creates naturally constant slope surface, the sand is added at specific points and the crest lines create a Voronoi diagram [114] *(picture:sandworks)*.

2.2.3 Ruled surfaces

As reinforced concrete shell gained in popularity, new shapes imposed by fabrication constraints arose. The formwork has a high impact on the cost of construction, and represent approximately 30% of the cost of the structure. An economical solution was to build the formwork with straight timber laths. Surfaces containing a family of straight lines are called *ruled surfaces*. An example of ruled surface and its application to a formwork for a concrete shell is shown in Figure 2.5.

Hyperbolic paraboloids are of particular interest because they are doubly ruled surfaces: two families of straight lines can be found on those surfaces. They have been used for the first time by the French engineer Fernand Aimond, followed by Bernard Lafaille [78]. Mexican structural engineer Felix Candela designed iconic shells using those shapes [51]. Like Dischinger before him, Candela developed

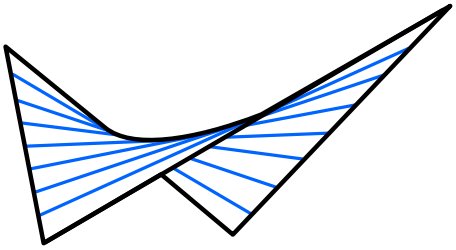

(a) Generation principle for a ruled surface

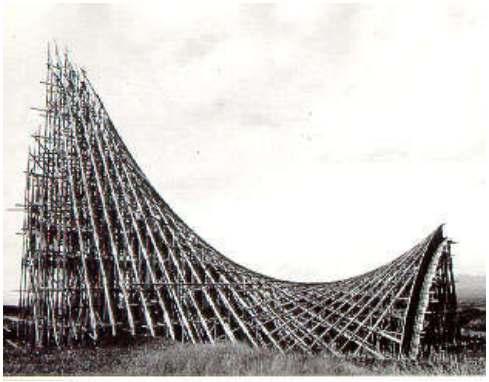

(b) Formwork of the Chapel Lomas de Cuernavaca (eng. Felix Candela)

Figure 2.5 – Generation principle for a ruled surface

analytical models for the shapes he implemented in his projects: he published results on the shell theory applied to hyperbolic paraboloids [52]. The design space used by CANDELA considers thus mechanical and constructional aspects and reflects his holistic approach.

Ruled surfaces have a negative gaussian curvature, so the formal freedom offered by hyperbolic paraboloids might seem restricted. The richness of Candela's work demonstrates how inventive designers can generate diversity from simple rules. This richness can also be found in the ornaments of another master designer: Antoni GAUDI. Although known for his experiments on funicular networks, GAUDI based his shapes on ruled surfaces. The strive for efficiency was not GAUDI's only inspiration, as he praised the æsthetic value of ruled surfaces. According to him *Paraboloids, hyperboloids and helicoids, constantly varying the incidence of the light, are rich in matrices themselves, which make ornamentation and even modelling unnecessary.* A new look on hyperbolic paraboloids was proposed by Hans SCHOBER recently and complete this short overview on ruled surfaces [226].

2.2.4 Scale-trans surfaces

Iron and steel appeared in the construction industry in the end of the nineteenth century. Those materials withstanding both tension and compression offered new possibilities for the design of transparent enclosures. The popularity of botanical gardens in the England of the nineteenth century was concomitant with the appearance of daring greenhouses. There are many examples that still stand today in England, but also in other countries, see for example the greenhouse of Auteuil, shown in Figure 2.6. Notice that no triangulation is visible in the picture: the glass panels are used as bracing elements, yielding a maximal transparency.

Figure 2.6 – The palm greenhouse in les Jardins des Serres d'Auteuil *(picture retrieved on Wikipedia and distributed under Creative Commons license)*

The first greenhouses were surfaces of revolution or cylinders, in the fashion of ancient vaults and domes. The emergence of a new formal vocabulary specific to doubly-curved glazed structures, later called *gridshells*, was only possible with the maturity of Computer-Aided Design tools for architecture. The German structural engineer Jörg SCHLAICH and his collaborators developed innovative structural concepts in the second half of the twentieth century and contributed to a revival of transparent gridshell structures. Jörg SCHLAICH and Hans SCHOBER designed glazed gridshells from the 1989 and the completion of a dome spanning over a swimming pool in Neckarsulm [110, 226]. This first realisation was not covered with planar facets, which lead to high cost for the manufacturing of the glass panels. SCHLAICH and SCHOBER proposed then the use of surfaces of translation for gridshells [224]. Surfaces of translations are defined by the translation of a curve (called generatrix) along another curve (called directrix), the principle of generation is given in Figure 2.7. Since opposite edges of quadrilateral facets generated by this principle are parallel, the facets are planar parallelograms. Surfaces of translation were first used by SCHLAICH and SCHOBER for the House for Hippopotamus in Berlin [224, 223]. The gridshell, spans 29 meters and achieves high transparency thanks to a cable bracing system developed specifically for the needs of the project.

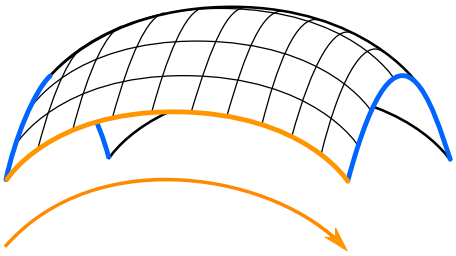

(a) Generation principle of surface of translation

(b) Gridshell covering the court of the Deutsches Historisches Museum *picture: SBP*

Figure 2.7 – Generation principle for surfaces of translation: directrix (light orange) and generatrix (blue)

Surfaces of translation were later generalised after a collaboration between Schlaich Bergermann und Partner, and Frank Gehry. The generalisation, called *scale-trans surfaces*, is based upon a simple remark: the property of parallelism is preserved by scaling. Therefore, a combination of a translation and scaling also yields opposite parallel facets, and therefore planar facets. The generation of scale-trans surfaces gives more freedom to the designer and provides more flexibility than regular surfaces of translation [98].

2.2.5 PQ-meshes from De Casteljau's algorithm

Bagneris proposed the generation of PQ-meshes by using De Casteljau's algorithm [15]. Starting from two curves, the method is based on the generation of developable strips as NURBS patches, each strip being controlled by two scalar parameters λ and μ. Developable strips can be viewed as a collection of small planar quadrilaterals, the method guarantees that the ruling lines of the developable surface are following the isoparametric lines. The technique offers additional shape control compared to surfaces of translation through the introduction of the supplementary parameters. This allowed explorations on boundary fitting problems.

2.2.6 Composition

If architecture is compared to a language, forms could be identified to vocabulary. Just like meaning is constructed from the combination of grammatical rules and vocabulary, composition of shapes is an essential tool used by architects. Such compositions can be based either on empirical rules or on computational approaches using shape grammars [240]. Composition of shapes is used in many styles, from gothic vaults to Frank Gehry's architecture, which is a composition of developable surfaces. Even if the considered surfaces are simple taken individually, their intersections create complex geometries.

(a) Cross-ribbed vaults of the Saint-Séverin church in Paris (*picture: Roman Bonnefoy*)

(b) Walt Disney Concert Hall (*picture: Romain Mesnil*)

Figure 2.8 – Examples of composition in architecture.

2.2.7 Comments on geometrically-constrained design approach

Geometrically-constrained design approach has been used extensively by designers throughout centuries. Simple generation rules can create wide design spaces, in particular when composition rules are applied. The different generation principles often use two or three curves and an euclidean motion (translation, rotation). It can be noticed that constrained geometrical approaches have often been used in accordance to mechanical theories, like demonstrated by Dischinger and Candela.

This approach has however been challenged in the recent years, with projects which cannot be described with usual shapes. Other geometrical frameworks allow more flexible shape generation and have gained popularity in the architecture community. As an example, NURBS modelling software use some intuitive shape modelling tools, like the two rails sweep, that do not have any counterparts in geometrically-constrained design approaches. Likewise, boundary fitting remains a complex task when one is using analytical shapes. These limitations led to the development of post-rationalisation techniques in the twentieth century. However, we will see in Section 2.3.1 that the idea of finding a unifying geometrical description of feasible architectural designs dates back from the eighteenth century.

2.3 Architectural geometry and post-rationalisation

This section reviews the literature on architectural geometry. This discipline lays at the intersection of analytical and computational geometry. Recent advances in those fields made the post-rationalisation of complexly shaped buildings possible, but also provided a sound theoretical foundation on some previously unsolved issues. A brief historical overview is first presented, then the two main technical problems addressed by architectural geometry are reviewed.

2.3.1 Geometry and stereotomy: the pioneering work of Gaspard Monge

Gaspard Monge was a French mathematician who had a great influence on architectural geometry. He developed descriptive geometry, which was a sound method to represent complex objects into two dimensions. Monge was driven by application to stereotomy: his lectures on geometry are often applied to architecture. An interesting example is the way Monge introduced his students to lines of curvature. Rather than taking an analytical approach, Monge defined lines of curvature as the only curves on a surface where the ruled surface generated by the normal vectors of the surface is developable. Monge saw opportunity to build vaults where blocks follow lines of curvature, because developable surfaces can be built as envelopes of planes and could simply be fabricated with tools used by builders. Figure 2.9 is

typical drawing of descriptive geometry: it describes an ellipsoid with a plane view, displayed with some elevations. The curve network corresponds to the horizontal projection of lines of curvature [142, 215].

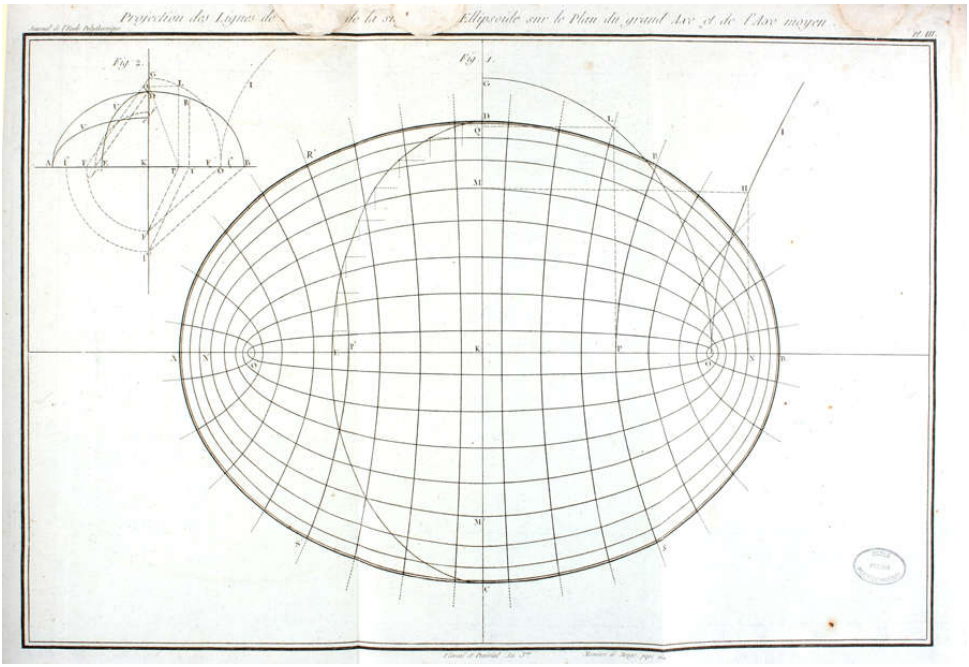

Figure 2.9 – Lines of curvatures of an ellipsoid with descriptive geometry [142].

Sakarovitch makes the hypothesis that Monge's vision of lines of curvature was driven by a constructive perspective, because Monge always presented lines of curvatures and stereotomy together in his lectures [215]. No evidence can confirm this statement for certain, as Monge did not leave any note on the genesis of lines of curvature. His approach blends however mathematics and architecture in a unique way.

Gaspard Monge aimed at generalising his approach to new shapes tailored to architectural constraints. He deplored indeed that *'artists almost always excluded from the composition of vaults the curved surfaces for which they did not know the lines of curvature, even when circumstances demanded them imperatively; and it is mainly to this that we must attribute the poor effect that parts of mortarless vaults often produce in architecture because in order to make a tracing doable, one does not always choose the most appropriate vault surface'* [5][171].

Mortarless architecture did not develop as Monge intended, and the generalisation of his method to arbitrary shapes remained beyond the computational capabilities of engineers at this time. Nevertheless, Monge proposed the first systematic approach for surface parametrisation in architecture, a method that would reveal to be fruitful with *Computer-Aided Geometric Design* tools. Gaspard Monge thus opened the possibility of performing post-rationalisation of architectural shapes, although he clearly stated that the problem to solve was to find appropriate surfaces for stereotomy and was thus more inclined to geometrically-constrained design methods. His intuition on the rationalization is still valid more than two hundred years after he wrote his first essay on geometry. As an example, the parametrisation of architectural shapes by lines of curvatures is reconsidered more than two hundred years after Monge's first publications [148].

2.3.2 A new science for complex shapes: discrete differential geometry

Buildings are complex objects by essence: different parts, like beams, or cladding have to be physically assembled. The introduction of doubly curved shapes makes each element unique and each interaction

[5] The text has been translated by [215]

peculiar. The emergence of this new complexity occurred in parallel of the developments of computer-aided design. The modelling of discrete surfaces or meshes for animation or rendering appeared in the 1970's, but with little knowledge transfer to the architectural community until the years 2000.

Remarkable advances have been made in the field of discrete differential geometry in the last decade, and especially at the TU Berlin, TU Graz and TU Wien. The first book dealing exclusively with this topic, titled *Discrete Differential Geometry* was published in 2007 by Bobenko and Suris [40]. The interaction between computer scientists, mathematicians, and architects has been influenced by the collaboration between the TU Vienna, the geometry consulting start-up Evolute and structural and façade engineering office RFR through the european project *Architectural Freeform Structures from Single Curved Panels (ARC)* [2][6].Two research axes can be identified in the followings of this project: one dealing with the properties of the cladding, the other dealing with the geometrical properties of the structural layout. Those two topics are closely related to the speciality of RFR, namely steel structures covered with glass panels.

The next paragraphs expose a state of the art on these two problems, with concrete examples demonstrating the technological challenges faced by designers and builders, as well as a exposure of the underlying mathematical theories. We will consider representation of free-form structures by meshes: the faces corresponding to cladding elements and the edges to support structure (beam elements).

2.3.3 Polyhedral surfaces: covering free-form architecture with planar facets

The most active field of research in architectural geometry is the question of shape discretisation with planar panels. The problem of covering an arbitrary shape with planar quadrilaterals was identified by Schlaich and Schober [224, 223]. It is of high importance for glazed roofs and façades, but is irrelevant in some cases. This section presents thus the appropriate literature on this topic, but also recalls the technological possibilities offered to a designer of free-form projects.

Technological alternatives

Four families of technological solutions for covering doubly curved surfaces can be identified. They are identified either by their mechanical properties (flexible or rigid), and by their gaussian curvature.

Flexible envelopes The advances in free-form architecture made by Frei Otto and his team in the 1960's are indissociable of membrane structures. New materials, like glass-fiber reinforced textiles or ETFE made possible the covering of large enclosures with extremely lightweight roofs [130]. Figure 2.10 displays an ETFE membrane structure: the thinness of the material can be observed during the installation of the membrane, proper pre-stress and boundary conditions assure then that the shape corresponds to a pre-determined state. Membrane structures constitute an economically viable alternative to glass panels and offer a great formal freedom. Their lightness is an advantage in terms of embodied carbon, but affects the acoustic, optic and solar performance of the envelope. In projects with high requirements, flexible envelopes might be less suited than glass.

Application of flexible moulds to free-form architecture have also been considered recently. [75] An overview of fabric used as formwork is proposed in [255]. The potential of such technologies remains to be explored, as it could provide the economical advantages of flexible envelopes with higher comfort. Notice that the design fabric formwork is guided by mechanical constraints linked to the pre-stress of the membrane and its interaction with the concrete during pouring. This is a topic on its own which should be treated separately from conventional solutions used for façade. Planarity of facets is important for many commonly employed materials, but it is irrelevant for fabric formwork, as rigidity of membranes stems from their curvature.

[6]Grant number: 230520

(a) Membrane structure during installation *(picture: LEICHT GmbH)*

(b) Membrane structure after completion *(picture: Romain Mesnil)*

Figure 2.10 – A tensile structure: 'les Vergers de la Plaine' (arch.:SCAU)

Doubly-curved panel The lens of the Saint Lazare station in Paris is a fine application of doubly-curved glass in architecture. The dome, designed by the architect Jean-Marie Charpentier in collaboration with engineering firm RFR, is a concatenation of a torus and of a sphere [18]. Doubly-curved glass panels were chosen in order to fit the geometry as smoothly as possible, like seen in Figure 2.11. Thanks to a double symmetry, the number of different panels was reduced from 108 to 54. The glass panels were heated and pressed onto custom-made moulds, the technological process is explained in [102]. The cost of the moulds and the work involved in the making of the glass panels makes this technological solution inadequate for large scale projects.

Figure 2.11 – The 'lens' of Saint-Lazare station *(picture: Jacques Mossot)*

Because of its high transforming temperature ($600°C$) and of the implications on the mould properties, glass is less suited than other materials, like FRP or concrete for application to doubly curved panels. So, built projects featuring doubly curved concrete or plastic panels are more common. Late work by architect Zaha Hadid, like the Heydar Aliyev Cultural Centre, feature doubly curved glass fiber reinforced concrete [268].

Singly-curved panels The development of singly-curved glass panels was made possible by advances in the domain of cold bent glass. One of the early examples of application of cold bent glass is the new façade of Strasbourg train station [27]. The reference geometry is a portion of torus, meshed along its meridians. The glass is bent along the lines of maximal curvature (the meridians). The envelope is not smooth in the direction of the parallels, but the resulting envelope achieves nonetheless an impression of visual smoothness and continuity. A more recent example of singly curved panels is the Fondation Louis Vuitton in Paris. Designed by architect Frank Gehry and engineering office RFR, the veils cover 13,500 m^2. In order to rationalise the fabrication process, each individual panel was approximated by a cylinder. The discontinuity of reflections due to the fitting process is highlighted in Figure 2.12.

Figure 2.12 – The Louis Vuitton Fondation: the panels have a cylindrical shape, yielding non-smooth reflections *light orange curve highlighted by us (picture: Romain Mesnil)*

Planar panels The most economical alternative is to fabricate planar panels. This solution is suited for extruded material, like glass, steel, aluminium. EIGENSATZ *et al.* list typical relative costs of panels, which are recalled in Table 2.1: planar panels are several times less expensive than singly or doubly-curved panels. Some doubly-curved panels might be easier to construct due to congruence of curves. Hyperbolic and elliptic paraboloids can be seen as surfaces of translation and have two families of congruent curves. Surfaces of revolution, like tori have one family of congruent curves.

		plane	cylinder	paraboloid	torus	cubic	custom
Glass	panel	1	2	5	5	5	35
	mould	-	2	18	24	30	-
Metal	panel	1	3	6	6	6	12
	mould	-	3	6	6	6	-

Table 2.1 – Comparison of the cost of typical panels (from [76]).

Triangular panels are always planar, while quadrangular or hexagonal panels are not. The trade-off is that triangular meshes have higher node valence than quadrilateral or hexagonal meshes, and thus higher node complexity, like illustrated in Figure 2.13, where the letter v represents the average node valence. Triangular gridshells can also appear to be less transparent than quadrilateral gridshells (although they are structurally more efficient), and other patterns are often preferred for architectural reasons. Finally, we point out that the high degree of hyperstaticity of triangulated gridshells make their fabrication tedious: the respect of tight tolerances is crucial to the construction of such systems.

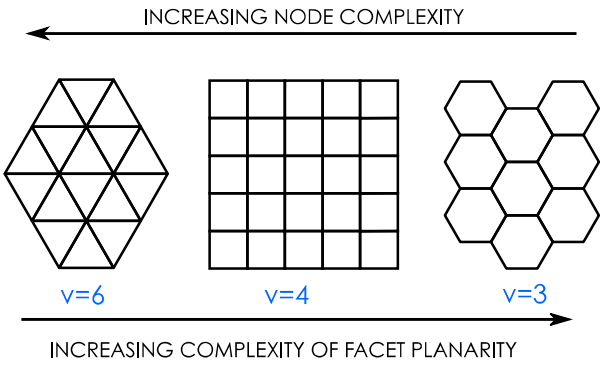

Figure 2.13 – Comparison of triangular, quadrilateral and hexagonal mesh.

PQ-meshes

Covering architectural envelopes with planar quadrilaterals was as important question for researchers in the late 2000's. SCHLAICH and SCHOBER demonstrated their practical interest, and Liu *et al.* made a link between this question and surface parametrisation [148]. Quadrilateral meshes covered with planar facets (also known as PQ-meshes) are indeed closely related to so-called networks of conjugate curves. These curves are obtained by integration of vector fields $(\partial_{\mathbf{u}}, \partial_{\mathbf{v}})$ satisfying a differential equation written as follows [40]:

$$\det\left(\partial_{\mathbf{u}}, \partial_{\mathbf{v}}, \partial_{\mathbf{uv}}\right) = 0 \tag{2.2}$$

Any smooth surface admits several conjugate curve networks. As an example, it is clear that lines of curvature satisfy equation (2.2). The principal curvature parametrisation is an orthogonal parametrisation defined by $\partial_{\mathbf{uv}} = \mathbf{0}$.

Equation (2.2) does not correspond to the exact planarity of quadrilateral following the conjugate lines. It denotes planarity of infinitesimal quads: writing ε the side lengths, (2.2) implies that the volume of the defect of planarity is at most of the order of ε^4. This statement is proven by doing a simple Taylor approximation. A quadrilateral pattern following conjugate curve network is thus almost planar, and planarisation is then needed. Planarisation is usually performed by minimisation of the sum of a planarity defect E_{planar} and of a fairing function $E_{fairness}$ (see for example [148]).

$$E_{planar}\left(q_{ABCD}\right) = \det\left(AB, AC, AD\right)^2 \tag{2.3}$$

The fairness function is usually computed on polylines. Writing $(\mathbf{v_i})_0^N$ the vertices of a polyline $\mathcal{P}$, a common definition is to use a quadratic functional:

$$E_{fairness}\left(\mathcal{P}\right) = \sum_{i=1}^{N} \mathbf{v_{i+1}} - 2\mathbf{v_i} + \mathbf{v_{i-1}} \tag{2.4}$$

Another possibility is to use Laplacian smoothing, introduced in [179]. Writing $\mathbf{E}$ the edges, and $(\mathbf{v_i})$ the vertices of the mesh, and ω_{ij} some weighting factors, it is defined by:

$$E_{fairness}\left(\mathcal{P}\right) = \left(\sum_{i,j\in\mathbf{E}} \omega_{ij}\mathbf{v_j}\right) - \mathbf{v_i} \tag{2.5}$$

Those theoretical results led to a better understanding of panelisation with planar quadrilaterals. Conjugate curves can be found by integration of conjugate vector fields. This can be done either on smooth surfaces, like NURBS [272], or on triangulated meshes [149]. Such top-down strategies are guaranteed to solve the problem of facet planarity, but the topology of the conjugate curve network remains imposed by the input shape. A slight change of form could yield different network topologies, so that top-down approaches are not suited for such explorations.

Planar hexagonal meshes

Like quadrilateral meshes, the properties of planar hexagonal meshes have been studied extensively. In plated structures, the valence of three of hexagonal meshes guarantees structural stability. This property has been used in some pavilions [105], one of the most notable one being the pavilion built for the Bundesgartenschau by the ITKE shown in Figure 2.14 [143].

The first operational technique for architectural design was based on *tangent plane intersection* [61, 250]. The principle of this method is to generate a set of points on a surface, to generate the plane tangent to the surface at each point, and finally to perform the intersection between the different planes: the final mesh is defined as the envelope of the different planes. The technique is easily understood, but the manipulation of seed points can be cumbersome. Some improvements of the method, combining tangent plane intersection and optimisation have been proposed in [273].

Planar Hexagonal meshes (PH meshes) have a close relation with lines of curvature, as it was shown that the edges of planar hexagons converge towards the Dupin indicatrix of a surface [261, 260]. Hexagonal

Figure 2.14 – Fortspavilion: a plated shell structure covered with planar hexagons *(picture: ITKE Stuttgart)*.

meshes follow thus lines of curvature, with additional constraints: in negative curvature area, planar hexagons have a bow-tie shape. This is undesirable in gridshells for structural reasons. Based on the understanding of the properties of PH meshes, a method for the parametrisation of meshes with planar hexagons was proposed in [144].

Constrained mesh generation

Several algorithms proposing modelling with PQ-meshes have been proposed in the recent years. The difficulty of modelling with PQ-meshes lies within the fact that they admit local deformations. Hoffmann studied local deformations of planar quadrilateral facets by performing offsets of a single face [109]. His method demonstrates that it is possible to make changes that are localised to a few panels only: for an arrangement of nine panels, it is possible to modify the geometry of the central panel without changing the mesh boundaries. This method is not directly oriented towards applications in architecture, but could be used with more global modelling tools.

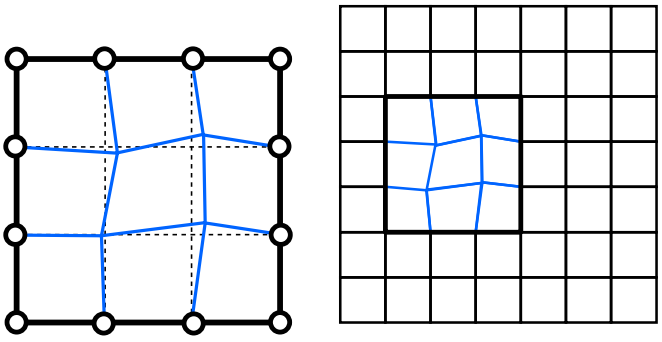

(a) A possible local deformation of a PQ mesh

(b) Influence on mesh regularity

Figure 2.15 – Local deformation of PQ meshes can yield poor smoothness while preserving planarity.

In practice, the planarisation of PQ-meshes can therefore yield local optima that are non-smooth because of the malleability of PQ-meshes. Smoothness measurements must thus be added: it is often based on the bending energy of polylines [148]. To this smoothness measurement $E_{fairness}$, a term taking into account the distance to the reference geometry $E_{closeness}$ (if the problem is a surface fitting problem). A typical planarisation algorithm minimises thus a functional E of the form:

$$E = E_{planarity} + \alpha \cdot E_{smoothness} + \beta \cdot E_{closeness} \tag{2.6}$$

The scalars α and β are weighing the influence of the different terms. They are global parameters for the optimisation: different values of α or β will yield different optima, with a limited control on the properties of the final result.

Several algorithms proposing to minimise the quantity written in equation (2.6) have been proposed. Bouaziz *et al.* implemented an optimisation algorithm based on projection [44]. Deng *et al.* studied the exploration of appropriate subspaces for the modelling with planar facets, but also with other constraints [65, 64]. The result is a framework for the manipulation of constrained meshes in real-time [123].

Tang *et al.* proposed a general framework for the form-finding of meshes with planar facets using an optimisation solver handling quadratic constraints [245]. The advantage of such method is that it is suited for various optimisation problems, like the form-finding of PQ-meshes or circular meshes, mechanical constraints can be added as well. Moreover, the method is not limited to quadrilateral meshes and different patterns can be studied. Jiang *et al.* studied the planarisation of periodic patterns, beyond quadrilateral meshes by looking at the invariance of such patterns under specific deformations [118]. They observed that periodic pattern mapped along the lines of curvature are easier to planarise and result in smoother appearance.

Several mesh modelling methods based on the solution of optimisation problems formulated on meshes have been implemented. The space of solutions satisfying geometrical constraints can be viewed as a manifold in a space of high dimension. The most common strategy found in the literature is to perform a local approximation of this manifold. Yang *et al.* computed appropriate subspaces based on linear and quadratic approximations of the manifold (the manifold is locally approached by a tangent hyperplane and an osculant quadratic hypersurface). The method was applied to the form-finding of PQ-meshes and circular meshes [271]. Bouaziz *et al.* use another approach to handle constraints by using an optimisation routine involving projections on constrained shapes (e.g. vertices of a quadrilateral facet are projected onto the best-fitting plane) [44]. Efficient implementation of this method guarantees real-time manipulation of meshes for various set of constraints [123].

Optimisation frameworks aim at versatility and are applied to various problems. There is another research direction that considers a specific point of view, suited for a specific problem. Such tailor-made methods explore the point of view discussed by Bobenko on invariance in discrete differential geometry, and generally have a rich interpretation. Vaxman proposed an original approach for PQ-mesh modelling, starting from the idea that affine maps preserve facet planarity. By assigning affine maps to each facet and ensuring compatibility of the transformations, his framework guarantees facet planarity throughout modelling [252]. He proposed later to use composition of projective transformations applied to each facet [253]. Following the same philosophy, Vaxman proposed an equivalent framework based on Möbius transformation for manipulation of circular meshes [254]. Poranne *et al.* proposed a framework based on planar projections and computes optimal lifting of meshes [192, 193].

Finally, note that developable surfaces can be defined as envelopes of planes and can be obtained from methods generating PQ-meshes. This point of view was considered in [148], but is not new, since Leonhard Euler and Gaspard Monge simultaneously proposed to define developable surfaces as strips with infinitely small planar quadrangles. The two technological alternatives *'planar facets'* and *'developable strips'* are therefore equivalent, if one is able to perform unidirectional mesh subdivision.

2.3.4 Discrete offsets

The previous paragraphs considered a representation of free-form structures by meshes, the facets corresponding to panels and the mesh edges representing beams for gridshell structures. Lines are indeed the simplest way to represent beams. This representation has the benefit of being extremely light and sufficiently accurate in preliminary steps of the design process. For instance, in structural mechanics, a beam is identified to its neutral axis, and the equations of elasticity can be simplified greatly with good accuracy.

Structural or cladding elements have however a certain depth that makes the offset of discrete geometries a key issue for builders. The notion of offset is well-defined for smooth objects, but is more complex for discrete objects. Different strategies for materializing offsets, depending on the available technologies, can be employeed. A review on so-called *cell-packing structures* is proposed in [197].

Technological possibilities: examples

In practice, three configurations of beam-offsets can be observed. These three alternatives are presented with a reference to built projects in the followings.

Centre Pompidou Metz The Centre Pompidou in Metz was designed by architect Shigeru Ban and by the engineering office Arup. The roof is a free-form shape covered by a wooden grid composed of triangles and hexagons, a pattern also known as Kagome lattice. The beams are following the orientation of the surface and are all doubly-curved. The use of 6 axes CNC machines was mandatory, so that only two contractors were able to answer to the bid. Due to the wood anisotropy, the twisting made it difficult to justify the structural integrity of wooden elements [217].

Figure 2.16 – The doubly-curved beams of the Centre Pompidou Metz *(picture: Romain Mesnil)*

This technological solution can be found predominantly with timber structures, because wood can easily be milled. Applications to other materials like steel or concrete were not found in the literature review, most likely because of prohibitive cost.

MyZeil The gridshell MyZeil is a triangulated free-form gridshell spanning over a shopping-mall in Frankfurt. Despite the great quality of planning detailed in [131], some areas are subject to important nodal torsion. In those areas, the defect of orientation of the beams is compensated by the construction of bigger connections. Some examples of nodes with torsion are shown in Figure 2.17. These connection details are more difficult to fabricate and might also lead to additional forces in the structure.

Kogod Courtyard, Smithsonian Institution The gridshell covering the courtyard of the Smithsonian Institution in Washington was designed by architects Foster+Partners and by the structural engineering office Buro Happold. The extrusion of the structural layout allowed the planners to introduced acoustic insulation within the structural depth[7]. The torsion-free beam layout, shown in Figure 2.18, creates also interesting visual effects. The gridshell, built in 2007, is the most ancient realisation featuring a torsion-free beam layout referenced in a review on this topic [197].

[7]Source Foster+Partners

(a) General overview *(picture: Knippers-Helbig)*

(b) A node with torsion *(picture: Romain Mesnil)*

Figure 2.17 – The triangulated gridshell 'MyZeil'

(a) Support structure *(picture distributed under Creative Commons licence)*

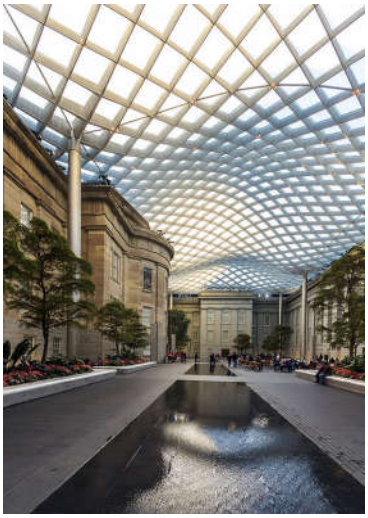

(b) Overview *(picture distributed under Creative Commons licence)*

Figure 2.18 – Gridshell of the Kogod courtyard, the support structure is a torsion-free beam layout.

General framework for offsets

The most economical solution is to build with planar beams and with torsion-free nodes, like the ones shown in Figure 2.18. Mathematically, this translates in the fact that the optimal offset of the structural layout is a geometrical configuration where all beams are planar, and all the planes containing the beams meet exactly along one axis, later called the nodal axis. The notion of offset can be understood with different mathematical tools. The most simple one is to consider that, for each torsion-free layout, it is possible to construct a mesh which has all its edges parallel to the initial edges. Likewise, if two meshes have their respective edges parallel to each other, it is possible to trace planes between them and to construct a torsion-free beam layout. These remarks introduce the notion of *mesh parallelism*, which has been used for architectural application in [198]. We can define this notion as follows:

Two meshes are said to be parallel if they have the same combinatoric (same number of edges, vertices, faces) and their respective edges are parallel.

The transformation that relates two parallel meshes is called a Combescure transformation [198]. Consider a mesh $\mathcal{M}$ and two Combescure transformations f and f'. For each edge, we write v_i the starting vertex and v_j the end vertex. The parallelism condition writes:

$$(v_j - v_i) \wedge (f(v_j) - f(v_i)) = \mathbf{0} \tag{2.7}$$

This relation is linear in f and it is then easy to see that this equation is preserved for any linear combination $f + \lambda f'$. The space of Combescure transformations related to a given mesh is therefore a vector space. An estimation for the dimension D of this vector space was proposed in [198]: based on the number of edges E and the number of faces F:

$$D = E - 2F + 3 \tag{2.8}$$

The formula can be understood as follows: each edge can be scaled, but for each face with n edges, one can prescribe exactly $n - 2$ edge lengths, the other two being found as the intersection of two lines. The number 3 corresponds to the degrees of freedom in translation, which preserves parallelism. With this point of view, it is clear that triangular meshes are rigid with respect to Combescure transformation. Two triangles with parallel edges are homothetic, compatibility between facets means that the only parallel transformation for triangular meshes are homothetic transformations.

In torsion-free beam layouts, the lines passing through each node belonging to a same edge are by definition coplanar. Such network of lines is known as a 'line congruence' in differential geometry [195]. Their relation to surface curvature is well understood in the case of smooth differential geometry, and many recent literature focuses on discrete offsets. Discrete equivalents to the Gauss map can be constructed for some meshes with planar facets, and these methods based on mesh parallelism led to fruitful developments in the field of applied mathematics [41].

Three families of quadrilateral meshes play a special role in discrete offset theory. They derive from three different ways to measure distance between meshes. Consider two parallel meshes, since the respective faces normals (and likewise respective edges) are parallel, it is indeed possible to consider distance between them. We should add the distance between nodes which can be measured without ambiguity even for non-parallel meshes. The three distances are depicted in Figure 2.19. The families of meshes presented in the followings admit parallel meshes with constant face, vertex or edge distance.

Conical meshes

Let us consider meshes that admit constant face offset: in other terms, there exist a parallel mesh where the face distance is a constant. Equivalently, Pottmann *et al.* showed that constant face-offset meshes have a cone tangent to each face, giving the name *conical mesh* [148]. Meshes of valence three (like hexagonal meshes) always admit constant face offset [260]. In meshes where all nodes have a valence of four, conical meshes can easily be characterised with a simple equation on the internal angles around an axis, demonstrated by Wang and Liu [262]. Writing ω_i the angles around a vertex, the equality reads:

$$\omega_1 + \omega_3 = \omega_2 + \omega_4 \tag{2.9}$$

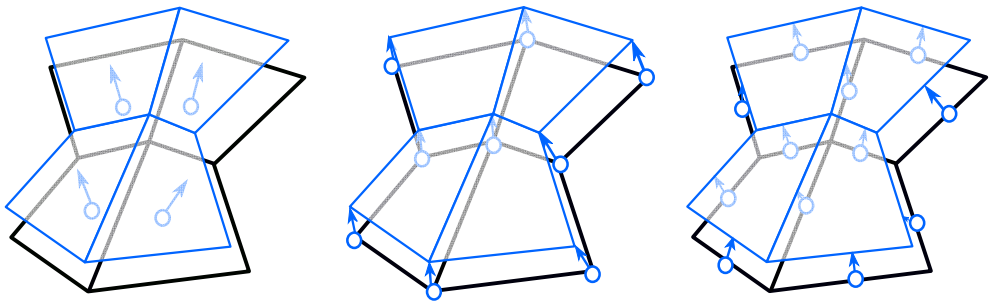

Figure 2.19 – Three distances between two parallel meshes: faces (left), vertex (center) and edge (right).

Equation (2.9) can thus be interpreted as follows: conical meshes are discrete version of a network of perpendicular curves. The associated parametrisations are known as *conformal parametrisations*, they are a rich area of research in the field of computer graphics, see for example an application to texture mapping in [101]. Applications of conformal maps for architectural design with a special focus on surfaces having the topology of cylinder have also been proposed in [212].

Consider now conical meshes with planar facets. It was shown in [200] that such meshes are parallel to meshes with their faces tangent to a sphere. PQ-conical meshes are seen as discrete equivalent to networks of lines of curvature, as lines of curvature are indeed only perpendicular conjugate curve network on a surface.

Applications of conical meshes for architecture, with a strong focus on glazed gridshells were proposed in [199]. However, we point out that, PQ-conical meshes are not more relevant than circular and Edge-Offset Meshes for applications in glazed structures because in such structures, only nodes and beams are constructed: the glass panels remain much thinner than the structural system. PQ-conical meshes have a yet unexplored potential for structures constituted of solid plate elements of constant thickness. One could think of Cross-Laminated Timber (CLT) panels, which have predefined thickness imposed by manufacturers.

Circular meshes

The second family of meshes has both planar facets and constant vertex offset. Circular meshes are quadrilateral meshes where all the facets are inscribed within circles [159]. Such quadrangles are defined by a simple equation, stating that the opposite inner angles are complementary.

$$\begin{cases} \alpha + \gamma = & \pi \\ \beta + \delta = & \pi \end{cases} \tag{2.10}$$

Like PQ-conical meshes, circular meshes are viewed as discrete equivalent of parametrisation by lines of curvature [35]. They are indeed left invariants of transformations preserving lines of curvature: Möbius transformations. Furthermore, Pottmann *et al.* demonstrated that PQ-conical meshes and circular meshes are related by a duality relationship: it is possible to transform a circular mesh (without singularity) into a conical mesh and *vice versa* [200].

Bobenko *et al.* studied circular meshes and their convergence to smooth parametrisation, for example towards two-dimensional conformal maps. They also discuss discretisation of triply orthogonal systems by hexahedral mesh with faces inscribed within circles (which can be viewed as three distinct intersecting circular meshes): the notion of triply orthogonal systems relates to lines of curvature as found in a famous theorem by Charles Dupin [37]. The relation between these two notions is well illustrated by so-called *cyclidic nets*, which are C^1 surfaces supported on circular meshes [159]. The properties of cyclidic nets have been studied in [36]. They constitute an interesting alternative to other surface-modelling tools in architecture. The most limiting factor of cyclidic nets is the modelling of complex topologies, although some solutions have been proposed recently in [33].

Circular meshes constitute the second important family of meshes, because they generally have constant-vertex offset. The condition is however not necessarily verified. Constant vertex offset meshes admit indeed a image by mesh parallelism mapping each vertex on a sphere. When the mesh features closed loops, this implies that each closed curve has to be quasi-spherical, which implies some restrictions on circular meshes with closed loops. For a more complete discussion on this technical topic, see [147].

Edge-offset meshes

So-called *edge-offset meshes* constitute the last family of meshes of particular interest: such meshes admit a parallel mesh with constant edge distance. This is particularly convenient for the manufacturing of steel gridshells, with beam of constant height being perfectly aligned at each node. Like conical and circular meshes, edge-offset meshes are related with specific meshes on the sphere by a Combescure transformation. Namely, edge-offset meshes admit a parallel mesh whose edges are tangent to a sphere. When the facets are planar, facets with edges tangent to a sphere have an incircle, and the mesh facets form thus a circle packing on the sphere and the spherical mesh is called a Koebe polyhedron [196].

This remark has important implications, because circle packing are closely related to conformal geometry and isothermic parametrisations of the plane and the sphere (the notion is invariant by Möbius transformation). A good hint for the reader is to consider circle packing not as a collection of faces and vertices, but rather by the circles themselves. By doing so, it becomes clear that circle packing are invariant by Möbius transformations (which map circle to circles and preserves tangency between curves), isothermic surfaces are also invariant by Möbius transformations.

Bobenko *et al.* constructed discrete minimal surfaces by duality of Koebe meshes [39]: the surfaces are called *S-isothermic surfaces*: they constitute a mesh where facets have incircles. An application of circle and sphere packing for the generation of patterns on free-form structures is proposed with a discussion on the links between circle packing and conformal geometry in [221].

2.3.5 Comments on the contribution of architectural geometry

The recent contributions of discrete differential geometry and of numerical methods led to a significant improvement in the understanding of key concepts of free-form architecture. The appropriate parametrisation of surfaces is of high importance, both for planarity of facets, and for beam offsets. In particular, the parametrisation by lines of curvature has many advantages, since it can yield planar quads or hexagons as well as torsion-free beam layout with constant face or vertex offset. This parametrisation had been previously identified in the end of the eighteenth century by Gaspard Monge, who advised to apply it for stereotomy.

Geometrical rationalisation of free-form envelopes have been implemented successfully in the context of research projects. However, their application is often envisioned as post-rationalisation tools, which allows us to categorise them as flexible design approach, using the terminology of Bagneris. Numerous examples of geometrical optimisation or rationalisation stemming from the computer graphics community can be found in our review, but they remain very scarce in the engineering or architecture communities. The gap between the two communities recalls the one observed for structural optimisation in academia or in practice (and 'solution seeks problem' vs.'problem seeks solution' philosophies). Practical applications of the most recent advances in architectural geometry need yet to emerge: proposing intuitive design tools for architects and engineers would constitute an important step in that direction.

2.4 Mechanically-constrained design approach

This section presents literature review on the third design strategy identified by Bagneris: mechanically-constrained design approach. The design of daring and transparent enclosures cannot be achieved without close relationship between architects and structural engineers. In his book *Leicht und Weit*, the german engineer Jörg Schlaich identifies three arguments advocating for the use of lightweight structures [222]. The first one is ecological: lightweight structures use less primary resource by design, and are generally easy to disassemble and recycle. The second one is economical: lightweight structures require more

detailed design studies, and qualified employment. Finally, lightness is culturally considered as more valuable than heaviness.

2.4.1 Mechanical form-finding

The most popular discipline linked to mechanically-constrained design approaches in architecture is most likely the domain of *form-finding*. Form-finding aims at finding shapes at equilibrium under a specific load case. This load case is either a pre-stress if the structure is extremely lightweight, or self-weight. Additional conditions can be added on the distribution of stress in the structure: up to recent research, most form-finding approaches aimed at finding equilibrium without bending.

Physical form-finding

Physical modelling plays an important role in architecture and is suited for research on equilibrium, because equilibrium is preserved by scaling (note that the relative values of bending moments and axial forces depend on the scale of the structure, making small scale models difficult to use for structures subject to bending). Robert Hooke discovered an experimental method for the modelling of compression-only structures which he encrypted as an anagram, and can be translated by *'As hangs the flexible line, so but inverted will stand the rigid arch.'* [111]. A physical model using flexible rods deforms naturally into a state with pure tension (bending stiffness can indeed be neglected). By reversing the geometry, one can find a compression-only structure. This principle of hanging models was used by numerous engineers and architects. For example Antoni Gaudi used cable nets and weights to find funicular shapes. More recently, Heinz Isler used fabric that was later covered with plaster, or even ice. Fabric is an orthotropic material, so that Isler could use the orientation of wrap and weft to change the shape of his hanging models [116, 25].

One of the most important research effort on physical form-finding was carried out by Frei Otto and his research team of the Institut für leichte Flächentragwerke. Although some of Frei Otto's projects are closely linked to advances in computational mechanics, like the force-density method [216], Otto's work was fundamentally based on physical experiments. He believed indeed that *'The computer can only calculate what is already conceptually inside of it; you can only find what you look for in computers. Nevertheless, you can find what you haven't searched for with free experimentation.'* [235].

The concept of hanging cable nets was used for the design of the Multihalle in Mannheim, which was design in collaboration with Edmund Happold, engineer at Ove Arup and partners [103]. For a more detailed discussion on the role of physical modelling of gridshells by Frei Otto, see [145]. Frei Otto also experimented with soap films and bubbles for applications to tensile architecture [189]. Soap films are indeed membrane structures that minimise free energy and experience isotropic membrane stress: if no external pressure is applied, soap film take the shape of minimal surfaces. By applying inner pressure, one obtains constant mean curvature surface, which can be used in pneumatic architecture. Frei Otto worked in collaboration with the *Institut für Ingenieurgeodäsie* in order to measure precisely the form-found shapes, which allowed to construct daring structures before engineers were able to analyse them with numerical methods.

Numerical form-finding

Physical modelling had a great influence on the emergence of new structural shapes in the twentieth century. Their handling was however cumbersome and time consuming[8], and did not provide estimations of the forces inside the structural elements. Numerical methods were thus needed to provide the designers with estimates of the stresses in the structures. Numerical form-finding has now the favour of a large part of the engineering community: many methods have been developed, and are often much easier to implement or use than optimisation techniques. Form-finding techniques identify geometry with internal stress state, which make them play a particular role in structural morphology.

[8]Form-finding problem, like funicular shape design are often *elliptic* problems: changing the boundary condition requires the computation of the whole problem. From a practical point of view, this means that when moving a mass attached to a cable net, it is likely that some cables will not be in tension anymore: all the lengths have to be adjusted to solve this issue.

Force-density method The first numerical method proposed to find the equilibrium of cable nets is the force-density method [146, 216]. Consider a node P_0 with n cables attached, its equilibrium is given by a vectorial equation depending on the tension force in the cables $\mathbf{T_i}$: $\sum_{i=1}^{n} \mathbf{T_i} = \mathbf{0}$. Projecting on the three components (x, y, z), one gets:

$$\begin{cases} \sum_{i=1}^{n} T_i \cdot \dfrac{x_0 - x_i}{l_i} = 0 \\ \sum_{i=1}^{n} T_i \cdot \dfrac{y_0 - y_i}{l_i} = 0 \\ \sum_{i=1}^{n} T_i \cdot \dfrac{z_0 - z_i}{l_i} = 0 \end{cases} \tag{2.11}$$

The problem is non-linear because the lengths l_i depend non-linearly on x_i. The force density method introduces the so-called *force-density* q_i, defined as T_i/l_i. The equilibrium equation can then be written and becomes a linear equation in q. The linearity is very convenient, as linear constraints (like node position) can be handled simply, and quadratic problems can be solved with least-square methods. We notice also that the method does not depend on the initial position of the nodes, which is a major difference with other form-finding techniques. The main limitation of the force-density method is that it does not take bending into account, so that interaction between cable nets and supporting structure cannot be assessed properly.

Surface stress-density method Maurin and Motro proposed the stress density method, that generalises the approach of the force density to membrane element. The method was first proposed for tensile structures [160] and generalised later for the form-finding of concrete shells [161].

Thrust Network Analysis In structures where all the members exhibit pure axial forces, there is a close relation between the geometry and the forces in the structure. The forces in members are indeed aligned with their axis. The equilibrium of one node $\sum_{i=1}^{n} \mathbf{T_i} = \mathbf{0}$ can be represented as a closing condition for a polygon with edges $\mathbf{T_i}$. Notice that the equation remains a vectorial equation, and that changing the sign of the force (from compression to tension) changes the edge orientation. For a network at equilibrium, one can thus construct a dual diagram based on this principle, like illustrated in Figure 2.20. The concept of reciprocal diagram was introduced in the nineteenth century and is often referred as Maxwell dual diagram or Cremona's diagram by reference to James Maxwell [162] or Luigi Cremona [59]. Notice that the duality proposed is invariant under what we called a Combescure transformation.

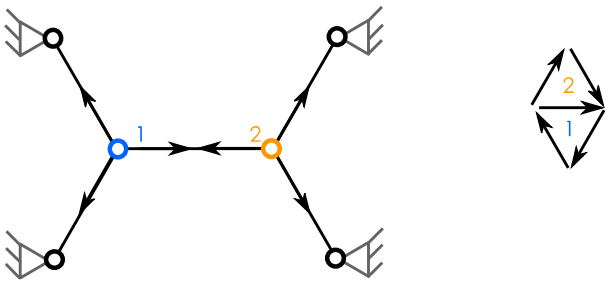

Figure 2.20 – A network at equilibrium (form-diagram) and the corresponding force-diagram (right).

The advantage of graphic statics is that it could be drawn directly for two dimensional problems. The generalisation to three-dimensional structures was impractical with the technologies offered to engineers in the nineteenth century. Block and Ochsendorf generalised the construction of reciprocal diagrams to three-dimensional structures based on the remark that for structures submitted to vertical loads only, the computation of vertical and horizontal equilibrium can be done separately [32]. First, they compute the horizontal equilibrium, which corresponds to the creation of a two-dimensional reciprocal diagram. Then

the vertical equilibrium can be computed without modifying the constructed reciprocal diagram. Graphic statics gives control over both the geometry and the force pattern in the structure, its authors advocate for a *geometry-based understanding of structures* [251]. Indeed, the method has nice interpretation in projective geometry and highlights some tools used in shell theory, like the Airy stress functions.

Dynamic relaxation So far, the form-finding algorithms considered that the internal stress could only be axial force. Such approaches minimising bending are compatible with the idea of minimising the quantity of material employed, because elements under axial forces are used much more efficiently than elements subject to bending. However, many physical phenomena requires to take bending into account. For example, if cable nets or membranes are used as secondary structure, the bending stiffness of the primary structure needs to be considered in order to measure the interaction between the membrane and the primary structure. Another example is the design of elastic gridshells, which are obtained by the deformation of a square grid with no in-plane shear stiffness. The Mannheim Multihalle shown in Chapter 1 is the most notorious built example of elastic gridshell. In this case, bending is the governing phenomenon and the methods described previously are not relevant tools.

Dynamic relaxation was introduced by Otter and Day [188]. It considers the simple fact that static equilibrium can be obtained as the limit of the evolution of a damped dynamic system. Writing $\mathbf{M}$, $\mathbf{C}$ and $\mathbf{K}$ the mass, damping and stiffness matrices of a discrete system, and $\mathbf{F}$ the external loads, the dynamic equilibrium is given by:

$$\mathbf{M}\ddot{\mathbf{X}} + \mathbf{C}\dot{\mathbf{X}} + \mathbf{K}\mathbf{X} = \mathbf{F} \tag{2.12}$$

When damped, the system will naturally dissipate energy, and the speed $\dot{\mathbf{X}}$ and acceleration $\ddot{\mathbf{X}}$ will go down to zero, so that the system is a static equilibrium. There are two ways to introduce damping, the first one is by using viscous damping, the other is to consider kinetic damping. With kinetic damping, there is no viscous damping (the matrix $\mathbf{C}$ is equal to zero), so that mechanical energy is preserved. Mechanical energy being the sum of kinetic and potential energy, it is clear that maxima of kinetic energy correspond to minima of potential energy.

First considered for cable nets, the dynamic relaxation is compatible with the elements in pure axial action, but also in bending due to contribution of Adriaenssens *et al.* [5, 4]. A review on the use of the dynamic relaxation is made by Barnes in [21]. It was applied by Douthe and Baverel for the form-finding of reciprocal frames [70] and for elastic gridshells [71]. We notice here that the point of view taken by the dynamic relaxation is numerical: it can be used in various contexts and not just for the computation of equilibrium.

Update Reference Strategy The finite element method is commonly used by structural engineers to assess the behaviour of structures. Usual method for non-linear analysis, like the Newton-Raphson method, are however not suited for form-finding tasks, because the problem is difficult to linearise near equilibrium. Bletzinger and Ramm proposed the so-called *update reference strategy*, which updates and regularises the stiffness matrix [29]. The update reference strategy differs from other form-finding methods in the sense that it considers not only equilibrium, but also material properties: it can indeed be generalised to any type of element. This is particularly meaningful for fabric membranes, which are orthotropic, and allows the engineers to take into account physical phenomena that are not considered by other methods, like the force density method (like Poisson's effect).

Form-finding algorithms and pattern generation The form-finding algorithms presented in this review are generally not restricted to mechanical problems. A unified treatment of geometry and of the theory of shell structures using tensor calculus was proposed by Green and Zerna [74]. For example, with some knowledge of geometry, it possible to use dynamic relaxation to find appealing smooth patterns on a free-form shape. Chris Williams used the dynamic relaxation for smooth triangulation of surfaces: the first application was the relaxation of the grid covering the court of the British Museum [265], and the concept was extended to other patterns in [266]. Notice that the shape of the roof of British Museum was defined as the sum of three analytical functions, so that the design approach used mixes analytical shapes and optimisation. The engineering office Knipper Helbig uses also the concept of 'relaxation' to generate smoothly parametrised gridshells on surfaces, but the relaxation uses actually the force-density

method together with a constraint keeping the mesh on a target surface [67]. We should mention the popularity[9] of the plug-in KANGAROO for GRASSHOPPER™, which, in the first version, implemented the dynamic relaxation to solve various problems related to geometry or structure.

2.4.2 Design space exploration by structural optimisation

A complimentary approach to mechanical form-finding is structural optimisation. While form-finding usually prescribe a state of stress under a given load in a structure, optimisation can deal with various objectives. This approach is based on mathematical formulation. As we shall see, when form-finding is focused on form, optimisation can generate mechanically-constrained shapes, but also structural systems, as the topology and members can be modified by optimisation procedures. We present here a brief background on structural optimisation and identify potential for future research.

What is optimisation?

Optimisation is a mathematical dealing with the minimisation of a quantity m with respect to certain design variables ($\mathbf{x_i}$), subject to a set of equality or inequality constraints. In practice, the designer aims at minimising cost, but creating an objective function for cost is not straight forward and depends on the context. In many industries, we notice that for a given material (and a given technology or fabrication process), the cost is proportional to the mass of the structure [12]. In civil engineering, the quantity to minimise is thus generally the mass m, and the structure has to satisfy some constraints on maximal displacements, stress or critical buckling load. By achieving proper optimisation of a mechanical problem, the designer is getting closer to Robert LE RICOLAIS' guiding inspiration of *zero weight and infinite span.*

Mathematically, the optimisation problem usually solved in civil and structural engineering can be written as follows:

$$\min_{x_i, \sigma_{max} < \sigma^d, \delta_{max} < \delta^d} m\left(\mathbf{x_i}\right) \tag{2.13}$$

Classification of optimisation problems

Three categories of structural optimisation problem can be identified:

- Sizing problems, which consider a fixed shape and topology, and proposes to vary only the sizing of beams or the thickness of a shell. This problem is typically solved in the detailed design stage: it is the most restricted type of optimisation problem and generally improves marginally the structural behaviour. It is the algorithm most commonly used in practice, see an example of application in [150].

- Shape optimisation problems, which consider a structure with a fixed topology (number of holes). The design variables describe the overall shape and eventually sizing. Shape optimisation problems are solved in conceptual design stages, as it affects the appearance of the structure. They provide more efficient solutions than sizing problems, because the shape affects both the stiffness distribution and the internal loads in a structure. Consider for example a parabolic arch: changing the rise affect directly the axial force in the structure. On contrary, changing the cross-section of the arch does not change the forces in the members.

- Topology optimisation problem consider shape, topology (number of holes) and sizing. It is the most general formulation for optimisation problems. It is used in mechanical engineering, but rarely in civil engineering, where some notable contributions were made by [60, 187, 23].

This dissertation focuses on the relation between geometry, structure and fabrication. The shape optimisation problem links geometry and mechanical behaviour, and is therefore relevant in our study. Topology of meshes for application in gridshell structures is studied in the present work. The possibility to change the topology of a shell structure by adding holes can however be questioned in practical applications in building design, as shell must provide shelter against elements. The literature review

[9] The 27^th of October, more than 158000 downloads of the plug-in have been made.

presented in the followings of this section does therefore not consider topological optimisation of shell or solid structures, and focuses on shape optimisation.

Shape optimisation

We have seen that form-finding techniques generally aim at minimising bending to find shell structures under pure compression or tension. An alternative point of view would be to consider that the contribution of bending to total strain energy is superior to the one of axial forces. Minimising the strain energy of a shell therefore gives close-to-funicular shapes with limited bending moment[10] if the design space is wide enough [30]. Notice that the problem is not the one exposed in the previous section, since it is not constrained. Bletzinger and Rahm proposed to perform form-finding by the means of structural optimisation and showed similarities between classical methods, like hanging chains and shape optimisation [28, 30].

The proper parametrisation of the design space, i.e. the definition of the optimisation variables, is key to the performance of optimisation algorithms. Two approaches are opposing in shape optimisation problems: the first one considers description of surfaces by Computer-Aided Design (CAD) tools, like NURBS modelling. The size of the design space remains limited (below 100 variables), which allows for a complete exploration of the design space and also sensitivity analysis of the solution. CAD-based design space description might however lead to suboptimal solutions if the number of degrees of freedom is too low. The second approach proposes to overcome this limitation by parametrising the design space by the node coordinates in (x, y, z). The fitness function has then many local optima, and the computation is mesh sensitive. The found optimum can thus be undesired because of æsthetics, and more importantly because highly distorted meshes yield unreliable structural analysis. To overcome those difficulties, regularisation techniques have to be employed in order to filter solutions with small radii of curvature [84, 238].

Shape optimisation is not limited to linear elastic models. Firl optimised thin-wall structures with a nonlinear path-following strategy: the optimal shapes differ from the ones found with linear analysis [83]. More general optimisation problems with constraints on maximal displacement or buckling capacity are not as broadly studied. Adding constraints can however be done simply by using augmented Lagrangian methods or penalty methods [180].

Structural optimisation in practice

Structural optimisation is an active field of study, with a rich literature, see for example a review of optimisation of truss in [242]. However, practical applications of structural optimisation in buildings remains rare [19]. In his PhD, Clune identified the difficulty for engineers, who are not experts in optimisation, to choose among the many optimisation schemes available. Moreover, algorithms have different performances and yield different results: the objective function is generally non-convex and has several local minima [55]. Benchmarks of optimisation schemes are also often limited to few specific problems, like the mass minimisation of a cantilever beam. This makes the generalisation of knowledge on structural optimisation difficult.

We might add that some peculiarities of the construction industry make the implementation of optimisation problems tedious. First, due to their large scale, the mass of buildings is not negligible compared to live loads, like snow or wind, and this even for static analysis. The mass affects therefore the stiffness, but also the loads applied to the structure. For heavy structures, like masonry structures, a simple but efficient approach is to consider that the governing load is the self-weight. The design space to consider for structural optimisation can thus be restricted to funicular form-found shapes, like proposed in [31]. In lightweight structures however, this choice is more difficult to justify, as the live loads are comparable to dead loads. Consider for example the Multihalle in Mannheim: the structure is a double-layer elastic gridshell. The design load for snow is of 40kg/m^2, whereas the estimated self-weight of the structure and its cladding is of 20kg/m^2 [103]. In such cases, the restriction of the design space to funicular shape cannot be justified as convincingly, as the governing load case is a combination of dead and live load. The designer is left without intuitive tools or approach to tackle the optimisation of lightweight structures in architecture.

[10] Notice that a thin shell solution with zero bending moment cannot exist if the boundary conditions are not set properly.

The second limitation of structural optimisation is that optimisation problems are solved for a given load case. Small variations of the applied loads might affect dramatically the performance of optimal design: the optimal solution of the 'perfect' problem can then be outperformed by other solutions when considering robustness. In civil engineering, loads cannot be determined precisely and such variations are bound to happen. Likewise, a structure is built within some fabrication tolerances, and the built shape is different from the ideal shape that is computed. Sensitivity analysis both on geometry and applied loads is therefore mandatory to guarantee the optimality of a solution in practical situations. This fact is well-known in the analysis of the stability of shells [132] or gridshells [96]. Optimisation of lightweight structures should ideally be robust optimisation, as optima of the perfect problem might not be satisfactory. We recall again the work of Firl, which performed sensitivity analysis of optimal solutions with the application of geometrical imperfections [83]. Robust optimisation is however difficult to implement in early stages of design: no real-world application to the building industry was found.

The third limitation is that optimisation yields a unique solution to a problem. The solution depends on the chosen design space, the optimisation target. The result of the optimisation can be of no value, for example because the solution is too sensitive to geometrical imperfections and does not fulfil the design requirements. Many realisations of master structural engineers demonstrates also that different designs can achieve similar performances. Mueller advocates for an exploration of the design space with feedback from the user based on non-structural criteria [176]. The feedback is performed as an enforced selection in an optimisation scheme using genetic algorithm [177].

Finally, structural optimisation does not take fabrication into account, so that an optimal solution might be infeasible and uneconomical. We discuss thus the possibilities offered by multi-criteria optimisation and present some literature on fabrication-aware design.

2.4.3 Multi-criteria optimisation

Any real engineering problem is a multi-criteria optimisation problem. In architecture, the designer has to conciliate different aspects: structural performance, thermal performance, acoustics, etc. A multi-criteria optimisation problem with only mechanical variables can be the trade-off between force in the structure and horizontal reaction forces for the design of foundations [66]. Finding a common optimum for all the design objectives is generally not possible. The optimal compromise is found by computing Pareto optima. A solution is a Pareto optimum if there is no other solution that improves one design criterion without degrading the performance on any of the other criteria.

The search for multi-criteria optimum is different from single-valued optimisation problem. The notion of Pareto is meaningful if considered on a global level. Global optimisation algorithms - especially genetic algorithms - are popular in the field of multi-criteria optimisation. A review of the most employed techniques is proposed in [157].

2.4.4 Fabrication-aware mechanical form-finding

The question of fabrication rationality is rarely considered by mechanical form-finding algorithms: a design that result from an optimisation procedure is not necessarily constructible [42]. Indeed, form-found shapes usually require post-rationalisation in order to simplify their construction. The physical experiments by the team of the Institute for Lightweight Structures of the university of Stuttgart constitute an exception, because the cable nets used in their experiments have a constant edge length [226]. Numerical experiments of mechanical form-finding with embedded fabrication constraints were only considered more recently, for example in Douthe's PhD thesis which explored formal possibilities offered by mechanically stable elastic gridshells with constant edge length [69].

A variational approach was used on to optimise the structural behaviour of elastic gridshells in [107]. The constraints and objective functions used are different from the ones presented in this literature review. They deal indeed with the construction process of elastic gridshells, which rely on bending of flexible elements to generate doubly-curved shapes. Starting from a mesh with constant edge-length, an optimisation procedure is used to decrease the stresses in the members, while preserving sufficient regularity.

As seen in our discussion on architectural geometry, fabrication rationality is often solved by appropriate shape parametrisation. The literature review shows that the main research focus on structurally-aware

design is set on form-finding. However, for structures composed of beams, the orientation of the structural layout is also of importance. The study of relationship between structural performance, fabrication and shape parametrisation remains an open research question. SCHIFTNER and BALZER studied the parametrisation of previously form-found shapes by structurally efficient PQ-mesh layouts [220]. The process remains however a post-rationalisation process and does not allow the designer to interact with the shape and the force pattern simultaneously. Form-finding of polyhedral meshes without bending was performed by [245]. The two methods consider one unique load case, with the intrinsic limitations discussed hereabove when one aims at designing lightweight structures. The combination of structural optimisation and fabrication-aware design has not been proposed yet.

2.4.5 Comments on mechanically-constrained design approaches

There is a close relation between geometry and structural performance of shells and gridshells. Two points of view, form-finding and shape optimisation allow to determine efficient shapes. The first approach is limited to one load case, which can be justified for masonry structures, but not necessarily for the lightest structures. The second approach can handle non-linearities and multiple load cases, and can avoid non-robust solutions, with a much higher modelling effort to be done by the structural engineer.

Physical models often took fabrication constraints into account: think of Frei OTTO's models which have a constant edge length. Numerical structural optimisation generally does not consider fabrication. Optimal solutions can be difficult to construct. Some methods have been proposed for fabrication-aware form-finding, but they do not harness the full power offered by structural optimisation. With the constant increase of computational power, optimisation methods become more and more accessible to the designers. The definition of wide design spaces for structural optimisation could overcome this difficulty and open new possibilities for practical applications of structural optimisation in architecture.

2.5 Challenges for structural design of free-form architecture

2.5.1 State of the art on structural morphology

Two opposing design approaches exist in free-form architecture. The first one considers restricted families of shapes, either by fabrication or mechanical constraints. The second approach considers the shape as a given input that has to be rationalised by structural engineers and geometry experts. This *make it work* philosophy and the design process of master builders are poles apart and this leads to further remarks.

Architecture is a cultural discipline, and it is reasonable to state that the tools for free-form modelling used today do not relate to the cultural background of architects and engineers. Optimisation is often presented as a silver bullet that can solve the problems of fabrication rationality. Rich developments in this field have been made in recent years, but architects and engineers fail to apply them to real-life projects. As stated by BORGART *'a generic tool that is suitable for solving all problems is virtually impossible, if it is indeed desired'* [42].

The research on free-form structures is at the intersection of different disciplines: architecture theory, geometry, computer graphics, optimisation, structural mechanics. As such, this research topic is addressed by several communities: architects, computer scientists, mathematicians and engineers. This diversity leads to insightful contributions illustrated in this literature review. However, little exchange can be noticed between the different communities.

2.5.2 Research goals

The review of existing literature shows some limitations of the existing design approaches. This dissertation has specific research goals aiming at bridging the gap between computational methods developed in structural engineering and discrete geometry.

- Expand the formal possibilities of geometrically-constrained design approaches by creating fabrication-aware equivalents of the existing tools generating free-form shapes in NURBS modelling software. Works that address this question are presented in Chapters 3, 4 and 5.

- Propose alternatives to NURBS modelling for the drawing of complex architectural shapes. Those alternatives should embed fabrication constraints so that drawing of non-constructible shape discretisations is impossible. Chapter 4 proposes one alternative with illustrations of its potential for structural design.
- Link the tools of architectural geometry with the cultural background of the architectural community. This question is addressed specifically in Chapter 5, where descriptive geometry is reinterpreted as a modelling tool for shapes covered with planar facets, and called the *marionette technique*.
- Explore the possibilities offered by fabrication-aware structural optimisation, in the spirit of the form-finding by structural optimisation philosophy. This issue is studied in Chapter 6, where the *marionette technique* is used to generate a large design space for the shape optimisation of shell structures.
- In the manner of Candela or Dischinger, assess the structural behaviour of the shapes proposed for geometrically-constrained design approach. In that way, the design of those shapes can become structurally-informed as well as constructible. The present work aims at generality and does not focus on a given structural system or material, so different structural systems should be studied. Work in this area is presented in Chapter 7.

Part II

Design space generation

There are many solutions, good, bad or indifferent. The art is, by a synthesis of ends and means, to arrive at a good solution. This is a creative activity, involving imagination, intuition and deliberate choice.

Ove Arup

Chapter 3

Element congruence in free-form structures

This chapter investigates the question of repetition of elements in free-form structures and presents new results on high-node congruence in doubly-curved systems. The main tool used is a geometrical transformation that preserves symmetries of the structural layout. The result is a family of shapes with high node repetition.

3.1 State of the art and problem statement

3.1.1 On repetition of elements in free-form structures

The study of repetition of elements in free-form structures is an active topic of research, as repetition decreases the construction costs and tends to rationalise the fabrication process. Some strategies for element repetition consider an imposed shape, others tend to generate shapes with interesting properties. Each method shows limitations: the repetition of elements is limited by the overall curvature of the form to construct. More precisely, it will be shown that the mathematical formulation of the different methods is related to the integral of gaussian curvature.

Length repetition and the compass method

The first systematic procedure to generate repetition in curved structures was developed at the Institute for Lightweight Structures (IL) in Stuttgart by Frei Otto's team in 1975. The method aims at meshing a surface with a quadrilateral lattice with edges of constant length. Such meshes are known as *Tchebycheff nets*: their properties are recalled by Etienne Ghys [94]. The team of the IL proposed the *compass method* to generate those meshes. Given two curves on a surface and an edge length L, it is possible to propagate a Tchebycheff net by reporting the length on each curve with a compass. The method is used extensively in the design of elastic gridshells [45][141].

The existence of a Tchebycheff net on a surface is not guaranteed, and it was proven that it is not possible to cover surfaces whose integral of gaussian curvature exceeds 2π. Tchebycheff nets are governed by a differential equation. Writing ω the angle between two curves of the Tchebycheff parameterization (u, v), and $K(u, v)$ the gaussian curvature of the surface, this equation is written as follows:

$$\frac{\partial^2 \omega}{\partial u \partial v} = -K(u, v) \sin \omega \tag{3.1}$$

Gaussian curvature plays thus an important role in the theory of Tchebycheff nets and is a limiting factor for practical applications of structures with high length repetition.

Length repetition and specific methods

The concept of geodesic dome was introduced by the german engineer Bauersfeld and popularised by Buckminster Fuller. It is based on a subdivision of the icosahedron an successive projections on a sphere. Depending on the type of subdivision chosen, one can achieve regularity in lengths, but also in nodes. There is a rich literature that considered such strategies for platonic solids, but also for archimedean solids, which have a constant edge length. For an overview on design with polyhedra, see an anthology by Gabriel [89]. Such methods remained however restricted to relatively simple configurations. More general methods were only envisioned with the involvement of the computer graphics community. As an example, a method was proposed to approximate arbitrary shape by assembly of Zometool models, which consists of only nine different edges [274].

Panel repetition and Lobel frames

Huard *et al.* studied panel repetition with planar elements [112]. The planarity constraint is hard to handle for arbitrary meshes, but is instantly satisfied for triangular meshes. Following a concept developed by Alain Lobel, they study the design space offered by meshes constituted of equilateral triangles only. An example of such is displayed in Figure 3.1.

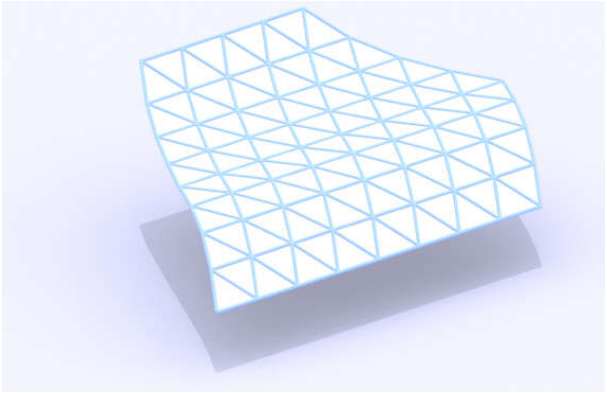

Figure 3.1 – A *Lobel mesh*, constituted only of equilateral triangles.

It is easy to see that the gaussian curvature of *Lobel frames* is zero, in other terms, that only developable surfaces can be meshed with one unique triangular panel. Consider the fact that the gaussian curvature at a vertex of a mesh is defined by equation 3.2:

$$\kappa = 2\pi - \sum_i \omega_i \tag{3.2}$$

In the case of Lobel frames, where the panels are equilateral triangles, $\omega = \frac{\pi}{3}$ and we see that a node of valence N has a gaussian curvature of $\frac{6-N}{3}\pi$. Nodes of valence 6 have thus zero gaussian curvature. Nodes of valence 7 correspond to negative gaussian curvature and nodes of valence 5 correspond to positive gaussian curvature. This restricts considerably the design space with extreme panel repetition. It is also noticed that node repetition is not achieved with Lobel meshes.

Panel repetition and clustering techniques

The example of Lobel frames shows that building with one unique panel restricts drastically the design space. From a practical point of view, constructing with a restricted family of panels could be just as economically efficient. There is a strong interest on clustering techniques, which have been combined with optimisation several times in order to minimise the number of families of panels necessary to approximate a given shape.

A combination of clustering technique with optimisation has been proposed for triangular meshes by Singh *et al.* [232] and for quad meshes by Fu *et al.* [87]. Both methods implement the k−mean algorithm

and approximate a surface by a mesh where facets belong to k different families. Compatibility between adjacent faces is ensured by the computation of an edge-adjacency graph after clustering.

A comprehensive method based on clustering for panels approximation was developed in [76]. The user can assign costs to each technological solution (flat, cylindrical, developable, toroidal panels) and reduce the number of different panels or moulds used. The algorithm does an optimal fitting of the surface for each geometry of panel and can discard solutions where the approximated panels do not meet within a given tolerance.

Notice finally that the methods existing in the literature focus only on face repetition, without taking into account their thickness. While probably negligible for thin cladding elements, the consideration of offsets should play a role for a wide family of applications in architectural design.

Node repetition

The main research on repetition of elements in free-form structures were focused either on panel or beam repetition, but little research was available on the repetition of connections. A notable exception in the technical literature is the work developed in [34], were extreme node repetition is reached for different mesh topologies. The method relies on the generation of *Circular Arc Structures (CAS)*, where all beams are circular arcs. Arbitrary surfaces can be covered with a constant angle via conformal mapping and optimisation. The complexity is then reported from the node to the supporting beam layout, in the manner of the Centre Pompidou Metz, shown in Chapter 2. When the beam have circular-hollow cross-section, the method could eventually be economically efficient. Other cases are likely to be much more expensive.

Node repetition was also considered in the design of the gridshell of the Aquatoll swimming pool in Neckarsulm. The engineers of the office Schlaich, Bergermann und Partner proposed a spherical cupola covered by a Tchebycheff net. The members are curved circular arcs, and although the angle of the Tchebycheff net varies with the law described in equation (3.1), only one connection was used. The built node has one degree of freedom in rotation in order to accomodate the angular variations. This ingenuous solution requires however the introduction of a cable bracing to guarantee the structural stability [226, 110].

Research on node repetition with straight elements was not given the same attention.The most notable exception is a recent publication dealing with optimisation of three-valent meshes towards symmetric,planar joints (T-shape) or repetition by using a representation in a 3-dimensional hyperbolic space [208]. The method remains limited to three-valent meshes, which have poor structural performance. The aim of this chapter is to provide some methods for achieving node repetition in free-form structures.

3.1.2 Connections in gridshells

Steel gridshells are structure made of beams, but that act as continuous shells. Their fabrication requires particular efforts, and especially the connection details. The complexity of node manufacturing is recalled by Knippers and Helbig in [131]. Most of the connections are indeed patented and require advanced numerically controlled tools. Stefan *et al.* identified the main connection typologies and measure their relative performance [239]. This review demonstrates that connection details are key to the economy of steel gridshells. Unlike cladding elements, connections are indeed structural elements and have to transmit efforts. Their properties can influence the overall structural behaviour: for example Hwang *et al.* showed that the joint stiffness has a strong influence on the buckling capacity of steel gridshells [115]. Another review of the different connections used in the projects of the firm Schlaich Bergermann und Partner is proposed by Hans Schober in [226].

3.1.3 Combescure transformations

Following the guiding principle of this thesis, we study the invariance of properties of repetition by geometrical transformations. This approach gives numerous possibilities to obtain high node congruence in doubly-curved systems. Consider first the parameters describing the geometry of a single node in a mesh. Like shown in Figure 3.2, a node can be described as a collection of vectors $(\mathbf{t}_k)$ corresponding to

the beams neutral axis, and by a normal $\mathbf{n}$. It is clear that the node geometry is described entirely up to a rigid body motion by the value of relative angles between the $(\mathbf{t}_k)$ and between each vector $\mathbf{t}$ and $\mathbf{n}$.

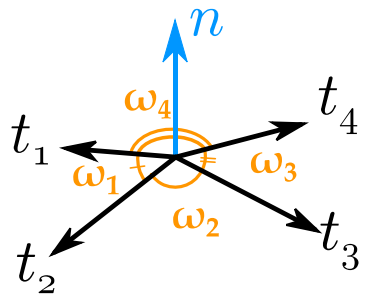

Figure 3.2 – The parameters describing the geometry of a node.

A transformation that preserves angles between the edges of a mesh preserves thus the nodes properties, including node repetition. We propose therefore the use of *Combescure transformations*, also known as transformation by *mesh parallelism*. Parallel meshes have the same combinatoric (same number of vertices, faces, edges and connectivity) and their respective edges are parallels [198]. As an example, Figure 3.3 shows three parallel quadrilaterals. By definition, Combescure transformations preserve discrete angles and leave the node properties (and specifically repetition) invariant.

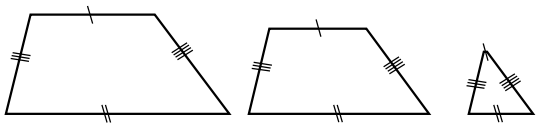

Figure 3.3 – Illustration of mesh parallelism for a single planar polygon: all the figures are parallel to each other because their respective edges are parallel.

It can be noticed that conformal maps preserve angles for smooth surfaces or curves, but do not preserve *discrete* angles. Such transformations, which include inversion with respect to spheres, are of interest in the case of structure composed of curved members, and were used by [34] for that purpose.

3.1.4 Organisation of the chapter

New results on node repetition in free-form structures are presented in this chapter. Mesh parallelism is used in an original way to generate structures with high node congruence. The pertinence of the method is illustrated with the introduction of several families of shapes derived from meshes with symmetry of revolution. Section 3.2 introduces isogonal moulding surfaces, which are images of surfaces of revolution by Combescure transformation: a smooth point of view of this notion is presented in Section 3.3. Section 3.4 discusses the implementation of the technique and the link with smooth geometry. Opportunities and pitfalls related to the use of Combescure transformation are discussed and illustrated with examples.

3.2 Isogonal moulding surfaces

3.2.1 Mesh parallelism and surfaces of revolution

Consider a surface of revolution meshed by its lines of curvature. We emphasize here meshes with a symmetry of revolution: it is obvious that all the nodes along a parallel are identical. We study now the meshes that are parallel to surfaces of revolution and call them *isogonal moulding surfaces* [168]. Such meshes have all their edges parallel to the ones of the surface of revolution and have thus the same

congruence properties. An example of isogonal moulding surfaces and the associated surface of revolution is proposed in Figure 3.4.

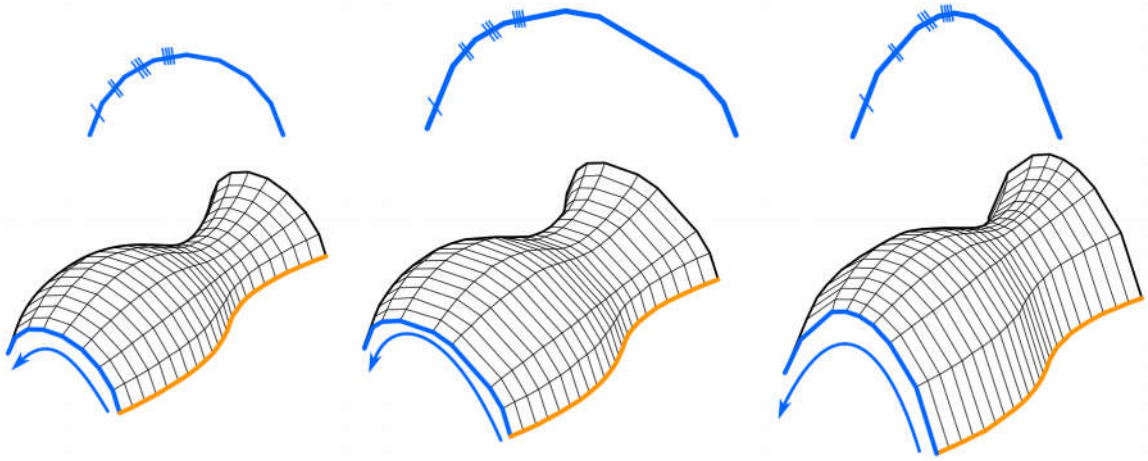

Figure 3.4 – A set of parallel isogonal curves: the circle generates a surface of revolution, the other two curves generate isogonal moulding surfaces.

For a given mesh on a surface of revolution, it is possible to prescribe parallel meshes just by changing the lengths edges on one parallel of the surface of revolution (blue curve depicted on top of Figure 3.4). The resulting curve, also called *parallel* on the resulting surface is discretised with a unique angle. Since Combescure transformations preserve discrete angles, it is easy to see that all the parallels are planar curves discretised with the same angle. This gave the name *isogonal*, which translates to 'having the same angle'.

Following statements can be made, based on the properties of discrete surfaces of revolution and of transformations by mesh parallelism:

- for a given parallel of an isogonal moulding surface, all the vertices are identical;
- all the panels between two given consecutive parallels of an isogonal moulding surface are isosceles trapezoids;
- all the edges between two given consecutive parallels of an isogonal moulding surface are identical; The faces of isogonal moulding surfaces are inscribed in a circle, creating so-called *circular meshes* and the possibility to build with constant height nodes.

The introduction of isogonal moulding surfaces gives therefore a simple way to compute quad meshes that are conical and circular meshes. They have a constant face or a constant vertex offset, giving interesting properties for fabrication. Therefore, the gain in cost of the connections for gridshells is made both by repeatability and by an intrinsic ease of manufacturing. Beyond the fact that a lot of nodes are identical, it seems that all nodes can be produced with the same rules, especially if the generatrix is an isogonal figure as well.

The formal universe of isogonal moulding surfaces reveals archetypal shapes in architecture, and some doubly-curved surfaces can easily be reinterpreted with this family of shapes. Figure 3.5 shows the rendering of a barrel vault interpreted as an isogonal moulding surface. The structure can be covered with planar quadrilateral panels and features remarkable offset properties. The rail curve is a parabolic arch with 20 nodes. There are 34 arches. Without geometrical rationalization, there would be 680 types of nodes. A regular isogonal moulding surface would have 34 types of nodes.

If there are P peaks and V valleys on the generatrix, then the number of different node types can be reduced with an appropriate isogonal subdivision of the generatrix. The number of different node types

Figure 3.5 – Free-form generated as an isogonal moulding surface.

can be approximated by Equation (3.3). The case of Figure 3.5 is illustrated on Figure 3.6: there are 2 peaks and 2 valleys, which reduces the total number of nodes to 8.

$$N_{nodes} \simeq \frac{N_{parallels}}{2\,(P+V)} \tag{3.3}$$

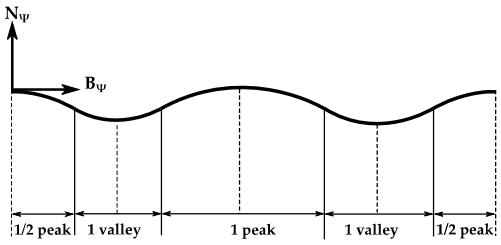

Figure 3.6 – Peaks and valleys on the generatrix used on Figure 3.5

Isogonal moulding surfaces can also be used to generate doubly-curved facades using a horizontal rail curve. The parallelism property implies that all the parallels (same family as the blue curve) are horizontal, simplifying the connection of the surface with an underlying structural layout. The generatrices (in light orange) can easily withstand loads such as self-weight, since they lay in a vertical plane and are likely to be main structural members. The length repetition property is here key to cost reduction: if the surface is an isogonal moulding surface, all the main structural members will be identical. An example of application of these properties is the construction-aware design of stadia.

3.2.2 Edge Offset Mesh and moulding surfaces

Mesh parallelism can also be used to derive exact edge offset mesh from isogonal moulding surfaces. It has been shown in [198] that edge offset meshes feature vertices where all edges are tangent to the same right circular cone. This makes them interesting from a technological perspective. They are parallel to meshes whose edges are tangent to a sphere, also known as *Koebe meshes*. The polyhedra of Figure 3.8 are Koebe meshes: their edges are tangent to a sphere, and, as a result, their faces have touching incircles. Many Koebe meshes exist, from Platonic solids such as the cube displayed on the left to more complex polyhedra.

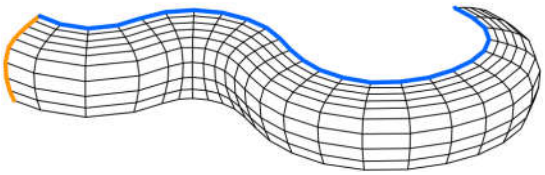

Figure 3.7 – A vertical doubly-curved facade as an isogonal moulding surface, all the generatrices are equal.

As explained in Section 3.2.1, all the parallel meshes to meshes with a rotational symmetry are isogonal moulding surface. This means that all the possible shapes parallel to the canonical Koebe Meshes, such as the ones displayed on Figure 3.8 represent a subset of isogonal moulding surfaces. This section thus aims at explaining which moulding surfaces are constructible with edge offset mesh, and what kind of limitations this implies for a design purpose.

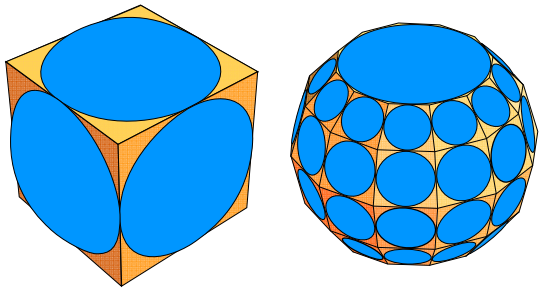

Figure 3.8 – Canonical Koebe Meshes, the edges are tangent to a sphere and the incircles of the faces form a circle packing.

The construction of a Koebe mesh with a rotational symmetry is equivalent to a circle packing problem between two meridians of a sphere, as illustrated on Figure 3.9. Given $\Delta\theta$ an angular subdivision of the parallel, or equivalently two meridians (displayed in red) and λ_0, the latitude of the tangency point between an edge of the Koebe Mesh and the sphere (displayed in blue and dashed lines on the left of the Figure), the problem becomes one-directional and can thus be solved very efficiently. The problem is indeed the construction of a circle that is tangent to the three aforementioned circles, which has two solutions (one circle on each side of the blue dashed circle). It is then possible to establish a non-linear recurrence for the admissible values of the latitude λ defining tangency points between consecutive circles. Introducing $t_i = \tan\frac{\lambda_i}{2}$ and the constant $K_\theta = 1 + 2\sin^2\frac{\Delta\theta}{2}$, the solution of this recurrence follows.

$$t_{i+1} = \frac{2t_i \pm \left(1 - t_i^2\right)\sqrt{1 - K^2\theta}}{\left(1 - K_\theta\right)t_i + 1 + K_\theta} \tag{3.4}$$

Recalling Figure 3.13 and the fact that the angles at a vertex of an isogonal moulding surface are only influenced by the slope of the generatrix in the normal plane of the rail, the recurrence relation leads to admissible values of λ, i.e. of admissible slopes for the subdivision of the generatrix. These values can be used on any isogonal moulding surface, leading to a propagation method which implementation is discussed in Section 3.4. The result is a method to generate edge offset meshes with a total control of the shape.

3.3 A second point of view on isogonal moulding surfaces

It is noticed that the curves that were called *parallels* form a family of parallel curves in isogonal moulding surfaces. This is a property that defines a family of smooth surfaces called *moulding surfaces* introduced by the french mathematician Gaspard Monge [173] and were later studied by Gaston Darboux

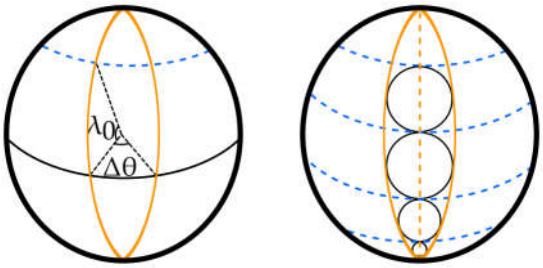

Figure 3.9 – Perspective view of the parameters of the circle packing problem: for two given meridians (continuous) and one parallel (dotted), a unique solution exists.

[62]. This Section makes a connection between smooth moulding surfaces and discrete isogonal moulding surfaces. The advantage of taking this point of view is to simplify the design process for architects and engineers: it might not be straight forward to work with Combescure transformations, but we show that isogonal moulding surfaces can be generated from two planar curves. We first introduce the broadest class of surfaces that generalises moulding surfaces. We discuss then their discrete counterpart and expose the link between discrete moulding surfaces and the isogonal moulding surfaces created by Combescure transformations.

3.3.1 Monge's surfaces

Monge's surfaces (also known as generalised moulding surface) are a family of surfaces introduced by the French mathematician Gaspard Monge at the beginning of the nineteenth century in his lectures on differential geometry [173]. Several equivalent definitions of these surfaces are given in lectures and are recalled in [194]. The generation of Monge's surfaces can be described by a kinematic procedure, represented on Figure 3.10. The surface is generated by the *sweeping* of a planar curve, called generatrix (in orange on the Figure) along another curve, called rail-curve (in blue). If the rail-curve is planar, then the surface is called a *moulding surface*. There are some restriction on the kinematic of the generatix, since it has to lay in the normal plane of the rail curve and it has to follow a *rotation minimizing frame*. Monge's surfaces are therefore a specific case of sweeping surfaces, which makes them a very familiar set of surfaces for designers.

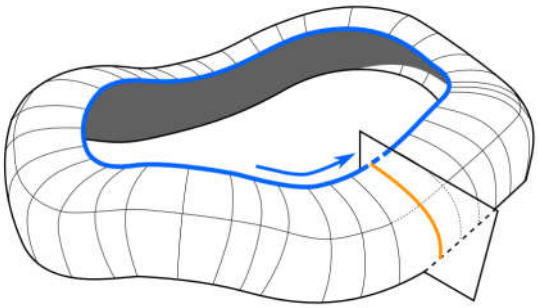

Figure 3.10 – Kinematic shape generation of Monge's surface: generatrix (red) and parallel (blue).

The iso-curves of the surface are called respectively generatrices and parallels. Generatrices and parallels are the curvature lines of Monge's surfaces, and therefore form a conjugate-curves network. A discrete version of these lines is therefore close to a conical PQ-mesh [148]. Monge also demonstrated [173] that generatrices are geodesics of Monge's surfaces, making them interesting for the design of developable strips. Indeed, if geodesics are known to be the shortest path between two points, another property (which is actually more general) is that the normal vector of a geodesic is the same as the normal vector of the surface at any point. This explains their "straightness property", which implies that when unrolled, developable strips cut along geodesics remain almost straight, minimizing the loss of material through

cutting. This property is well known and used in the construction industry, especially for the cutting pattern of tensile structures [99].

3.3.2 Discrete Monge's surfaces

When both the generatrix and the rail curve are polylines, the resulting surfaces are naturally called discrete Monge's surfaces. Discrete Monge's surfaces are generated as depicted on Figure 3.11. Consider two consecutive edges on the rail curve $E_{i,j}$ and $E_{i,j+1}$. The next parallel of the discrete Monge's surface is generated with an offset of $E_{i,j}$ by a vector $\mathbf{V}$ of length h. The resulting line $E_{i+1,j}$ is intersected with P, the bissecting plane of $E_{i,j}$ and $E_{i,j+1}$, which gives the new vertex of the parallel. The next edge $E_{i+1,j+1}$ is chosen to be parallel to $E_{i,j+1}$.

This generation principle implies that there is a local symmetry for each node. It follows that the angles between the generatrix and two consecutive edges of a parallel are equals. These surfaces have therefore intrinsic properties that make them interesting for construction purpose:

- the panels are planar trapezoids. The parallelism of opposite edges makes the use of cost-effective standard opening mechanisms based on rack and pinions possible;
- the trapezoids have a constant height, which is optimal for nesting the panels within a rectangular bounding box;
- the nodes of discrete Monge's surface are torsion-free.

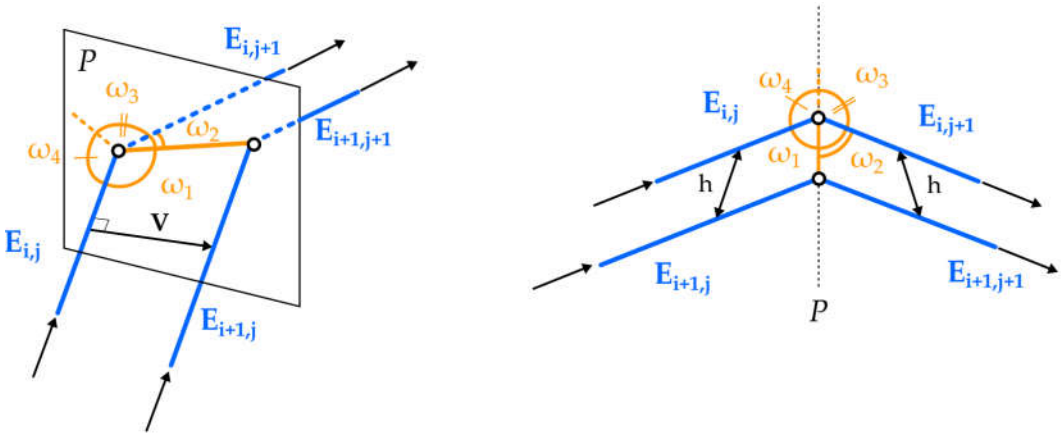

Figure 3.11 – Generation of a discrete Monge surface by edge offset: perspective (left) and top view (right).

The first statements come directly from the generation principle presented on Figure 3.11. The last proposition can be proven by recalling that any conical mesh respects Equation (3.5), as proven in [262].

$$\omega_1 + \omega_3 = \omega_2 + \omega_4 \tag{3.5}$$

where ω_i are the angles between consecutive edges around a vertex. Here, due to symmetry with respect to the bissecting plane, one gets:

$$\begin{cases} \omega_1 = & \omega_2 \\ \omega_3 = & \omega_4 \end{cases} \tag{3.6}$$

which proves that discrete Monge's surfaces are indeed PQ-Conical Meshes.

The consequence of these propositions is that all Monge's surfaces can be considered as optimal for the most typical geometrical optimisation goals. Indeed, they guarantee both faces planarity and torsion-free nodes. Nonetheless, the user has an intuitive understanding on how to generate them. This makes them interesting for typical applications of free-form structures such as glazed gridshells, an illustration of which is given in Figure 3.12.

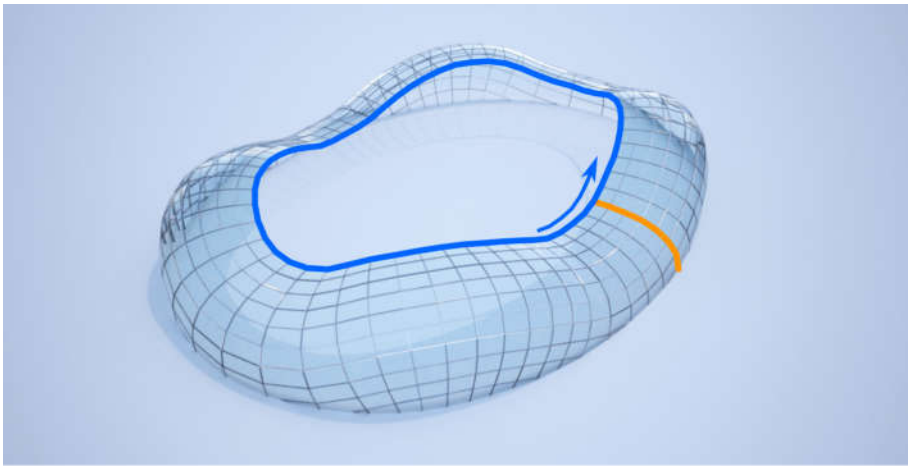

Figure 3.12 – Free-form as a Monge's surface, the surface is covered with planar panels and torsion-free nodes.

3.3.3 Isogonal moulding surfaces as discrete Monge's surfaces

Moulding surface are defined as a specific subset of Monge's surfaces, the rail curve being constrained to be planar. The design of moulding surfaces thus follows the simple procedure described for Monge's surfaces with a planar curve for the generatrix and a planar curve for the rail. Discretising the surface following lines of curvature, it is noticed that the parameter influencing the angle at a vertex are limited. Indeed, as one can see on Figure 3.13, the only values of interest are the subdivision angle α_i of the rail (in blue) and the slope β_j of the generatrix (in light orange) within the normal plane of the rail. A consequence is that for a given parallel of a discrete moulding surface, the angles of a vertex only depend on the subdivision angle of the rail. It follows that a moulding surface where the rail is a polyline with only one angle has a unique set of vertex angles for each parallel and therefore, that the nodes along the same parallel are identical.

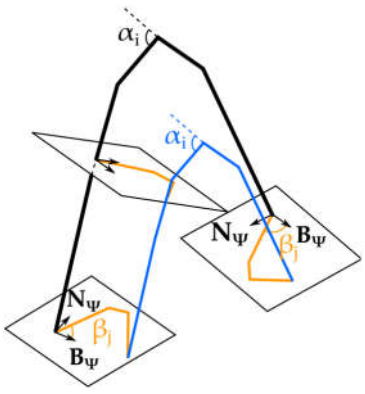

Figure 3.13 – The angle of subdivision of the rail curve α_i and the slope of the generatrix with respect to the discrete rotation minimizing frame β_j are the only parameters influencing the vertex angles.

From a practical point of view, this means that isogonal moulding surfaces can be generated from two planar curves. This simplifies the generation process compared to the prescription of Combescure transformations. The use of two curves for shape generation is indeed highly intuitive, like demonstrated by the success of surfaces of translation in glazed gridshells [226]. Some notorious examples of built moulding surfaces exist, like the SAGE Music Centre [57] shown in Figure 3.14 or the Odate Dome [246].

This illustrates that moulding surfaces have entered the formal vocabulary of some architects. However, the property of conical mesh for Monge's surfaces did not seem to have been discussed before in the general case.

Figure 3.14 – Sage Gateshead Music Centre (architect: Norman Foster): an example of moulding surface covered with planar facets, (*picture: Graham Robson, distributed under Creative Commons licence*)

3.4 Application and computational aspects

3.4.1 Isogonal subdivision of a convex planar curve

The main challenge left with the design of isogonal moulding surfaces is the isogonal subdivision of a planar curve. A strategy that guarantees an isogonal subdivision of a smooth convex curve is proposed in this section. The method can be interpreted graphically, as pictured in Figure 3.15. The basic algorithm steps follow:

1. Find the tangent vectors $\mathbf{T_A}$ and $\mathbf{T_B}$ at the ends of the curve, and measure their angle α_{AB} (if the curve is closed and convex, chose $\alpha_{AB} = 2\pi$);

2. Divide α_{AB} by the desired number n of inner nodes. Create the vectors $(\mathbf{T_i})_{i=1}^{n-1}$, where each $\mathbf{T_i}$ is obtained by a rotation of $\mathbf{T_A}$ by an angle of $\alpha_{AB} \cdot i/n$;

3. Find the points corresponding to the tangency to $(\mathbf{T_i})_{i=1}^{n-1}$ on the initial curve;

4. Intersect the corresponding lines with each other.

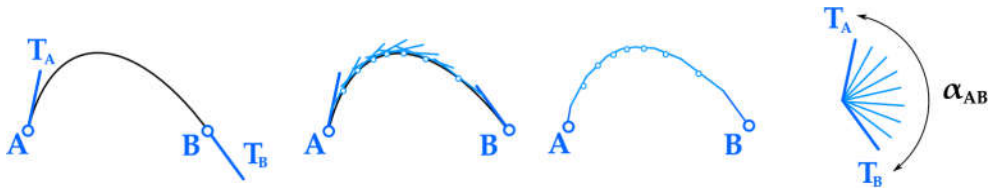

Figure 3.15 – A graphical method for the isogonal subdivision of a planar curve.

With this formulation, only angles that are a unit fraction of the total angular variation of the tangent vector are admissible.

$$\alpha_{ext} = \frac{\alpha_{AB}}{n} \tag{3.7}$$

It is possible to be even more specific: the points of tangency P_i found at step 3 form a partition of the curve with a constant integral of curvature.

$$\alpha_{ext} = (\mathbf{T_i}, \mathbf{T_{i+1}}) = \int_{P_i}^{P_{i+1}} \kappa ds \tag{3.8}$$

Intuitively, the consequence is that areas with low curvature will feature longer elements, which can already be noticed on Figures 3.5 and 3.15. This criterion also means that fully numerical approaches based on the integral of curvature are applicable to the search of isogonal polylines.

It has to be noticed that the algorithm can be made more flexible by letting the user prescribe an angle of subdivision and a first point of tangency. The last two steps of the method described above can be implemented with the prescribed value of the subdivision angle.

3.4.2 Isogonal subdivision of a planar curve

Consider now the case of a curve that is not convex and more precisely with varying curvature signs. The strategy proposed above does not apply directly, but it can be generalised. Indeed, the procedure to follow is simple:

1. Find the inflection points of the curve and use them to make a partition of the curve ;
2. Apply the procedure described in Section 3.4.1 for each part.

By doing so, one is sure that each part will have an isogonal subdivision. The last problem to solve is to know whether it is possible or not to have the same subdivision for each part with the simple graphical method described above. Equation (3.8) gives an answer to this problem: it is possible to have the same subdivision angle for two parts whose integral of curvature are commensurable (their ratio must be a rational number). This restriction is too strong for a general purpose. For this reason, a propagation algorithm where the user chooses the angle of subdivision is more convenient. The algorithm implemented follows the same principle of tangency point and adapts the sign of the subdivision angle by checking the sign of the curvature.

The algorithm proposed hereinabove has been implemented as a *PythonScript* in the drawing software *Rhinoceros*. The benchmark for the isogonal subdivision algorithm studies two typical curves. The first one is a parabola and has no inflection point. The second one is a fourth order spline with four inner inflection points recalling a sine function. Both curves are shown on Figure 3.16. The inflection points and tangency points are found by means of a binary search algorithm.

Figure 3.16 – Benchmark curves (continuous) with end points and inflection points, and the result of our algorithm (dashed lines).

As seen on Table 3.1, the computation time is low, even for a large number of subdivisions. It can be noticed that the convergence of the algorithm does not vary linearly with the number of inner nodes: doubling the number of inner nodes will not double the computation time. The partition into several domains with the inflection points makes the computation slower for the sine curve. These examples show that the algorithm proposed allows a real-time manipulation of isogonal planar curves and isogonal moulding surfaces.

3.4.3 Computation of edge offset meshes from moulding surface

The computation of edge offset meshes from isogonal moulding surfaces is closely linked to the construction of a Koebe mesh with a rotational symmetry, see Section 3.2.2. Such a mesh can be determined

Type of curve	Number of inner nodes	Computation time [s]
Parabola	25	0.04
	50	0.06
	100	0.12
	200	0.21
Pseudo-Sine	25	0.10
	50	0.11
	100	0.17
	200	0.27

Table 3.1 – Computation time for the isogonal subdivision algorithm, the computation was performed on a computer with 2.4 GHz and 2 GB memory.

with two given meridians on a sphere, or equivalently, with a subdivision angle of the parallels, as a starting point. Due to its symmetries, the problem to solve can be represented on a plane, as shown in Figure 3.17. Consider the bisecting plane of the two meridians. The projection of these curves into the plane gives an ellipse (dashed figure), whereas the meridian in the bisecting plane is a circle (thick continuous line). The Koebe Mesh has its edges tangent to the sphere, which means that the projection of an edge on a meridian (blue continuous line) has to be tangent to the ellipse. In the plane displayed on Figure 3.17, the projection of an edge along a parallel is a point (in blue on the figure). The condition of edge tangency for Koebe mesh means that this point has to be on the central meridian (thick black circle). The symmetry of the problem guarantees indeed that the contact has to be on the central meridian and on the two pre-determined meridians. By this mean, starting from a point P_1, one is able to find a point P_2 so that the line (P_1P_2) is tangent to the ellipse at the point P_1'. The procedure can be repeated to construct other points P_2' and P_3, and so on.

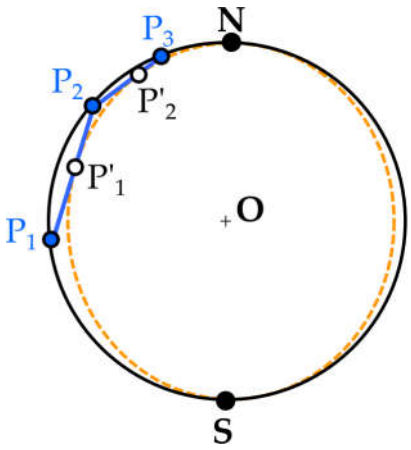

Figure 3.17 – Propagation technique for a sphere, the dashed line is the projection of a meridian within the plane of the central meridian

For a given point P_1 and a propagation direction (either towards the North pole N or the South pole S), there is one unique way to construct a valid trapezoid that respect the rotational symmetry and the edge offset property. This leads to the incremental construction of the sets of points $(P_i)_{i=1}^{n}$ on the circle and $(P_i')_{i=1}^{n-1}$ on the ellipse. The key information for the construction of edge offset mesh on moulding surface is the computation of the slope of the generatrix, which is the slope of the line $(P_{i-1}P_i)$. This calculation gives therefore admissible values of the slope of the generatrix for the construction of an edge offset mesh. The computation is very efficient, since the problem is fundamentally one-directional.

Once the problem of the Koebe mesh on the sphere is solved, it is possible to apply this approach to

any moulding surface. The procedure follows:

1. Subdivide the rail curve into an isogonal figure;
2. Measure the initial slope of the generatrix;
3. Determine the propagation direction (North pole or South pole);
4. Solve the equivalent problem on the sphere with these initial values (the result is a set of tangent vectors);
5. Find the tangency points on the generatrix, a suitable curve for an edge offset mesh being the envelope of the tangent lines.

The simplicity of this formulation leads to good computational performances, the calculation time being typically below one second, even for meshes with thousands of faces. A set of typical values of computation is given in Table 3.2, the geometry considered is a mesh on a sphere with a symmetry with respect to the equator, as the mesh displayed on Figure 3.8. In this case, the computation time is mainly governed by the isogonal subdivision of the rail curve.

$\Delta\theta$	$\Delta\lambda$	Number of Faces	Computation time [s]
5°	30°	504	0.19
	60°	936	0.20
	120°	2232	0.24
	160°	3384	0.32
15°	30°	72	0.18
	60°	120	0.20
	120°	264	0.22
	160°	384	0.16

Table 3.2 – Computation time for the Edge Offset Mesh algorithm for a sphere.

The method presented hereinabove is not free from simplifications and from hypothesis. The first one is that the generatrix has to exhibit curvature in order to use the propagation technique. If it is not the case, the algorithm will fail to find admissible values for the slope of the generatrix. This is rather an intrinsic limitation of these surfaces than a weakness of the algorithm. For example, a cylinder cannot be given an edge offset mesh, since its Gaussian map is a circle.

Another difficulty in the use of the edge offset mesh algorithm is that the procedure described does not allow to cover the entire sphere with a quad mesh. Graphically, it can be seen on Figure 3.17 that the ellipse and the circle get closer as one moves away from the equator, which means that each "step" is smaller. Figure 3.8 shows this narrowing of the faces as the latitude is larger. Numerically, this means that the algorithm, as it is presented here, would not converge if the normal of the generatrix is the same as the normal of the plane containing the rail curve, which corresponds to the poles in the case of a sphere. From a practical point a view, it is therefore necessary to prescribe a minimal angle between these normals to stop the computation. An illustration of the practical limitations of Koebe mesh on moulding surfaces with respect to this point is given on Figure 3.18, where a torus is meshed with our algorithm. The narrowing of the elements towards the top of the small circle is clearly visible, and would be likely to be considered undesired from an architectural and technological point of view. The mesh exhibited is still an edge offset mesh, but it does not only feature quad elements. This simple shape illustrates some of the intrinsic limitation of edge offset meshes in practical cases.

3.4.4 Gridshells with planar facets

In this section, an evaluation of the design possibilities offered by moulding surfaces, isogonal moulding surfaces and edge offset meshes for gridshells with planar faces is proposed. In particular, the analytical link between the discrete mesh and the smooth surfaces leads to some remarks on the malleability of

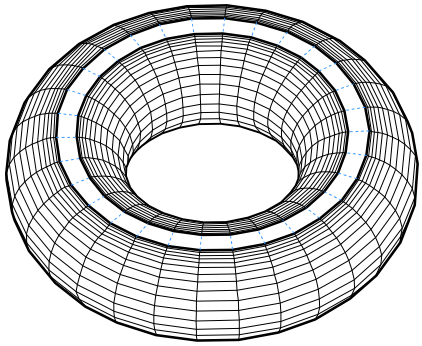

Figure 3.18 – Edge offset mesh on a torus, a particular case of isogonal moulding surface where the algorithm proposed in this article does not provide a mesh with quads only due to intrinsic limitations of the shape.

edge offset meshes. A case study is proposed for two archetypical examples of doubly curved shapes in architecture: domes and barrel vaults.

Moulding surfaces are indeed well-suited for the generation of domes. The form generation principle is illustrated on Figure 3.19: the rail curve is vertical and the generatrix is a curve with no inflection point. The surface generated is cut by an horizontal plane in order to illustrate possible real life application. Three geometries of dome are considered: the rail curve (in blue) is a third order spline and remains

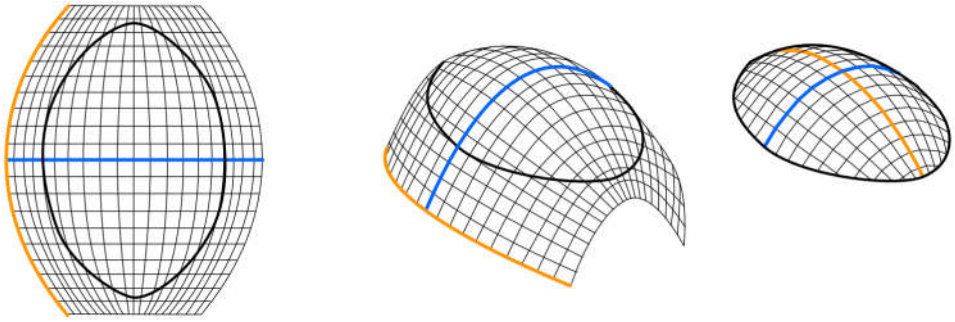

Figure 3.19 – Dome as a moulding surface: top view and isometric view.

unchanged, whereas the generatrix (in light orange) varies. This gives three geometries: an oblong shape, a nearly-spherical one and an intermediate shape. A relatively coarse and a fine edge offset mesh have been generated on each shape, the coarse meshes can be seen on Figure 3.20. The computation of the meshes is instantaneous. The number of subdivisions of the rail-curve is identical for the three geometries, which implies that all the three edge offset meshes are parallel to each other and derive from the same Koebe mesh on the sphere.

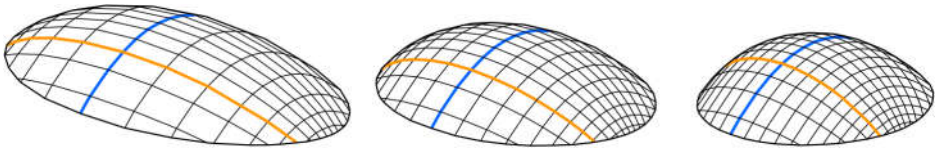

Figure 3.20 – Perspective view of the three domes as edge offset meshes.

Let us define the aspect ratio of a panel as the ratio of its length (maximum of the mean value of the

lengths of two opposite edges) over its width (minimum of the mean value of the lengths of two opposite edges). In Table 3.3, a comparison between the aspect ratio of the panels L/l and the ratio of principal curvatures at the apex of the dome R_1/R_2 is made. It appears that these quantities are very similar, especially when the mesh is refined. For 50 subdivisions of the rail curve, the difference between these quantities is below 2%. This simple example shows that the ratio of principal curvatures is likely to be a key factor in the anisotropy of edge offset meshes. Keeping this in mind, some precautions can be taken to improve the quality of an edge offset mesh, or controlling intuitively its anisotropy:

- Reduce the variation of curvature of the rail curve;
- Avoid areas with low gaussian curvature, as they are hard to cover with edge offset meshes;
- Even the curvature between parallel and generatrix in order to deal with eventual mesh anisotropy.

Number of subdivisions of the rail curve	Type of Dome	L/l	R_1/R_2
15	Oblong	3.50	3.60
	Intermediate	1.88	2.01
	Quasi-spherical	1.12	1.13
50	Oblong	3.53	3.60
	Intermediate	2.02	2.01
	Quasi-spherical	1.13	1.13

Table 3.3 – Relation between aspect ratio of the panels L/l and the ratio of the curvatures R_1/R_2.

Isogonal moulding surfaces are also of interest for the generation of shapes with varying curvature, such as corrugated barrel vaults. Figure 3.21 demonstrates this possibility: the rail curve (in blue) is a B-spline of degree 3 with a rise over span ratio of 37.5 %. The generatrix is a spline curve which is also divided as an isogonal polyline (with the exception of the inflection points, where flat node are introduced). The structure features nearly 700 nodes, but thanks to the isogonal moulding surface properties and to the symmetries of the shape, only 8 types of nodes are used. Height lengths of members are required to span between any parallels.

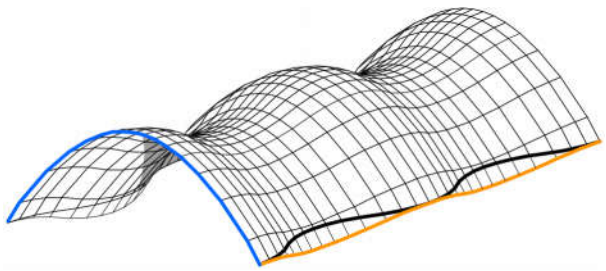

Figure 3.21 – Corrugated barrel vault as an isogonal moulding surface.

It can be noticed on Figure 3.21 that the panels are longer towards the supports of the structure, which can be explained by equation (3.8): the isogonal subdivision has to define a constant integral of curvature for the rail curve. The Figure 3.22 shows that the curvature is bigger on the top of the rail curve, which is a well known fact for curves such as parabolæ for example. The dots represent the points of tangency found with our algorithm. This phenomenon of shortening of elements in areas of high curvature can be problematic if the variations are important. In this case, the designer can choose to divide straight lines by adding intermediary elements or to divide the rail curve with two angles, instead of only one.

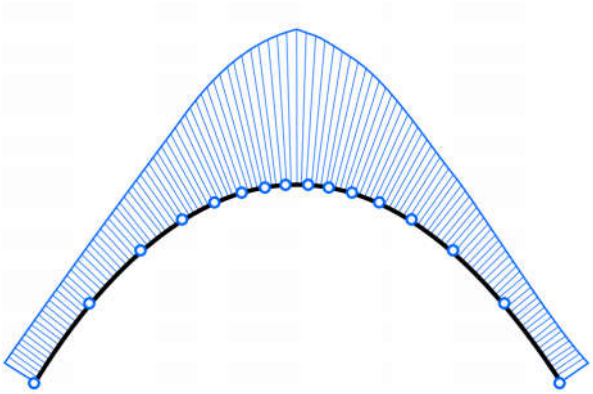

Figure 3.22 – Curvature graph of the rail curve in Figure 3.21, the dots represent the tangency points found with the algorithm presented in this paper.

3.5 Extension to other shapes

This chapter proposed a methodology for the generation of element repetition in free-form structures based on the invariance of node repetition by Combescure transformation. An application to a specific family of meshes (surfaces of revolution) was shown. The methodology can be extended to other meshes with high node congruence. This section explores some developments of our framework.

3.5.1 Fitting of Monge's surfaces by surfaces of revolution

Congruence in Monge's surfaces

This chapter has demonstrated a clear link between surfaces of revolution and Monge's surfaces. Surfaces of revolution are indeed Monge's surfaces with a circular rail curve. It can be noticed that if the rail curve is a collection of surfaces of revolution, then the resulting Monge's surface is a concatenation of surfaces of revolution. As such, the symmetries of surfaces of revolutions can be used to generate repetition of panels, nodes and edges. The congruence increases as the number of patches decreases, it is therefore important to approximate a given curve with as little patches as possible. This motivates the implementation of an optimisation algorithm that allows the approximation of an arbitrary curve with a minimum amount of circular arcs.

Algorithm principle: bi-arcs

The approximation of a given set of points by circular splines has already been used in architecture and other fields of computer-aided design [234, 34]. The aforementioned papers use the fact that two prescribed points and two tangent vectors admit a one-parameter family of bi-arcs (two circular arcs), like the one represented on Figure 3.23.

Circular arcs are here described as Non Rational Bézier curves of degree 2. Only three control points are required, one at each end, and one on the line sector bisector. Consider a bi-arc with prescribed points A and B and prescribed tangents $\mathbf{T_A}$ and $\mathbf{T_B}$. The two arcs are meeting tangentially at point C following an unknown vector $\mathbf{T_C}$. The control points M_A and M_B are at the intersection of the lines $(C, \mathbf{T_C})$ and$(A, \mathbf{T_A})$ or $(B, \mathbf{T_B})$ respectively. They are defined by the equation:

$$\begin{cases} \mathbf{M_A} = & A + l_A \mathbf{T_A} \\ \mathbf{M_B} = & B + l_B \mathbf{T_B} \end{cases} \tag{3.9}$$

The two arcs meet tangentially, meaning that M_A , M_B and C are aligned:

$$\|M_A - M_B\|^2 = (l_A + l_B)^2 \tag{3.10}$$

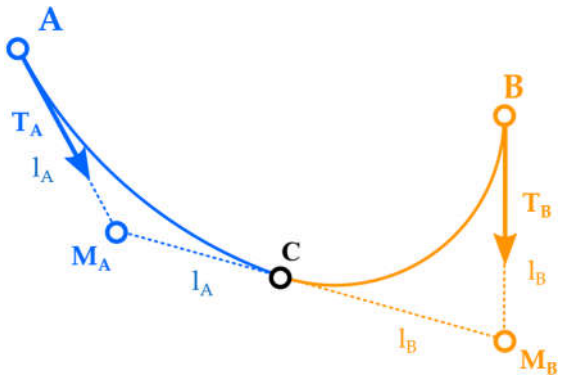

Figure 3.23 – A bi-arc and the associated notations

Equations (3.9) and (3.10) lead to an equation with two unknowns that any bi-arc has to satisfy (3.11), found in [234]:

$$\mathbf{V}^T\mathbf{V} + 2l_A\mathbf{V}\mathbf{T_A} + 2l_B\mathbf{V}\mathbf{T_B} + 2l_Al_B\left(\mathbf{T_A}\mathbf{T_B} - 1\right) = 0 \tag{3.11}$$

where $\mathbf{V} = B - A$. This equation has an infinity of solutions. It can be transformed into a parametric equation, for example by introducing the parameter $r = \frac{l_A}{l_B}$. The equation becomes then a second order polynomial equation in l_A, which has one positive solution for any value of r.

Two points and two tangent vectors give a one-parameter family of bi-arcs. In the followings, a set of points is chosen on the curve to approximate. The associated tangent vectors are the tangent vectors of the curve. The approximation of the curve is the set of bi-arcs generated on each set of consecutive points of the curve. The parameters of the problems are therefore the U-values of the points on the curve and the ratio r for each bi-arc. For N bi-arcs, there are therefore $N - 1$ values for U_i , and N values for r_i.

Error formulation and optimisation

We showed how to generate a N-parameter family of circular splines approaching a reference curve. The question of the estimation of the similarity between two curves remains. A common approach would be to minimise the Euclidean distance $\mathcal{L}^2$ [43], but two curves can be close in terms of Euclidean distance and have very different features, as illustrated in Figure 3.24. When dealing with free-form curves, it is more important to preserve some key visual references, like peaks and valleys.

Mathematically, this means that the criterion has to compare the orientations of the normal vectors, as illustrated in Figure 3.24. The error metric chosen here was first introduced in [56] and called $\mathcal{L}^{2,1}$ is also discussed in [43]. Writing s the arclength parameter of the reference curve Γ, $\mathbf{n_0}(s)$ the normal on the reference curve and we write $t(s)$ the arclength parameter on the circular spline corresponding to the point closest to $\Gamma(s)$. The penalty functional $E(\mathbf{U}, \mathbf{R})$ is a quantity to minimise proportional to the defect of orientation between the evaluated shape and a reference geometry.

$$E(\mathbf{U}, \mathbf{R}) = \sum_{\text{bi-arcs}} \int \|\mathbf{n_0}(s) - \mathbf{n}(t(s))\|^2 \mathrm{d}s \tag{3.12}$$

The functional penalizes changes of curve inflection and gives satisfactory results. The integrals are computed numerically as finite sums for a finite number of values of s. We write $(s_i)_0^n$ the values taken by s from the sampling and $\mathbf{P_i}$ the associated points, and d_i the curve length between $\mathbf{P_i}$ and $\mathbf{P_{i+1}}$:

$$E(\mathbf{U}, \mathbf{R}) = \sum_{\text{bi-arcs}} \sum_{i=0}^{n} d_i \cdot \|\mathbf{n_0}(s_i) - \mathbf{n}(t(s_i))\|^2 \tag{3.13}$$

The number of sampling points is chosen so that the estimation does not vary by more than 0.1% when doubling its value. With the curves studied in this paper, this led to values between 10 and 20 sampling points.

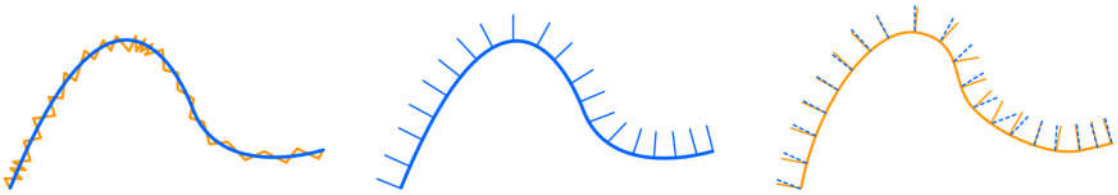

Figure 3.24 – Curve fitting and metrics: fitting with euclidean distance can yield non-smooth results (left), a fitting based on the orientation of the normals and the $\mathcal{L}^{2,1}$ metric gives more natural results (middle and right).

The optimisation problem is an unconstrained smooth problem, which hints the use of descent algorithm. The error functional is minimized by a quasi-Newton scheme: the BFGS method. This method computes an approximate value for the Hessian matrix based only on the estimation of the gradient. The method is easy to implement and has a good convergence: it is one of the most popular quasi-Newton methods [180]. Once the descent direction is found, it is necessary to find an optimal step, which is checked using Armijo's rule. This scheme converges quickly to solutions and works well for convex functions.

Application

The optimisation algorithm has been applied to the rail curve of Monge's surface displayed on Figure 3.10. In this picture, the resulting Monge's surfaces are also shown, and the surfaces of revolution are coloured in blue and white. The reference curve is non-planar and has numerous inflection points, but it has a double symmetry. Therefore, only an even number of bi-arcs are used. As the number of bi-arcs increases, the curve becomes more and more similar to the reference curve, as seen on Figure 3.25. However, this also increases the number of different nodes, or panels when a Monge's surface is generated.

	Reference Surface	16 arcs	12 arcs	8 arcs
Number of families of panels	200	70	50	30
Number of families of nodes	200	40	30	20
Number of families of generatrix	20	4	3	2

Table 3.4 – Repetition of elements in Monge's surfaces.

This aspect of repetition of elements is explored in Table 3.4, for a subdivision with 80 elements on the rail and 10 elements on the generatrix. The formula for the number of families of elements is given in equations (3.14) and (3.15):

$$n_{panels} = n_{generatrix} \cdot (2n_{arcs} - 1) \tag{3.14}$$

$$n_{nodes} = n_{generatrix} \cdot n_{arcs} \tag{3.15}$$

In this case-study, the symmetry decreases further the number of different elements. Finally, the high congruence of lengths in isogonal moulding surfaces means that there a lot of identical generatrix in toric Monge's surfaces. This is of particular interest when the main structural elements are along the generatrix, like in stadium design.

This case study shows that optimisation of Monge's surfaces or moulding surfaces towards concatenation of surfaces of revolution is well performed by the algorithm proposed in this paper. The algorithm reached convergence (variation of the error functional of less than 0.1%) in less than 100ms, which allows real-time manipulation. It also illustrates the compromise that have to be met between fidelity to the

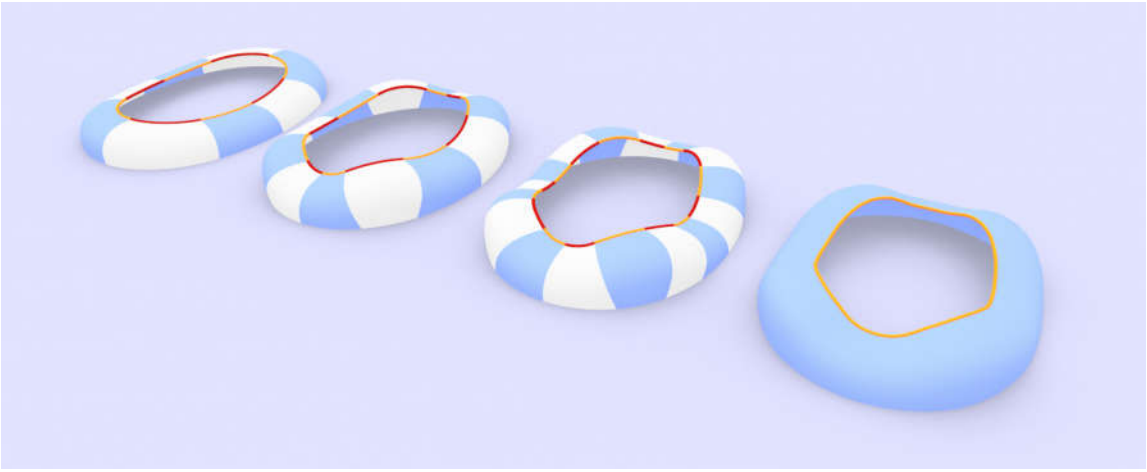

Figure 3.25 – The reference curve and the associated Monge's surface (right), and its approximation with 8,12,16 arcs (from left to right).

design intent and the project economy. In Figure 3.25, it is clear that the approximation of the rail curve with 8 arcs is far from the initial design. The approximations with 12 and 16 arcs are much better, and not significantly different, as they have the same inflections as the reference curve.

3.5.2 Another symmetrical pattern: loxodromic surfaces

Other patterns with a symmetry of revolution could be used to generate high node congruence in curved surfaces. However, most of them cannot be covered with planar facets and do not have particular offset properties. Among all the meshes that have a symmetry of revolution, loxodromic parametrisations are of interest. Loxodromes (also known as rhumb lines) on surfaces of revolution are lines that make a constant angle, noted α, with the parallels. Some examples of loxodromic parametrisations of a sphere are shown in Figure 3.26.

Figure 3.26 – Loxodromic parametrisations of a sphere: with $\alpha = 20°$, $30°$, $45°$ and $60°$ from left to right

The network constituted of the smooth loxodromes on a surface of revolution has a unique angle. In order to better understand this statement, consider Figure 3.27, which displays two loxodromes making a constant angle α with the parallels. We write β the angle made by the rhumb lines with the meridians. Keeping the notations of Figure 3.27, it is clear that:

$$4\,(\alpha + \beta) = 2\pi \tag{3.16}$$

Since α is constant, then β is also a constant. The angles between the two loxodromes $(2\alpha, 2\beta, 2\alpha, 2\beta)$ are therefore constant.

The case $\alpha = 45°$ is of particular interest, since in this case the two curves cross perpendicularly and the loxodromic parametrisation is a conformal parametrisation of the surface. Such networks are close to conical meshes, but are not covered with planar facets [262]. The only exception is the sphere, where all

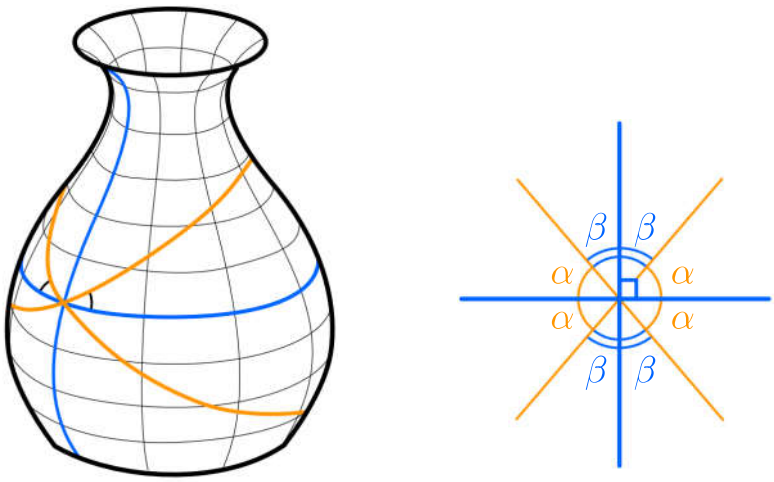

(a) A surface of revolution and loxodromes.

(b) The angles between the loxodromes are constant.

Figure 3.27 – Symmetries of a loxodromic parametrisation (in light orange) on a surface of revolution.

conformal parametrisations are parametrisations by lines of curvatures. A practical consequence is that the parametrisation of the sphere by the network of loxodromes of 45° are close to conical meshes with planar facets or circular meshes, which is an advantage for the cost-rationalisation. This parametrisation has very likely been used in Paul Andreu's design for the Osaka Maritime Museum, although the designers generated the curve network in order to guarantee the planarity of the panels and are not sure of the nature of the curves drawn on the spherical dome [133]. The design is shown in Figure 3.28, where the loxodromes are highlighted in orange.

Figure 3.28 – The Maritime Museum of Osaka (architect: Paul Andreu) is meshed with rhumb lines (orange curve) making an angle of 45° with the meridians and parallels (blue) (*picture retrieved on Wikipedia and distributed under a Creative Commons license*)

Loxodromic parametrisations offer thus a good potential for node repetition, as they feature a symmetry of revolution, and all the nodes of the smooth parametrisation are identical. Beyond the symmetries, it seems that nodes based on loxodromic parametrisations of surfaces of revolution can be constructed using a common rule. The spiraling geometry created by the loxodromic parametrisation has an undeniable æsthetical appeal, like illustrated in Paul Andreu's design. In a loxodromic parametrisation, the two families of curve play the same role: this is a fundamental difference with Monge's surface, where the parallels and rails have different properties.

In the followings, we call *loxodromic surfaces* the meshes created by Combescure transformations of loxodromic nets with a symmetry of revolution. The formal potential of loxodromic surfaces has not

been investigated as precisely as the one of isogonal moulding surfaces in this chapter. We recall some considerations of so-called lamella-domes in [226], which illustrates the possibilities of spiraling patterns for glazed grid-shells.

Two difficulties arise however, and would require more development if one were to design loxodromic surfaces with two input curves. The first limitation is that the two input curves should have symmetrical spherical images, like the curves shown in Figure 3.26. This is not obvious to add this constraint in CAD tools. The second limitation is that the design space offered by Combescure transformation is not as broad for loxodromic parametrisation compared to the canonical meshes of revolution, especially for closed nets.

The most meaningful strategy to evaluate the design space of loxodromic surfaces is therefore to generate loxodromic meshes on surfaces of revolution and to deform them with Combescure transformations. Combescure transformations for a given mesh constitute a vector space [198]. They can be computed through Singular Value Decomposition (SVD), and fitting problems can be solved on the vector space.

3.6 Summary of intellectual contribution

This chapter has introduced a methodology for the generation of shapes covered with high node repetition. We showed that Combescure transformations preserve the properties of node congruence, and used it to create isogonal moulding surfaces, a family of shapes having the same repetition properties as surfaces of revolution. A link was made between these surfaces and smooth geometry, which allowed the generalisation of the repetition of elements to Monge's surfaces. Like in previous research on element repetition in free-form surfaces, the role of the integral of curvature is a key notion for the understanding of the phenomenon.

Although one application on a specific family of surfaces was presented, the same methodology could be generalised to other patterns, like the loxodromic parametrisation of surfaces of revolution. Hexagonal or kagome pattern could be studied as well, as hexagonal patterns have more flexibility than quadrilateral patterns under Combescure transformation. Archetypal building typologies, like domes or stadia can be described with our method.

Chapter 4

Möbius geometry and generalised cyclidic nets

Circles are ubiquitous in classical architecture. Surfaces of revolution were used to construct domes on all continents, as circles can be drawn with a simple compass. The ancient Greeks and the engineers building masonry bridges used circles to approximate complex shapes [227]. The geometry of circles in space, also known as *Möbius geometry* is also a rich field of mathematics and plays a special role in the study of lines of curvatures of smooth surfaces. However, there is little exchange between the two disciplines, and the potential of Möbius geometry for architectural design is globally under-utilised.

The aim of this chapter is to link Möbius geometry with the flexible generation of architectural shapes that satisfy different fabrication constraints. In the followings of [73], we propose to parameterise shapes by patches of Dupin's cyclides instead of NURBS. The resulting shapes have nice properties for architectural design: they can be covered by planar facets and by torsion-free nodes.

4.1 Cyclidic Nets and Möbius geometry

4.1.1 Geometry of circular meshes

This section defines some key concepts related to architectural design of curved shapes. It recalls the link between continuous and discrete geometry, and especially the role of lines of curvatures for geometrical optimal design of quad meshes.First, we recall the role of circular meshes (introduced in Section 2.3.4) for architectural geometry.

Circular Meshes

The importance of using planar elements for cladding has been identified early in the history of free-form architecture. Triangular meshes provide planar elements, but quad meshes are often preferred because of simpler connection details. Due to their lower node valence, quad meshes also achieve a higher transparency than triangular meshes. This led to a research effort towards planar quads (PQ)-meshes [98, 148, 167].

Architectural designs require a structural depth, and therefore, an offset of the reference geometry, generally defined as a mesh. The notion of *torsion-free node* was thus introduced to define meshes where planar beams resting of the mesh edges meet along a common axis at each node. Trivial solutions for this problem exist (like translation along a constant vector), but non-trivial solution for layouts with torsion-free nodes requires some restrictions, like the notion of Conical Meshes introduced in [148]. Circular meshes constitute another important class of quadrilateral meshes where each face is inscribed in a circle. Writing α, β, γ and δ the consecutive inner angles of a quadrangle, a circular quad is characterised by following equation:

$$\begin{cases} \alpha + \gamma = & \pi \\ \beta + \delta = & \pi \end{cases} \tag{4.1}$$

Circular meshes have two interesting charateristics for architecture. First they admit constant vertex offset, a non-trivial torsion-free layout. Second they are seen as a discrete parameterization of surfaces by lines of curvature [200]. The notion of non-trivial mesh offset is actually closely linked to the lines of curvature of smooth surfaces. A surface parameterised by its lines of curvatures yields automatically meshes that are close to circular meshes [37, 196, 198]. It has also been noticed that planar hexagonal meshes are closely related to Dupin indicatrix of smooth surfaces, and that the optimal placement of hexagonal cells follows lines of curvature [261]. An example of such a mesh is shown in Figure 4.1. The hexagonal layout has been generated following lines of curvatures of the surface, the optimisation towards planarity being performed using dynamic relaxation [70, 228].

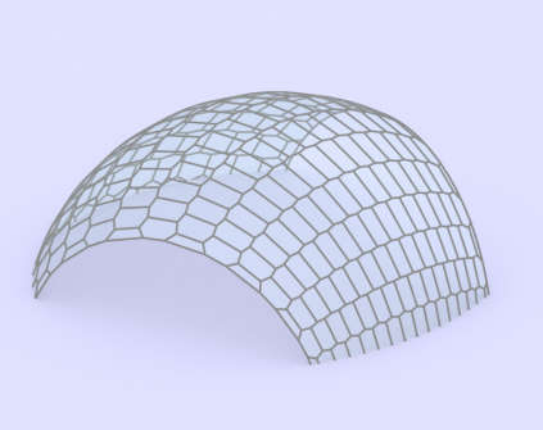

Figure 4.1 – A surface covered with planar hexagons, the panels layout follows lines of curvature.

Möbius transformations and Möbius Geometry

Lines of curvature play a crucial role in the efficient discretisation of complex shapes. It is therefore legitimate to study transformations that preserve lines of curvature. A particular group of such transformations is known as Möbius transforms, which are combinations spherical inversions and of homothetic transformations. These transformations also map circles to circles, and therefore map circular meshes to circular meshes. We will thus focus here on discrete surface where all faces are inscribed within circles [35], and thereby surfaces naturally meshed by their lines of curvature. So, the general framework of this study is the geometry of circles in space, also called Möbius Geometry.

More precisely, an inversion is defined by a center and a ratio. Consider a point $\mathbf{C}$, later called center of inversion, and a real number k. The inversion of center $\mathbf{C}$ and ratio k applied to a point $\mathbf{M}$ is a point $\mathbf{M}'$ defined by the well-known equation:

$$\mathbf{CM}' = \frac{k}{\| \mathbf{CM} \|^2} \cdot \mathbf{CM} \tag{4.2}$$

In the complex plane, the inversion of ratio k with center $\mathbf{C}$ (complex number z_C) reads as:

$$f_{k,\mathbf{C}}(z) = z_C + \frac{k}{\overline{z} - \overline{z_C}} \tag{4.3}$$

An elementary property of inversions is that they are involutions, which means that inversions are their own inverse transformations. This property is used in many applications shown in this chapter. It can finally be noticed that the ratio k is nothing more than a scaling factor. The position of the point $\mathbf{C}$ is the parameter that has a true impact on the shape deformation. It is interesting to notice that Möbius transformations do not preserve the global shape. These transforms give therefore a way to apply global deformations to meshes while preserving local properties. Indeed Möbius transformations preserve not only circles, but also local angles (two perpendicular curves remain perpendicular after inversion), and are thus conformal maps. The potential of these simple transformations is illustrated in section 4.5.1.

Combescure transformations

It has just been seen that Möbius transformations allow to modify the overall appearance of circular meshes by preserving the circumcircles of all quads. Another transformation that has the same property is the *Combescure transformation* already discussed in Section 2.3.4 [198]. By definition, Combescure transformations preserve discrete angles. Therefore they map circular meshes to circular meshes, as equation (4.1) is unchanged. Combined with Möbius transformations, they offer a wide range of possibilities to deform circular meshes.

Two meshes related by a Combescure transformation, with respective edges $(\mathbf{e_i})$ and $(\mathbf{e'_i})$, have to satisfy a linear equation:

$$\forall i, \mathbf{e_i} \wedge \mathbf{e'_i} = \mathbf{0} \tag{4.4}$$

Solutions for this equation are usually found using Singular Value Decomposition (SVD) [198]. We introduce in Section 4.3.1 a different original approach, restricted to quadrilateral meshes, but that offers a better performance than SVD. This technique takes inspiration from the one employed in [167], which is applied to the form-finding of planar-quadrilaterals meshes and discussed in Chapter 5.

4.1.2 Geometry of cyclidic nets

Circular meshes are considered as discrete equivalents of lines curvatures. The following of this section deals with the construction of smooth surfaces parametrised by their principal curvatures from circular meshes. The basis element used for this construction, known as Dupin cyclide, is introduced first.

Dupin cyclides

Dupin cyclides were discovered by the French mathematician Charles Dupin, who studied some of their remarkable properties in 1803. Dupin cyclides can be defined as inversion of tori in the sense of Section 4.1.1. Some special cases of Dupin cyclides include tori, cylinders and spheres. An example of a cyclide with patches following the lines of curvature is shown in Figure 4.2.

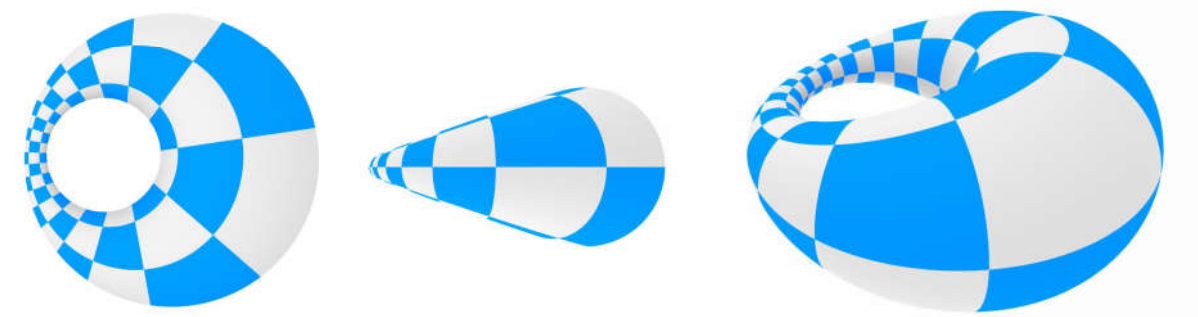

Figure 4.2 – Dupin's cyclide parameterised by its lines of curvature: top (left), front (center) and perspective (right).

For application in architecture, some properties of cyclides are particularly appealing:

- their lines of curvature are circles;
- a quad whose edges are lines of curvature is inscribed in a circle: lines of curvatures thus create naturally circular meshes;
- they are isothermic surfaces [3] and can therefore be covered with Edge Offset Meshes [198].

Beside, Dupin cyclides are easily parameterised by lines of curvature (think of them as inversions of tori). This guarantees easy subdivision of the mesh and good properties for other meshes than quad meshes, like hexagonal meshes [261] and Tri-hex meshes.

Cyclidic Patch

The four intersections of four lines of curvature in cyclides naturally define a circle. Conversely, a cyclic quadrilateral and a frame give a unique portion of cyclide, later called *cyclidic patch* in this chapter. Several algorithms have been proposed to convert a cyclidic patch to a NURBS surface, the one chosen here has been proposed in [91]. The algorithm requires a cyclic quadrilateral and an orthogonal frame (one blue and one red arrow in Figure 4.3). The other frames are generated by reflection with respect to the median plane of each edge of the quad and define the tangent vectors of the borders of the cyclidic patch. Notice how the median planes of each edge intersect at the center of the circumcircle of the quadrangle in Figure 4.3: this only occurs for circular quadrilaterals, and is the reason why the initial frame is unchanged after the four successive reflections. The boundaries of the patch are circles which are uniquely defined by two points and an orthogonal frame defining tangent vectors of the patches.

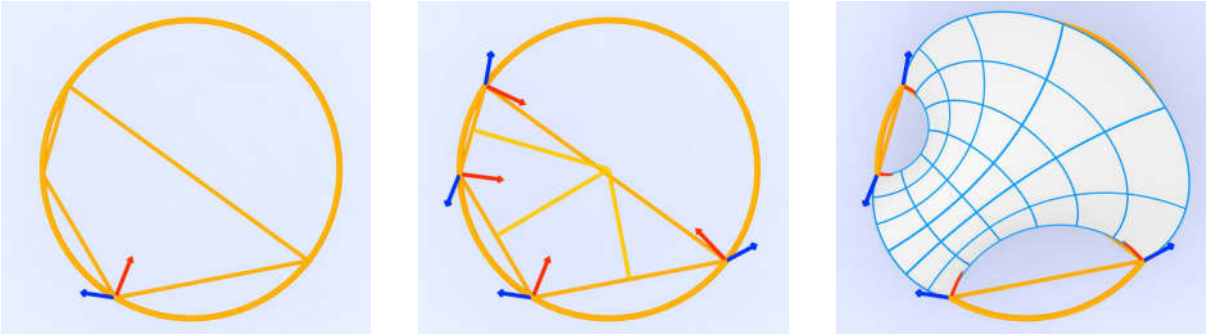

Figure 4.3 – Cyclidic patch: the four corners are on the same circle, the surface is naturally parameterised by its lines of curvature. The frames define tangent vectors for the edges of the patch.

The resulting surface is naturally parameterised by its lines of curvatures, since the underlying surface is a Dupin cyclide. This means that the trivial quad meshes on cyclidic patches like the one displayed in Figure 4.3 or Figure 4.4 are exact circular meshes.

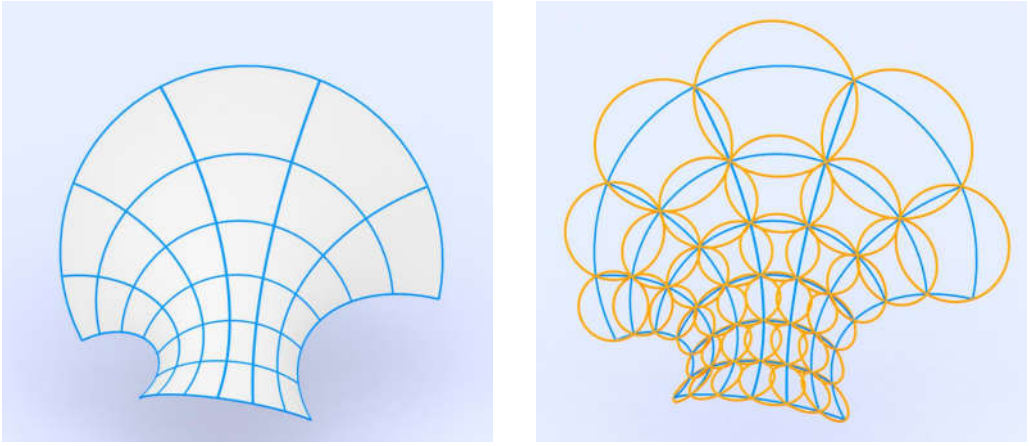

Figure 4.4 – Cyclidic patch meshed along its lines of curvature (left) and the associated circumcircles (right).

Cyclidic Nets

The properties of cyclides and the existence of a conversion algorithm to NURBS led to the idea of representing shapes as a collection of cyclidic patches. The mathematical properties of such shapes, called cyclidic nets, have been studied in [36]. Cyclidic nets are based on Circular Quadrilateral Meshes

and require only one frame vector, the others being generated by reflection if they belong to the same cyclidic patch. A simple reflection rule illustrated in Figure 4.5 allows the propagation of the frame to adjacent patches, so that the resulting surface is C^1

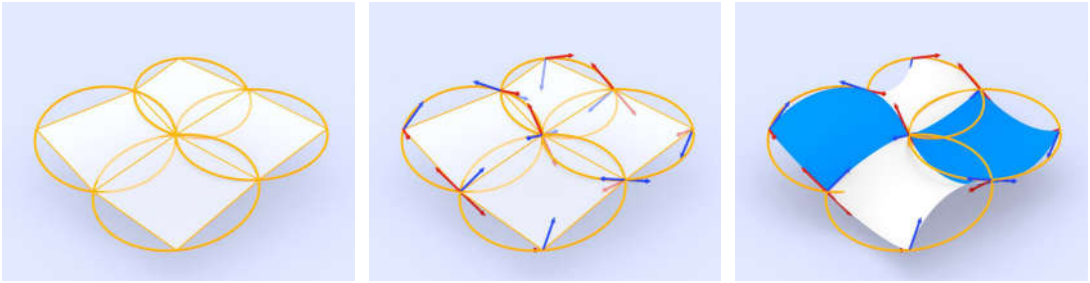

Figure 4.5 – A coarse circular mesh (left), the frames propagated by reflection (middle), and the resulting cyclidic net (right).

4.1.3 Limitations of current approaches and specific research objectives

The use of cyclidic nets in the field of computer-aided geometric design has been proposed as early as in the 1980's [163, 73]. Some of their properties are particularly interesting: they have a rational offset and a low algebraic degree, meaning that geometrical operations can efficiently be performed on cyclidic nets. However, practical limitations, the main one being the difficulty to model surfaces with umbilical points, restricted their possible field of application. We present here the main limitations of cyclidic nets for architectural design and establish three research objectives addressed in this chapter.

Primitives for circular meshes

Cyclidic nets require circular meshes as input. We aim here at using them to generate easily parametrised circular meshes. This approach is meaningful only if the size of the cyclidic patch exceeds the one of the panels built in reality. The problem of specifying appropriate initial input for cyclidic nets remains however open. Some shapes give trivial conical or circular meshes. Among them, surfaces of revolution, moulding surfaces or Monge surfaces [168]. This formal vocabulary is however restricted and other primitives are needed for cyclidic nets.

Complex topologies and umbilical points

Dupin's cyclides do not have umbilical points: their lines of curvature and therefore the edges of cyclidic patches are thus strictly perpendicular. Consequently, smooth cyclidic nets require that exactly four patches meet along a common vertex, so that shapes with complex topologies cannot be modelled. This can also be seen considering the reflection rule applied in Figure 4.3 and 4.5: the perpendicularity of the frames is necessarily preserved by the reflection operations. To cope with this limitation, the next sections develop three new strategies that extend the field of possible shapes and topologies for smooth and non-smooth cyclidic nets.

Closed loops

A significant issue linked with the practical modelling with cyclidic nets is the construction of closed nets forming loops. Indeed, a closed circular mesh does not necessarily yield valid cyclidic nets, as illustrated in Figure 4.6. In this figure, the reflection rule is applied along the closed strip, and the resulting surface is not continuous. Closed surfaces are required for the modelling of building façades or roofs, so that this limitation is problematic for architectural design.

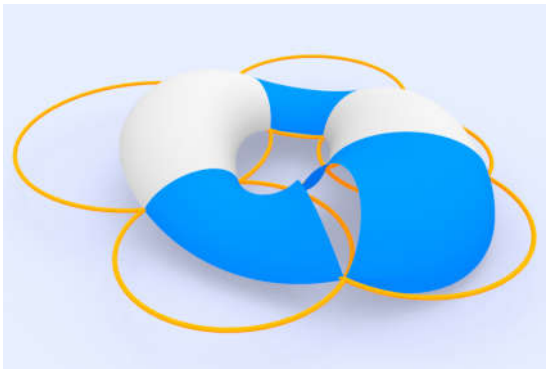

Figure 4.6 – A closed circular mesh which yields invalid cyclidic nets

Surface smoothness

Creases, understood as normal vector discontinuity, are an essential feature of free-form architecture. As an example, they are a well-known feature of Frank Gehry's architectural language and were also used by master designers like Eduardo Torroja for the Zarzuela Hippodrome or Nicolas Esquillan in several designs [25, 158, 174]. However, their construction remains a challenge, as creases are generally not aligned with lines of curvature, excluding the possibility to build them as conical meshes. Nicolas Esquillan's works give good examples of creased shells, like illustrated in Figure 4.7. However, each solution was tailored for a specific project, leaving no general method to generate constructible creases [174].

Figure 4.7 – The CNIT: a creased shell designed by Nicolas Esquillan

The usual modelling tools, even based on post rationalisation of geometry hardly deal with the problem of discontinuity of normal vector in the rationalisation of free-form structures. The only recent examples dealing with curved crease in architecture consider developable surfaces [128], which are sensitive to local buckling due to their zero Gaussian curvature.

Research questions

Applications of cyclidic nets for architecture have already been proposed in [34], the cyclidic patches being typically the size of panels. This solution has the advantage of generating one unique type of node, but it requires building with circular arcs. Besides, if the designer wants to modify the structural layout, with this solution a complete remeshing is required. Moreover, considering the fact that a cyclide can easily be meshed by its lines of curvature to form a circular mesh, one might see cyclidic nets as a tool to define the global shape and the underlying discretisation of each cyclidic patch as the real structural layout. Doing so, the designer works with circular meshes, keeping the density of the mesh as a parameter almost independent of the shape. The opportunity offered by larger cyclidic patches as global modeling tool is unexplored up to now, although the potential for automation of the mesh generation with cyclidic nets seems promising.

We propose here to explore the possibilities offered by this strategy and to address the limitations presented in this section. The main contributions of this chapter follow:

- The extension of cyclidic nets to arbitrary topologies by the implementation of a hole-filling algorithm.
- The construction of cyclidic nets with creasing by the adaptation of their rule of construction.
- The construction of closed cyclidic nets without discontinuity in Section 4.4.2.
- The creation of a family of shapes called *super-canal surfaces*, derived from simple primitives for cyclidic nets is proposed in Section 4.2.
- Some problems for the practical modelling with super-canal surfaces are presented in Section 4.3, like curve-fitting problems are solved and constitute an original contribution of this chapter.
- Some rules for shape composition with super-canal surfaces and generalised cyclidic nets are presented in Section 4.5.

4.2 Constructing new families of shapes with cyclidic nets: super-canal surfaces

Cyclidic nets and Möbius geometry offer a rich potential for the modelling of free-form architecture. They require however coarse circular meshes as input. This section considers the simplest input possible for cyclidic nets: a circular strip. By using transformations that preserve circular meshes, the formal possibilities offered by this simple approach are expanded. We call the shapes generated with this method *super-canal surfaces*, by reference to *super-cyclides*, which are extensions of Dupin cyclides [8]. In this Section, the generation principles for super-canal surfaces are introduced.

4.2.1 Canal surfaces

Consider a circular strip supporting a cyclidic net such as the one displayed in Figure 4.8. The resulting surface has circular lines of curvature in one direction. Such surfaces are called *canal surfaces*. Canal surfaces are a fundamental family of surfaces in the context of Möbius geometry, as this family is indeed invariant by Möbius transformations. Canal surfaces are defined as envelopes of spheres. They are commonly used in computer-aided design, as spheres can be manipulated interactively by the designers. The definition of properly parametrised envelopes of spheres is still a topic of research [20]. In the example of Figure 4.8, eight circles in the same plane are used to generate a canal surface. Only the portion of the canal surface above the construction plane is shown.

Canal surfaces can be defined as surfaces such that lines of curvatures are circles. With this point of view, the invariance of canal surfaces under Möbius transformations is obvious, because inversions preserve lines of curvatures and circles. Another way to look at it is that Möbius transformations preserve both spheres and angles, therefore an envelope of spheres is preserved by inversions. Notice that the shape-generation of canal surfaces with Dupin cyclides has been studied in [237]. We use an optimisation approach introduced in [33] to obtain shapes with smooth parametrisations.

These surfaces are very easily parameterised by cyclidic patches, as Dupin cyclides are particular cases of canal surfaces. The C^1 continuity and generalisation to C^0 continuity is insured by reflections according to the method described in [36].

4.2.2 A general framework for shape generation

In this section, we propose to extend to formal vocabulary of canal surfaces by using combinations of Combescure and Möbius transformations. We have seen that the generation of canal surfaces requires a simple input: a circular strip. Therefore, the proposed methodology translates into a simple framework where the end-user has the control of three curves: the two boundaries of the circular strip and one curve crossing the strip. This makes the proposed shapes comparable to two-rails sweeping surfaces, which

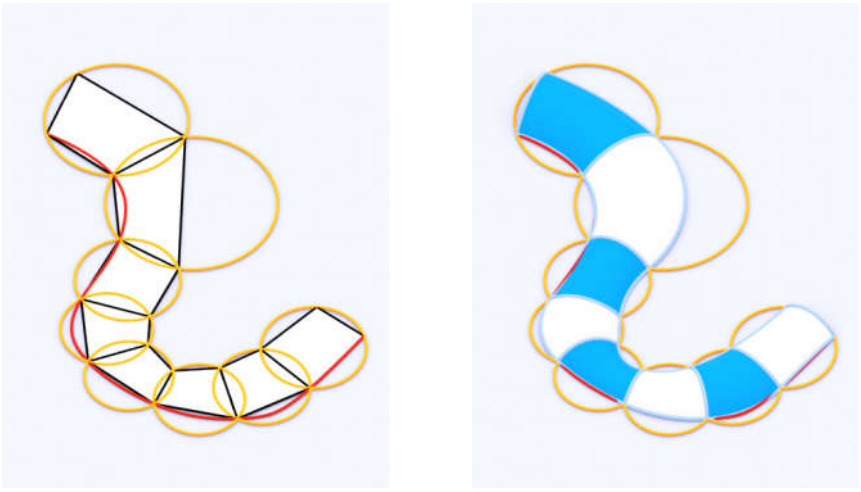

(a) Circular strip supported on a given curve (red)

(b) One of the cyclidic nets supported on the circular strip

Figure 4.8 – A canal surface created from a coarse circular strip

are commonly used in Computer-Aided Geometric Design. The three curves used for construction are necessarily perpendicular to each other. Indeed, canal surfaces do not have umbilical points (except poles), and consequently, their lines of curvature are necessary perpendicular. The designer thus chose a rule of construction for the surface, i.e. a specific combination of Combescure and Möbius transformations. Each rule giving eventually additional degrees of freedom further discussed in the next sections. The identified families are proposed in Figure 4.9. The nomenclature for the different surfaces follows:

- the letter C denotes that the initial shape was subjected to a Combescure transformation;
- the letter M denotes that the initial shape was subjected to a Möbius transformation;
- the order of the letters gives the order of composition of the transformations: CM means that the initial shape was subject to a Möbius transformation, then a Combescure transformation;
- the name of the initial shape subject to the transformations stands at the end: for example a $M-$revolution surface is an inversion of a surface of revolution.

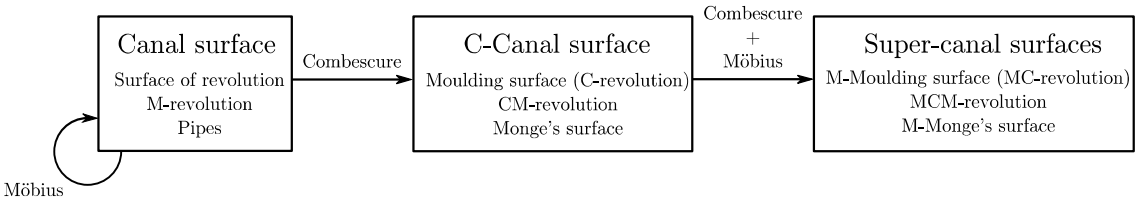

Figure 4.9 – Shapes created with our method

Many surfaces well-identified in the literature can be generated with this method as illustrated in Figure 4.9. All the common surfaces used for geometrically-constrained methods for PQ meshes fall into the category of super-canal surfaces, with the exception of scale-trans surfaces. The curves used in surfaces of translation and scale-trans surfaces do not correspond in general to lines of curvatures and cannot be approached by circular meshes. It appears that moulding surfaces and Monge's surfaces discussed in chapter 3 are a subset of the shapes generated by Combescure transformations of canal surfaces. From a practical point of view, shapes with a family of planar curves are of great interest in construction. For that reason, we restrict the examples of application to $CM-$surfaces, where the families of circles are transformed into planar curves.

4.2.3 Mechanical properties of super-canal surfaces

We propose here a comment on the mechanical properties of canal and C-canal surfaces. We have seen in chapter 2 that structural artists like Dischinger or Candela developed theories to analyse the structural performance of the shells they designed. Such developments are not necessary here. C-canal surfaces play indeed a particular role in shell theory, as Rogers and Schief proved that their lines of curvatures are also lines of principal stresses under a uniform external load [211, 219]. This result was also proven for canal surfaces before in [236]. This induces two remarkable features for the behaviour of the shapes previously presented:

- principal stresses lines following principal curvature lines, the natural mesh of C-canal surfaces is an optimal mechanical layout for a grid structure;
- all closed shapes generated by this method are in equilibrium under uniform pressure and therefore suited for pneumatic structures.

Therefore, C-canal surfaces can be considered as the results of some form-finding problem. We point out that this result is limited to closed surface: free edges must be treated with special attention. Before showing the shape generation framework, we should make a comment on potential applications for shallow roof structures. A normal pressure load is surely very close to a uniform distributed load for surfaces with moderate curvature. It can be concluded that shallow canal surfaces are close to funicular shapes under uniformly distributed load. This kind of consideration has been documented for shallow arches: shallow circular arcs, parabola or catenary have similar geometry and mechanical behaviour, especially buckling capacity. For more comments on this topic, the reader can refer to [249]. From this short literature review, we conclude that C-canal surface are interesting in terms of fabrication, but also because of their mechanical performances.

4.2.4 Properties of the structural layout

Table 4.1 sums up the different properties of the surfaces created with our framework. As one applies Möbius and Combescure transforms, some properties are lost a priori. Among other remarkable properties, it may be noticed that the images of surfaces of revolutions are isothermic surfaces, and it possible to parametrise them with conformal squares. C-canal surfaces are of interest because they have a network of planar curves that simplify manufacturing and an interesting structural behaviour.

<table>
<tr><th colspan="2"></th><th>Isothermic</th><th>Planar curves</th><th>Stress lines</th><th>Circular mesh</th></tr>
<tr><td rowspan="3">Canal surface</td><td>revolution</td><td rowspan="2">Yes</td><td rowspan="5">Yes</td><td rowspan="5">Yes</td><td rowspan="5">Yes</td></tr>
<tr><td>M-revolution</td></tr>
<tr><td>General case</td><td>No</td></tr>
<tr><td rowspan="3">C-canal surface</td><td>C-revolution (moulding)</td><td rowspan="2">Yes</td></tr>
<tr><td>CM-revolution</td></tr>
<tr><td>General case</td><td>No</td></tr>
<tr><td colspan="2">Super-canal surfaces</td><td>No</td><td>No</td><td>No</td><td>Yes</td></tr>
</table>

Table 4.1 – Properties of the shapes developed with our framework.

4.2.5 Input for design with super-canal surfaces

In the following of Glymph *et al.*[98], we propose to design super-canal surfaces from two curves. The simplest way to parameterise a canal surface is to take a strip of circles as input parameters, as pictured in Figure 4.8. A two parameters family of cyclidic nets can be supported on the circular mesh: the choice of those parameters can be done to fulfill some design requirements, like the shape smoothness, evaluated for example with conformal Willmore energy [38].

To define the strip of circles, the user can draw manually a collection of circles, or entirely parametrised it by a boundary curve and the radii of circles or a target length for each border. The latter parametrisation is depicted in Figure 4.10, whose input data follows:

1. a list of points on a curve in space;
2. one point **P** in space defining the first circle;
3. a function describing the lengths of each edge crossing the strip (thick orange lines on Figure 4.10).

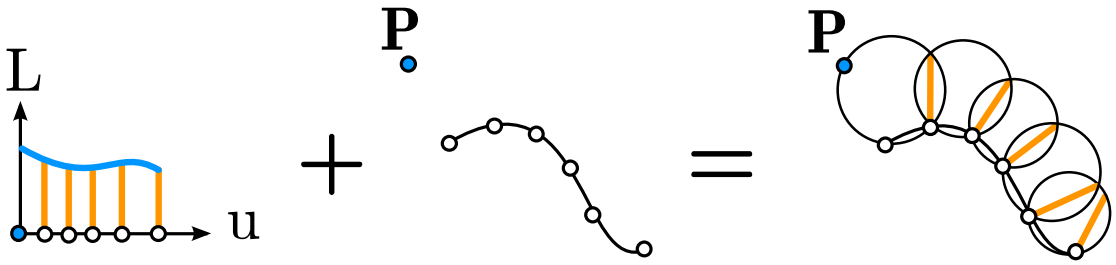

Figure 4.10 – Parameters creating a circular strip that can support a canal surface

It is then possible to construct one unique circular strip passing through the input points by propagation, in the manner of [72]. The construction of a circular strip restricts the two boundaries to be lines of curvature of the resulting surface. Section 4.3.2 will show how this condition can be relaxed, while keeping the parametrisation of the shapes by cyclidic nets and circular strips.

4.3 Implementation of super-canal surfaces

The implementation of super-canal surfaces within modelling software requires the solution of several problems, like the optimal fitting of curves by canal surfaces, or the efficient computation of transformations preserving circular meshes. This Section deals with the solution of such problems, which make super-canal surfaces an interactive tool for complex shape modelling.

4.3.1 Efficient computation of Combescure transformations

The generation of super-canal surfaces requires the computation of Combescure transformations. A new algorithm for computation of Combescure transformations of quadrilateral meshes is proposed in the followings. It will be shown that it outperforms techniques classically used, and that it requires the minimum number of operations possible.

Let us consider two parallel quadrilaterals, like the ones shown in Figure 4.11. Up to a translation, prescribing the lengths of two sides l_0 and l_3 (thick lines on the figure) is sufficient to determine a unique quadrilateral with internal angles α,β,γ,δ. The last point C (white dot on the figure) is found by intersecting two lines (dashed lines on the figure). For the sake of simplicity, we consider planar quadrilaterals in the reference plane (ABD): the equations are written in a frame centered in A and represented by the blue arrows in the figure. The intersection is found by solving the following equations:

$$\begin{pmatrix} l_0 + l_3 \cos\alpha \\ l_3 \sin\alpha \end{pmatrix} = \begin{pmatrix} \cos\beta & \cos(\alpha-\delta) \\ -\sin\beta & \sin(\alpha-\delta) \end{pmatrix} \cdot \begin{pmatrix} l_1 \\ l_2 \end{pmatrix} \tag{4.5}$$

In the same way, prescribing the lengths of all edges on two intersecting lines, as shown in Figure 4.12 is sufficient to determine the entire parallel mesh. In this image, the thick lines correspond to edges which have prescribed lengths. Starting from a quadrilateral with two prescribed lengths, it is possible to apply equation (4.5) and find the last point of the quadrilateral (white dot). It is then possible to apply this procedure to the next quadrangle in the same row, and so forth, up to completion of each strip.

This iterative procedure is computationally efficient. The number of operations and the use of memory is proportional to the number of faces in the mesh, as the solution of the propagation requires NM applications of equation (4.5) for a mesh of N times M facets. Therefore, the computation time varies also

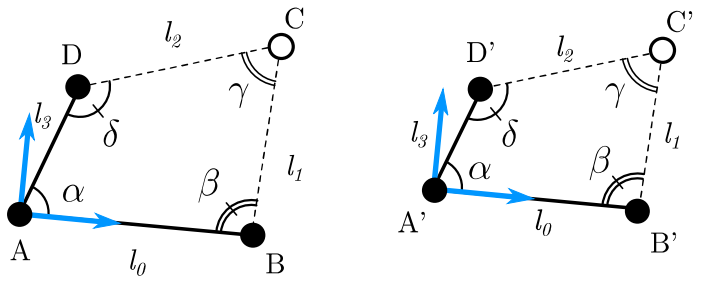

Figure 4.11 – Two quads related by a Combescure transformation.

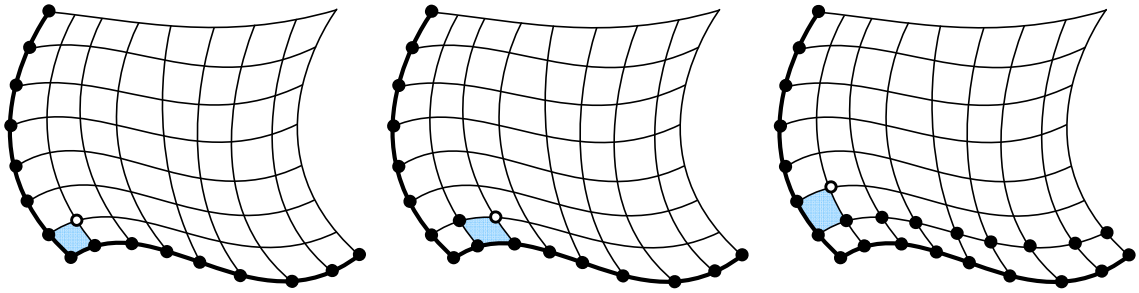

Figure 4.12 – Propagation method for the computation of a Combescure transformation with quadrangles.

linearly with the number of faces, as discussed in [167]. This technique is thus more efficient than SVD, which requires assembling of matrices and has a complexity of $\max(N^2M, NM^2)$. The computational gain is especially important for large meshes and makes the method proposed in this chapter suited for real-time applications.

Constructing a Combescure transformation is equivalent to solving a linear system of equations. It can be noticed that the method proposed in this Section is equivalent to write this linear problem in a sparse form: if written in a matrix form, the matrix would be tri-diagonal.

4.3.2 Generation of canal surfaces

The previous section discussed how canal surfaces can be parametrised with circular strips supporting cyclidic nets. This generation method leads however to a strong formal restriction, as it imposes the two boundaries of the strip to be lines of curvature of the resulting canal surface. The practical consequence is that the second curve is restricted to be on a developable surface passing through the first curve, whereas the designer would prefer to define it independently. In modelling applications, specifying contour curves of canal surfaces is of interest and is still an active topic of research, like illustrated in [26] for example. This section introduces thus an original algorithm for the shape generation of canal surfaces from two curves where only one of the two curves is a line of curvature of the canal surface. The problem is illustrated in Figure 4.13 and it will be shown that it admits a one parameter family of solutions.

Preliminary considerations

The relevant definition of canal surfaces in this case is to consider them as the envelope of a family of spheres. Remarkable properties of canal surfaces, and of lines of curvature in general can be mentioned:

1. Canal surfaces are envelopes of spheres, and as such, the spheres generating the surface meet tangentially with any curve of a canal surface.

2. The envelope of the lines directed by the normal of the surface along a line of curvature is a developable surface.

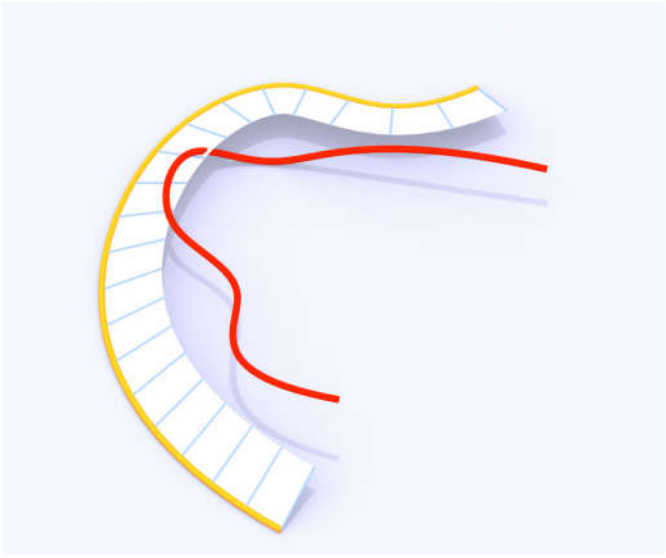

Figure 4.13 – Input data for the curve-fitting problem. Line of curvature (orange), line to fit (red), and surface containing the centers of the spheres (white).

From remark 1, we get that the locus of the centers of the spheres generating the canal surface is on the surface generated by the normals of the surface. From remark 2, we get immediately that this is a developable surface. Actually, it is a specific case of Monge's surface [168]. Hence, once one normal has been chosen, the other normals are determined uniquely so that the envelope is a developable surface. The locus of the centres of the spheres is therefore controlled by one orientation parameter. This is illustrated in Figure 4.14: choosing the orientation of the normal is equivalent to choosing a surface tangent to the resulting canal surface.

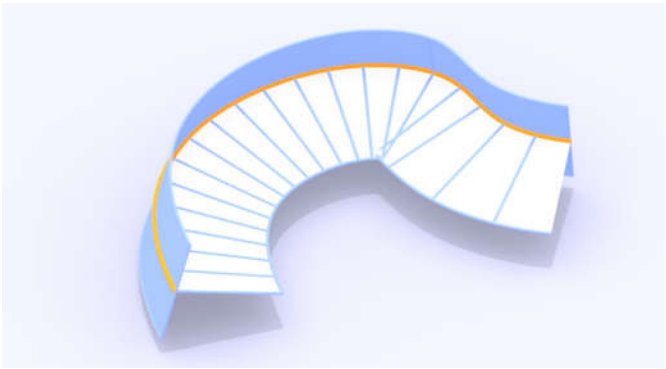

Figure 4.14 – Line of curvature: one developable surface containing the centres of the spheres (white). The developable surface perpendicular to it (blue) is tangent to the resulting canal surface.

Computation of the locus of centre

Consider now that a normal vector and a line of curvature have been specified for the canal surface. The locus of centres is on a developable surface. So far we did not use any property of the second curve. We notice however that the centres of the spheres are on the *bisector surface of the two curves*. Such surface is defined as the envelope of the points which are equidistant to both curves. They have been studied in [77] for example.

Therefore, the centres of the spheres can be found by intersecting the bisector surface of the two curves and the developable surface constructed from the normals. Both surfaces are infinite, and it seems

intuitive that they will have an intersection in non-degenerate cases. The construction of the whole bisector surface is however not necessary, as it is meaningful to consider only a finite collection of spheres that will construct the cyclidic net that parametrise the canal surface.

Consider the first curve discretized with n subdivisions, as depicted in Figure 4.15. The centres of the spheres belong to n lines belonging to the developable surface. Let $\mathbf{P}_k$ be the k^{th} point on the first curve, $\mathbf{C}_k$ the centre of the bi-tangent sphere on the corresponding line and $\mathbf{C'}_k$ the closest point to $\mathbf{C}_k$ on the second curve. We minimise the following functional:

$$F = \sum_{k=0}^{n} \left(\|\mathbf{C}_k\mathbf{P}_k\| - \|\mathbf{C}_k\mathbf{C'}_k\| \right)^2 \tag{4.6}$$

The positions of the $\mathbf{C}_k$ are encoded with independent unique parameters. Each term of the sum can thus be minimised individually by the means of Newton's method.

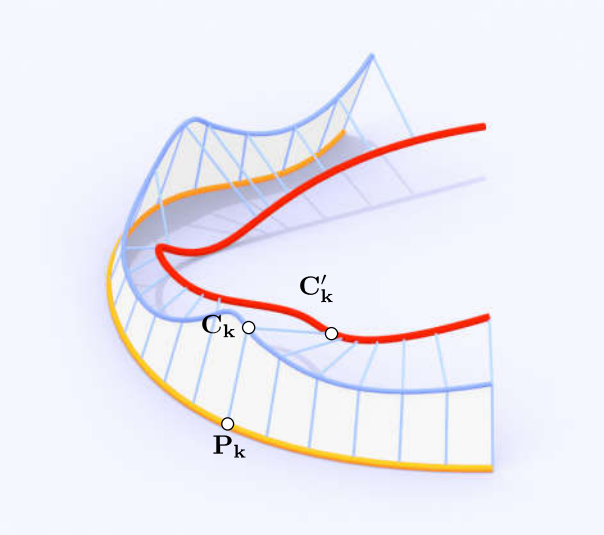

Figure 4.15 – The curve fitting problem: the locus of the sphere centres (in dark blue) belongs to the developable surface chosen by the user, and each $\mathbf{C_k}$ belongs to a straight line of this surface. The locus of centres is equidistant to both input curves.

Algorithm for spheres generation

The algorithm for the generation of a canal surface from two curves follows:

1. Select two curves, one of them being the future line of curvature on the final surface.
2. Choose a slope or orientation of the canal surface: specifying one orientation restricts the locus of centers to be in a uniquely defined developable surface.
3. Discretise the line of curvature with points $\mathbf{P}_k$, and generate the lines containing the centres of the spheres on the developable surface.
4. Initialise the $\mathbf{C}_k$ with $\mathbf{C}_k = \mathbf{P}_k$.
5. Minimise Equation(4.6) with Newton's method.
6. Construct the sphere $\mathcal{S}_k$ of center $\mathbf{C}_k$ and radius R_k, with $R_k = \|\mathbf{C}_k\mathbf{P}_k\|$.

Generation of a supporting cyclidic net

We have seen that given two curves and a supplementary condition, it is possible to define one unique family of spheres that fits optimally the two curves. Consider now the circles $\mathcal{C}_k$ defined as the intersection of successive spheres $\mathcal{S}_k$, $\mathcal{S}_{k+1}$, like shown in Figure 4.16. $\mathbf{P_k}$ is the point of $\mathcal{C}_k$ on the input curve.

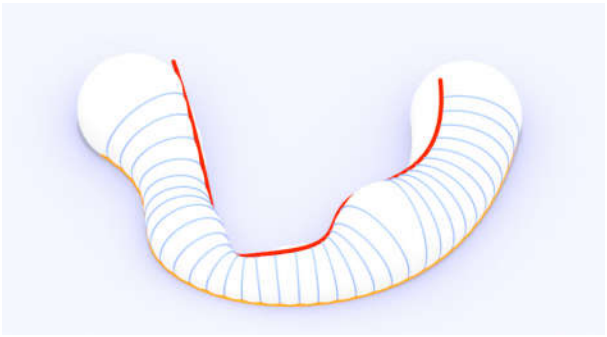

Figure 4.16 – A family of spheres (white) fitting two curves (red and orange), and their successive intersection (blue).

It is clear that for any k, $\mathcal{C}_k$ and $\mathcal{C}_{k+1}$ both belong to the sphere $\mathcal{S}_{k+1}$. Consider Figure 4.17. Choosing one point $\mathbf{V}_k$ on C_k there is exactly one point $\mathbf{V}_{k+1}$ on $\mathcal{C}_{k+1}$ so that $\mathbf{P}_k\mathbf{V}_k\mathbf{V}_{k+1}\mathbf{P}_{k+1}$ is inscribed within a circle. The point $\mathbf{V}_k$ is not necessarily on the curve fitted by our method. Indeed, the fitted curve is generally not a line of curvature of the resulting canal surface.

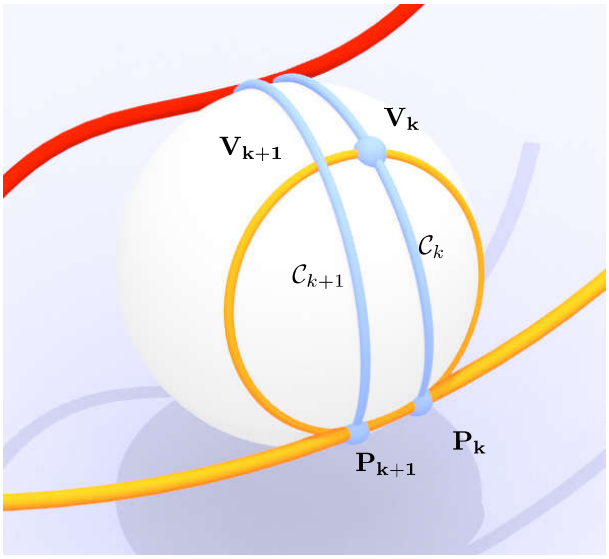

Figure 4.17 – Two circles $\mathcal{C}_k$ and $\mathcal{C}_{k+1}$: by choosing one point $\mathbf{V_k}$ on $\mathcal{C}_k$, one defines a circle and a one parameter family of cyclidic patches.

Applying iteratively the procedure to $\mathcal{C}_{k+1}$ and so on, we can generate a circular strip and then build on it a cyclidic net. The circles $\mathcal{C}_k$ are edges of a cyclidic strip because successive circles belong to the same sphere [36]. There are actually infinitely many cyclidic strips supported on the created circular strip and having the circles $(\mathcal{C}_k)$ as edges. On degree of freedom remains: the orientation of the frames used for construction of the cyclidic patches. Only one vector is constrained by the construction of the $(\mathcal{C}_k)$. The other vector of the frame is chosen in order to smooth the resulting canal surface.

Comment

The proposed method allows for the construction of a canal surface that fits optimally two input curves. The surface can be parametrised instantly with cyclidic patches and covered with a circular mesh. The tool recalls the two-rails sweep commonly used in CAD software. One curve is a line of curvature of the resulting shape. It provides proper alignment of the mesh with the borders, which often dictate the mechanical behaviour of the structure.

4.3.3 Generation of M-revolution surfaces

The most well-known canal surfaces are surfaces of revolution. They indeed correspond to the case of a straight generatrix. Surfaces of revolutions have many interesting properties for applications in architecture. They are isothermic surfaces, which means that they can be discretised as Edge-Offset Meshes. Yet, isothermic surfaces are preserved by Combescure and Möbius transformations and they thus inherit this property.

An interesting case of *'super-surfaces of revolutions'* occurs when the center of inversion and the axis of revolution are in a horizontal plane, as shown in Figure 4.18. One family of curvature lines on the surface of revolution is then vertical, and so is their image by inversion. Combescure transformations preserve planarity: applying Combescure transformation after the inversion yields a surface with planar arches. This additional property is particularly interesting for applications to hierarchised structural system with continuous arches and secondary structure. A specific method has therefore been developed specifically to generate these surfaces, it consists of solving the inverse problem detailed in the followings.

The input data for the problem are displayed in Figure 4.18. The user prescribes one planar curve, one circle in the same plane comprising the ends $\mathbf{P_1}$ and $\mathbf{P_4}$ of the curve, and two points $\mathbf{P_2}$ and $\mathbf{P_3}$ on this circle. The objective is here to reconstruct the initial surface of revolution, therefore the problem is to find a center of inversion $\mathbf{C}$ so that the image of the quadrangle $P_1P_2P_3P_4$ is an isosceles trapezoid.

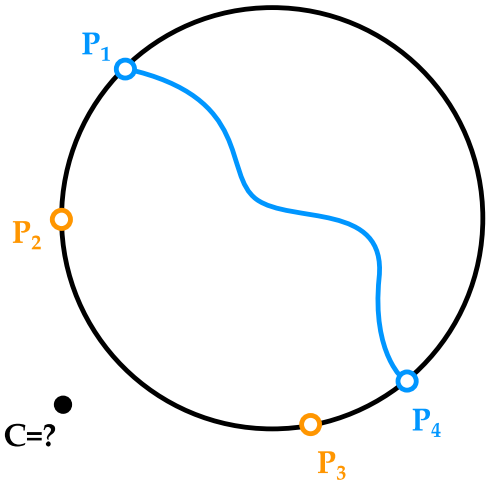

Figure 4.18 – Problem for the practical design with inversion of surfaces of revolutions.

Isosceles trapezoids are the only cyclic quadrilaterals that have parallel opposite edges. Notice that the problem is planar and can thus be formulated with complex numbers. The parallelism corresponds to the fact the direction vectors are colinear (identical up to a scaling by a real number t). Assigning the complex numbers z_1, z_2, z_3 and z_4 to the points $\mathbf{P_1}$, $\mathbf{P_2}$, $\mathbf{P_3}$ and $\mathbf{P_4}$, and writing $z_{j,C}$ the complex number associated to the image of z_j by an inversion of center $\mathbf{C}$, we obtain equation (4.7):

$$\frac{z_{2,C} - z_{1,C}}{z_{3,C} - z_{4,C}} = t \in \mathbb{R} \tag{4.7}$$

We can use the equation (4.3) to express equation (4.7) with respect to the z_j and obtain equation (4.8).

It is independent of the ratio of inversion k: the position of the center of inversion is the only value of interest in this problem.

$$\frac{\left(\dfrac{z_2 - z_1}{(z_1 - z_C)(z_2 - z_C)}\right)}{\left(\dfrac{z_3 - z_4}{(z_3 - z_C)(z_4 - z_C)}\right)} = t \in \mathbb{R} \tag{4.8}$$

After simplifications, this equation leads to a second order equation in z_C. The general form of (4.8) can be written as:

$$A_t z_C^2 + B_t z_C + D_t = 0 \tag{4.9}$$

with

$$\begin{cases} A_t &= z_2 - z_1 + t \cdot (z_4 - z_3) \\ B_t &= -(1+t) z_1 z_3 + (t-1) z_1 z_4 \\ & \quad + (1+t) z_2 z_4 + (1-t) z_2 z_3 \\ D_t &= z_3 z_4 (z_2 - z_1) + t z_1 z_2 (z_4 - z_3) \end{cases}$$

The case of $A_t = 0$ can occur only when the quad $P_1P_2P_3P_4$ is already an isosceles trapezoid. In the other cases, for each value of t, there are two complex solutions giving two positions for the center of inversion in the complex plane. It is thus possible to solve this inverse problem with a straight-forward solution based on complex analysis.

An illustration of this problem is shown on Figure 4.19. On this image, all the facets are inscribed within circles. The free-form shape is thus covered with planar facets and torsion-free nodes. Since the circle shown in Figure 4.19 is in the horizontal plane, it is noticed that one family of lines of curvature consists of planar vertical arches. The solution proposed here can easily be extended to the case of a spherical guide curve with two successive inversions.

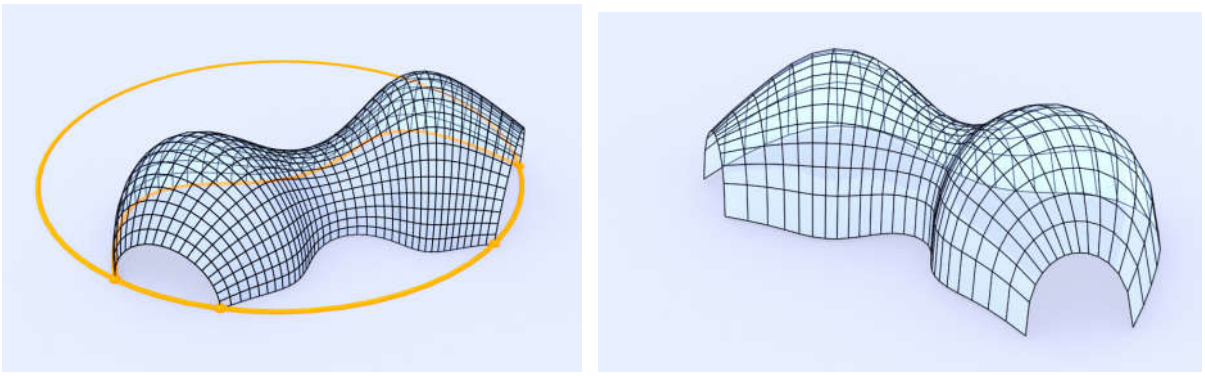

(a) M-revolution surface

(b) CM-revolution surface obtained by a Combescure transformation

Figure 4.19 – Surfaces generated by inversion of a surface of revolution constructed from one curve and two points on a circle.

4.3.4 C-canal surfaces

C-canal surfaces are defined as the surfaces resulting from Combescure transformations of canal surfaces. We consider the meshing of canal surfaces by their lines of curvature: on family of which is made of circles. The image of those circles by Combescure transformation is therefore a family of planar curves, as Combescure transformation preserve planarity. There is therefore a practical interest for the builder, since large portions of the structure can be prefabricated and pre-assembled easily as planar elements. We discuss here practical generation of C-canal surfaces.

Figure 4.20 shows the three input data for the generation of a C-canal surface. In the generation method proposed here, the user can specify one curve, a collection of lengths defining indirectly a second

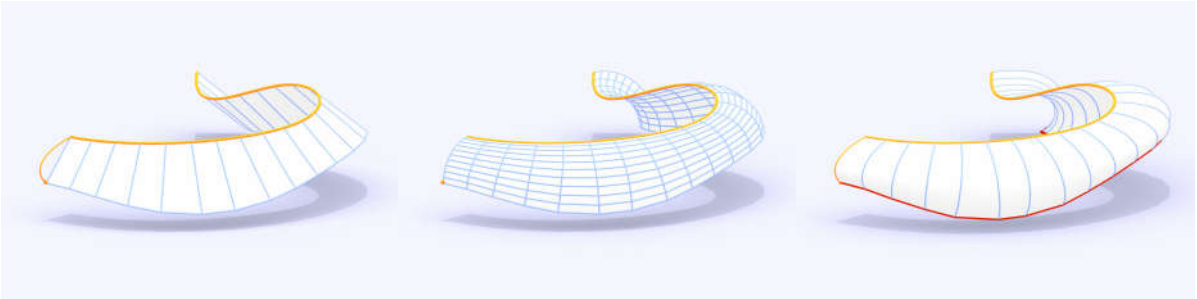

(a) Circular strip (b) A canal surface supported on the strip (c) A C-canal surface covered with D-strips

Figure 4.20 – Generation of a C-canal surface

curve, and a planar cross-section that is obtained by Combescure transformation of a circle. The inputs controlled by the designer are thus the same as the one described in Figure 4.10, with the control of one section curve in addition.

The lengths of the edges are specified for the C-canal surface, but at the beginning, only the canal surface can be computed. An optimisation procedure is thus required to find the canal surface that will fit the input data after Combescure transformation.

Writing $\mathbf{L}$ the target lengths for the curves crossing the C-canal surface (see Figure 4.10), we generate first the canal surface $\mathcal{F}(\mathbf{u}, \mathbf{L})$. There is one Combescure transformation f that maps the first circle of the canal surface to the section curves chosen while preserving the rail curve. After the Combescure transformation, the resulting lengths $\mathbf{L}'$ on the C-canal surface differ from $\mathbf{L}$. However, Figure 4.20 shows that a canal surface and a C-canal surface related by a Combescure transformation have similar boundaries, even if they do not perfectly coincide. Therefore, a descent method can be used to minimise the error:

$$E(L_k) = \sum_k (L'_k - L_k)^2 \tag{4.10}$$

The minimisation of this error is not difficult. The optimisation is done for each L_k successively. This prevents from computing the whole Combescure transformation at each iteration, but only the strip where the error is evaluated. With this precaution, the computation remains lightweight and stable. This optimisation procedure can be extended to the fitting of two curves, like done in 4.3.2.

4.3.5 Meshing of super-canal surfaces

A key feature of the proposed method is that it operates fundamentally on smooth surfaces. It is therefore independent from the mesh density. For example, the solution of equation (4.9) does not require any knowledge on the discretisation of the curves, but only the four prescribed points. Therefore, remeshing of super-canal surfaces is extremely simple.

Given a discretisation on the guide curves, it is possible to find their image by a composition of Combescure and Möbius transformations f so that they fit with the boundaries of a canal surface. The meshing on the canal surface is done using cyclidic patches, like explained in Section 4.2.1. The inverse transformation f^{-1} is then computed and maps the mesh so that it fits the reference curves. It has already been pointed out that inversions are involutive maps. Combescure transformations are linear maps and can easily be inverted with the algorithm proposed in Section 4.3.1. The computation of inverse transformation is thus extremely light. These properties are used extensively to remesh super-canal surface and is illustrated in Figure 4.21.

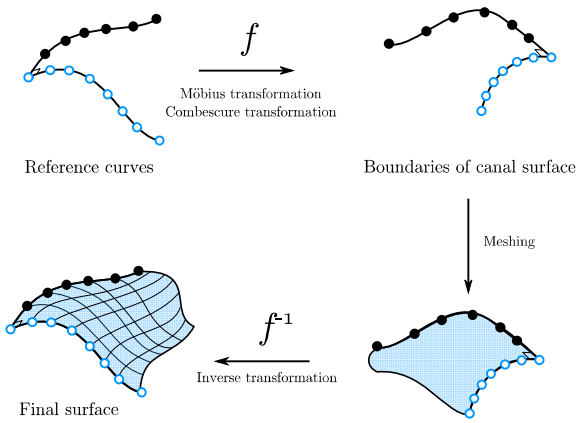

Figure 4.21 – Remeshing procedure for a super-canal surface.

4.4 Generalised cyclidic nets

The term *generalised cyclidic net* regroups cyclidic nets and their extension to doubly-curved creases, closed nets, and nets with singularities, via a hole-filling strategy. These three issues are developed in the following.

4.4.1 Doubly curved creases with generalised cyclidic nets

In this section, we generalise the construction rules of Cyclidic Nets to deal with discontinuities of normal vectors. The fundamental shapes remain cyclidic patches, the only difference with the usual cyclidic nets as defined in [73, 36] is the reflection rule for the normal vectors, as illustrated in Figure 4.22a.

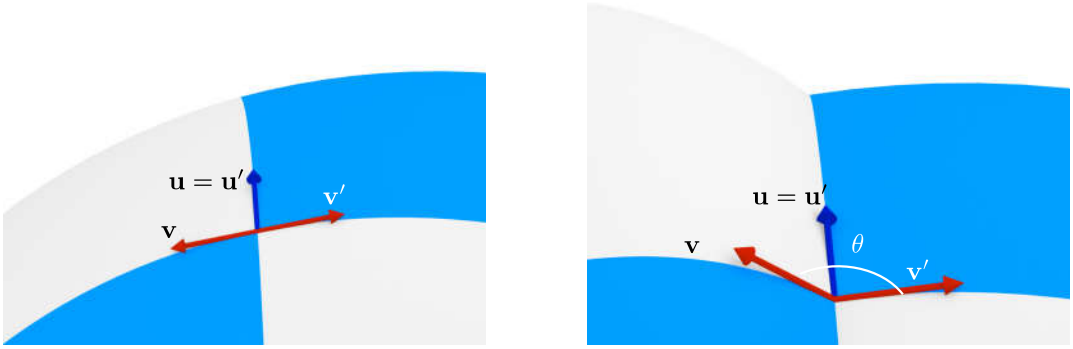

(a) Classical smooth rule

(b) Generalised rule with crease

Figure 4.22 – Reflection rule for cyclidic patches.

When propagating the frame of the cyclidic patch from one face to the other, the classical approach keeps one vector and inverts the other:

$$\begin{cases} \mathbf{u}' = & \mathbf{u} \\ \mathbf{v}' = & -\mathbf{v} \end{cases} \tag{4.11}$$

In equation (4.11), $\mathbf{u}$ refers to the common edge between the two patches. The first equality means that two patches have the same boundary; the second equality translates the continuity of tangent vectors to form a C^1 surface. Therefore the second equality is not necessary if one only deals with C^0 surfaces.

Equation (4.11) can thus be written in a more general form, illustrated in Figure 4.22b:

$$\begin{cases} \mathbf{u}' = & \mathbf{u} \\ \mathbf{v}' = & \mathbf{R}_{\mathbf{u},\theta} \cdot \mathbf{v} \end{cases} \tag{4.12}$$

$\mathbf{R}_{\mathbf{u},\theta}$ is a matrix representing the rotation along the vector $\mathbf{u}$ with an angle θ called crease angle in this chapter. Equation (4.11) is therefore a specific case of (4.12), with an angle $\theta = \pi$. This generalised definition has to be consistent for any patch, which implies that the crease angle has to be constant along a polyline, i.e. a line of curvature of the resulting cyclidic net. This restriction is not surprising, as it is the result of one of Joachimsthal's theorem on lines of curvatures: given two surfaces that cross along a curve $\mathcal{C}$ which is a line of curvature of both surfaces, then the angle between the two surfaces is constant along $\mathcal{C}$ [62]. Intuitively, this constraint can be understood by the fact that lines of curvature have zero geodesic torsion: the angle made by the surface normal and the rotation-minimising frame of lines of curvature is a constant. The crease angle must thus be kept constant along a line of curvature.

Another restriction is that it is not possible to introduce creases in two different directions. The continuity of the surface would be lost otherwise. A few examples of creased structures are shown in section 4.5.5.

4.4.2 Closed nets

General problem formulation

We deal now with the problem of closed cyclidic nets. Indeed, the reflection rule determining the edges of cyclidic nets does not take closed loops into account and the modelling with closed cyclidic nets is generally not possible. For the sake of simplicity, consider a unique strip constituted of circular quads. A cyclidic net can be generated by propagating an orthogonal frame chosen arbitrarily on the first quad. Consider the frame vectors $\mathbf{u_i}, \mathbf{v_i}$ that define the boundaries of cyclidic patches, and their propagation along a closed polyline. They are defined by:

$$\forall i > 0, \mathbf{u_i} = T_{i-1} \circ T_{i-2} \circ \ldots \circ T_1 \circ T_0 \left(\mathbf{u_0}\right) \tag{4.13}$$

where T_i is the reflection with respect to the median plane of the i^{th} edge. A closed smooth cyclidic net should reconnect itself with a continuity of tangent vectors, and therefore should verify the following equation:

$$T_N \circ T_{N-1} \circ \ldots \circ T_1 \circ T_0 \left(\mathbf{u_0}\right) = \mathbf{u_0} \tag{4.14}$$

Ideally, the designer would like to select any $\mathbf{u_0}$ arbitrary and that it verifies equation (4.14). Mathematically, this problem is exactly the same as the existence of constant vertex-offset for circular meshes, a topic covered in [147].The following statements can thus be made:

- closed continuous cyclidic nets are supported on circular meshes admitting a constant-vertex offset;
- this is equivalent to the fact that the boundary has to be quasi-spherical (there exists a parallel curve which has its vertices inscribed in a sphere);
- the border of a continuous cyclidic net can be filled with a continuous net, since it is a pseudo-spherical curve.

The second proposition can be simplified in the case of a planar curve discussed further. The closing condition is equivalent to the fact that the boundary curve is parallel to a curve inscribed in a circle. This is expressed simply with an angular criterion used within the proposed framework. For an even-sided planar curve, we introduce (α_k) the external angles of the curve, shown in Figure 4.23 and have:

$$\sum_{k=0}^{N} (-1)^k \alpha_k = 0 \tag{4.15}$$

The composition rule for reflections applies if the transition between two cyclidic patches is governed by equation (4.11). Since the first equalities of equation (4.11) and (4.12) are identical, the reflection described in (4.14) are unchanged. It follows that the statements made on cyclidic nets can be extrapolated to generalised cyclidic nets.

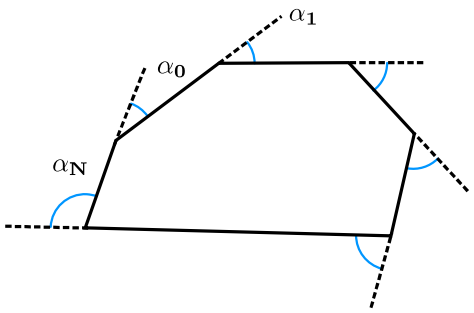

Figure 4.23 – A closed curve and its external angles.

Generation of closed canal surfaces

The construction of canal surfaces proposed in Section 4.2 can be extended to closed strips with several limitations. The first one has just been discussed: a closed cyclidic net gives a smooth closed surface if and only if the discrete guide curve is a pseudo-spherical curve (it is parallel to a curve which has all its vertices inscribed within a sphere). The second condition corresponds to the possibility of drawing the last circle of the strip. Consider Figure 4.24: the first circle of the strip is written C_0, the penultimate circle C_f, the initial point $\mathbf{P}$ and the first and last point of the curve $\mathbf{P_0}$ and $\mathbf{P_f}$ respectively. There are two cases:

- C_0 and C_f belong to the same sphere, then the circle going through $\mathbf{P}$, $\mathbf{P_0}$ and $\mathbf{P_f}$ intersects the circle C_f in two points. This circle is the solution we are looking for and is represented with dashed lines on Figure 4.24.
- In the other cases, the spheres $(C_0, \mathbf{P_f})$ and $(C_f, \mathbf{P_0})$ are distinct. Their intersection is a circle intersecting the circle C_0 and C_f in two different points. This circle is the only solution that allows the closing of the circular strip, and it does not intersect C_0 in $\mathbf{P}$.

In the first case, only the intersection of the last circle and C_f is unknown. In the second case, the position of $\mathbf{P}$ cannot be specified arbitrarely (as in set 2. for open strips). Compared to open strips, there is therefore a loss of at most two degrees of freedom for the control of the shape.

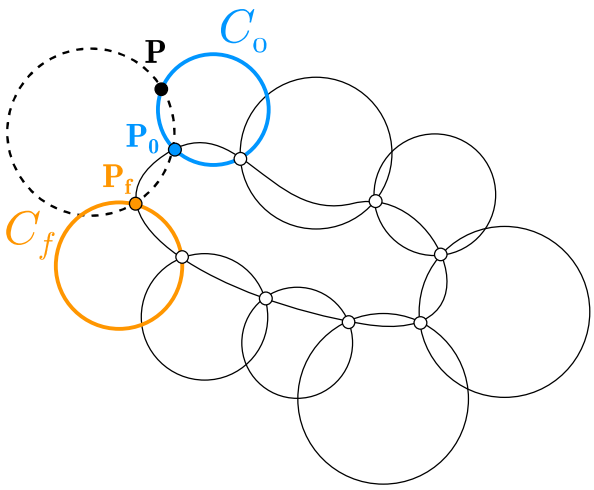

Figure 4.24 – Problem of a closing strip

Figure 4.25 shows a rendering of a façade covered with a canal surface inspired by the transportation hub of San Francisco designed by SOM and Schlaich Bergermann und Partner (the structural system

supporting the cantilevering façade is not shown). The modelling of surfaces with closed loops is particularly crucial for façade design, as they generally provide full enclosure for buildings. A typical example is the construction of stadia, which have the same topology as tori.

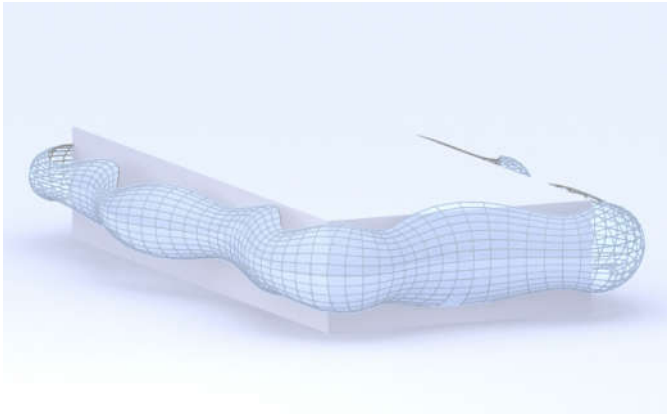

Figure 4.25 – A visualisation of a façade as a canal surface, covered with a circular mesh.

4.4.3 Hole filling problem

Principle of the algorithm

The main limitation with cyclidic nets as a design tool is the design of complex topologies. The fact that two consecutives edges on a cyclidic patch have to be perpendicular makes it impossible to assemble more than four patches around a vertex. This difficulty has already been pointed out in [135], where a hole-filling strategy has been proposed. This method only works for symmetrical shapes and can therefore not be applied in a general framework. A general method extending this proposition and allowing for non-symmetrical hole-filling is thus proposed here.

From a practical point of view, the designer shrinks the opening down to a hole of the size of a panel. This requires an iterative procedure: in the example of Figure 4.26, the filling strategy has been applied three times. The proposed method leaves n parameters for the designer for each step of a hole filling strategy, which makes it difficult to control the overall smoothness of the surface. It is therefore necessary to automate the choice of these variables. A simple way to do this is to minimise a smoothness functional. An example of target functional is the distance of the new corner points to a circle. The choice of other functionals is discussed in Section 4.4.4.

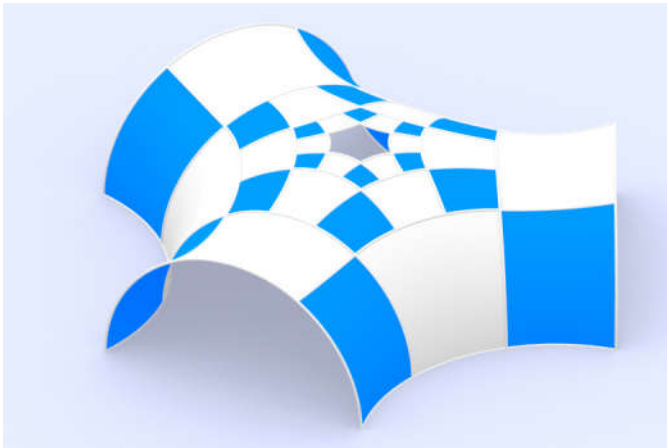

Figure 4.26 – The result of the hole filling strategy, with smooth T-joints between patches.

Krasauskas' algorithm

Consider Figure 4.27, the hole to fill has six edges. We write $\mathbf{C_i}$ the vertices and $\mathcal{C}_i$ the circular edge going from $\mathbf{C_i}$ to $\mathbf{C_{i+1}}$.

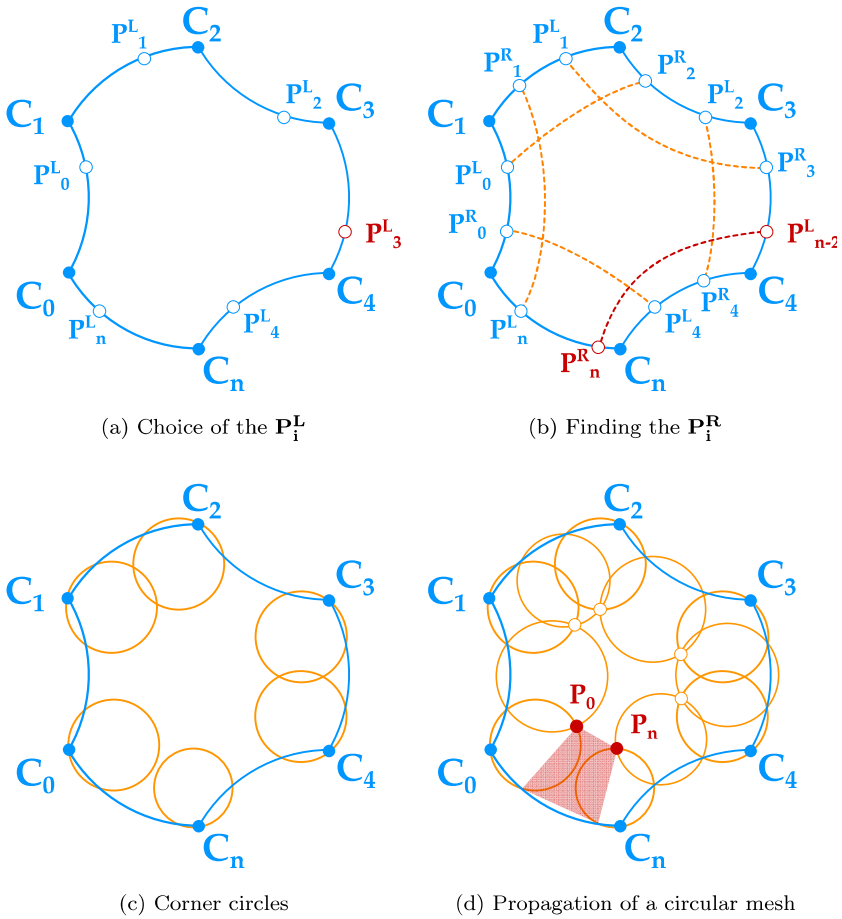

(a) Choice of the $\mathbf{P_i^L}$

(b) Finding the $\mathbf{P_i^R}$

(c) Corner circles

(d) Propagation of a circular mesh

Figure 4.27 – The steps of the hole filling strategy, the choice of $\mathbf{P^L_{n-2}}$ is constrained in order to have a closed circular strip.

The designer must chose two points $\mathbf{P_i^L}$ and $\mathbf{P_i^R}$ on each circular arc $\mathcal{C}_i$. The algorithm proposed in [135] follows:

1. Choose arbitrarely the $\mathbf{P_i^L}$;
2. Find the $\mathbf{P_i^R}$ so that $\mathbf{P_i^L}$, $\mathbf{P^R_{i+2}}$ and $\mathcal{C}_{i+1}$ belong to the same sphere. At this step all the points on the boundaries are chosen.
3. Draw the corner circles, which are determined by this procedure;
4. Choose any point $\mathbf{P_0}$ on the first circle and create the middle circles by propagation.

The main difficulty with this method is that the last quadrangle, highlighted in red on Figure 4.27 is *a priori* not inscribed within a circle, unless some symmetries are at stake. The system is thus over-constrained. We prove here that one additional condition has to be imposed on one of the $\mathbf{P^L_{i,i+1}}$ in order to yield exact circular meshes supported on the boundary arcs, and thus valid cyclidic nets.

Preliminary statements

We suppose that the $\left(\mathbf{P_i^L}\right)_0^{n-1}$ are chosen arbitrarely, the $\left(\mathbf{P_i^R}\right)_0^{n-1}$ are chosen with the rule explained in Section 4.4.3. We also suppose known the point $\mathbf{P_0}$. This section shows how to determine a value of $\mathbf{P_n^R}$ (equivalently $\mathbf{P_{n-2}^L}$) so that the quad mesh depicted on Figure 4.28 is a circular mesh. The circles are generated with intersection of particular spheres described in this section.

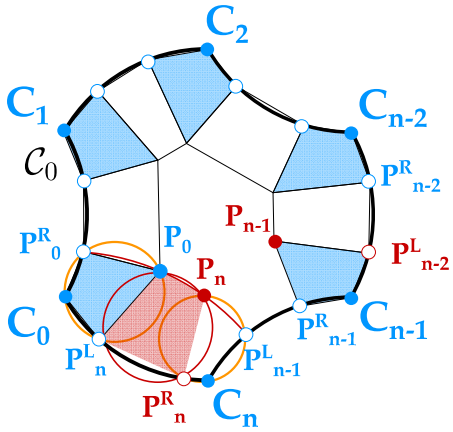

Figure 4.28 – Notations of the hole filling problem.

We call $\mathcal{S}_n$ the sphere defined by the points $\left(\mathbf{C_0}, \mathbf{P_n^L}, \mathbf{C_n}, \mathbf{P_{n-1}^L}\right)$. We call $\mathbf{P_n}$ the intersection of the circles $\left(\mathbf{P_n^L}, \mathbf{P_0}, \mathbf{P_n^R}\right)$ and $\left(\mathbf{P_n^R}, \mathbf{C_n}, \mathbf{P_{n-1}^L}\right)$. We call $\mathbf{P'_n}$ the intersection of the circles $\left(\mathbf{P_{n-1}}, \mathbf{P_{n-1}^R}, \mathbf{P_{n-1}^L}\right)$and $\left(\mathbf{P_n^R}, \mathbf{C_n}, \mathbf{P_{n-1}^L}\right)$.

The mesh generated is valid if and only if $\mathbf{P'_n}$ and $\mathbf{P_n}$ are identical. We thus study more precisely the envelopes of this points when varying $\mathbf{P_n^R}$ (equivalently $\mathbf{P_{n-2}^L}$). Three statements can be made:

1. The envelope of all the possible $\mathbf{P_n}$ and $\mathbf{P'_n}$ are in $\mathcal{S}_n$;
2. The envelopes of all the possible $\mathbf{P_n}$ is a circle going through $\mathbf{P_0}$ and $\mathbf{P_{n-1}^L}$;
3. The envelopes of all the possible $\mathbf{P'_n}$ is a circle going trough $\mathbf{P_{n-1}^L}$.

The first statement is not difficult to prove: by construction $\mathbf{P_n^R}$, $\mathbf{C_n}$ and $\mathbf{P_{n-1}^L}$ belong to $\mathcal{S}_n$. Therefore, the circle going through these points belong to $\mathcal{S}_n$.

The other two statements are less immediate. Consider the envelope of the $\mathbf{P_n}$: we can do an inversion with respect to any point of the circle $\mathcal{C}_n$. The problem becomes then planar and is depicted in Figure 4.29. Notations for angles are introduced in Figure 4.30. The subscript $\mathbf{X_{,i}}$ indicates the image of $\mathbf{X}$ by the inversion.

The image of $\mathcal{C}_n$ is a straight line, we introduced the point $\mathbf{I}$, intersection of the lines $\left(\mathbf{P_{0,i}P_{n,i}^L}\right)$ and $\left(\mathbf{P_{0,i}P_{n,i}^L}\right)$. By construction, we thus have:

$$\begin{cases} \gamma_0 = & \pi - \alpha_0 \\ \gamma_1 = & \pi - \beta_0 \\ \gamma_0 + \gamma_1 = & \pi - \gamma_2 \end{cases} \tag{4.16}$$

Recall that in circular quadrilaterals, the sum of opposite angles is equal to π. This yields:

$$\begin{cases} \alpha_1 = & \pi - \alpha_0 \\ \beta_1 = & \pi - \beta_0 \end{cases} \tag{4.17}$$

Combining equations (4.16) and (4.17), we get following result:

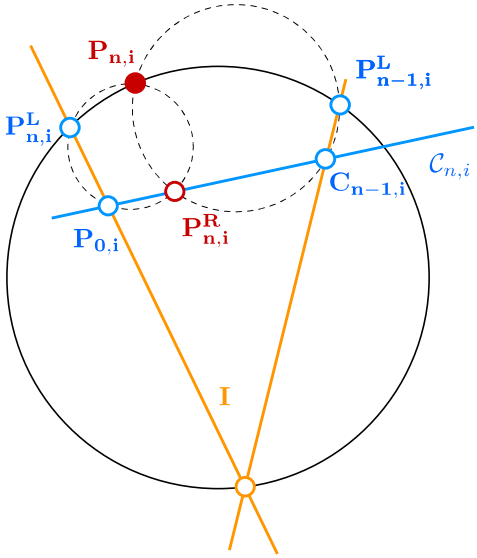

Figure 4.29 – Trajectory of all the possible $\mathbf{P_n}$ after inversion.

$$\alpha_1 + \beta_1 = \pi - \gamma_2 \tag{4.18}$$

This proves that the planar quadrangle $\mathbf{IP^L_{n,i}P_{n,i}P^L_{n-1,i}}$ is inscribed in the circle circumscribed to the triangle $\mathbf{IP^L_{n,i}P^L_{n-1,i}}$. This remains true regarless the choice of the point $\mathbf{P_{n,i}}$: the envelope of all possible $\mathbf{P_{n,i}}$ is on a circle. This property is preserved by inversion, and gives the proof of the second statement.

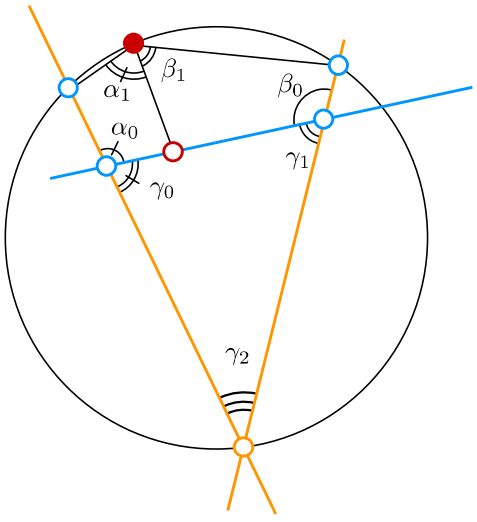

Figure 4.30 – Notations for angles.

The same argument can be used for $\mathbf{P'_{n,i}}$, leading to the proof of the third statement.

Filling algorithm

The filling with a circular mesh is valid if and only if the points $\mathbf{P_n}$ and $\mathbf{P'_n}$ are identical. This discussion shows that this is equivalent to look for intersection of two circles belonging to a same sphere

$\mathcal{S}_n$. The algorithm proposes thus to determine the two circles, to compute their intersection and adapt the existing algorithm:

1. Choose arbitrarely the $\mathbf{P_i^L}$, except $\mathbf{P_{n-2}^L}$;
2. Find the $\mathbf{P_i^R}$ so that $\mathbf{P_i^L}$, $\mathbf{P_{i+2}^R}$ and $\mathcal{C}_{i+1}$ belong to the same sphere.
3. Choose any point $\mathbf{P_0}$ on the first circle.
4. Compute $\mathbf{P_{n-2}^L}$ (equivalently $\mathbf{P_n^R}$) by intersecting the two circles described in Section 4.4.3;
5. Compute all the circles by propagation.

The additional step is not computationally intensive: the algorithm is almost identical to the one proposed in [135], but with more generality. It can be repeated *ad libitum* to the new hole generated in the middle of the new mesh.

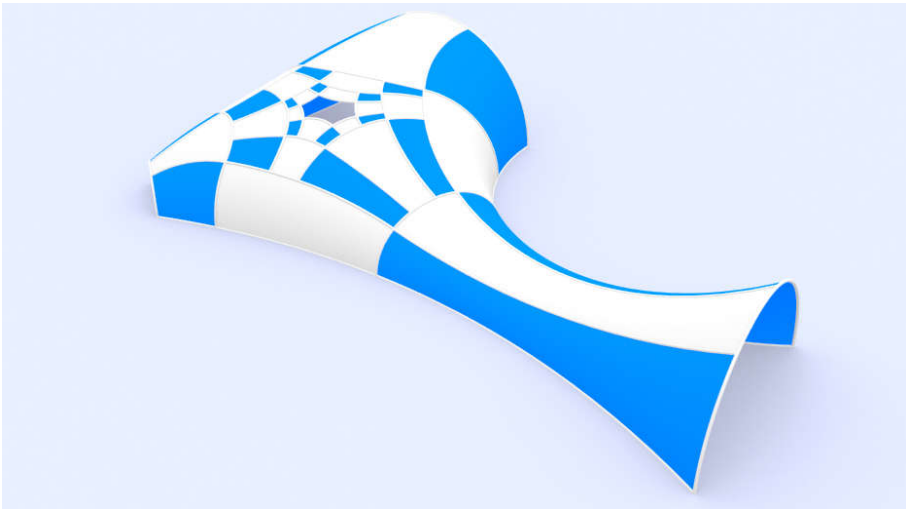

Figure 4.31 – Hole-filling strategy applied iteratively three times on a non-regular hole.

4.4.4 Implementation and numerical issues

Smoothness of cyclidic nets

The framework proposed in this chapter has been implemented within Grasshopper™. The geometrical tools generate the cyclidic nets and the associated subdivisions. Once the circular mesh is chosen, an infinity of frames can be chosen. All the underlying surfaces are C^1, but some are visually more pleasant than others, as seen in Figure 4.32. To take this aesthetic aspect into account, a fairness-functional has been introduced to give the smoothest possible shape for a given circular mesh. The fairness function minimised here is defined by:

$$E_\alpha(\theta, \lambda) = \int_S \left(H^2 - \alpha\kappa\right) \mathrm{d}S \tag{4.19}$$

Some values of the parameter α give well-known energies:

- $E_0 = \int_S H^2 \mathrm{d}S$ is the Willmore energy;
- $E_1 = \int_S \left(H^2 - \kappa\right) \mathrm{d}S$ is the conformally invariant Willmore energy;
- $E_2 = \int_S \left(\kappa_1^2 + \kappa_2^2\right) \mathrm{d}S$ is a bending energy;

The case of $\alpha = 1$ has been extensively discussed in the domain of computer graphics: the energy obtained is invariant by inversions, which makes it particularly suited for a framework based on Möbius geometry [38]. It is commonly used as an aesthetic fairness measurement for shape modeling [229, 121]. A discrete integration of the E_α was implemented within the proposed framework, which minimizes automatically the bending energies of the cyclidic mesh by the means of a BFGS algorithm [180]. In this chapter, the value of α was set to 2. For the example of Figure 4.32, with 24 patches, the minimisation of the bending energy takes 150 ms. Figure 4.32 shows two surfaces: one with a random choice of frame, and the other with an optimised value of the bending energy. The second surface is visually very regular and validates the choice of fairness functional made in this chapter.

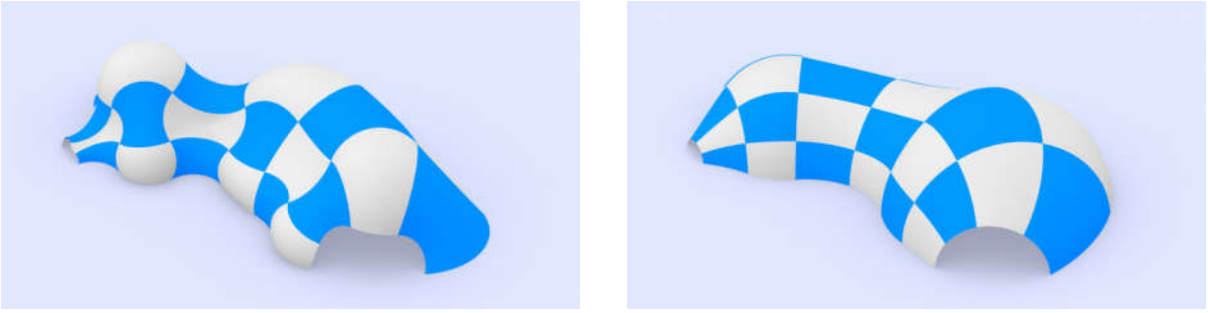

(a) $E_2 = 112$ (b) $E_2 = 29.9$

Figure 4.32 – Two cyclidic nets supported on the same base circular mesh, before and after optimisation of the bending energy.

The same fairness functional is used for the solution of the hole-filling problem. The hole-filling algorithm yields surfaces of varying smoothness, depending on the boundaries. Figure 4.33 shows some solutions of the hole-filling problem: the location of the singularity remains almost unchanged while several smooth configurations can be obtained with the strategy proposed in this chapter. However, the smoothest configuration (Figure 4.33b) corresponds to the case where the hole is shrunk towards a regular hexagon.

(a) $E_2 = 38.7$ (b) $E_2 = 36.5$ (c) $E_2 = 38.2$

Figure 4.33 – Several solutions obtained with hole-filling problem for an irregular hole

Shape smoothing of super-canal surfaces

Some input data for curve subdivision and initial frame orientation might lead to visually unpleasant results. Therefore, we use the strategy proposed in [33] by taking the position of the vertices and the orientation of the normal vector to the cyclidic net at one node as variables and we optimise the smoothness and fit exactly the input curve. More precisely, the points on this curve can be parametrised by the vector $\mathbf{u}$. The other parameter governing the shape of the canal surface is the length of the edges crossing the circular strip $\mathbf{L}$. The cyclidic net is also generated by the choice of an orthogonal frame,

parameterised by two angles λ and θ. We minimise the following functional:

$$\mathcal{F}_1(\mathbf{u}, \mathbf{L}, \lambda, \theta) = \sum_{\text{edges}} \frac{1}{R^2_{edge}(\mathbf{u}, \mathbf{L}, \lambda, \theta)} \tag{4.20}$$

Where R_{edge} is the radius of the edge of the cyclidic net. The computation of the function is immediate and does not require additional, and its minimisation gives satifying results and is done in real-time. The user can specify additional constraints, like the angle made by the normal and a reference plane. In such cases, the degrees of freedom λ and θ become coupled, and the normal rotates along a cone. The choice of the functional described in equation (4.20) is motivated by its simplicity, as it can be computed efficiently. Indeed, it does not require the construction of NURBS patches and the evaluation of smoothness function defined in equation (4.19). A possible improvement would be to consider a quaternionic parametrisation of cyclidic nets, as an analytical formula for the Willmore energy of a cyclidic patch was computed in this framework by [275].

The minimisation is done by the means of the BFGS algorithm. Figure 4.34 shows the smoothing of a canal surface based on the introduced energy. Notice that only local changes are made, but that the problematic area with high curvature is solved.

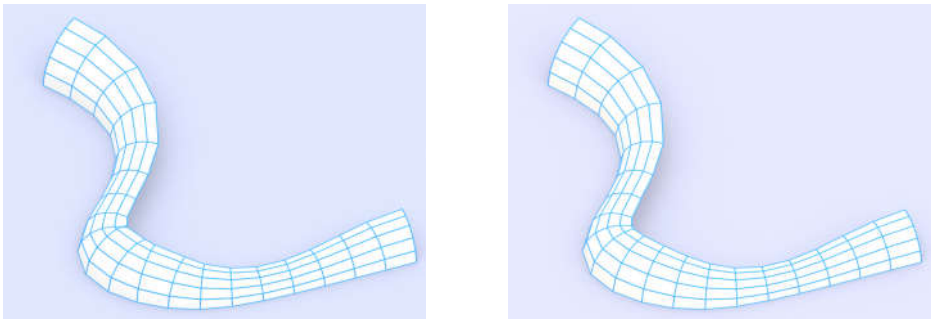

(a) Before optimisation (b) After optimisation

Figure 4.34 – Optimisation of the smoothness of a canal surface.

4.5 Practical use for architectural design

The previous sections presented improvements of cyclidic nets for the modelling of complex architectural shapes. We propose here a discussion on the use of generalised cyclidic nets in architecture and structural engineering.

4.5.1 Shape generation framework

The study of cyclidic nets demonstrates that a circular mesh and a frame can generate a collection of NURBS parameterised by their lines of curvature. This collection of surfaces can then be easily meshed with conical or circular PQ-Meshes or planar hexagonal meshes. Unlike previous applications of cyclidic meshes in architecture, we suggest that the shapes can be described with large cyclidic patches, the subdivision of the patches being kept as a design parameter serving other function than form, for example mechanical performance. The result is a framework for shape modelling tailored for architectural constraints.

This framework is presented in Figure 4.35. Starting from a coarse circular mesh, it is possible to generate a generalised cyclidic net. The designer is free to add normal discontinuity with our method at this step. One can then choose a panelisation strategy, depending on constructional constraints or æsthetics. The most common design strategies for structural and façade layout yield interesting geometrical properties without post-rationalisation. This method is thus a bottom-up approach, allowing designers to check different construction solutions for the same shape.

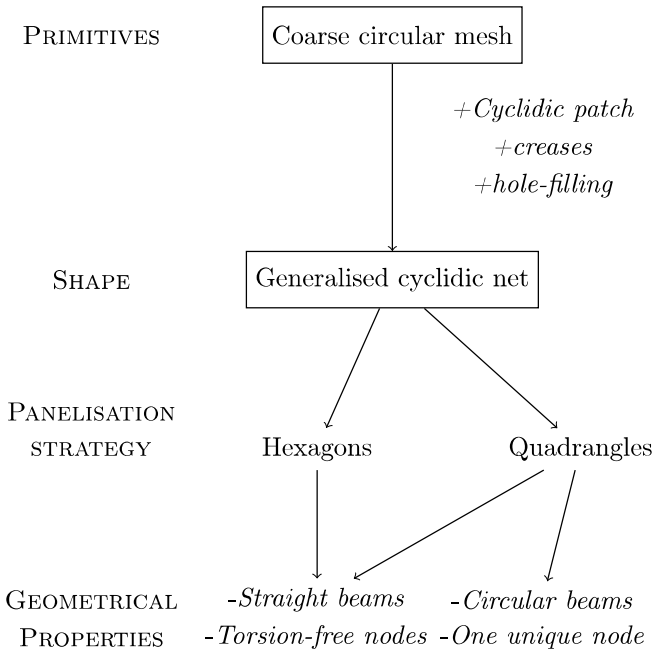

Figure 4.35 – Framework for shape generation with generalised cyclidic nets

A brief comparison with NURBS is proposed in Table 4.2. A parallel can be found between the control polygon of NURBS and the circular mesh of cyclidic nets. Unlike control points in NURBS modeling, the vertices of Cyclidic Nets are all on the modeled surface. The surface resulting from cyclidic nets are only C^1, which is a drawback in many industries, but is not a very serious issue in architectural design. Indeed, the final shape is very often built with flat or developable panels, which makes the built envelope at most a C^1 surface. Finally, it is noticed that NURBS have some limitations when complex topologies are concerned, a popular alternative is the use of subdivision surfaces, mainly based on the Catmull-Clark subdivision scheme [53]. A review of existing methods is proposed in [151].

	NURBS	Cyclidic Net
Base shape	Control Polygon	Circular Quad Mesh + one frame
Interpolation	Bernstein polynomial	Cyclidic Patch
Surface regularity	from C^0 to C^∞	from C^0 to C^1
Isoparametric lines properties	None	Curvature lines
Complex topologies	Subdivision surfaces	Hole filling strategy

Table 4.2 – Comparison of the NURBS and Generalised Cyclidic Net frameworks

Shape modeling with inversions

We have seen with super-canal surfaces that Combescure and Möbius transforms can be applied on circular meshes to offer a rich variety of shapes supporting cyclidic nets. They considerably enrich the design possibilities of conventional geometries. We propose a simple example in Figure 4.36: a simple surface of revolution is inverted to give a less obvious 'peanut-shaped' geometry, keeping the notations introduced in this chapter, this shape is thus a M-revolution surface.. The inversion of surfaces of revolution allows to model very efficiently shapes recalling existing projects, like the forum of the Soliday's festival [248].

The computation of the Möbius transform is based on Equation (4.2), it requires no optimisation or matrix manipulation and can therefore be done as quickly as other simple transformations, like transla-

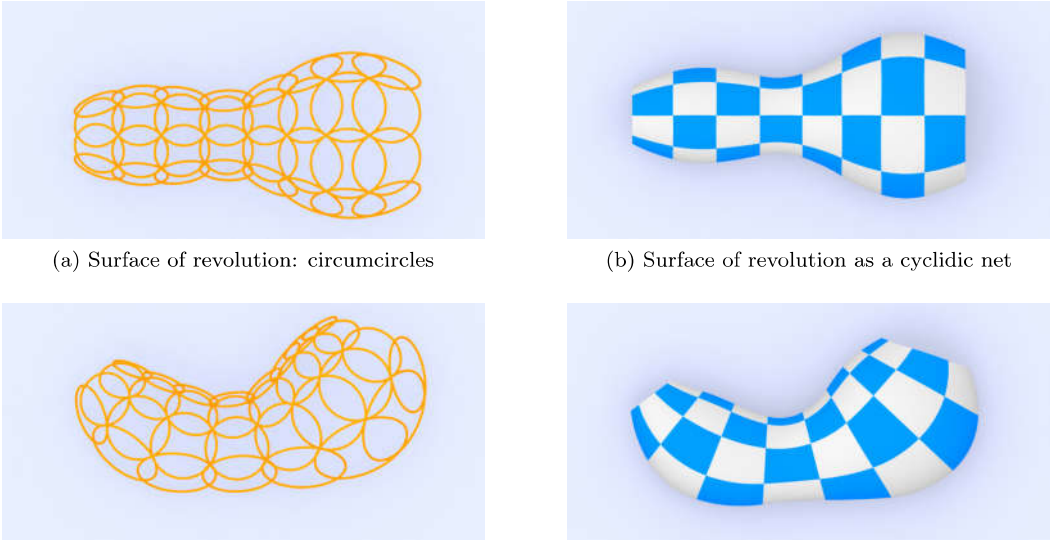

(a) Surface of revolution: circumcircles

(b) Surface of revolution as a cyclidic net

(c) Inversion: circumcircles

(d) Inversion: cyclidic net

Figure 4.36 – A surface of revolution and an inversion to a 'peanut-shape' geometry

tions. The cyclidic net laying on the circular mesh is also generated in real-time, since it only consists in the propagation of a frame along the net. The shape can then be subdivided in a uniform pattern.

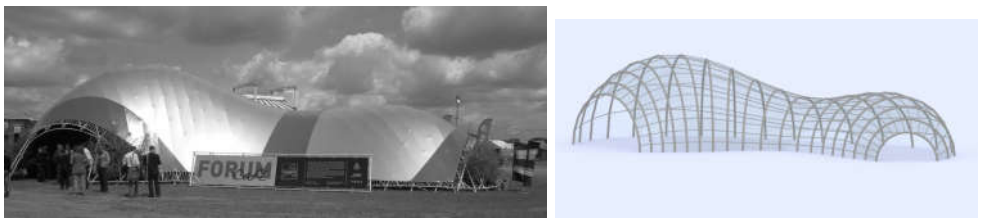

Figure 4.37 – The 'peanut' gridshell of the Solidays forum: built project and interpretation with the inversion of a surface of revolution.

Möbius transforms can be applied on more complex shapes than surfaces of revolution, for example on Monge's surfaces or moulding surfaces [168, 164]. Figure 4.38 shows some inversions of the mesh displayed in Figure 4.39, the reference geometry is at the bottom right of Figure 4.38. Although the Möbius transform does locally preserve the shapes, the overall aspect of the models varies substantially. All the shapes displayed in this image can be covered with circular meshes and be parameterised by cyclidic nets.

4.5.2 Shape composition with super-canal surfaces and complex topologies

The hole-filling strategy introduced in this chapter allows the modelling of complex topologies.The combination of this strategy with the use of super-canal surfaces creates a rich design space. Figure 4.39 gives an example of the shapes obtained with shape composition and hole-filling strategy. In this image, the thicker arches correspond to boundaries of cyclidic patches. The grid structure is covered with quadrangular panels, except two hexagons. All the circles supporting the patches lay on the (XY) plane, with the exception of the patches used for the hole-filling strategy. Figure 4.40 shows the circles used for the generation of this shape. Therefore, the surfaces apart form the holes are canal surfaces, as they are supported on circular strips. The holes are non-symmetrical hexagons. The holes boundaries fulfill the condition described in equation (4.15).

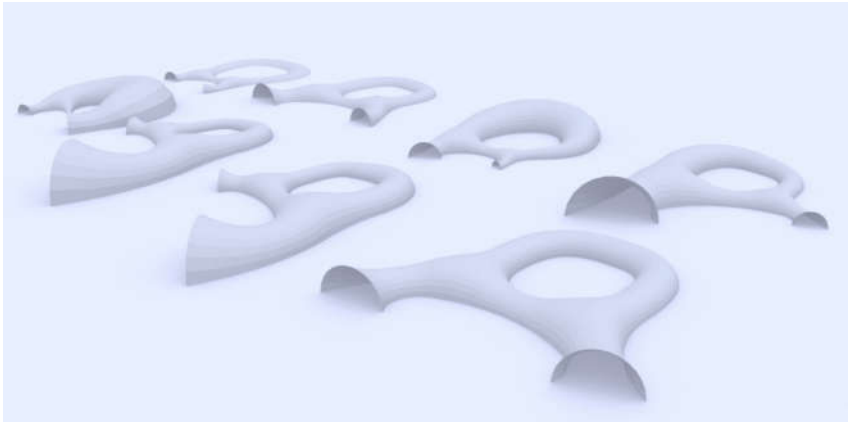

Figure 4.38 – A family of shapes produced by inversions of the same geometry.

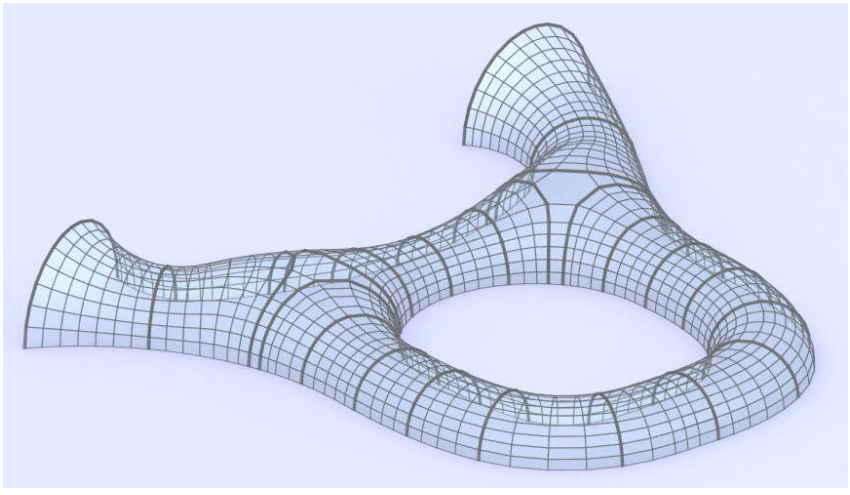

Figure 4.39 – A geometry with a complex topology modeled with cyclidic nets.

The control of the shape can be done by moving the circles in the (XY) plane. In this example, the circular strips were computed by intersecting a collection of circles which were manipulated through the viewport of Rhinoceros.

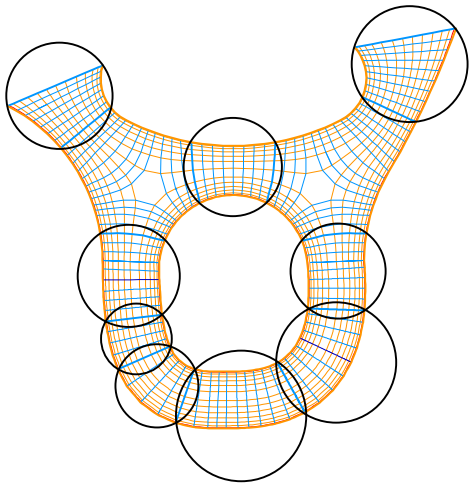

Figure 4.40 – Only a few circles can describe a complex shape: top view of the Figure 4.39.

The formal potential of composition super-canal surfaces used in the context of generalised cyclidic net seems important. It is possible to specify a topological skeleton corresponding to the curve supporting the centers of canal surfaces. From this skeleton, a collection of circular strips can be generated, supporting canal or super-canal surfaces. The main difficulty is to guarantee an intuitive manipulation of the shape by the end user. For example, the automation of the conversion of a graph to a collection of strips is a possible improvement of our method. Creating a library of predefined topologies could also be of interest to provide the designers with guidance on the shape generation with generalised cyclidic nets.

4.5.3 Towards double layer free-form structures

Generalised cyclidic nets offer other possibilities than gridshells with torsion-free nodes: octahedral trusses can indeed easily be constructed from circular meshes. Figure 4.41 shows the construction of the octahedral truss: thick grey or black lines represent the bottom and top layer respectively, thin blue lines represent diagonals. Consider that the top layer is a circular mesh: the diagonals are constructed by creating the joining the center of the circles to the vertices of the top layer. The centres can then be moved in the direction that is normal to the circles, like shown in Figure 4.41b. In that manner, all the diagonals created from a same circle have the same length, which simplifies manufacturing. From a circular mesh on the top layer, one can thus create the bottom layer on a family of lines. The design space offered for the bottom layer is similar to the input of a marionette mesh, which will be presented in Chapter 5. The planarity of the panels of the bottom layer can thus be described with the marionette technique and can be computed efficiently. The planarity of facets on upper and lower layers is however not necessarily mandatory in practice, and other constraints could be considered, like uniformity of lengths, node repetition, etc.

4.5.4 Practical applications

The method presented here has been used during a one week workshop in 2015. Architecture and engineering students had to design and build a 30 m^2 free-form pavilion, the only material available was polystyrene in flat rectangular sheets. The shape is a super-canal surface meshed with circular quadrilaterals. The pavilion, shown in Figure 4.42 is a grid structure with a torsion-free beam layout. The offset was computed with a reflection rule similar to the one generating cyclidic nets. An optimisation was performed in order to minimise the height gap at the nodes between beams of constant height. The

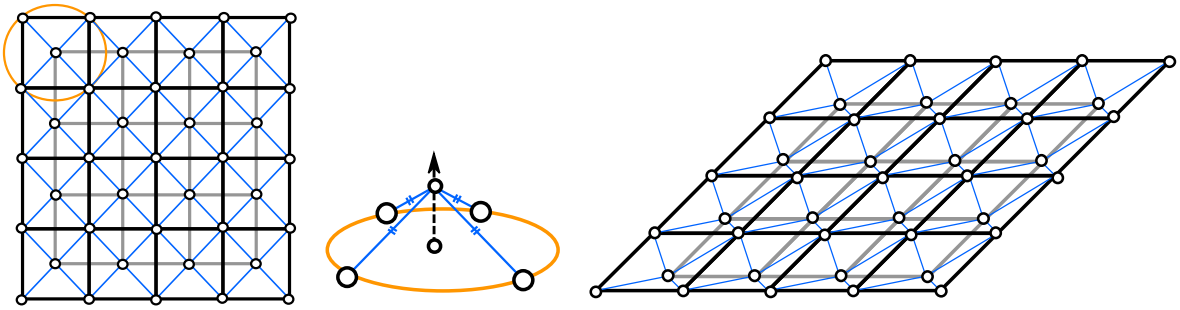

(a) Top view (b) Center offset (c) Axonometric view

Figure 4.41 – Construction of an octahedral truss from a circular mesh.

fast computation of the space of solutions was key to the success of this operation within a limited time frame (5 days).

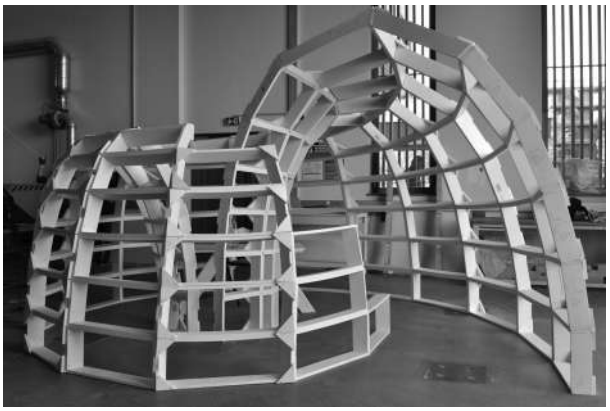

Figure 4.42 – A pavilion built with torsion free-nodes on a super-canal surface.

The tools presented here were used then for shape generation as well as fabrication. Hundreds of polystyrene elements were cut according to the 3D model and assembled. The planarity of the panels was considered for use as bracing elements and was validated on a $5m^2$ model, shown in Figure 4.43. Flat panels used as bracing elements improve the overall stability and stiffness [1].

Figure 4.43 – A model of a canal surface with planar quadrangles used for bracing.

[1] More details and pictures can be found on www.thinkshell.fr.

The construction of the pavilion validates the use of the numerical tools presented in this chapter. The user feedback allowed us to identify the most relevant way to model super-canal surfaces. In particular, the students found important to control at least one boundary curve. This explains why the method of generation of canal surfaces presented in this work focuses on the prescription of a boundary curve, and not on the curve supporting the centers of the sphere for example.

4.5.5 Application of curved creased

Generalised cyclidic nets offer the possibility to create non-smooth surfaces with a straight forward folding strategy. An example of this strategy is proposed in Figure 4.44: the same base circular mesh is used for three designs of a tribune cover but different values have been chosen for the folding angle θ. All the surfaces are regularized with the bending energy discussed in this chapter. All solutions are visually regular, which further demonstrates that such energy is appropriate, even for C^0 surfaces. Although the overall geometry is preserved, the visual aspects of the three solutions varies significantly.

(a) Smooth surface: $\theta = 180°$ (b) Creased surface: $\theta = 135°$ (c) Creased surface: $\theta = 225°$

Figure 4.44 – Three different generalised cyclidic nets supported on the same circular mesh.

The three solutions can lead architects and engineers to choose different technological solutions. The smooth surface is more suited for a grid structure. The two other solutions increase significantly the local curvature. The variant with $\theta = 225°$ recalls tensile structure, which are known for their efficient use of material. The variant with $\theta = 135°$ works with compression-dominant forces. It recalls some of Nicolas Esquillan's shells, where creases were used to increase the buckling capacity of thin shells.

4.5.6 Non-continuous cyclidic nets

We discussed briefly the potential offered by doubly-curved creases in free-form design. Another possibility is to consider the loss of the C^0 continuity, i.e. the creation of openings in doubly-curved shapes. This kind of strategy is often employed to bring light into buildings: we can think of saw-tooth roofs and their application to industrial buildings, but also to train station or airports, which have large span and complex requirements. Consider for example the roof covering the railway station of Leuven shown in Figure 4.45. The opaque surfaces resemble to portion of cyclidic nets (although the profile curve is parabolic and not circular), filling transparent covering can be set between the opaque surfaces. The example shown here could be obtained by simple geometrical considerations, but exploring the possibilities of discontinuous cyclidic nets could expand the versatility of such solution.

4.6 Summary of intellectual contribution

This chapter has introduced *generalised cyclidic nets*, a generalisation of the previous implementations of cyclidic nets. Arbitrary topologies and creased structures can now be generated with these shapes, the resulting meshes have their facets inscribed in circles. Many technological solutions can be adapted to cyclidic nets: from quadrangular meshes with torsion-free nodes to planar hexagonal meshes or developable strips.

A generalisation of canal surfaces by a combination of Combescure and Möbius transformations was proposed and applied to architectural shape generation. Curve fitting problems are solved in real-time to provide the designer with immediate feedback. The methodology described here is general and other families of shapes could arise from this framework. For example, it is well-known by mathematicians

Figure 4.45 – An envelope with varying materials illustrating surface discontinuity *(picture: Samyn and Partners, architects and engineers)*

that Möbius transformations of minimal surfaces are a subset of Willmore surfaces, and a lot of effort has been put into the discretization of minimal surfaces as circular meshes [39].

The extension of canal surfaces proposed in this chapter have the remarkable property that their lines of curvature are also lines of principal stress under uniform pressure when proper boundary conditions are ensured. The gridshells derived from the can be viewed as Michell gridshell: the curve network proposed for fabrication aspects is therefore also very efficient from the perspective of structural engineering. Super-canal surfaces constitute a subset of the so-called *O-surfaces* studied by Rogers and Schief, and merge fabrication and mechanical considerations. The method proposed in this chapter could be used to generate other meshes satisfying this double optimality criterion, for example by considering isothermic planar parametrisations and their image by combination of Möbius and Combescure transformations.

Chapter 5

Marionette meshes: from descriptive geometry to fabrication-aware design

The design of complex architectural shapes has benefited from great advances from the computer graphics community in the last decade. For instance, significant efforts were made to develop numerical methods for the covering of free-form surfaces with planar panels. These methods differ from the common knowledge of architects and engineers, making them hard to use for non-specialists. The technique proposed in the present article aims thus at bridging this gap with a method that takes inspiration from descriptive geometry, a tool used by architects for centuries, and turns it into a real-time design tool for PQ-meshes.

5.1 Marionette Meshes

5.1.1 Research statement

In the recent years, many tools for the modelling of shapes with PQ-meshes have been proposed. The different methods, reviewed in Section 2.3.3, are mostly based on optimisation-based approaches and on the computation of admissible subspaces. Most of the applications are based on local mesh editing, and on the deformation of meshes with control handles, in the manner of NURBS modelling. Optimisation-based approaches are arguably very efficient, but they rely on a background totally different from the one of architects. Architecture is a cultural discipline, and the tools used for shape representation and generation are also the result of a cultural evolution. The relation between the tools proposed for fabrication-aware design and the cultural aspect of the architectural practice is rarely discussed, so that it is difficult to know whether the new tools will be used effectively. On top of *fabrication-aware design* we propose to study *cultural-aware design* in order to bridge the gap between research and the architectural practice.

In this chapter, we propose a method, that we name *'marionette technique'*, for shape generation with PQ-meshes. It relies entirely on descriptive geometry, a discipline invented in the eighteenth century. Although not as general as other methods based on optimisation, the method makes reference to items that are well known by architects, like plane views and elevations, so that the vocabulary of the marionette technique is totally transparent for architects and engineers.

5.1.2 Descriptive geometry

Descriptive geometry is a technique of shape representation invented by French mathematician Gaspard Monge [172, 117]. It is based on planar orthogonal projections of a solid. The planes in which the projections are done are usually the horizontal and vertical planes.

Because architectural objects have to deal mainly with gravity and vertical forces, it makes naturally sense to separate projections in vertical and horizontal planes. The idea to use these projections to guide structural design was used recently in the framework of the *Thrust Network Analysis* where compression-only structures are found from a planar network at equilibrium [209, 170]. A link between the construction

the graph of an Airy stress function and meshing with planar facets was used to cover the roof of the Dutch Maritime Museum with planar facets [6].

The objective of this chapter is to show that descriptive geometry can be turned into a general tool for the design of PQ meshes and their structural optimisation. The method, called *Marionette method* is presented in Section 5.1, where the relation between smooth and discrete geometry for PQ-meshes is discussed. Section 5.2 extend it to close strips or other topologies. Section 5.3 explores then some applications in architecture. Section 5.4 shows finally the generality of the proposed method, which can be extended to meshes other than regular quadrilateral meshes and therefore constitute a promising versatile tool to integrate intuitively fabrication constraints into architectural design.

5.1.3 Marionette Quad

The principles of descriptive geometry can be transposed to architectural shape modelling. The use of appropriate projections provides a simple interpretation of the problem of meshing with flat quadrilaterals. For simplification, we discuss the case of a projection in the (XY) plane in this section: the generalisation to other projections is illustrated in Section 5.4.

Consider first Figure 5.1: four points have a prescribed plane view **ABCD** in the horizontal plane (P_1). Three points $\mathbf{A}'$, $\mathbf{B}'$ and $\mathbf{D}'$ have prescribed altitudes z_A, z_B and z_D. In general, there is only one point $\mathbf{C}'$ with the imposed projection **C** so that $\mathbf{A}'\mathbf{B}'\mathbf{C}'\mathbf{D}'$ is planar.

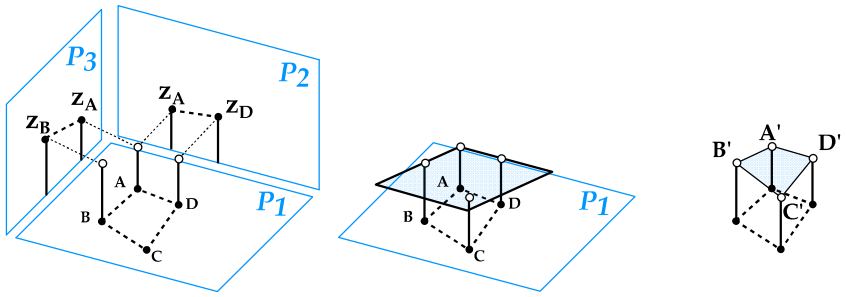

Figure 5.1 – Creation of a *Marionette Quad* with a plane view and two elevations.

The planarity constraint reads:

$$\det\left(\mathbf{A}'\mathbf{B}', \mathbf{A}'\mathbf{C}', \mathbf{A}'\mathbf{D}'\right) = 0 \tag{5.1}$$

Expressing coordinates in a cartesian frame of (P_1), and writing $d_{BC} = \det_{2D}(\mathbf{AB}, \mathbf{AC})$, $d_{BD} = \det_{2D}(\mathbf{AB}, \mathbf{AD})$ and $d_{DC} = \det_{2D}(\mathbf{AD}, \mathbf{AC})$, if the points A, B and D are not aligned, then, one gets:

$$(z_C - z_A) = \left(\frac{d_{BC}}{d_{BD}}\right) \cdot (z_D - z_A) + \left(\frac{d_{DC}}{d_{BD}}\right) \cdot (z_B - z_A) \tag{5.2}$$

Figure 5.1 shows vertical lines used for construction, recalling the strings of a marionette, which gives the name *marionette quad*. Note that the system is under-constrained if the points A, B and D are aligned, which corresponds to a vertical quad. A projection in the horizontal plane thus allows only for the modelling of height fields. This limitation can be overcome by using other projections (see Section 5.4).

5.1.4 Regular Marionette Meshes

Consider now a quadrangular mesh without singularity as depicted in Figure 5.2. The plane view in the horizontal plane is fixed, and the altitude of two intersecting curves is prescribed. Then, provided that the planar view admits no 'flat' quad (i.e. quad where three points are aligned), equation (5.2) can be propagated through a strip, and by there, through the whole mesh. Indeed, on the highlighted strip of

Figure 5.2, the first quad (top left) has three prescribed altitudes, and equation (5.2) can be used and so forth. The same applies for all the quads of the strip. For a $N \times M$ mesh, the propagation requires NM applications of equation (5.2), the memory needed is $3NM$. The marionette technique guarantees hence that the number of operations varies linearly with the number of nodes within a structure. The method performs thus in real time even for meshes with thousands of nodes, as discussed in Section 5.3.1.

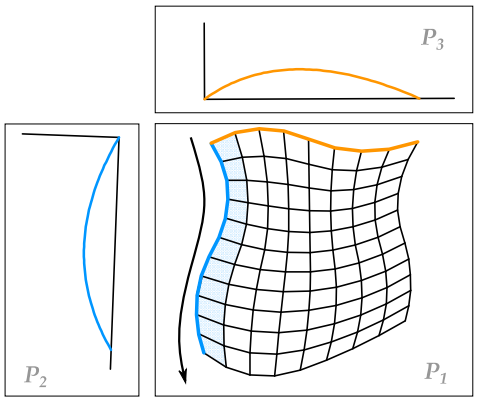

Figure 5.2 – Two elevations and a planar view define a unique Marionette Mesh.

5.1.5 Link with smooth geometry

Partial differential equation

The proposed method has some interesting relations with smooth geometry. The problem of covering curved shapes with planar panels is linked with the integration of *conjugate curves networks* [148, 35]. Conjugate networks correspond to parameterisations (u, v) satisfying the following equation [35]:

$$\det\left(\partial_{\mathbf{u}}, \partial_{\mathbf{v}}, \partial^{\mathbf{2}}_{\mathbf{uv}}\right) = 0 \tag{5.3}$$

Consider now that the components in x and y are fixed, like in the problem solved by the Marionette technique. We are looking for the height functions f^z satisfying equation 5.3. Adopting the notation f_u to denote differentiation of f with respect to u, equation (5.3) is reformulated into:

$$\det\begin{pmatrix} f^x_u & f^x_v & f^x_{uv} \\ f^y_u & f^y_v & f^y_{uv} \\ f^z_u & f^z_v & f^z_{uv} \end{pmatrix} = 0 \tag{5.4}$$

Equation (5.4) is defined if the parameterisation in the plane (XY) is regular, which means if the study is restricted to height fields. We expand (5.4) using adjugate matrices:

$$\begin{vmatrix} f^x_u & f^x_v \\ f^y_u & f^y_v \end{vmatrix} f^z_{uv} + \begin{vmatrix} f^x_v & f^x_{uv} \\ f^y_v & f^y_{uv} \end{vmatrix} f^z_u - \begin{vmatrix} f^x_u & f^x_{uv} \\ f^y_u & f^y_{uv} \end{vmatrix} f^z_v = 0 \tag{5.5}$$

Equation (5.5) is a second order linear equation in $f^z(u, v)$. The only term of second order is f^z_{uv}: the equation is thus *hyperbolic*. Hyperbolic equations often correspond to the propagation of informations in a system (think of the wave equation). It is thus no surprise that the marionette method corresponds to a propagation algorithm. Loosely speaking, it can be shown that solutions of hyperbolic equations retain discontinuities of initial conditions. The smoothness of the shape obtained by the marionette method is thus dependent on the smoothness of the input data (plane view and elevation curves) [7].

Boundary conditions

With the marionette method, we prescribe the values of f^z on two boundaries. Mathematically, we choose two functions $f_1(v)$ and $f_2(u)$ which correspond to the height of the two guide curves:

$$\begin{cases} f^z(u = u_0, v) = & f_1(v) \\ f^z(u, v = v_0) = & f_2(u) \\ f_2(u_0) = & f_1(v_0) \end{cases} \tag{5.6}$$

The last equality correponds to a compatibility condition between equation $f_1(v)$ and $f_2(u)$, so that the altitude of $f^z(u_0, v_0)$ is known without ambiguity. This equation corresponds to an integration of the second member of equation (5.7). Writing $f_3(u) = \frac{\partial f_2}{\partial u}(u)$, we have:

$$\begin{cases} f^z(u = u_0, v) = & f_1(v) \\ \dfrac{\partial f^z}{\partial u}(u, v = v_0) = & f_3(u) \end{cases} \tag{5.7}$$

We see now that we specify the altitude of a guide curve and the slope on the second curve. This kind of boundary condition based on both values and derivatives is called *Cauchy boundary condition* and is particularly suited for hyperbolic equations [7]. The smooth problem solved by the marionette method is thus a classical problem in the theory of partial differential equations. Classical results on the existence, uniqueness and regularity of solution can be applied, even though it is not the purpose of this dissertation.

5.1.6 Marionette Meshes with singularities

The modelling of complex shapes requires the introduction of vertices with a different valence, called singularities in the following. For example, the mesh displayed in Figure 5.3a has one singularity: the central node has a valence of six. The mesh can be subdivided into six patches with no inner singularity (in blue and white). This kind of procedure can be applied to any quad-mesh. Each patch is a regular mesh, and the Marionette technique can be applied. There are however restrictions on the curves used as guide curves due to compatibility between patches. For example, in Figure 5.3a, it is clear that the six curves attached to the singularity can be used as guides for the six patches, whereas choosing the 12 curves on the perimeter over-constrain the problem.

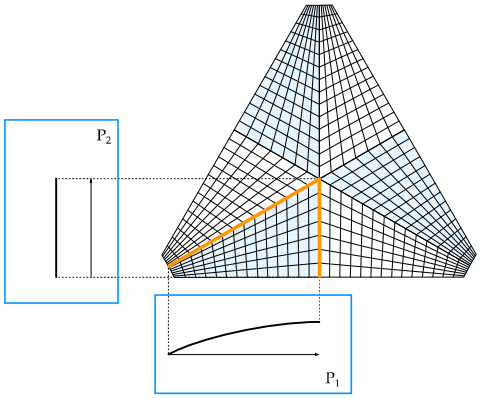

(a) Decomposition of a complex mesh into simple patches.

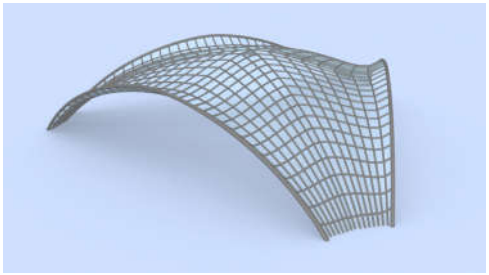

(b) The corresponding lifted mesh

Figure 5.3 – A Marionette Meshes with a singularity.

For an arbitrary quad-mesh, it is possible to compute the number of guide curves that can be used to generate a Marionette Mesh. The mesh can be decomposed into simple quad domains without any singularity by using the methods described in [247] or [244]. For example, Figure 5.3a has six domains, the mesh in Figure 5.4a has nine domains. These domains are four sided, and it is possible to extract

independent families of strip-domains, like displayed in Figure 5.4. Depending on the n-colorability of the mesh, the number of families varies. The example showed is two-colorable. As a result, two families of strips can be found and are shown in Figure 5.4b and 5.4c. Exactly one curve can be chosen across each strip-domain. Since strips are independent, the height of these nine curves can be chosen independently and will not over-constrain the problem.

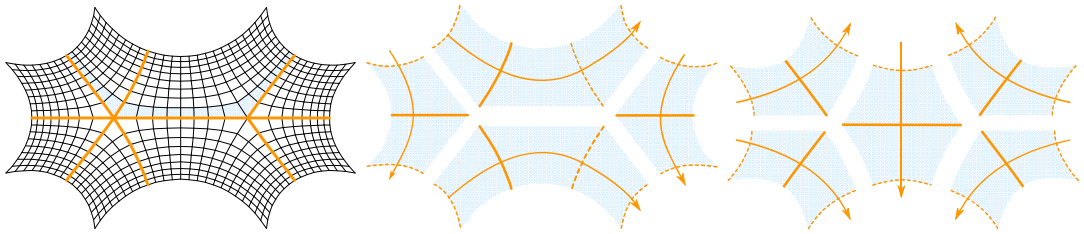

(a) Initial mesh (b) Family of four strip-domains (c) Family of five strip-domains

Figure 5.4 – Decomposition of a mesh into 2 families of strip-domains. Marionette Meshes can be generated by choosing one guide curve across each strip-domain.

5.1.7 Closed Marionette Meshes

Closed strips

Marionette Meshes create PQ-meshes by propagation of a planarity constraint along strips. One can easily figure that if the strip is closed, the problem becomes over-constrained. Indeed, consider Figure 5.5: the plane view of a closed strip and the altitudes z_i of the points (P_i) of one polyline are prescribed. If the altitude z_0^* of the first point used for the propagation P_0^* is chosen, the planarity constraint can be propagated along the strip. The points of the outer line are therefore imposed by the method, and the designer has no control on them. The last point P_N^* is therefore generally different from the initial point P_0^*, leading to a geometrical incompatibility of PQ-meshes.

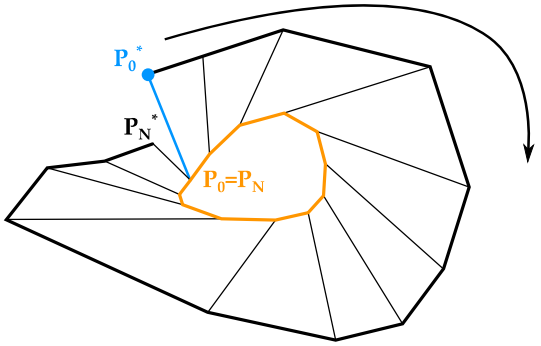

Figure 5.5 – Closed Marionette Strip with incompatible closing condition induced by the prescription of the plane view of the whole strip (yellow) and the altitudes of the inner curve (blue).

In the following, we develop a method to deal with the geometrical compatibility of closed strips. The results however can then be extended to general Marionette Mesh with closed strips. Suppose that the two prescribed curves are defined as the inner closed curve and one radial curve (see Figure 5.5). By propagation of equation (5.2), we easily see that the altitude of the last point z_N^* depends linearly on the altitude of the first point z_0^* and on the altitudes of the points on the inner curve $\mathbf{Z}$. It also depends on the in-plane projection of the strip. Formally, there exists a vector $\mathbf{V}$ and a scalar a, both functions of the plane view, so that:

$$\mathbf{V} \cdot \mathbf{Z} + a \cdot z_0^* = z_N^* \tag{5.8}$$

We are interested in the case where $z_0^* = z_N^*$. There are two possibilities:

1. $a = 1$: in this case, the condition restricts to $\mathbf{V} \cdot \mathbf{Z} = 0$ and does not depend on z_0^*. The vector $\mathbf{Z}$ is in the hyperplane of $\mathbf{V}$, which leaves $N - 1$ degrees of freedom.
2. $a \neq 1$: there is only one solution for z_0^*. This is the most constrained case: the designer can only control the inner curve of the strip.

Detailed calculations on closed strips and particular examples satisfying the condition $a = 1$ are developed in Section 5.2.

Closed meshes

The meshes with one solution are less flexible, but they can still generate interesting shapes, like the one displayed on Figure 5.6, which recalls the example of Figure 5.5. The designer has a total control on the altitude of the inner curve and the plane view, but cannot manipulate freely the outer curve. Note that in Figure 5.6, the strings of the marionette are materialised as columns in the rendering, illustrating the geometrical interpretation of the method.

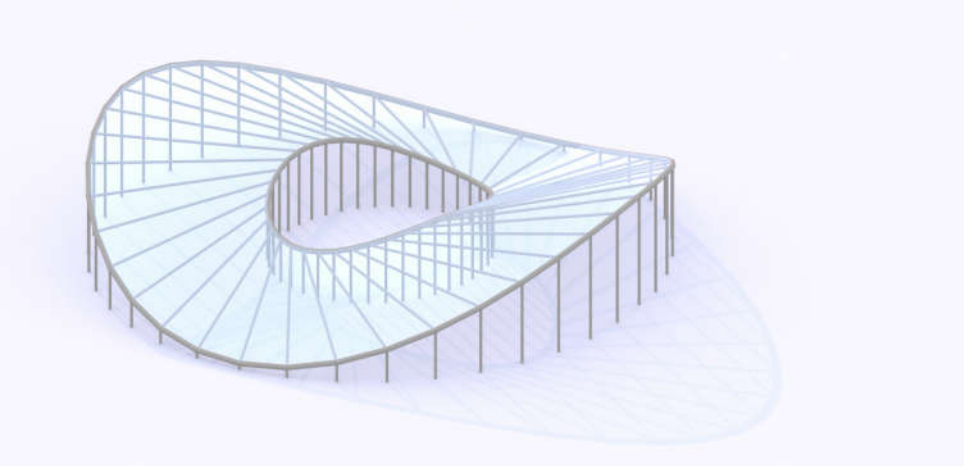

Figure 5.6 – Architectural design with a closed Marionette Mesh, the altitude of the inner curve is prescribed, the designer does not have control on the outer curve.

The most interesting case occurs when the designer has potentially the control of two curves. It relies on a condition on the planar view explained above. A simple case where this condition is fulfilled is when it has a symmetry. In this case, there is a $N - 1$ parameters family of solutions for the altitude of the inner curve. The elevation of a closed guide curve can be chosen arbitrarely and projected into the hyperplane of normal $\mathbf{V}$, keeping the notations of equation (5.8). This operation is straight forward and allows to control the elevation of a second curve, like for open meshes. An example of this strategy is displayed in Figure 5.7, where all the meshes have the same planar view.

Another look at the problem

The problems specific to closed strips or meshes can be understood by the consideration of the equivalent smooth problem. The partial differential equation (5.5) remains unchanged but the boundary conditions expressed by equation (5.7) are not valid anymore. Indeed, a closed surface imposes a periodicity of the solution. Consider the case where we want the curves ($u =$ constant) to be closed, there exist a certain period T so that:

$$\begin{cases} f^z\left(u = u_0, v\right) = & f_1\left(v\right) \\ \dfrac{\partial f^z}{\partial u}\left(u, v = v_0\right) = & f_3\left(u\right) \\ \forall u, f^z\left(u, v + T\right) = & f^z\left(u, v\right) \end{cases} \tag{5.9}$$

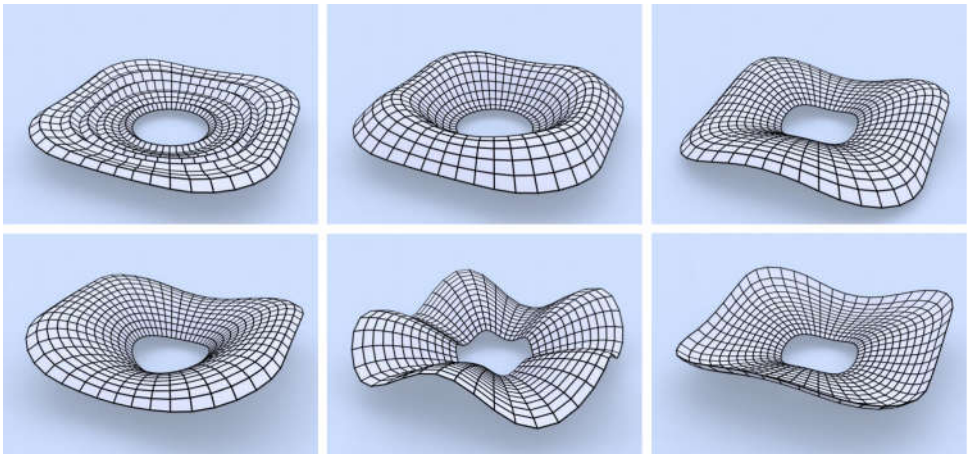

Figure 5.7 – Some shapes with planar faces and a closed mesh generated with the method proposed in this chapter.

This additional boundary condition might over-constrain the problem and the existence of a solution is not certain.

5.2 Some results on closed strips

The aim of this section is to discuss with more detail the problem of closed strips. First, we write the propagation problem on a strip. This step is purely computational, but is necessary to introduce a quantity of interest. We interpret then the geometrical meaning of the compatibility condition with respect to the mathematical formalism introduced. Then, we present some particular cases where the closing of a strip is possible regardless of the choice of the altitude on the outer curve.

5.2.1 Propagation equation

Consider the closed strip discussed in Section 5.1.7. For each facet, we can apply the planarity constraint of equation (5.2). Writing z_i the altitude of the i^{th} point of the inner curve and z_i^* the altitude of the i^{th} point of the outer curve, we can rewrite this equation. For the sake of simplicity, we replace the ratios of the 2D determinants by scalars a_i and b_i. We make following identifications:

$$\begin{cases} P_i \Leftrightarrow & A \\ P_{i+1} \Leftrightarrow & B \\ P_i^* \Leftrightarrow & C \\ P_{i+1}^* \Leftrightarrow & D \\ a_i \Leftrightarrow & \dfrac{\det_{2\text{D}}(\mathbf{AB}, \mathbf{AC})}{\det_{2\text{D}}(\mathbf{AB}, \mathbf{AD})} \\ b_i \Leftrightarrow & \dfrac{\det_{2\text{D}}(\mathbf{AD}, \mathbf{AC})}{\det_{2\text{D}}(\mathbf{AB}, \mathbf{AD})} \end{cases}$$

We get hence following equation:

$$z_{i+1}^* = (1 - a_i - b_i)\, z_i + a_i z_i^* + b_i z_{i+1} \tag{5.10}$$

We make the following hypothesis, which is easily verified by recurrence:

$$\forall i > 0, z_i^* = \sum_{k=0}^{i} v_k z_k + A_i z_0^* \tag{5.11}$$

In fact, we can be even more precise and compute the value of A_i. We make the hypothesis that:

$$\forall i > 0, A_i = \prod_{k=0}^{i-1} a_k \tag{5.12}$$

Proof This is true for $i = 1$ due to equation (5.10). Then, we proceed by recurrence. Assume that (5.12) is true for i, then we show that this is true for $i+1$. We plug equation (5.11) into equation (5.10) and get:

$$z^*_{i+1} = (1 - a_i - b_i)\, z_i + a_i \left(\sum_{k=0}^{i} v_k z_k + A_i z^*_0 \right) + b_i z_{i+1} \tag{5.13}$$

There is only one term in z^*_0, and it verifies equation (5.12). Our hypothesis is thus proved.

5.2.2 Geometrical interpretation

The ratios a_i can be interpreted with elementary plane geometry. Consider Figure 5.8a: the ratio a is defined with 2D determinants and can be expressed with the vectors norms and angles. We have:

$$a = \frac{\|\mathbf{AB}\|\|\mathbf{AC}\| \sin\beta}{\|\mathbf{AB}\|\|\mathbf{AD}\| \sin\alpha} \tag{5.14}$$

We recognise the areas of the triangles ABC and ABD, so that a can be rewritten as:

$$a = \frac{\mathcal{A}_{ABC}}{\mathcal{A}_{ABD}} \tag{5.15}$$

The two triangles used for the computation of a_i are shown in Figure 5.8b.

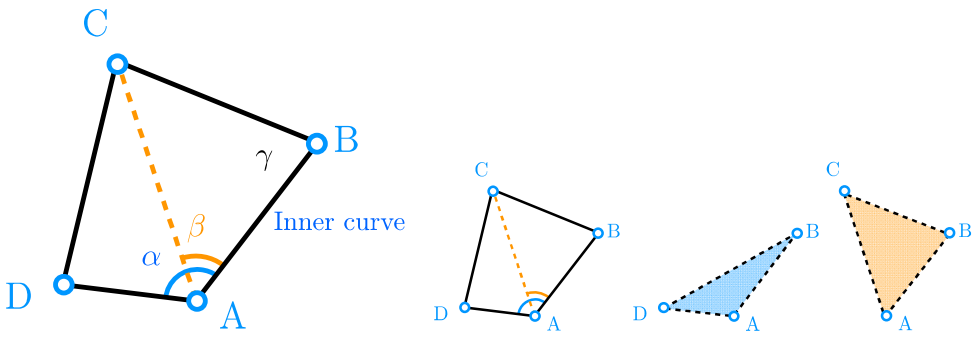

(a) Angle notations

(b) The two triangles used to compute a_i.

Figure 5.8 – Planar view of a quadrilateral

5.2.3 General solutions for a closed strip

Recall that we are interested in finding the solutions so that $z^*_N = z^*_0$, which also writes:

$$z^*_N - z^*_0 = \sum_{k=0}^{N} v_k z_k + \left(\prod_{k=0}^{N-1} a_k - 1 \right) z^*_0 = 0 \tag{5.16}$$

We also want the space of solutions to be as large as possible, and therefore, we don't want it to depend on the choice of the altitude on the outer curve z^*_0. This implies a new condition:

$$\prod_{k=0}^{N-1} a_k = 1 \tag{5.17}$$

In the following, we discuss the invariance of this equation under some transformations and show some particular cases where it is satisfied.

5.2.4 Invariance

To have a complete overview on the problem of closed strips, we provide transformations that map compatible strips to other compatible strips. The study of group of transformations that preserve a given quantity is at the core of modern geometry, and for the sake of completeness, we show this point of view dating back from Felix Klein [129].

Linear maps

The transformations we are interested in preserve equation (5.17). The most straight forward way to do this is to preserve each a_i. It is clear that all linear transformations in the plane (translation, scaling, shearing) preserve each individual ratio. Consider indeed transformations defined by:

$$f(x,y) = \begin{pmatrix} m_{11} & m_{12} \\ m_{21} & m_{22} \end{pmatrix} \cdot \begin{pmatrix} x \\ y \end{pmatrix} + \begin{pmatrix} X_0 \\ Y_0 \end{pmatrix} \tag{5.18}$$

For two points (x_0, y_0) and (x_1, y_1), we write their image by f respectively (x'_0, y'_0) and (x'_1, y'_1). We call $\mathbf{M}$ the matrix written in equation (5.18), then we have:

$$\det \begin{pmatrix} x'_0 & x'_1 \\ y'_0 & y'_1 \end{pmatrix} = (\det \mathbf{M})^2 \det \begin{pmatrix} x_0 & x_1 \\ y_0 & y_1 \end{pmatrix} \tag{5.19}$$

It is clear that the linear map preserves the ratio of 2D determinant, since the factor $\det\mathbf{M}$ depends only on the parameters of the transformations. Linear maps preserve thus the geometrical compatibility of closed strips. This is not a surprise, since linear maps preserve PQ-meshes [194].

Combescure maps

We give now another set of transformations that preserve the geometrical compatibility. We re-write now equation (5.14) by using the properties of area of triangles:

$$a_i = \frac{\|\mathbf{BC}\| \sin\gamma}{\|\mathbf{AD}\| \sin\alpha} \tag{5.20}$$

Computing the product of all these values, we notice that the lengths cancel out (each length is exactly one time at the numerator and one time at the denominator, so that:

$$\prod_{i=0}^{N-1} a_i = \prod_{i=0}^{N-1} \frac{\sin\gamma_i}{\sin\alpha_i} \tag{5.21}$$

Therefore, a transformation that preserves discrete angles preserves also the geometrical compatibility. Such transformations are known as *Combescure transformation*. The image of a mesh by a Combescure transformation has its edges parallel to the initial mesh, but it does not necessary preserve lengths. Examples of such transformations are given in [168].

5.2.5 Particular cases

We give three simple examples where equation (5.17) is verified.

Example 1: parallel edges

Equation (5.17) is verified when all the a_k are equal to one. This condition translates into:

$$\frac{\|\mathbf{AC}\|}{\|\mathbf{AD}\|} = \frac{\sin\beta}{\sin\alpha} \tag{5.22}$$

We write the equation of $\mathbf{A}, \mathbf{B}, \mathbf{C}, \mathbf{D}$ in the cartesian plane where $\mathbf{e_X}$ is parallel to $\mathbf{AB}$, we have:

$$\begin{cases} \mathbf{AB} = \begin{pmatrix} \|\mathbf{AB}\| \\ 0 \\ 0 \end{pmatrix} \\ \mathbf{AC} = \|\mathbf{AC}\| \begin{pmatrix} \cos\beta \\ \sin\beta \\ 0 \end{pmatrix} \\ \mathbf{AD} = \|\mathbf{AD}\| \begin{pmatrix} \cos\alpha \\ \sin\alpha \\ 0 \end{pmatrix} \end{cases} \tag{5.23}$$

We plug then equation (5.22) into equation (5.23) and compute the vector $\mathbf{CD}$. We get following result:

$$\mathbf{CD} = \|\mathbf{AD}\| \begin{pmatrix} \frac{\sin\alpha}{\sin\beta}\cos\beta - \cos\alpha \\ 0 \\ 0 \end{pmatrix} \tag{5.24}$$

Remarkably, we notice that the vectors $\mathbf{CD}$ and $\mathbf{AB}$ are parallel. Reciprocally, if these two vectors are parallel, then equation (5.22) is satisfied. Therefore, a closed strip where all the projected quads are trapezoids satisfies equation (5.17). Such planar views provide thus a large design space and the maximal design flexibility for closed strips.

Example 2: symmetry

Consider the case where the planar view of the strip has an axis of symmetry. Consider Figure 5.8b: each a_i is defined as the ratio of the area of the blue and orange triangles. When the curve has a symmetry, like the one depicted in Figure 5.9, the role of orange and blue triangle is inverted by the symmetry. Two faces related by a symmetry have therefore inverse values of a_i. Their product is naturally equal to 1, which proves that strips with an axis of symmetry satisfy equation (5.17).

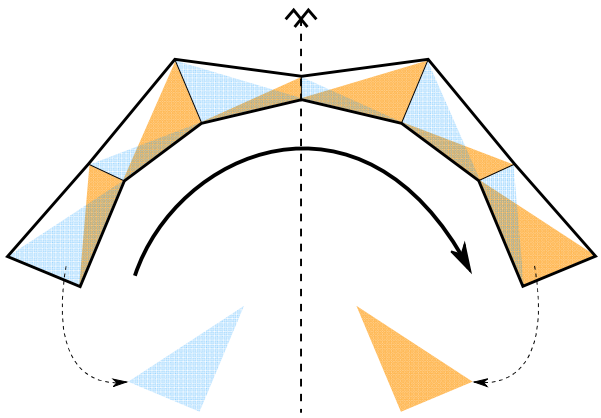

Figure 5.9 – A curve with an axis of symmetry and the inversion of the blue and orange triangles.

Example 3: orthogonal fields

The first two examples are based on equation (5.17) where the a_i are expressed as ratios of areas. The propagation rule is applied to each quadrilateral, but in the case of closed curves it is also interesting to look at each vertex.

Consider Figure 5.10, equation (5.21) is verified if $\gamma_0 = \alpha_1$, $\gamma_1 = \alpha_2$ and so forth. In other terms, if the transverse edge is the bisecting line of the inner curve, then we have a solution to the problem of closed

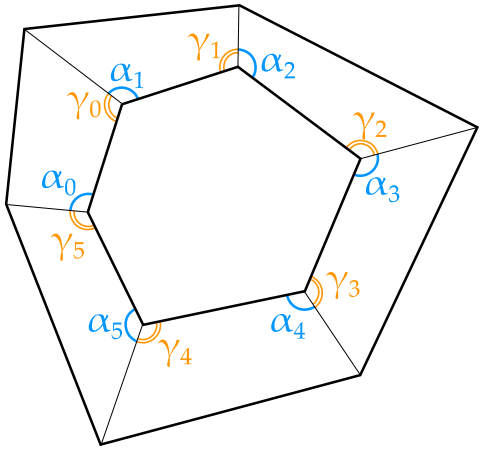

Figure 5.10 – A closed curve and the angles used in equation (5.21) .

strips. This condition is a discrete counterpart of orthogonality of vector fields. Examples of such meshes are obtained by planar discrete moulding surfaces [168]. Discretisation of orthogonal parameterisation of the plane will therefore yield strips that are very close to be geometrically compatible. The smooth counterpart of this problem would be looked at carefully in further work.

5.3 Architectural design with Marionette Meshes

5.3.1 Computational set-up

The algorithms described in this chapter have been implemented in the visual-scripting plug-in Grasshopper™for the modelling software Rhino™. This allows interaction with other numerical tools necessary for architectural design, like finite-element analysis software Karamba™. An example of interaction between fabrication-aware shape generation and structural analysis is shown in chapter 6.

Marionette Meshes only require the solution of a linear system. The computation time is thus low, typically it takes 3 ms to lift a mesh of 10,000 faces, with no pre-factorisation involved. Real-time computation provides great design flexibility, even for large meshes.

In our framework, the planar views are generated with NURBS patches, and the elevation curves are drawn as Bézier curves. The smoothness of the final mesh depends thus on the smoothness of the in-plane parameterisation. A C^0 projection yields a C^0 solution to the hyperbolic equation (5.4), so that shape functions with creases can easily be propagated through the mesh. Figure 5.11 shows a corrugated shape generated from a C^0 planar view and smooth guide curves. Such corrugations can be used in folded plate structures, and could extend the formal possibilities of methods developped in [210] or discussed in [137]. An application is shown in Chapter 7.

5.3.2 Geometrical optimisation

General remarks

The method described in the previous section of this chapter constructs a space of solutions with planar facets. This space is a vector space, which has some interesting implications for some optimisation problems. We can indeed see the planarity constraint as a linear constraint on the coordinates of all the vertices of a mesh. There exists a matrix $\mathbf{A}$ and list of altitudes $\mathbf{z}$ and $\mathbf{z_p}$ so that:

$$\mathbf{A} \cdot \mathbf{z_p} = \mathbf{z} \tag{5.25}$$

The marionette method gives an intuitive way to construct this matrix, as $\mathbf{z_p}$ corresponds to the altitudes of vertices on the guide curves and $\mathbf{A}$ depends on the planar view. For a mesh with NM faces, $\mathbf{A}$ is a matrix of size $(N+M+1, (N+1)\cdot(M+1))$

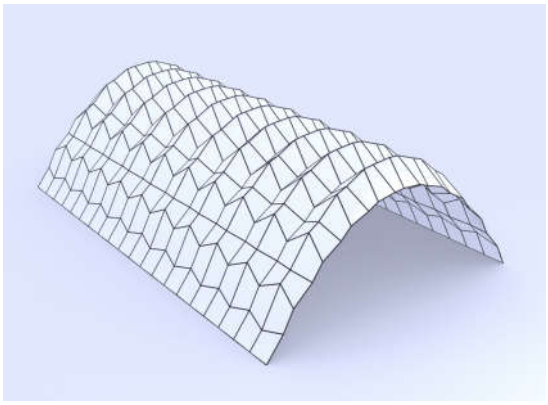

Figure 5.11 – A non-smooth mesh with planar facets generated with the Marionette method.

It is a well-known fact that minimisation of quadratic functions under linear constraints is equivalent to the solving of a linear system [180]. An example of such optimisation problems with useful applications for architectural design is given in the following.

Specific constraints

Some particular construction constraints can be applied to marionette meshes. For example, it is interesting to build with planar structural members, which can then easily be manufactured at a large scale (think of a construction with planar arches). Likewise, the installation and the mechanical behaviour of planar arches is expected to be better if they are vertical. Keeping the point of view of descriptive geometry, we see that this condition is realised when the plane view feature straight lines, like in Figure 5.12. This can be done without optimisation, by drawing a ruling between two planar curves.

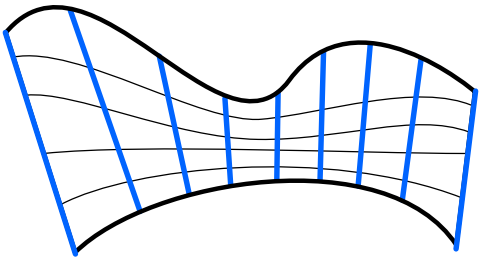

Figure 5.12 – A planar view that yields construction with planar arches.

Surface fitting

A common problem described in the literature is the approximation of a given shape with a PQ-mesh. In the followings, we consider that the designer prescribes a planar projection and looks for the closest Marionette Mesh to a reference surface.

The problem is illustrated in Figure 5.13: the altitude of the vertices in the Marionette Mesh are written $\mathbf{z}$, the altitudes of the points on the reference surface are written $\mathbf{z_0}$. The function to minimize is written as follows:

$$J(\mathbf{z}) = (\mathbf{z} - \mathbf{z_0})^T (\mathbf{z} - \mathbf{z_0}) \tag{5.26}$$

The design space is the Marionette Meshes which have the considered planar view. This constraint is written in equation (5.25). The optimisation problem follows:

$$\min_{\mathbf{z}=\mathbf{A}\mathbf{z_p}} J(\mathbf{z}) = \min (\mathbf{A}\mathbf{z_p} - \mathbf{z_0})^T (\mathbf{A}\mathbf{z_p} - \mathbf{z_0}) \tag{5.27}$$

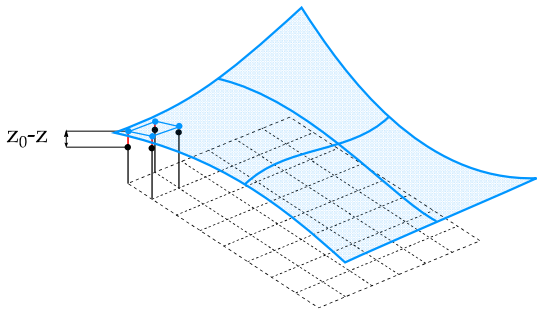

Figure 5.13 – Optimisation problem: approximation of a reference surface with a given planar projection (dashed lines).

Expanding the equation, one gets:

$$J_p(\mathbf{z_p}) = \mathbf{z_p}^T \mathbf{A}^T \mathbf{A} \mathbf{z_p} - 2\mathbf{z_p^T} \mathbf{A^T} \mathbf{z_0}^T + \mathbf{z_0}^T \mathbf{z_0} \tag{5.28}$$

A necessary condition to find a solution is to verify that $\nabla J_p = \mathbf{0}$. The system reduces therefore to:

$$\mathbf{A^T A z_p} = \mathbf{A^T z_0} \tag{5.29}$$

Equation (5.29) is typical of least square problem. It is clear that the rank of the matrix $\mathbf{A}$ is $(N + M + 1)$. It follows that the rank of $\mathbf{A^T A}$ is also $(N + M + 1)$. Since $\mathbf{A^T A} \in \mathcal{M}(N + M + 1, N + M + 1)$, this matrix is invertible. Equation (5.29) has therefore one unique solution. Since $\mathbf{A^T A}$ is clearly definite positive, it follows that the extremum is in fact a local minimum. Finally, the behavior when $\|\mathbf{z_p}\| \longrightarrow \infty$ demonstrates that this is a global minimum.

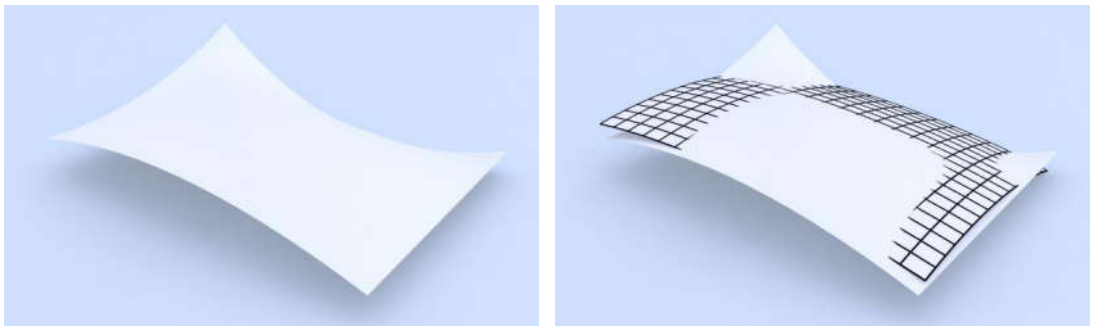

Figure 5.14 – A target surface (left), and the optimal approximation by a surface of translation (right).

An application is illustrated in Figure 5.14, where a target NURBS is approached by a surface of translation, which are well-known in architectural design [98]. This optimal can be considered poor, but the key information is that it is the best in the design space chosen by the designer, so that the designer knows that to improve the solution, he has to explore other planar views or mesh topologies. The surface displayed is indeed the best solution possible for the planar view chosen by the designer. As computation are done in real-time, it is easy to generate very quickly different plane views with different topologies, keeping control of the aesthetic and layout of the cladding.

5.3.3 Shape exploration with Marionette Meshes

The framework introduced here intrinsically account for planarity of panels. Its mathematical formulation is however suited for many architectural constraints. Hard constraints must be fulfilled exactly, whereas soft constraints are included into the function to minimize [180]. Since the planarity constraint is linear, soft constraints expressed as linear or quadratic functions can easily be included in the objective

function. In this case, the optimisation problem will be similar to a classical least square problem and can be solved efficiently.

Hard constraints defined by linear equations are treated effectively within the proposed framework. Examples of linear constraints are prescribed volume or a maximal allowable altitude. The marionette method imposes $NM - (N + M - 1)$ out of NM parameters, this means that another $N + M - 1$ linear constraints can be applied without over-constraining the optimisation problem.

Perhaps the most interesting application is the prescription of a boundary, as depicted in Figure 5.15. In this figure, the planar view is imposed and the user prescribes the altitude of some points of the mesh along a curve (white circles). In this case, the number of prescribed points is superior to the number of degrees of freedom, and the problem might be overconstrained. It might hence be preferable to turn this problem into a soft constrained problem with a quadratic function to minimize.

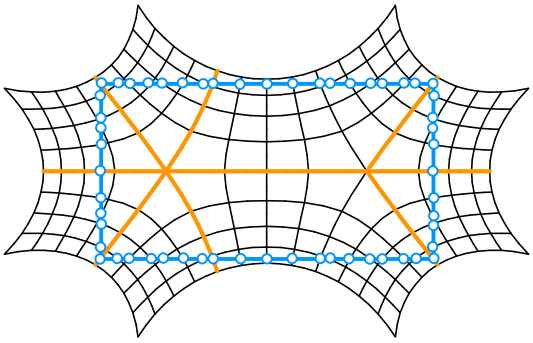

Figure 5.15 – A plane view (thin lines) with a prescribed boundary (thick lines).

Other constraints could be used. For example, in the manner of NURBS-modelling, the user could control the altitude of some handle-points, each handle decreasing the size of the space of solution by one degree of freedom. This kind of approach has been used in optimisation-based shape exploration, but it looses the notion of global shape control.

5.3.4 Controlling mesh distortion

In an approach using planar projection in the horizontal plane, the metric of the mesh is changed in function of the slope. If the plane view does not take this aspect into account, this can yield high distortions which are unwanted in practice . Consider for example that the plane view is a square grid: the resulting surface is obviously a surface of translation defined by equation (5.30):

$$z(x, y) = f(x) + g(y) \tag{5.30}$$

The functions f and g correspond to two elevation curves. Consider now a parallelogram on the surface of translation defined for $(x, y, x + \Delta x, y + \Delta y)$. It is immediate to get a first order development of the lengths of the edges l_x and l_y we compare it with the in-plane length Δx and Δy:

$$\begin{cases} l_x = & \sqrt{\Delta x^2 \left(1 + \left(f'(x)\right)^2 + o\left(\Delta x^2\right)\right)} \\ l_y = & \sqrt{\Delta y^2 \left(1 + \left(g'(y)\right)^2 + o\left(\Delta y\right)^2\right)} \end{cases} \tag{5.31}$$

The relative change of length $\Delta l_.$ is thus given by:

$$\begin{cases} \Delta l_x = & \dfrac{l_x - \Delta x}{\Delta x} = \dfrac{f'(x)^2}{2} + o(\Delta x) \\ \Delta l_y = & \dfrac{l_y - \Delta y}{\Delta y} = \dfrac{g'(y)^2}{2} + o(\Delta x) \end{cases} \tag{5.32}$$

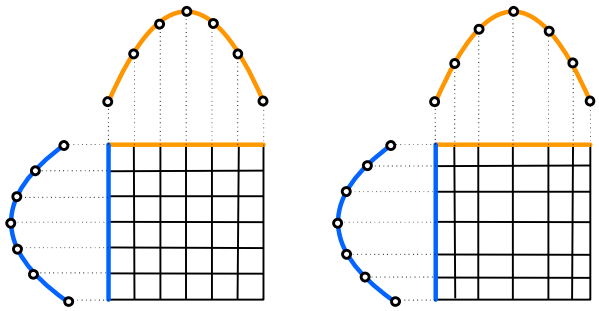

Figure 5.16 – A regular planar view can yield length distortion in elevation (left). The elevation can inform the plane view regularity to yield meshes without length distortion (right).

The relative length between the parallelogram and its projection is thus related to the slope. The problem is decoupled in x and y due to equation (5.30). In practice, it is possible to mesh a surface of translation with a constant edge length: Figure 5.16 shows two meshing strategies for a surface of translation, one with a regular planar view and irregular mesh, the other with an irregular planar view but constant edge length.

This remark shows that the problem of edge length regularisation can be easily solved with the marionette method if the elevation curves are continuous curves which can be subdivided. With surfaces of translation, a discretisation of the elevation curves with constant length yields a Tchebycheff net. This is not the case for general marionette meshes, so that the choice of uniform subdivision of the elevations is not necessarily the true minimiser of edge length distortion. Post-rationalisation techniques could then be implemented to minimise the variance of edge lengths in each direction and further simplify manufacturing.

5.4 Generalisation of the method

5.4.1 General projections

It appeared that prescribing a horizontal view and applying the propagation technique presented here only allows for the modelling of height fields. This is a limitation of this method, although height fields surfaces are commonly used for roof covering. Other projections can be used for more shape flexibility. The planarity constraint for a quad can be extendend to the case of non-parallel projections, like in Figure 5.17.

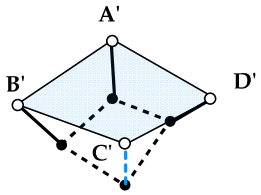

Figure 5.17 – A Marionette Quad with non-parallel guide lines.

Some projections are of practical interest for archetypal projects. Towers and facades can be modelled with cylindrical projections. Stadia can be designed using projections on torus or on moulding surfaces, the offset directions corresponding to the normals of the smooth surface. Indeed, moulding surfaces fit naturally the geometry of stadia (see Figure 5.18a) and have some interesting features, discussed in Chapter 3:

- Their natural mesh contains planar curves, which are geodesics of the surface: the planarity is preserved by the marionette transformation.

- They are naturally meshed by their lines of curvatures, which gives a torsion-free beam layout on the initial surface, and on the final shape.

(a) Reference moulding surface (b) Non-symmetrical design (c) Symmetrical design

Figure 5.18 – Design of stadia obtained from a projection on a moulding surface: the prescribed curves are the inner ring and a section curve.

5.4.2 Extension to other patterns

Application to non-standard patterns

Equation (5.35) can be applied to meshes composed of triangles and hexagons, also known as Kagome lattices. It reveals that the number of d.o.f is comparable to the one of quadrilateral meshes. There is therefore a straight forward way to lift Kagome lattices with the marionette technique. Figure 5.19a shows the guide curves for the Kagome pattern. Other isolated points are required to lift the mesh. The altitude of these points can for example be chosen in order to optimise mesh fairness, which has been characterised in numerous works by an energy $\mathcal{F}$ defined in equation (5.33), where $\mathbf{v_i}$ is the i^{th} vertex of a polyline:

$$\mathcal{F} = \sum_{polylines} \sum_{i} \|\mathbf{v_i} - 2\mathbf{v_{i+1}} + \mathbf{v_{i+2}}\|^2 \tag{5.33}$$

The functional is quadratic and is not difficult to minimise under linear constraints. Figure 5.19c shows a mesh derived from an hexagonal pattern: three guide curves can be used to lift the mesh. The number of degrees of freedom of the examples of Figure 5.19 are evaluated in Section **??**.

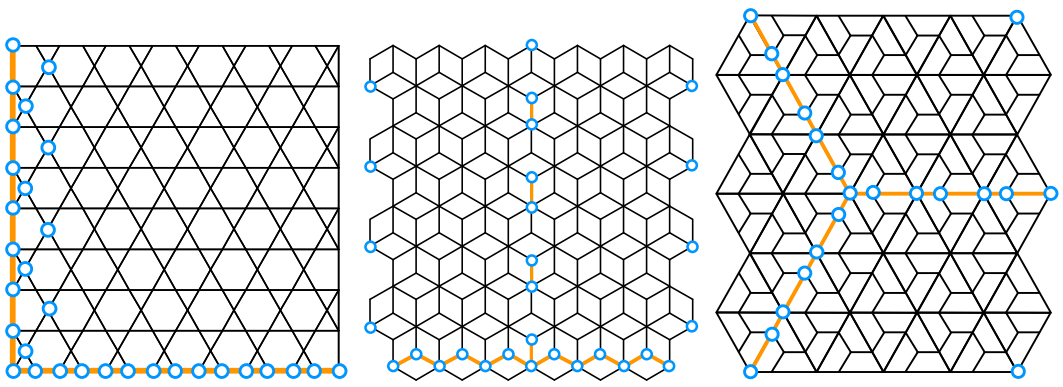

(a) Kagome lattice (b) Dual Kagome lattice (c) Hex pattern

Figure 5.19 – Marionette method applied to several patterns, white dots correspond to prescribed altitudes.

5.4.3 Evaluation of the dimension of the space of solutions

This section proposes to extend the Marionette method to other patterns than quads. First, we discuss the estimation of the size of the design space offered by the marionette technique in the most general cases. We illustrate then those remarks on the generality of the method with various patterns.

Size of the design space

The facet planarity constraint is linear, which means that the space of meshes with planar facets is a vector space. [65] proposed a criterion to evaluate the dimension of this vector space. For each facet, three points can be chosen independently (3 d.o.f for each points) and the remaining points must be chosen in the constructed plane (1 d.o.f deleted for these nodes). Writing n_F the number of vertices for each face, the estimation of the size of the space of meshes with planar facets follows [65]:

$$N \sim 3N_{nodes} - \sum_{Faces} (n_F - 3) \tag{5.34}$$

For a quad mesh, we get $N \sim 2N_{nodes}$. This number is high and is difficult to interpret for the designer. The projection technique used here reduces the size of the design space. Since the planar view is prescribed, each point looses 2 d.o.f. Equation (5.34) writes:

$$N_{marionette} \sim N_{nodes} - \sum_{Faces} (n_F - 3) \tag{5.35}$$

The size of the design space is reduced compared to general methods, but the smoothness of the final shape is easily controlled. Note that techniques relying on generation of the whole vector space have to introduce fairing energies, as the design space contains both smooth and non-smooth meshes.

For a quadrilateral mesh with $n \times m$ faces without singularity, we have $N_{nodes} = (n+1) \cdot (m+1)$, and nm faces. The application of equation (5.35) shows that the size of the design space is $n + m + 1$, which is exactly what is found by the marionette method.

We propose here to count the number of degrees of freedom for the meshes drawn in Figure 5.19. We use equation (5.35) to estimate the available degrees of freedom and compare this number with the number of prescribed points drawn in Figure 5.19. Each time, it is easy to propagate the altitudes in the manner of what has been done with quadrilateral meshes. We illustrate here the fact that the formula (5.35) is exact for meshes with no closed curves.

Kagome pattern

The Kagome pattern shown in Figure 5.19a features 191 vertices, 112 triangles, 48 hexagons and 8 pentagons. The estimated number of degrees of freedom given by the marionette method follows:

$$N = 191 - (112 \cdot (3-3) + 48 \cdot (6-3) + 8 \cdot (5-3))$$

$$N = 191 - (0 + 144 + 16)$$

$$N = 31$$

This is exactly the number of prescribed nodes in Figure 5.19a.

Dual-Kagome pattern

The dual-Kagome pattern shown in Figure 5.19b has 185 vertices and 156 quadrilateral facets.

$$N = 185 - 156 \cdot (4-3)$$

$$N = 29$$

This is the number of vertices with prescribed altitudes in Figure 5.19b.

Hexagonal pattern

The pattern derived from an hexagonal mesh has 183 vertices and 162 quadrilateral facets. The number of d.o.f is thus:

$$N = 183 - 162 = 21 \tag{5.36}$$

Remark

The calculation provided here shows hints for the number of guide curves to use to lift the mesh. Notice however that the d.o.f must be uncoupled: for example it is not possible to prescribe independently the 4 altitudes of the vertices of a quadrilateral face. Our choice of guide points does not violate this constraint.

For both the dual kagome and the hexagonal pattern, the planarity constraint cannot be propagated throughout the whole mesh, additional isolated altitudes have to be prescribed.

Illustration

Figure 5.20 shows a Kagome lattice covered with planar facets generated with the marionette method. The design started from a planar view generated with a NURBS patch, a Kagome was then generated following the isoparametric lines and lifted with the marionette technique. One of the guide curve is the parabolic arch of the entrance, the other is an undulating curve following the tunnel. Like for PQ-meshes, the computation is done in real time.

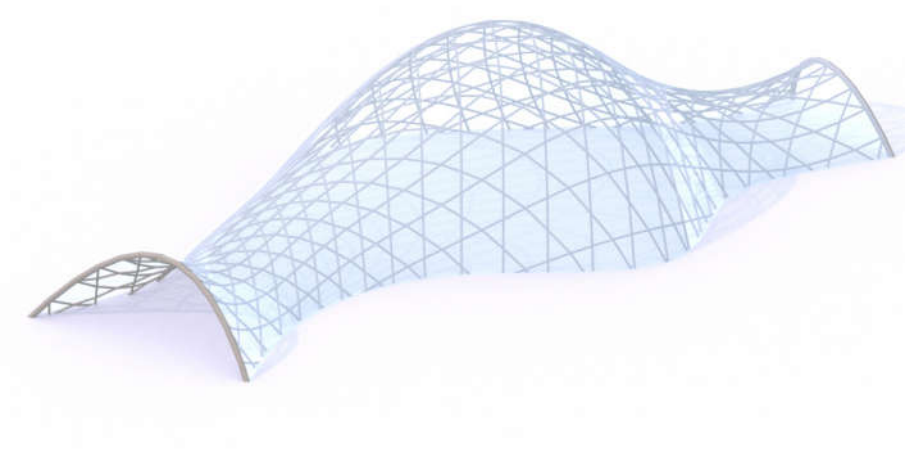

Figure 5.20 – Free-form design covered by planar Kagome lattice.

5.4.4 Equivalence between kagome and quad meshes

The short study done here shows that the generation of planar kagome meshes with the marionette technique require the input of two guide curves and of additional isolated points. It is therefore similar to the generation of PQ-meshes, and a natural conclusion would be that kagome and quadrilateral meshes can be obtained from the same parametrisations of surfaces. The following paragraphs demonstrate that it is possible to generate a planar kagome mesh from a planar quadrilateral mesh.

Systematic studies on the exploration of the design space offered by the kagome pattern are lacking, and this structural pattern is not fully understood and rarely considered for fabrication. Like quadrilateral grids, kagome grids present a node valence of four, which indicates a reasonable cost of fabrication. The kagome pattern can be found in Japanese basketry, where the members are woven. Among other usage, kagome grids have been used in the architecture of Shigeru Ban and for ornamentation purpose. Understanding their technological possibilities and mechanical performances could create new opportunities for the design of efficient structures.

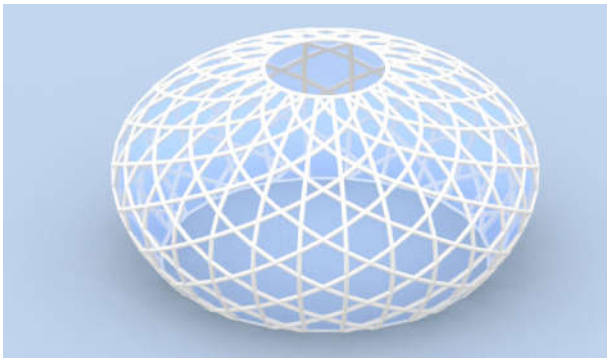

Figure 5.21 – A Kagome grid pattern covered with planar facets generated with the method described in this section.

An algorithm for Kagome pattern with planar facets

We present here an original method that converts planar quadrilateral (PQ) meshes to planar Kagome (PK) meshes. The algorithm takes a PQ-mesh as an input, like illustrated in Figure 5.22. Not all PQ-meshes are acceptable, but only those which can be coloured as a chequerboard. In the algorithm, the dark faces become hexagons and the white one become triangles. Starting from a quad mesh (left), one must determine intermediary points (middle) which define new vertices of the Kagome grid (right).

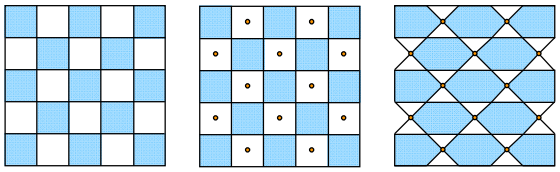

Figure 5.22 – Conversion of a quadrilateral mesh to a Kagome mesh

The choice of the intermediary point is restricted by the fact that the two adjacent hexagons have to be planar. Consider three consecutive planar quads Q_{i-1}, Q_i and Q_{i+1}. The algorithm determining the new vertices can be written as follows, and is detailed in Figure 5.23:

1. Compute the barycentre $\mathbf{G_i}$ of the quadrangle Q_i;
2. Compute the intersection of the planes (Q_{i-1}), (Q_{i+1});
   - If the intersection is a plane, create the node $\mathbf{N_i} = \mathbf{G_i}$;
   - If it is a line $(\mathcal{L})$, create the node $\mathbf{N_i}$ as the orthogonal projection of $\mathbf{G_i}$ on $(\mathcal{L})$. $\mathbf{N_i}$ is the closest point to $\mathbf{G_i}$ on $(\mathcal{L})$.
3. Repeat steps 1 and 2 in a chequerboard pattern.

Other points on $(\mathcal{L})$ could be chosen, but the choice proposed in this algorithm yields satisfactory and regular results, as illustrated in Figure 5.21.

Finally, we noticed in our formal explorations that the algorithm can encounter some difficulties if the curvature of the surface is very low. With numerical imprecisions, the binary choice of the second step of the proposed algorithm can lead to instabilities. Therefore, we introduce a number ε corresponding to the fabrication tolerance for planarity. If the distance between $\mathbf{G}$ and each of the two planes is inferior to ε, we set the point $\mathbf{G}$ as a vertex of the Kagome mesh.

It must be noticed here that the Kagome mesh obtained from a square grid in Figure 5.22 is irregular: the hexagons seem a bit stretched. Simple trigonometric considerations show that the regular Kagome pattern in the plane is obtained from a rectangular grid with an aspect ratio of $\sqrt{3}$. The grids generated

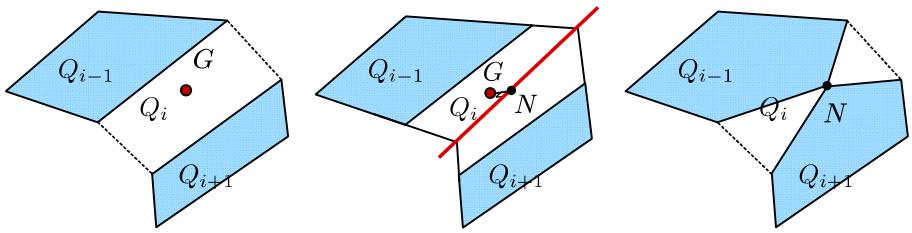

(a) Step 1 (b) Step 2 (c) Creation of the new edges

Figure 5.23 – Details of the conversion to a Planar Kagome mesh.

in Chapter 7 will use the same rule, as we aim for visually regular patterns, like the ones displayed in Figure 5.21 and 7.20. Some simple geometrical properties of these grids are discussed in Section 7.3.3.

In Chapter 2, we discussed the link between *conjugate curves network* and planar quadrilateral meshes. The conversion technique presented here and the results on the marionette method show that kagome and quadrilateral meshes have similar rigidity with respect to the planarity constraint. Therefore, PK meshes can be obtained from parametrisation by conjugate curves of a surface. In particular, the parametrisation by lines of curvature yields planar kagome meshes. Therefore, the framework developed with generalised cyclidic nets proposed in Chapter 4 could benefit from this finding and yield planar kagome meshes automatically. The possibilities offered by this pattern in gridshell structures are investigated in Chapter 7.

5.5 Summary of intellectual contribution

We have introduced an intuitive technique for interactive shape modelling with planar facets. It is based on descriptive geometry, which has been used by architects and engineers for centuries. The concept has many applications, in particular the modelling of PQ-meshes with or without singularity. Some examples show the formal potential of our method. The framework was also extended to Kagome and dual-Kagome lattices. It is likely that other polyhedral patterns can be treated with the Marionette technique. The generality of the method has also been demonstrated by changing the projection direction, a method with large potential if used on mesh with remarkable offset properties.

Quadratic optimisation problems, like surface-fitting problems can be solved efficiently with the marionette technique. A simple example where only the altitudes of the guide curve are the only parameters was detailed, but controlling the plane view with NURBS patches could allow for a more general solution of such problems. The separation of variables in horizontal plane and vertical plane can potentially give birth to efficient numerical methods for geometrical optimisation.

Furthermore, we made a comment on the underlying smooth problem solved by the method, which gives indications on the smoothness of the shapes arising form this framework. We have seen that this smoothness depends on the smoothness of both the planar projection and the guide curves, which can be generated with any usual modelling tool based on NURBS, T-spline and Bézier curves. Moreover, it was shown that marionette meshes give an intuitive illustration on the principle of subspace exploration, a powerful tool for constrained optimisation of meshes. The underlying smooth parameterisation of marionette meshes could hence open new possibilities for efficient parameterisation of fabrication-aware design space in structural optimisation problems.

Part III

Design space exploration and conclusion

I investigated the contours of an island, but what I discovered were the boundaries of an ocean.

Ludwig Wittgenstein

Chapter 6

Fabrication-aware structural optimisation of shell structures

The previous part introduced different methods for fabrication-aware shape generation without assessing their relevance for structural engineering applications. Conversely, the existing literature on shape optimisation of shell structures rarely considers fabrication. This chapter proposes to apply the marionette technique to the shape optimisation of shell structures and to merge fabrication and mechanical considerations. A benchmark comparing the marionette technique, presented in the preceding chapter, and NURBS modelling is hence performed and validates the potential of the marionette technique in applications to structural design.

6.1 Shape optimisation of shell structures

6.1.1 Design-space parametrisation

Parametric modelling is a popular approach used in the design of complexly shaped structures. In this section, we study parametric structural optimisation and more specifically, shape optimisation of shell structures. The proper parametrisation of the design space is indeed crucial for the reliability of the results. Opposing philosophies for domain parametrisation coexist, based on the number of degrees of freedom used in the optimisation problem.

CAD-based approach

Surface modelling is usually performed using Computer-Aided Geometric Design (CAGD). It is therefore natural to use the parameters generating the shapes for structural optimisation. This strategy was first introduced by Braibant and Fleury [46]. A common approach is to consider the surface as a linear combination of basis functions (e.g: NURBS) [10]. The shell thickness can also be considered as a design variable and can be encoded by NURBS as well. The parametrisation of such problems is thus light, as few design variables are required, typically a CAD-based parametrisation features less than 100 degrees of freedom: this makes sensitivity analysis easier to perform, and many algorithms can be used to solve small problems (gradient-based algorithms, variations of the simplex algorithm or even meta-heuristics like genetic algorithms, etc.). However we point out that the choice of the parametrisation is important because it can restrict the design space. Badly parametrised problems can potentially yield poor optima. This is surely a limitation in mechanical engineering, as well as for fabrication-aware design.

Node-based approach

The second parametrisation is to consider the data of the finite element model as design variables. Namely, node coordinates and shell thickness at nodes can be used, which involves a minimal modelling effort. The method is also called *finite element parametrisation* or *parameter-free optimisation* (which

should be understood as free of CAD-parameters). This point of view gives a very large design space, and better optima. However, the size of the design space has two drawbacks. First the problem is large and makes optimisation much longer than in CAD-based approaches. Sensitivity analysis is also harder to perform and requires experienced users and optimisation specialists. This disadvantage might be tempered by the increase of computational power, which makes the optimisation possible in a reasonable time. The second limitation, which is actually the biggest shortcoming of the finite element parametrisation, is that it leads to non-regular solutions, as illustrated in Figure 6.1. The 'optimal' result illustrated is distorted, so that the finite element analysis becomes unreliable. This explains that the method, although proposed early in the history of structural optimisation [86], was abandoned progressively. In order to deal with these limitations, new methods for regularisation and filtering have been introduced [84]. By implementing filter and choosing different filter radii, the designer can generate different optima.

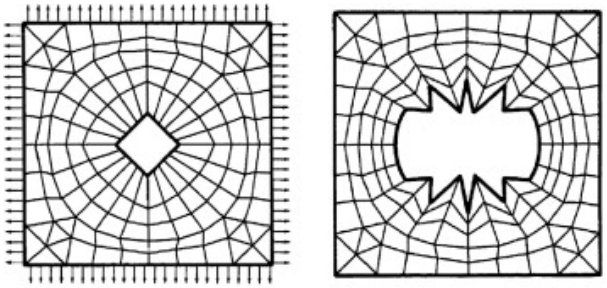

(a) Initial Design (b) Final Design

Figure 6.1 – Result of optimisation of a plate with a hole with a node-based parametrisation [46]

6.1.2 Handling fabrication constraints

Fabrication constraints are not usually considered in structural optimisation. In fact, no instance of geometrical constraint, like facet planarity, was found in our review on shape optimisation of shell or gridshell structures besides simple cases, like the optimisation of gridshells described with surfaces of translation [80, 270]. Fujita and Ohsaki considered the optimisation of shell by imposing constraints on surfaces invariants (for example a zero gaussian and developable surfaces) [88]. This point of view is different from the one adopted in architectural geometry, which considers that surface parametrisation is the key problem to be addressed for construction rationality. By definition, surface invariants do not depend on the chosen parametrisation: the method proposed by Fujita does therefore not give the ruling direction for developable surfaces and cannot be extended to the generation of PQ-meshes.

We shall make here a comment on how constraints are handled in optimisation and why existing techniques are not fully satisfying. We could view the fabrication constraint from a mathematical point of view. We consider a parametric space $\mathcal{S}$ of dimension n with parameters $\mathbf{x}$ and write g an operator (non necessarily linear), which encodes fabrication constraints. The constraint can be written as an equality constraint, which is the simplest case for the purpose of this discussion. The mathematical constraint reads as:

$$\forall i \in [0, p]\,, g_i\left(\mathbf{x}\right) = 0 \tag{6.1}$$

The optimisation problem, of the minimisation of a function f is therefore written as:

$$\min_{\mathbf{x}\in\mathcal{S}; g_i(\mathbf{x})=0} f\left(\mathbf{x}\right) \tag{6.2}$$

Typically, the planarity constraint corresponds to several thousands of constraints on a finite-element mesh. The most simple way to handle constraints is to use Lagrange's multipliers λ_i, which has p variables:

$$\min_{\mathbf{x}\in\mathcal{S},\lambda\in\mathrm{R}^p} L\left(\mathbf{x},\lambda\right) = \min_{\mathbf{x}\in\mathcal{S},\lambda\in\mathrm{R}^p} f\left(\mathbf{x}\right) - \lambda_i \cdot g_i\left(\mathbf{x}\right) \tag{6.3}$$

We see that we add p computations of gradient, which is not efficient for the kind of constraints we want to handle. Especially, in a CAD description of the design space, we have limited degrees of freedom and a much higher number of constraints, so there might not be a feasible design.

In practice, evaluation of Lagrange's multipliers is expensive. Constrained optimisation problems can be solved with other methods, for example by using the method of feasible directions. The method computes solutions that satisfy a constraint (which can be a fabrication constraint, as long as it can be expressed as an inequality). The method of feasible directions requires a feasible design as input and can be limited in spaces with a high number of constraints [82].

This brief discussion shows that handling multiple constraints is a tedious topic. The geometrical constraints envisioned in this dissertation are numerous: one constraint per face (and therefore thousands of constraints for a mesh used for finite element analysis). Usually, constraints in structural optimisation are related to maximal displacement or buckling loads for a finite set of load case combinations: their number remains therefore inferior to the envisioned constraints. In CAD-based approaches, the constraints on planarity of facets (or circularity, etc.) are far superior to the size of the design space and the problem might be over-constrained. The point of view taken by the marionette technique guarantees that the constraints are expressed as linear equations. Unfortunately, the planarity constraint in its more general formulation and the circularity constraints do not have the same properties. We might add that the smoothness of a PQ-mesh is not guaranteed, for reasons exposed in Section 2.3.3: PQ-mesh regularisation is also needed if a parameter-free optimisation is chosen. Integrating the fabrication constraints within the description of the design space $\mathcal{S}$ would avoid the handling of such complications and allow for a practical CAD-based approach.

6.1.3 Problem statement

The parametrisation of structural optimisation problems is crucial to the good performance of optimisation algorithms. Node-based approaches give good results, but require the end-user to have a good knowledge on regularisation and filtering, which should not be expected from a structural engineer or an architect. CAD-based approach considers fewer degrees of freedom: its results can more easily be understood by engineers, but they might not be true optima. In this chapter, we focus on the second approach in order to avoid regularisation problem.

Conciliating fabrication constraints with structural optimisation is not commonly done. With the tools and methods described in the second part of this dissertation, there is an opportunity for new description of design spaces for structural optimisation that would merge fabrication constraints and mechanical performance. This chapter presents practical implementation of the marionette method that is similar to NURBS and can be used easily by engineers. The relevance of the method compared to NURBS modelling is assessed with comparative studies and benchmarks. Since emphasis is made on the parametrisation of the design space, different optimisation algorithms are used.

In the spirit of form-finding by structural optimisation proposed by Ramm and Bletzinger [28], we propose to solve unconstrained optimisation problems and optimise the strain energy or linear buckling load. Section 6.2 presents the general methodology employed as well as the possibility to use the marionette technique in a CAD-based approach, comparable to NURBS modelling. Section 6.3 and 6.4 present comparative studies on domes and shell supported on three points. Section 6.5 proposes a discussion and an interpretation of the results.

6.2 Methodology: fabrication-aware structural optimisation

6.2.1 Design-space exploration by structural optimisation

The purpose of this chapter is to evaluate the potential of an innovative method for the structural optimisation of fabrication-aware design. The proposed methodology for this chapter is described in Figure 6.2 and relies on the shape generation of meshes with planar facets, the evaluation of their structural performance and their optimisation. The shape generation is described in Chapter 5. Two families of exploration strategies are envisioned to demonstrate the possibilities offered by Marionette meshes.

The first one considers a unique optimisation criterion and compares the results of optimisation both for the NURBS and Marionette method. Having a unique criterion makes the comparison of both design strategies more straight forward and some tendencies can be derived from this study.

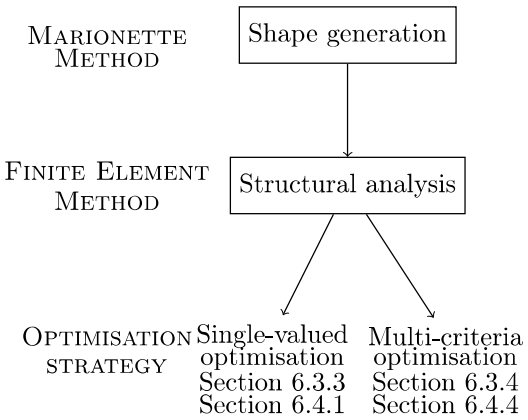

Figure 6.2 – Framework for the shape optimisation of shells

The second strategy considers several optimisation criteria. In real-life projects, engineers have indeed to deal with different constraints and have often opposing objectives. Solutions that satisfy all optimisation criteria at once do not generally exist, but design belonging to Pareto fronts are the most preferable options in practice. In conceptual design, global optimisation can be preferred to generate possibly unexpected efficient designs.

6.2.2 Marionette method as a CAD tool

Principle

We have seen in Chapter 5 that the marionette method can be used for the modelling of quadrangular meshes. The method is purely a mesh based approach, although we have already seen that it is the discrete version of a hyperbolic equation. Considering a regular mesh without singularity with $N \times M$ faces, there are $2\,(N+1)\,(M+1)$ degrees of freedom in the (XY) plane and $(N+M+1)$ degrees of freedom for the altitude of the guide curves. A mesh without planarity constraint has $3\,(N+1)\,(M+1)$ degrees of freedom. We can conclude that, for a mesh of given topology, the planarity constraints decreases the size of the design space by 30%.

The marionette technique can be adapted into a CAD tool similarly to NURBS. We propose here to parametrise the plane view by NURBS (or T-splines) and to use Bézier splines or other functions for the elevation curves. Consider Figure 6.3: the plane view is controlled by a NURBS patch with nine control points. The two elevations are Bézier splines with four and five control points respectively. The NURBS patch can be meshed by its isoparametric lines and the marionette method can be applied to the quadrilateral mesh. Notice that the marionette method naturally decouples the description of in-plane and out-of plane views. The number of control points used for the elevations and the in-plane view do not have to be consistent, like in the example of Figure 6.3. The number of degrees of freedom d of a pseudo-NURBS marionette mesh for a patch with $N \times M$ control points is thus:

$$d = 2NM + N_1 + N_0 \tag{6.4}$$

where N_0 and N_1 are the number of degrees of freedom for each elevation curve. In our example, there are thus $18+4+5 = 27$ degrees of freedom for the marionette mesh, which is the number of degrees of freedom of a NURBS patch with nine control points. Notice however that the two design spaces are different. This decoupling of horizontal and vertical description of the shape is a difference with NURBS modelling and can be an opportunity for structural optimisation. As an example, creases can be generated by modifying only the elevation, without adding unnecessary degrees of freedom for the plane view parametrisation.

Refinement strategies

Our proposition presents some advantages of NURBS modelling, in particular the possibilities of performing refinement. It is well-known that it is possible to perform degree elevation of a NURBS

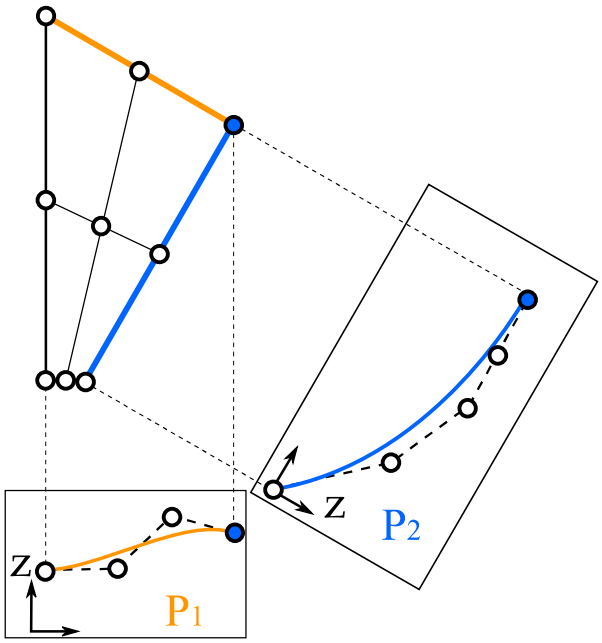

Figure 6.3 – The Marionette method as an alternative to NURBS.

surface via Forrest's algorithm. In other terms, it is possible to increase both the number of control points and the degree of the NURBS surface while preserving a shape. In optimisation, this means that one can start from a coarse control net for a NURBS surface, and perform iteratively operations of optimisation and degree elevation/refinement. This kind of strategy yields fast convergence and avoids the computation of local optima. Since marionette meshes as CAD tools are generated with NURBS patches and curves, this strategy of refinement can be used just like in NURBS modelling.

6.2.3 Choice of geometry

The comparison of the NURBS and marionette techniques is done on two geometrical configurations. The first case-study is a dome supported on an elliptical boundary. This shape does not feature free-edge, and is thus expected to have few local optima. It was chosen in reference to Monge's design for an ellipsoidal dome, and to investigations performed by the office Schlaich Bergermann und Partner on surfaces of translation.

The second case-study is a shell supported on three corners and with three free-edges. Several built examples allow for a comparison and problem initialisation. The first reference is the Kresge auditorium on the MIT campus, which has a spherical shape. It is a well-known building, but lesser known is the fact that due to poor understanding of the behaviour of the free-edges, the shell deflected badly and had to be repaired. The second built reference is the CNIT in Paris, which remains the largest spanning concrete structure to this day, and was constructed as a double-layer shell. It has also local corrugation, which is a rare feature in thin shell architecture, but can be found in other industries. Numerous numerical studies based on the geometry of the Kresge auditorium have been conducted. One of the first papers studying the possibilities offered by CAD-based description of the structural design space implemented this particular problem [28].

6.2.4 Structural analysis

Structural model

The model chosen for the shell is the Kirchoff-Love theory, which neglects the contribution of shear to the strain energy. The kinematic assumption made is that lines perpendicular to the mid-surface remain

straight (no warping) and perpendicular to the mid-surface. This theory is generally chosen for slender shells, as studied in this chapter. Writing t the thickness and R the radius of the mid-surface, a shell is considered to be thin if the ratio t/R is inferior to $1/20$ [186]. The stress are evaluated with the formula:

$$\begin{cases} N_{ij} = \int_{\frac{-h}{2}}^{\frac{h}{2}} \sigma_{ij}(z)\,\mathrm{d}z \\ M_{ij} = \int_{\frac{-h}{2}}^{\frac{h}{2}} z \cdot \sigma_{ij}(z)\,\mathrm{d}z \end{cases} \tag{6.5}$$

With the Love-Kirchoff theory, the kinematic assumption and the fact that materials with linear elastic behaviour are considered lead to the fact that σ varies linearly in z. Equation (6.5) can thus be used to compute the maximal stress by a simple integration, in the manner of what is done in Euler-Bernoulli beams. In reinforced concrete shells, the assumption of linear elasticity is not verified since concrete and reinforcement go in the plastic domain under ultimate limit state. The results on maximal stress should therefore be understood as qualitative indicators of the shell behaviour and not as design values.

Analysis

We use the finite element method to evaluate the structural behaviour. Two analyses are performed: linear elastic analysis and linear buckling analysis. The linear buckling analysis is the simplest performance metric considering geometrical non-linearity. Such effect is known to be determining for the design of slender structures, it is thus important to incorporate such considerations in optimisation. The case-studies are an occasion to illustrate the compromise between design criteria (geometrically linear or not) and to provide insight for the design of thin shell design.

Linear buckling suffers from some limitations: since the problem is linearised, we notice that the equilibrium is still computed on the initial configuration, so that linear buckling overestimates the bearing capacity of structures subject to high deflections before buckling. We should recall however that non-linear analysis without imperfection can be equally inaccurate [1].

Even without considering material non-linearities, a rigorous assessment of the bearing capacity of a shell is performed with a geometrically non-linear analysis with imperfection. The choice of the amplitude of the imperfection as well as its shape is not obvious, although the first buckling mode is often proposed. The analysis performed could have included imperfections and arclength analyses, but it was not performed due to the time necessary for the convergence. A more complete discussion on this topic is proposed in Section 7.2.3.

Loads, materials and boundary conditions

Different load cases are studied. The first one, later identified as $LC0$, is the self-weight of the shell, which can have an important contribution for large span structures. We will see that our models withstand such load with limited bending. The second load case considered in our study (written $LC1$) is a non-symmetrical load, for which the structure is subject to important bending moments. The pattern of the non-symmetrical load distribution is shown in Figure 6.4. A a pressure of 1kPa pointing downwards is applied globally to the areas coloured in blue. The material used has the properties of $C20/25$ concrete: its Young's modulus E is $30GPa$, its Poisson's ratio ν is 0.3, and its density is 2.2.

Performance criteria

A designer has several criteria as his or her disposal in order to evaluate the performance of a shell structure.

- the strain energy $\mathcal{E}$;

[1] To better understand this, consider an example given in the textbook written by Bathe [22]. An arch subject to a symmetrical load has a non-symmetrical first buckling mode. If no imperfection is applied, the load path preserves the symmetry and the arch will buckle following the second mode. In this case, the nonlinear analysis without imperfection gives a higher estimate of the buckling capacity than the linear buckling load. This problem vanishes as soon as a geometrical imperfection is added.

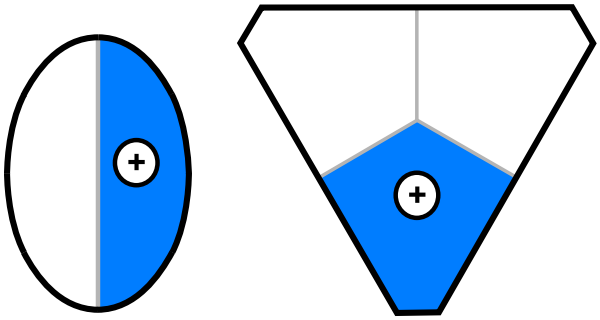

Figure 6.4 – Areas of application of non-symmetrical loads, top view

- the maximal tensile stress (for concrete shells) σ_{max};
- stress levelling which aims at specifying a stress state in the shell and to minimise the function $\int_S (\sigma - \overline{\sigma})\,\mathrm{d}S$;
- the maximal displacement under a design load δ_{max};
- the linearised buckling load;
- the mass;
- the limit load under geometric and material non-linear analysis.

Again, we stress that an optimisation problem is usually under some constraints so that mass minimisation under constraints of admissible displacement or stress has a practical interest. In mass minimisation problems under feasibility constraint, the governing constraint (displacement, buckling load, maximal stress) depends on the load case combination chosen, so that it is harder to come up with general statements. For that reason, in the followings, we consider maximal displacement, maximal tensile stress and linear buckling loads as performance criteria. By studying each performance metric separately, we aim at showing which formal strategy is chosen by the optimisation algorithm, so that an engineer could eventually use this information in practical applications.

Normalisation of criteria

In order to get more clarity when comparing optimisation algorithms, we will consider normalised values. The most efficient design regarding one criterion is assigned with the value 1. All the normalised values will be comprised between 0 and 1. The subscript $\sim$ indicates that the value is non-dimensional. The minimisation of maximal displacement is equivalent to the maximisation of its inverse, so that we create the following non-dimensional performance criterion:

$$\frac{1}{\underset{\sim}{\delta}} = \frac{\min \delta}{\delta} \tag{6.6}$$

Likewise, the normalised linear buckling load is defined as follows:

$$\underset{\sim}{p_{cr}} = \frac{p_{cr}}{\max p_{cr}} \tag{6.7}$$

The minimisation of the maximal tensile stress leads to the creation of a dimensionless value constructed from the highest and lowest value of σ found during exploration of the design space.

$$\underset{\sim}{\sigma} = \frac{\max \sigma - \sigma}{\max \sigma - \min \sigma} \tag{6.8}$$

Slenderness

Our study considers shells subject to both axial forces and bending. The relative value of the associated stiffness depends on the shell slenderness: this value has to be considered in our optimisation. Although thin shells are usually built in reinforced concrete, we adopt an isotropic shell model, in the following of the examples already cited in this dissertation. Writing $\mathcal{D} = D_{11} = D_{22}$ the bending stiffness and $\mathcal{A} = A_{11} = A_{22}$ the axial stiffness for an isotropic shell, we have the classical results:

$$\mathcal{D} = \frac{Et^3}{12\,(1-\nu^2)} \tag{6.9}$$

$$\mathcal{A} = \frac{Et}{(1-\nu^2)} \tag{6.10}$$

Introducing L the span of the shell, the non-dimensional ratio $\frac{\mathcal{D}}{L^2\mathcal{A}}$ is given by:

$$\frac{\mathcal{D}}{L^2\mathcal{A}} = \frac{1}{12}\left(\frac{t}{L}\right)^2 \tag{6.11}$$

Our study is based on fixed boundary conditions, we have to consider different shell thickness in order to explore plausible optimisation problems. This is especially the case for the dome with free-edges, where the bending stiffness of the edge can have an influence on the structural response. We choose thus two values for $\frac{t}{L}$ based on realistic values for the shell with free edge: $\frac{1}{250}$ and $\frac{1}{1000}$. These values might seem low, but we consider optimised shells, which can be highly efficient: such slenderness can be commonly reached. To get a point of comparison: the shell of the Kresge Auditorium has a span of 48 meters, and a thickness at the apex of 9.8 centimetres and a maximal thickness of 14 centimetres. Its slenderness is thus approximately 1/500. The effect of slenderness is less critical for the dome, which does not have free-edge. One slenderness of $\frac{t}{L} = \frac{1}{400}$ was thus chosen.

6.2.5 Derivative-free optimisation

We use derivative-free optimisation algorithms for the single-valued optimisation problems[2] (see Table 6.1). The optimisation algorithms are the one of the NLOpt library [119]. This library was used in structural optimisation by [55], where a comparison of the relative performance of all the algorithms is performed. More specifically, we use the plug-in Goat for Grasshopper, which interfaces the NLOpt library with the environment of Grasshopper.

Optimisation strategy	Algorithm
Local	Constrained Optimization by Linear Approximation - COBYLA [201]
	Bounded Optimization by Quadratic Approximation - BOBYQA [203]
	Subplex - SBPLX [213]
Global	Dividing Rectangles Method - DIRECT [120]
	Controlled Random Search - CRS2 [122]

Table 6.1 – Optimisation algorithms implemented in NLOpt used in this comparative study.

A review of derivative-free algorithms is done by Powell, who invented the COBYLA and BOBYQA algorithms used in this chapter [202]. From his point of view, such algorithms are suited for optimisation of problems with up to 100 parameters. This is in accordance with the size of problems we are aiming to solve in a CAD-based description of the design space, where the number of parameters is relatively low.

[2] Gradient-based algorithms could be used as well, but the finite element analysis software used in this work does not give access to gradient. Finite difference scheme would have had to be used, which would increases considerably the number of function calls. Isogeometric analysis is an adequate tool for exact gradient estimation with NURBS modelling. Isogeometric formulations for Love-Kirchoff shell model exist [127], but an isogeometric formulation of the marionette technique would need to be implemented. Gradient-based algorithms could be studied in future work.

Description of algorithms

In the following, we will refer to the algorithms by their acronym. We present here a brief description of their principle.

Constrained Optimization by Linear Approximation - COBYLA The COBYLA algorithm is an algorithm for constrained optimisation problems. We refer here to the definition by Powell of his algorithm in [202]. *'The COBYLA software [201] constructs linear polynomial approximations to the objective and constraint functions by interpolation at the vertices of simplices (a simplex in n dimensions is the convex hull of $n+1$ points, n being the number of variables).'* At each step of the optimisation, a linear programming problem is solved, its result is then evaluated and its value is used to improve the linear approximation.

BOBYQA algorithm BOBYQA algorithm was also invented by Powell [203]. Its principle is similar to COBYLA, but it performs quadratic approximation instead of linear approximation.

Subplex - SBLX Subplex[3] is a simplex searching algorithm and is a variation of the well-known Nelder-Mead algorithm [213].

DIRECT algorithm This algorithm samples the search space and creates hyper-rectangle, based on function evaluations, it identifies potentially optimal hyper-rectangles decides where to subdivide for the next step [120]. DIRECT is a global algorithm and eventually converges to the global optimum. The number of function calls can however be important, but it remains an efficient algorithm in its category [81].

Controlled Random Search - CRS2 Controlled random search is often compared to evolutionary algorithms. It shares some similarities with them: it starts from a random population and explores the design space by heuristic method, based on Nelder-Mead simplex algorithm [122].

Convergence criterion

Optimisation algorithms usually run uninterruptedly if a stopping criterion is not set. Such criterion can be based on a maximal running time or a maximum number of iterations. In our study, we restricted the optimisation time to 10 minutes for one optimisation run based on elastic linear analysis and 20 minutes for linear buckling analysis. An additional convergence criterion on the relative change of the optimum between two optimisation steps is set to 0.001. The maximal running time considers practical applications: in conceptual design stages, an engineer cannot spend much time on analysis and requires a quick feedback. The local algorithms regularly converged under 10 minutes, but global algorithms converge much more slowly because they explore the whole design space.

6.2.6 Multi-criteria optimisation

Guiding principles

In engineering practice, the designer has to make compromise between different optimisation criteria. Many competing methods exist, for example scalarisation aims at formulating a single-valued optimisation problem by aggregating the different objectives into one functional. The functional has to be constructed so that the minimum lies within the Pareto front. Another strategy is to use evolutionary optimisation. Evolutionary optimisation makes an analogy with the theory of evolution and natural selection. Starting from a random population, the individuals are selected based on their fitness and can reproduce for the next generation. The advantage of evolutionary algorithm is the diversity they can generate compared to scalarisation techniques.

[3]The implementation of Steven G. Johnson differs from Rowan's and gave it another name in NLOpt (SBPLX), due to Rowan's preference. In the following, we will write about the subplex algorithm as implemented by Johnson.

In multi-criteria optimisation, the choice of the fitness function is not straight forward. There are different aspects:

- *Dominance rank:* how many individuals dominate a given individual?
- *Dominance count:* how many individuals are dominated by a given individual?
- *Dominance depth:* at which front is an individual located?

The computation of all dominance indicators can be expensive if there are many individuals in the population. Multi-criteria optimisation can become very difficult when there are many objectives. Indeed, for a given population size, the proportion of individuals which cannot be compared increases with the number of objectives. One indicator has gained popularity to overcome this difficulty: the hypervolume indicator. In a case where we aim at maximising all objectives, we can compute the hypervolume of the set dominated by the Pareto front, like shown in Figure 6.5. Adding a point to the front increases the hypervolume of the grey area, so that the indicator is a single-value objective to maximise.

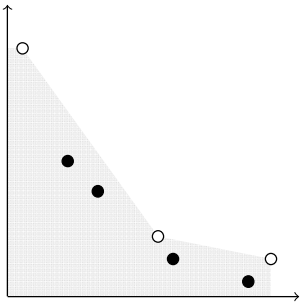

Figure 6.5 – Pareto front (white dots) and the associated hypervolume.

In the followings, we use an evolutionary algorithms using the hypervolume method. We use the HypE reduction and HypE mutation methods that address specific issues linked to the computation of hypervolumes in high dimension, although we deal mainly with few objectives [14]. The software used is Octopus for Grasshopper, which implements those algorithms.

Convergence criterion

Multi-objective optimisation (MOO) is used as a tool to compare in detail two design spaces. The maximal running time is set to 15 hours so as to guarantee a good representation of the Pareto front. We will see that the Pareto front found by multi-objective optimisation contains better solutions than what was found by single-objective optimisation. The reader should not attach too much importance on the difference between the performance of the two strategies, since one of them ran much longer and was used as a reference for comparison of the design spaces.

6.2.7 Comparison of the methods

Our methodology is based on the use of different optimisation algorithms. For each model (NURBS or marionette), the algorithms find different optimal values. Likewise, a same algorithm (for example COBYLA) will find two different optima for the NURBS or the marionette model. We want to assess whether the choice of the marionette method has an impact on the performance of optimisation algorithms.

For a non-dimensional performance criterion $\widetilde{a}$, we compare the average of $\left(\widetilde{a}_{Marionette} - \widetilde{a}_{NURBS}\right)$ to the standard variation s for all the realisations of $\widetilde{a}$. We define the dispersion indicator Δ as:

$$\Delta\left(\widetilde{a}\right) = \begin{cases} 0 \text{ if } s\left(\widetilde{a}\right) = 0 \\ \dfrac{< \widetilde{a}_{Marionette} - \widetilde{a}_{NURBS} >}{s\left(\widetilde{a}\right)} \end{cases} \tag{6.12}$$

The number Δ has a qualitative interpretation. First, notice that σ^* is always positive, so that positive values of Δ indicate that the marionette models perform better *on average*. If Δ is close to zero, then the marionette and NURBS model have similar performance. If the absolute value of Δ is larger than 1, this means that the difference between marionette and NURBS models is statistically significant. We are interested in normalised data (between 0 and 1), the absolute value of $\left(\widetilde{a}_{Marionette} - \widetilde{a}_{NURBS}\right)$ cannot exceed 1. Intuitively, the case with the greatest dispersion is when $\widetilde{a}$ take two distinct values $\widetilde{a_0}$ and $\widetilde{a_1}$ for the marionette and NURBS models. In such case, the only contribution to the standard deviation is due to the difference between the marionette and NURBS model. In this case, it is simple to compute Δ, writing n the number of algorithms tested, we have:

$$\Delta = \frac{n\left(\widetilde{a_1} - \widetilde{a_0}\right)}{\sqrt{2n\left(\frac{\widetilde{a_1} - \widetilde{a_0}}{2}\right)^2}} = 2 \cdot \text{sign}\left(\widetilde{a_1} - \widetilde{a_0}\right) \tag{6.13}$$

We thus gave an argument showing that Δ is bounded as follows:

$$-2 < \Delta\left(\widetilde{a}\right) < 2 \tag{6.14}$$

A more involved calculation can show that the considered configuration corresponds to a local extremum of Δ. Note that the absolute value of Δ does not indicate how much a model outperforms the other (in equation 6.13, the amplitude of $\left(\widetilde{a}_1 - \widetilde{a}_0\right)$ does not influence the value of Δ). The value of Δ simply indicates whether or not the difference between marionette and NURBS is statistically significant. To quantify the difference, we use the mean relative variation e which is defined by equation (6.15).

$$e\left(\widetilde{a}\right) =< \frac{\widetilde{a}_{Marionette} - \widetilde{a}_{NURBS}}{\widetilde{a}_{NURBS}} > \tag{6.15}$$

6.3 Shape optimisation of a dome

6.3.1 Geometric and mechanical constraints

The first case-study is a shell supported on a closed curve defined as a quadratic Bézier spline. Its topology is represented in Figure 6.6. It has a width of 40 meters and a length of 57 meters. The problem has two axis of symmetry, so that we can focus on one quarter of the structure. The NURBS model is generated with two NURBS patches, the plane view of the marionette mesh is generated with two NURBS patches as well. The elevation curves of the marionette mesh are represented in light orange in the middle of Figure 6.6. The parametrisation is kept as simple as possible: the two NURBS patches have both 3×3 control points and they share a common boundary, so that there are 15 control points in total. The notations for the control points are given in Figure 6.6.

We do not allow for normal discontinuities in the problem, so that some constraints on the positions of the control points arise. Table 6.2 shows the degrees of freedom for the NURBS and Marionette technique. All the points with the subscript 2 are fixed, both in the NURBS and Marionette models, and are not shown in the table. The sign $-$ indicates a constraint enforced by the symmetries of the problem. For example, the points $\mathbf{B_1}, \mathbf{C_1}, \mathbf{D_1}$ have to be aligned in order to guarantee a C^1 continuity of the surface parametrisation. There are 6 degrees of freedom in the plane view for both models and two degrees of freedom on the elevation for the NURBS.

The elevation curves of the marionette mesh are represented in orange in Figure 6.6. One elevation is constrained by the boundary. The other elevation is a curve crossing the boundary. It is represented as a

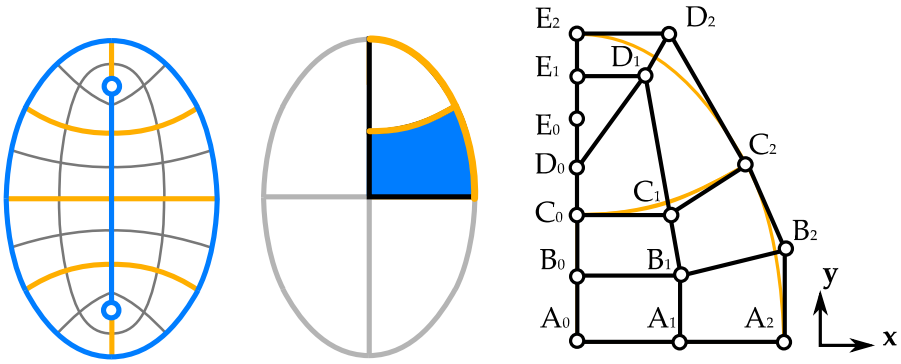

Figure 6.6 – Parametrisation of the elliptic dome

	$\mathbf{A_0}$	$\mathbf{A_1}$	$\mathbf{B_0}$	$\mathbf{B_1}$	$\mathbf{C_0}$	$\mathbf{C_1}$	$\mathbf{D_0}$	$\mathbf{D_1}$	$\mathbf{E_0}$	$\mathbf{E_1}$
Marionette	Fixed	x	y	$\mathbf{A_1}.x, \mathbf{B_0}.y$	y	$x, \mathbf{C_0}.y$	y	–	y	y
NURBS	z	$x, \mathbf{A_0}.z$	y, z	$\mathbf{A_1}.x, \mathbf{B_0}.y, \mathbf{B_0}.z$	y	$x, \mathbf{C_0}.y, z$	y	–	$y, -$	$y, -$

Table 6.2 – Degrees of freedom for the marionette and NURBS model in the dome problem.

quadratic Bézier spline. The continuity between patches creates one degree of freedom. The marionette mesh model has 7 degrees of freedom, whereas the NURBS model has 8 degrees of freedom. They are therefore expected to have similar performances.

6.3.2 Initialisation

The two models are initialised with similar geometry and similar performance criteria. The initial value is expected to be efficient: it has a parabolic section with a moderate rise-over span ratio ($\frac{h}{L} = 25\%$). The continuity between patches guarantees load transfer between patches. Figure 6.7 shows the initial geometries for the NURBS and marionette meshes. They are visually very close and their mechanical performances are similar.

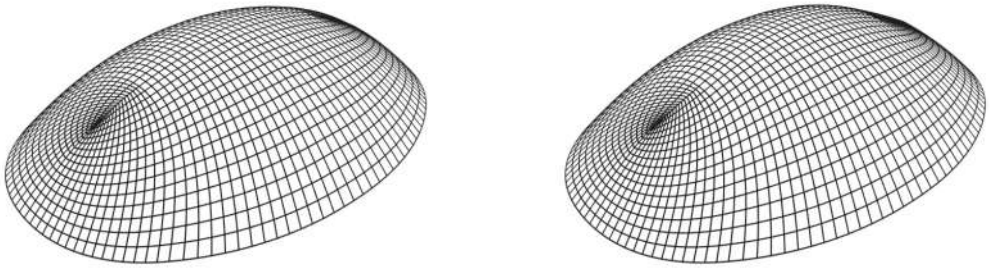

(a) Marionette mesh (b) NURBS

Figure 6.7 – Initial geometries for the domes.

6.3.3 Single-criteria optimisation

We present first results on single-criteria optimisation with the non-dimensional performance criteria defined in Section 6.2.4. The initial values are also shown for comparison. The relative performance of the different algorithms is discussed. Because we focus on several performance criteria, we provide a multi-criteria cartography and optimisation in the next subsection.

General comments

Figure 6.8 displays the optimal results for the minimisation of the maximal displacement. The initial design was already efficient. The best optimisation algorithm reduces the maximal displacement by more than 30%, which is a considerable improvement. The Marionette models yield in general better performances than NURBS models, although the best optimum is found in the NURBS design space. The different algorithms have similar performances for the Marionette method, but they have varying quality in the NURBS design space. The dispersion coefficient is positive and close to one which indicates that on average, Marionette outperforms NURBS. The relative difference between the Marionette and NURBS model is of 13%.

$$\Delta\left(\frac{1}{\tilde{\delta}_0}\right) = 0.97 \tag{6.16}$$

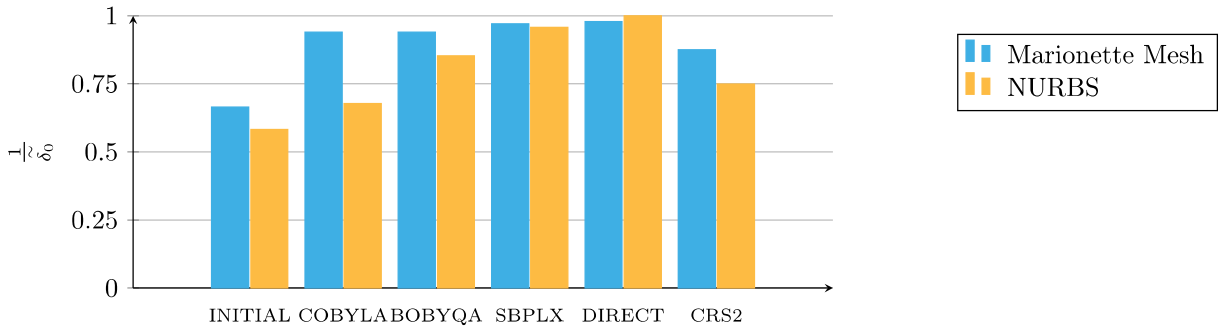

Figure 6.8 – Optimal values found for the minimisation of the maximal displacement under self-weight.

The minimisation of the maximal displacement under non-symmetrical loads gives more diverse results. The optimal designs cover a wide range of performance: the choice of the optimisation algorithm influences the final results, especially for the NURBS model. The results of optimisation are shown in Figure 6.9. The optimisation with marionette models outperforms clearly the optimisation with NURBS models, as shown by the indicator of dispersion computed in equation (6.17). The mean difference e is of 145%, so that the tendency is much more visible than for the optimisation of displacement under self-weight.

$$\Delta\left(\frac{1}{\tilde{\delta}_1}\right) = 1.56 \tag{6.17}$$

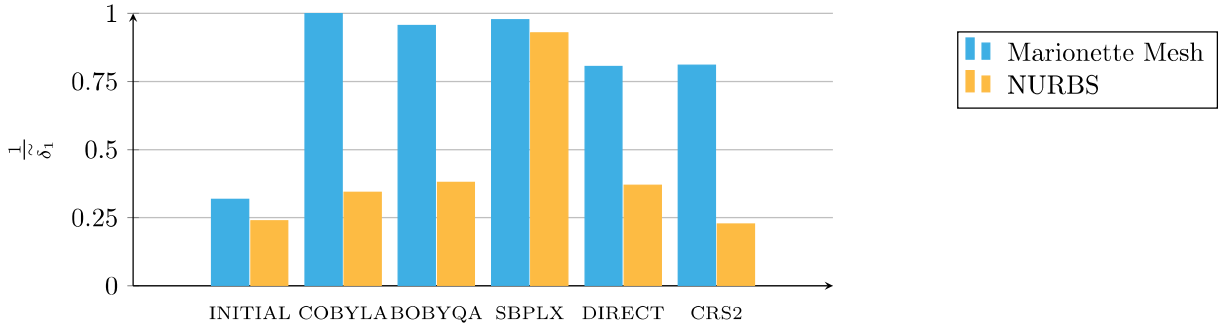

Figure 6.9 – Optimal values found for the minimisation of the maximal displacement under non-symmetrical load.

The maximisation of the buckling load improves the initial design significantly. The linear buckling load is indeed increased by a factor of 50% after optimisation. This is an important improvement in the context of slender structures, which are usually designed regarding non-linear criteria. We might add that engineers can lack of intuition when facing non-linear behaviour of structures. Optimisation can play an important role for the improvement of the design of structures sensitive to instabilities. The marionette mesh clearly outperforms the NURBS model for the COBYLA and CRS algorithms, which is illustrated by the dispersion coefficient.

$$\Delta\left(\widetilde{p_{cr}}\right) = 1.01 \tag{6.18}$$

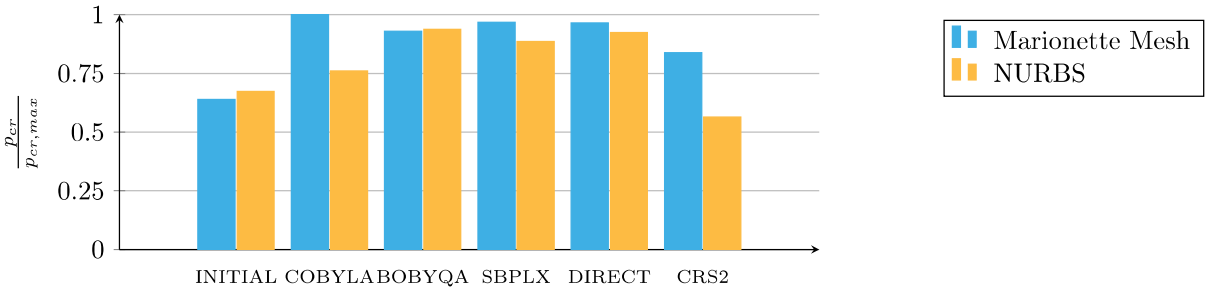

Figure 6.10 – Optimal values found for the maximisation of linear buckling load under self-weight.

Figure 6.11 shows the dimensionless tensile stresses after optimisation of both structures. There is no clear difference between the marionette and NURBS models, although the optimal designs with NURBS parametrisations have a better performance on average:

$$\Delta\left(\widetilde{\sigma_{max}}\right) = -0.41 \tag{6.19}$$

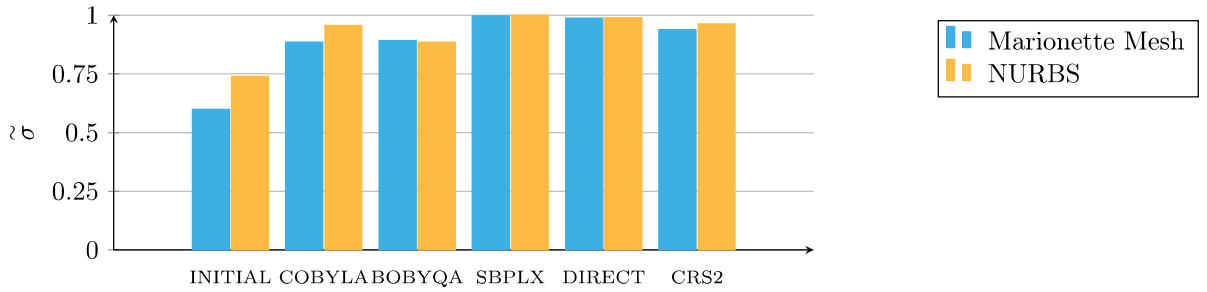

Figure 6.11 – Optimal values found for the minimisation of the maximal tensile stress under self-weight.

We should comment the absolute values found by this last optimisation as well. The minimisation of the maximal tensile stress shows that both marionette and NUBRS design spaces are wide enough to find compression-only solutions under self-weight. The SBPLX algorithm finds indeed configurations with compression-only structures. The DIRECT algorithm also finds near zero maximal tensile stress. The other algorithms do not succeed in eliminating tension in the structure, but decrease drastically the maximal tensile stress compare to the initial design.

Relative performance of the algorithms

The results of optimisation show that the algorithms have different performances. The coefficient of variation for the whole data set is of 6.0% for marionette meshes and 24.6% for NURBS models. This means that NURBS models are more sensitive to the choice of the optimisation algorithm. For example, for the minimisation of energy under non-symmetrical load, the relative difference between the worst

Figure 6.12 – Optimal values found for the minimisation of the maximal tensile stress under self-weight.

and best optimum is of 20% for the marionette model and superior to 300% for the NURBS model. There is no simple rule that would allow to select the best optimisation algorithm. We introduce a measurement for the comparison of optimality of algorithms and call an optimum with non-dimensional performance criterion superior to $n\%$ an $n\%$ optimal design. Table 6.3 shows the number of times that an algorithm succeeds in finding the $n\%$ optimal design. There are 4 optimisation problems solved (one for each objective function), each algorithm being run both on the marionette and NURBS design space, the maximal value within the table is of 8. SBPLX and DIRECT seem to dominate the other algorithms, but they can eventually fail to give an optimal design. For example, DIRECT finds very poor optima for the minimisation of displacement under non-symmetrical load.

	COBYLA	BOBYQA	SBPLEX	DIRECT	CRS2
100% optimal design	2	0	1	1	0
99% optimal design	2	0	2	3	0
95% optimal design	3	1	6	5	1
90% optimal design	4	4	7	6	2

Table 6.3 – Relative performances of optimisation algorithms: count of near optimal designs.

Interpretation of the results

The best optima found for the marionette and NURBS design spaces are shown in Figure 6.13. The optima of the NURBS and Marionette design spaces are visually similar, except for the minimisation of maximal tensile stress. The minimisation of energy under non-symmetrical load leads in both cases to an increase of the rise, the rise-over-span ratio reaching finally 50%. This noticeable change in the geometry might explain the various performances of the different optimisation algorithms. In other optimisations, the rise-over-span ratio remains limited to 25%. The in-plane parametrisation changes between the different optima, although it is not as immediate to see its influence. The most simple parameter to interpret is the position of the umbilical point, which tends to move away from the support after optimisation.

Comparison of Marionette and NURBS

The optimisation of NURBS and Marionette meshes shows some differences between the design spaces. There is indeed a significant dispersion for three of the chosen objective functions. It can be attributed to variations of the performance of optimisation algorithms for the NURBS parametrisation. Getting rid of the few outliers reduces greatly the dispersion Δ. We should state that besides those outliers, the NURBS and Marionette design space are highly similar. The optima of the marionette design space and of the NURBS design space are very close (they are all within a 5% range), so that differences between NURBS and Marionette can be attributed to the way algorithms tend to the optimum rather than on the value of the respective global optima themselves. This issue is not studied often, as literature on optimisation usually evaluates one specific optimisation algorithm to various problems. We show here that studying

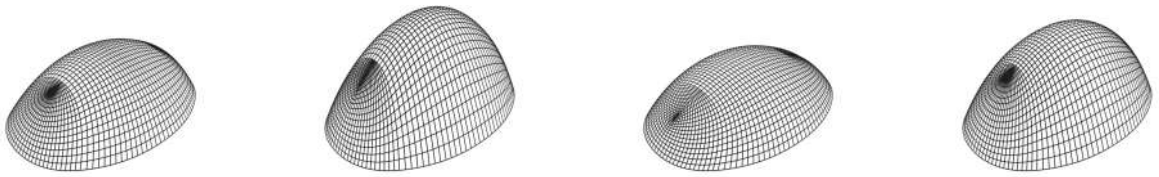

(a) Marionette, optimal δ_0 (b) Marionette, optimal δ_1 (c) Marionette, optimal buckling (d) Marionette, optimal σ

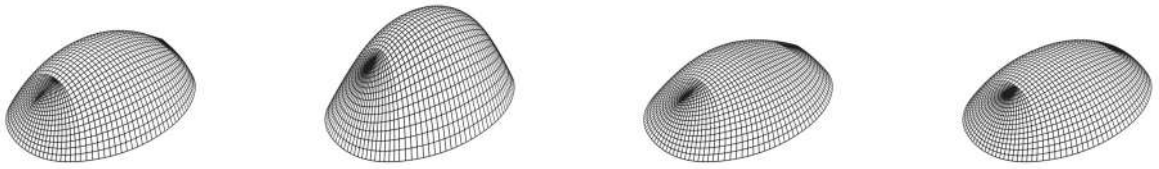

(e) NURBS, optimal δ_0 (f) NURBS, optimal δ_1 (g) NURBS, optimal buckling (h) NURBS, optimal σ

Figure 6.13 – Geometry of the best optima for each objective for the dome.

various algorithms for a same problem can lead to different optima, and that the choice of optimisation algorithm is a very sensitive topic. This fact lead to the contribution of Clune on appropriate algorithm selection for optimisation [55]. We propose a qualitative explanation on how optimisation algorithms explore the marionette design space in Section 6.5.

6.3.4 Multi-criteria optimisation

Single-objective optimisation gives a partial information about the performances of a design. For example, a solution that minimises the strain energy does not necessarily have a high buckling load. In this section, we represent the results of multi-objective optimisation in order to highlight areas of compromise. Figure 6.14 shows the Pareto front computed for the maximale tensile stress σ_{max} and the critical buckling factor λ under self-weight.

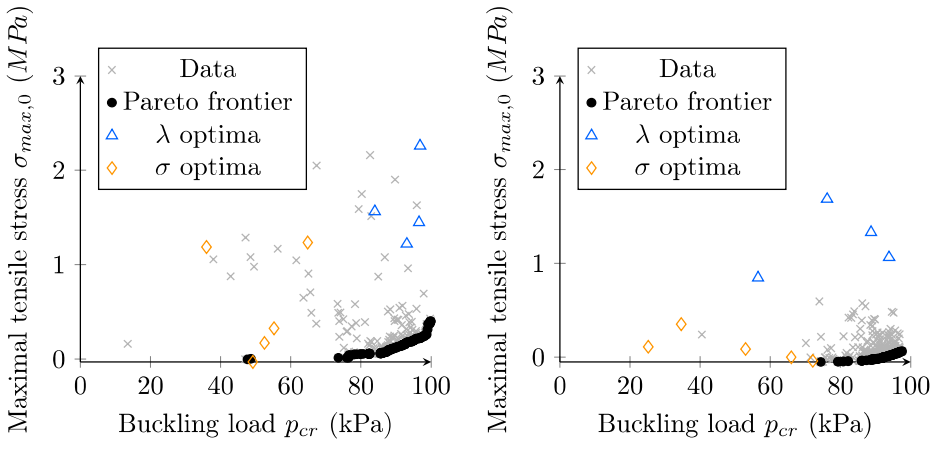

(a) Marionette design space (b) NURBS design space

Figure 6.14 – Multi-criteria optimisation

The results of single-valued optimisation are also added in the graph. Notice how optima for stress minimisation have a low buckling capacity in the NURBS design space. The comparison of the two Pareto fronts confirms the results of single-valued optimisation in the sense that the NURBS design space provides better optima for the minimisation of the maximal stress, whereas the marionette design space provides

better optima for the maximisation of buckling. The horizontal line in Figure 6.15 represents the minimal tensile stress in the marionette design space. The vertical line represents the maximal buckling load in the NURBS design space. It can be noticed that no Pareto front dominates entirely the other. Many points of the marionette frontier are dominated by the NURBS frontier because of the maximal tensile stress (some Pareto optima of the NURBS design space are below the horizontal line). Some points of the marionette frontier dominate the NURBS frontier because of a high linear buckling load (they are on the right of the vertical line). The distance between the two frontiers in the σ component is of $0.1MPa$. Since we are dealing with realistic loads, span and construction materials, such a difference can be considered as negligible from an engineering perspective. The maximal tensile stresses found by optimisation are indeed extremely low and inferior to the tensile strength of concrete for both design spaces. Likewise, the difference between linear buckling load is of a few percent only.

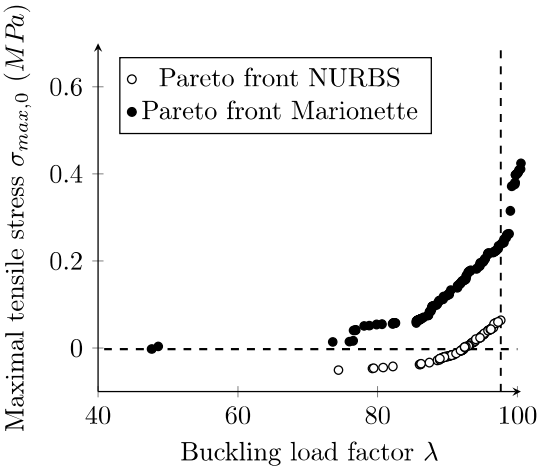

Figure 6.15 – Comparison of the Pareto fronts $(\mathcal{E}, \sigma)$ of the two design spaces.

The multi-objective optimisation shows that the Pareto fronts of the marionette and NURBS models are highly similar. The differences observed during single-valued optimisation seem to be linked to the performance of algorithms themselves rather than by differences between the NURBS and Marionette framework.

To go further, we study another multi-criteria optimisation problem: the minimisation of strain energy and maximisation of linear buckling load. Figure 6.16 represents the Pareto front found by evolutionary algorithm for the marionette framework together with the optima found by single objective optimisation which have been discussed before. Those optima are close to the Pareto frontier. The non-pareto data from the last generation is represented with grey crosses.

Figure 6.17 shows the Pareto front for the same objectives and the NURBS design space. The shape and amplitude of the Pareto front are comparable with the one of the Marionette design space. The optimal values of single-objective optimisation with the NURBS design space are also shown. It can be noticed that those optima are far away from the Pareto front compared to what is observed in Figure 6.16. This confirms our interpretation stating that 'true' optima of the marionette design space are not necessarily better, but they are easier to reach by single-objective optimisation algorithms in the case of the ellipsoidal dome.

The comparison of the two Pareto fronts is shown in Figure 6.18. The two fronts are close to each other for low values of δ_0: the NURBS front dominates then the front of the marionette design space (for p_{cr} between $80kPa$ and $95kPa$.The front of the marionette design space dominates the front of the NURBS design space for high values of p_{cr}. The vertical dashed line represents the maximal buckling load found in the NURBS design space.

The multi-objective optimisation demonstrates that the two design spaces have similar performance, and that a wide variety of designs can be selected following the structural imperatives. Both design spaces can yield structures with limited or non-existent tensile stress under self-weight. The differences revealed

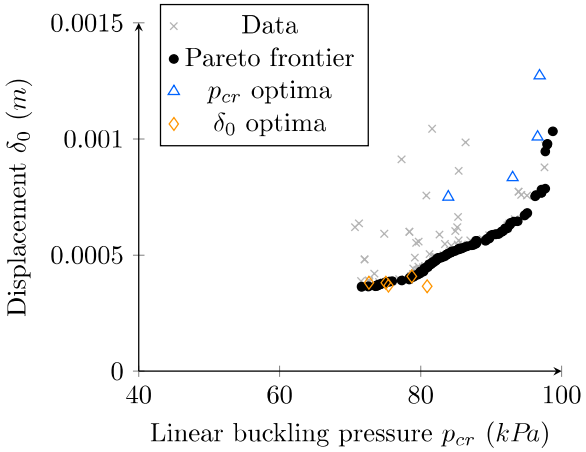

Figure 6.16 – Pareto front for the objectives 'maximal displacement' and 'linear buckling load' for the marionette design space.

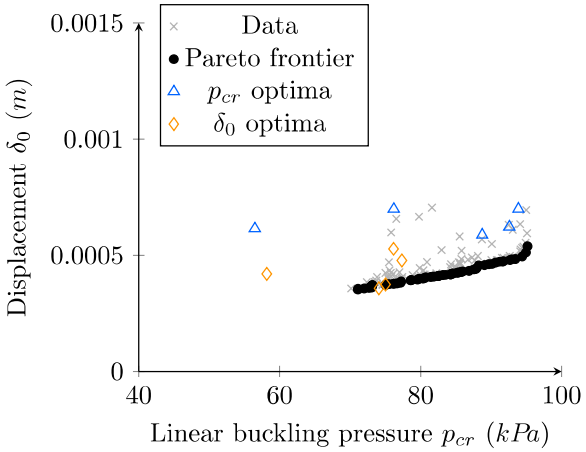

Figure 6.17 – Pareto front for the objectives 'maximal displacement' and 'linear buckling load' for the NURBS design space.

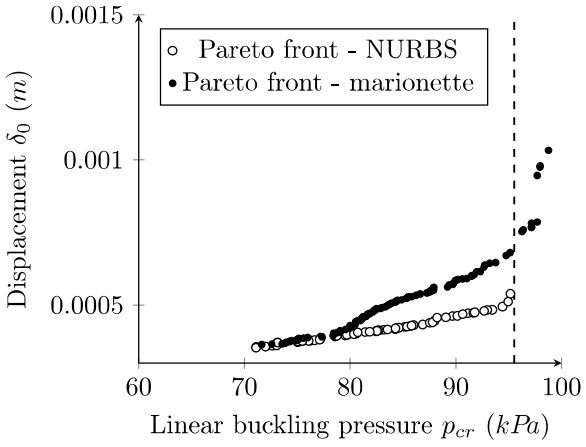

Figure 6.18 – Comparison of the Pareto fronts (p_{cr}, δ_0) of the two design spaces.

by single-valued optimisation are not necessarily found in this detailed analysis. The logical conclusion is that the marionette design space set in this comparative study is easier to explore with single-valued optimisation algorithms under time constraint. We propose now to study a second example in order to confirm these first observations on optimal shell design.

6.4 Shape optimisation of a shell with free-edges

6.4.1 Geometric and mechanical constraints

The second case study focuses on a shell supported on three corners. The geometry of the shell is illustrated by Figure 6.19. The shell has a span arbitrarily set to 130 meters. The geometry has six planes of symmetry and can be decomposed into six domains without singularity, where the marionette technique can be applied. The symmetry is chosen here to simplify the modelling and reduce the number of variables. The NURBS models are built from patches of degree 2 with 9 control points. The planar view of the marionette meshes is built with the same kind of patch, whose control points are shown in Figure 6.19. The orange area shows the admissible area for the supports of the structure (where $z = 0$). The shapes are trimmed with a horizontal plane.

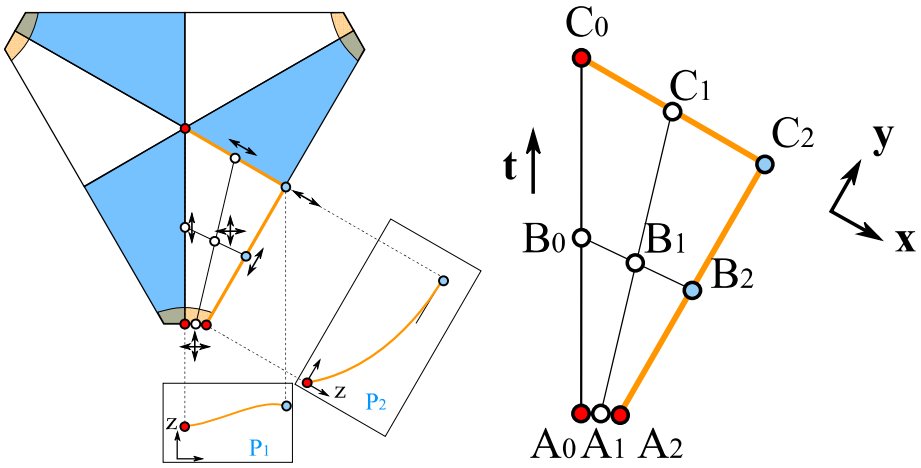

(a) Overall plane view (b) Plane view of one patch

Figure 6.19 – Parametrisation of the CNIT problem with the marionette technique

Like for the dome, the symmetry implies some constraints to the position of the control points. We recall the constraints in Table 6.4: notice that NURBS and marionette parametrisations have the same number of degrees of freedom in the plane, but that the planarity constraint reduces the number of parameters encoding vertical position of control points.

	$\mathbf{A_0}$	$\mathbf{A_1}$	$\mathbf{A_2}$	$\mathbf{B_0}$	$\mathbf{B_1}$	$\mathbf{B_2}$	$\mathbf{C_0}$	$\mathbf{C_1}$	$\mathbf{C_2}$
Marionette	Fixed	x, y	Fixed	t	x, y	x, y	Fixed	x	$\mathbf{C_2}.x = \mathbf{B2}.x$
NURBS	t	x, y	Fixed	t, z	x, y, z	x, y, z	z	x, z	$\mathbf{C_2}.x = \mathbf{B_2}.x$, $\mathbf{C_2}.z = \mathbf{B_2}.z$

Table 6.4 – Degrees of freedom for the marionette and NURBS model in the CNIT problem.

The marionette and NURBS models have 8 and 9 degrees of freedom in the horizontal plane respectively. The elevations of the marionette mesh are controlled with quadratic and cubic Bézier splines drawn in Figure 6.20. In plane P_2, we impose horizontal tangency at the crown, which leaves two degrees of freedom: the height of the crown h and the slope at $\mathbf{A_2}$. In plane P_1, we do not impose restrictions on tangency, which leaves three degrees of freedom: the height of three control points. We recall that a

cubic spline with control points ($\mathbf{P_i}$) and parameter t (between 0 and 1) is given by following equation:

$$\mathbf{B}(t) = (1-t)^3 \mathbf{P_0} + t \cdot (1-t)^2 \mathbf{P_1} + t^2 \cdot (1-t) \mathbf{P_2} + t^3 \mathbf{P_3} \tag{6.20}$$

For marionette meshes, the (x, y) components are determined by the planar view. Equation (6.20) has to be modified. We retrieve the corresponding u value of each raised point on the NURBS patch and create a normalised parameter $\overline{u}$ between 0 and 1. We introduce the altitudes of the control points z_i, so that for each point to raise $(x(\overline{u}), y(\overline{u}), 0)$, we can assign an elevation:

$$z(\overline{u}) = (1-\overline{u})^3 \cdot z_0 + \overline{u} \cdot (1-\overline{u})^2 z_1 + \overline{u}^2 \cdot (1-\overline{u}) z_2 + \overline{u}^2 \cdot z_3 \tag{6.21}$$

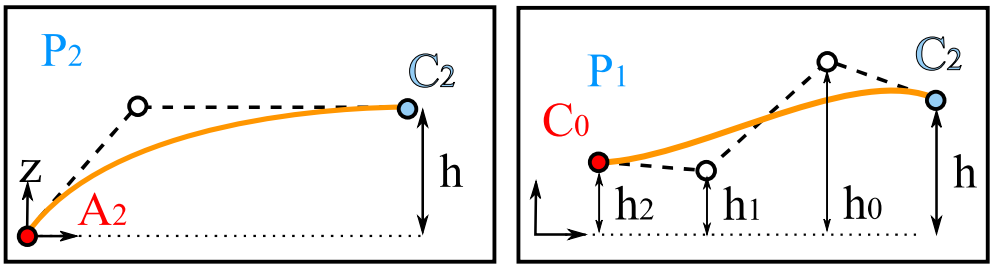

Figure 6.20 – Parametrisation of elevations for the marionette method.

In total, the marionette mesh and NURBS model both have 15 parameters. The size of the design space is identical due to enrichment of the description of the elevations for the marionette technique.

Supports We have defined an area of admissible location of the supports. Small changes of the shape of the support can indeed radically change the behaviour of a shell, and investigations on this aspect were of interest. Some shapes generated with the NURBS or marionette method do not fit within the prescribed domain (delimited by a line). We deal with this issue by using a penalty method. For a shell with parameter $\mathbf{x}$, we have a constraint on the support $d(\mathbf{x}) \leq 0$. A quadratic penalty is added to the initial objective function to minimise $f(\mathbf{x})$:

$$f^*(\mathbf{x}) = f(\mathbf{x}) + \mu g(\mathbf{x}) \tag{6.22}$$

where

$$g(\mathbf{x}) = \begin{cases} 0 \text{ if } d(\mathbf{x}) \leq 0 \\ d(\mathbf{x})^2 \text{ if } d(\mathbf{x}) > 0 \end{cases} \tag{6.23}$$

The scalar μ is a penalty factor, which is set arbitrarily to 1000. The initialisation is a feasible design, and we verified that all the algorithms converged indeed to feasible designs.

6.4.2 Initialisation

Local optimisation algorithms are sensitive to the initial position. We considered an initialisation with similar performances for NURBS and marionette meshes. Because NURBS patches are not necessarily parametrised by conjugate curve network, the starting point of optimisation is not identical for the NURBS and Marionette models. The initial geometries are shown in Figure 6.21. We chose surfaces with a straight profile, so that the Bézier patches are close to be developable surfaces. In that manner, the optimisation algorithm can converge towards shapes with either positive or negative gaussian curvature at the boundary. The height of both shells is set to 55 meters.

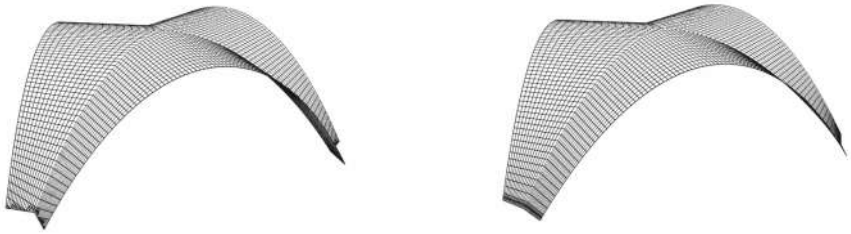

(a) Marionette mesh (b) NURBS

Figure 6.21 – Initial geometries for the shells on three supports.

6.4.3 Single-criteria optimisation

General comments

Shells with $\frac{t}{L} = \frac{1}{1000}$ The minimisation of displacement leads to differences between marionette and NURBS-based optimisation, as seen in Figure 6.22. On average, the marionette models have better results, which is illustrated by the dispersion criterion. Notice however that this is due to the poor performance of the NURBS model with the CRS2 algorithm. The best optimum is found within the NURBS design space. Unlike the results for the dome on an elliptical boundary, the performance metric is improved by an order of magnitude by structural optimisation.

$$\Delta\left(\frac{1}{\underset{\sim}{\delta_0}}\right) = 0.45 \tag{6.24}$$

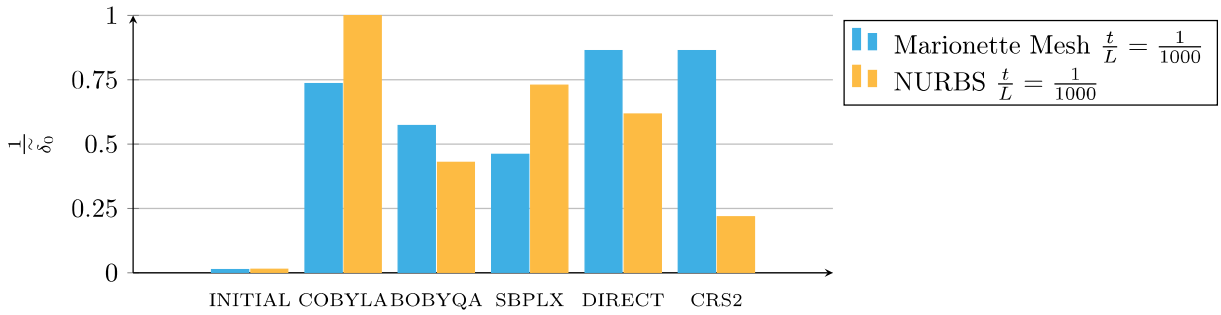

Figure 6.22 – Optimal values found for the minimisation of displacement under self-weight ($\frac{t}{L} = \frac{1}{1000}$).

The minimisation of the displacement under non-symmetrical loads is subject to high variations of algorithmic performance, as illustrated in Figure 6.23. The results on the marionette all outperform results of the NURBS framework (the mean relative variation e is 59%), but the coefficient of dispersion remains inferior to 1. It can be noticed that two different optimisation algorithms can indeed have very different output: choosing the right optimisation technique (in this case SBPLX) is more crucial than choosing between the Marionette or NURBS design space.

$$\Delta\left(\frac{1}{\underset{\sim}{\delta_1}}\right) = 0.91 \tag{6.25}$$

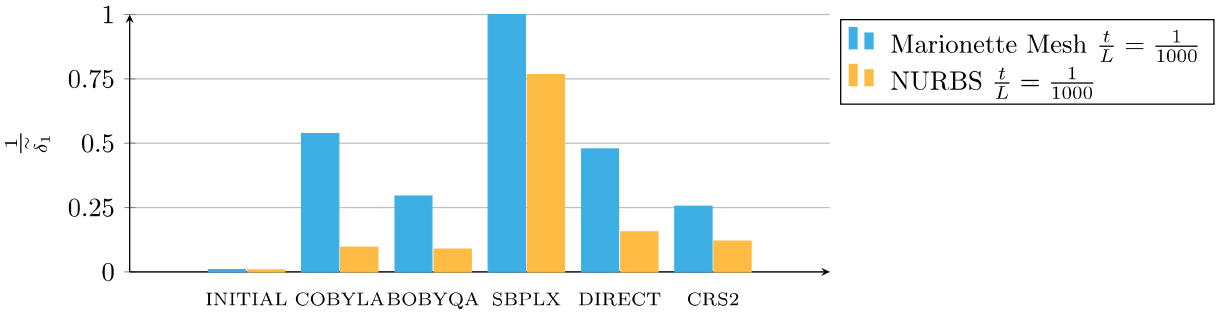

Figure 6.23 – Optimal values found for the minimisation of displacement under non-symmetrical load ($\frac{t}{L} = \frac{1}{1000}$).

The results of the optimisation for linear buckling are summed up in Figure 6.24. The optimisation of the linear buckling load shows a significant difference between the marionette and NURBS design spaces. Indeed, the best optimum found in the NURBS design space reaches 60% of the best optimum found in the marionette design space. Like for the minimisation of displacement under non-symmetrical load, the difference between optimisation algorithms is also significant, but the difference between marionette and NURBS models is more significant, as seen in equation (6.26).

$$\Delta\left(\frac{1}{\tilde{p_{cr}}}\right) = 0.98 \tag{6.26}$$

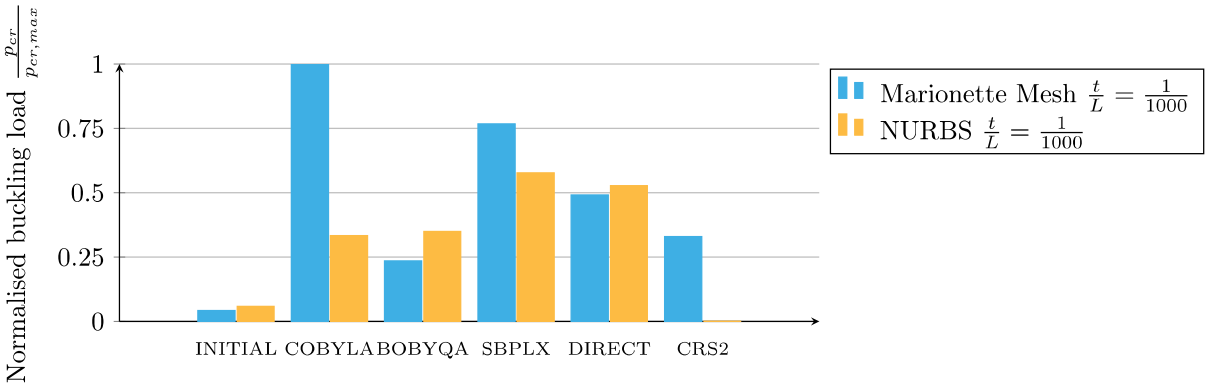

Figure 6.24 – Optimal values found for the maximisation of linear buckling load under self-weight ($\frac{t}{L} = \frac{1}{1000}$).

Shells with $\frac{t}{L} = \frac{1}{250}$ The result of the minimisation of displacement under self-weight for shells with a slenderness of $\frac{1}{250}$ are shown in Figure 6.25. Shells with lower slenderness show less differences between the NURBS and marionette frameworks. The best optima of each design space differ by 10%. The difference between the two parametrisations is not very significant, as shown by the dispersion indicator computed in equation (6.27).

$$\Delta\left(\frac{1}{\tilde{\delta_0}}\right) = 0.71 \tag{6.27}$$

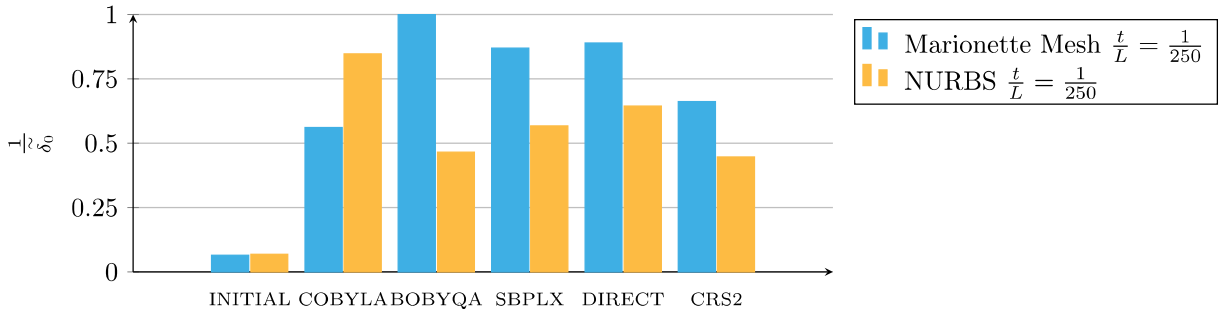

Figure 6.25 – Optimal values found for the minimisation of displacement under self-weight ($\frac{t}{L} = \frac{1}{250}$).

The shell with lower slenderness ($t/L = 1/250$) are subject to less dispersion than the highly slender shells ($t/L = 1/1000$). The bending stiffness seems to regularise the local exploration of the design space. This is particularly visible in the case of minimisation of displacement under non-symmetrical loads, which is shown in Figure 6.26. The marionette models performs better than the NURBS models by 16% on average, but this is not a strong trend. The difference between the best optima of two design spaces is indeed only of 10%.

$$\Delta\left(\frac{1}{\tilde{\delta}_1}\right) = 0.60 \tag{6.28}$$

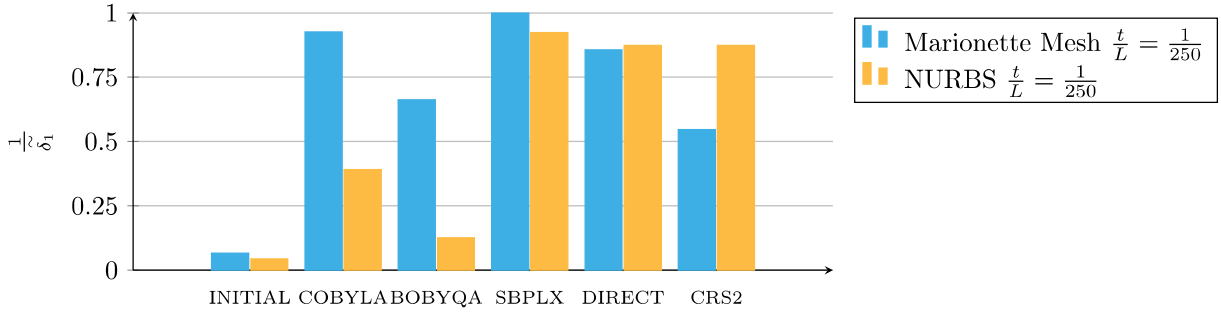

Figure 6.26 – Optimal values found for the minimisation of displacement under non-symmetrical load ($\frac{t}{L} = \frac{1}{250}$).

The objective function which presents the most significant differences between the NURBS and marionette design space is the maximisation of the linear buckling load. The best optimum of the NURBS framework reaches 70% of the best optimum of the marionette framework.

$$\Delta\left(\frac{1}{\tilde{p}_{cr}}\right) = 1.07 \tag{6.29}$$

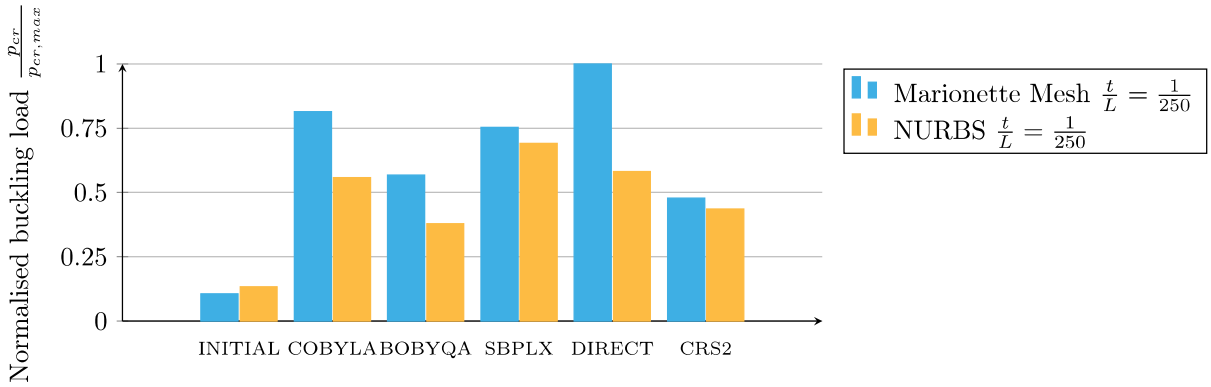

Figure 6.27 – Optimal values found for the maximisation of linear buckling load under self-weight ($\frac{t}{L} = \frac{1}{250}$).

Relative performance of algorithms

The optimisation of shell supported on three supports shows a higher dispersion of algorithm performance than with domes. The coefficient of variation is of 35% for the marionette design space and 52% for the NURBS design space. This dispersion can be explained by the fact that the initial design is far from being optimal and by the sensitivity of the performance with respect to the shape of the free-edge. We notice that the optimisation algorithms give very different optimal values, and that no optimisation method outperforms systematically the others. However, we can make some specific comments. Table 6.5 shows the number near-optimal designs found by optimisation algorithms for the 6 different optimisation problems.

	COBYLA	BOBYQA	SBPLEX	DIRECT	CRS2
100% optimal design	2	1	2	1	0
90% optimal design	3	1	3	1	0
85% optimal design	4	1	5	5	2

Table 6.5 – Relative performances of optimisation algorithms: count of near optimal designs.

First, the CRS algorithm never finds the optimal solution within the given time. The explorative nature of the algorithm requires many function calls before convergence, so that it is outperformed by the majority of the other algorithms. Likewise, BOBYQA never finds optimal or near-optimal solutions: we can deduce that the quadratic approximation of the objective function is not as efficient as the linear approximation performed by COBYLA. DIRECT generally has a better performance and regularly outperforms all the other algorithms used in the benchmark. The SBPLX algorithm gives regularly good results when using a design criterion based on linear analysis. In that case, a function call takes 200 milliseconds. In an optimisation run of 10 minutes, up to 3000 function calls can be made: the local algorithms have enough time to reach the (local) optima. The linear buckling analysis requires however approximately 2 seconds, so that local algorithms do not all reach optima and run through the 20 minutes.

Interpretation of the results

The best optimal results of the Marionette and NURBS design spaces for the shells with $\frac{t}{L} = \frac{1}{250}$ are shown in Figure 6.28. This overview of optimal design illustrates the variety of strategies that can be used by designers to improve the performance of shell structures. The solutions are indeed more diverse than the optimal designs of the dome problem in Figure 6.13. Optimisation algorithms explore different areas of the design space, so that several families of optimal design can be identified. The optima of the NURBS and marionette design space have a similar strategy for the minimisation of displacement under self-weight: the rise over-span remains approximately equal to 40%, and negative curvature is introduced

locally at the edge. The optimal designs for the minimisation of displacement under non-symmetrical load introduce negative curvature on the whole surface. This solution recalls some shells designed by Felix Candela. The shells maximising buckling have a very different strategy: the marionette mesh introduces a crease and the free-edge has a positive gaussian cuvature, whereas the NURBS model has a very high negative curvature at the free-edge.

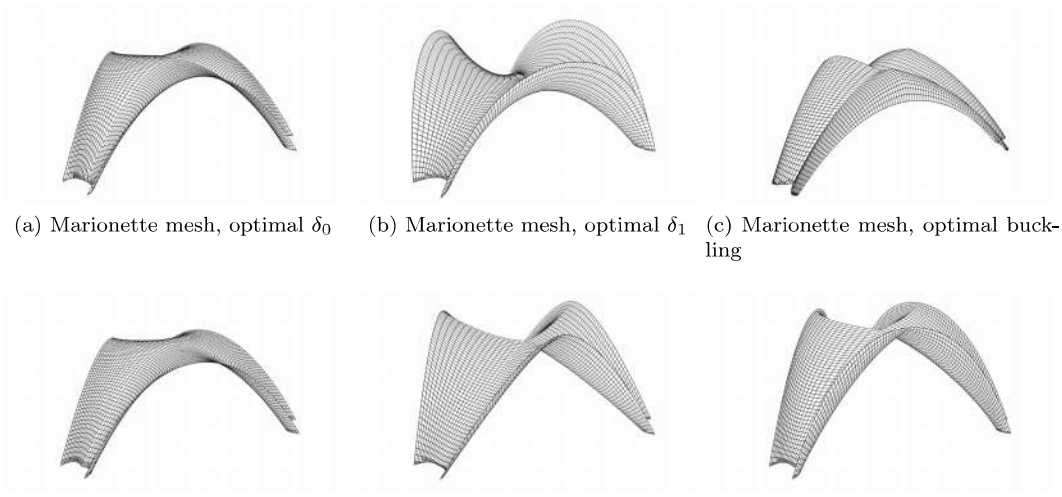

(a) Marionette mesh, optimal δ_0 (b) Marionette mesh, optimal δ_1 (c) Marionette mesh, optimal buckling

(d) NURBS, optimal δ_0 (e) NURBS, optimal δ_1 (f) NURBS, optimal buckling

Figure 6.28 – Geometry of the best optima for each objective $\left(\frac{t}{L} = \frac{1}{250}\right)$

For shell with slenderness of $\frac{1}{1000}$, optimal configurations have normal discontinuities between patches, both for the NURBS and marionette models. Many built examples show that this can indeed be a meaningful strategy. Consider for example notorious shells built on punctual supports: the CNIT (engineer: Nicolas Esquillan), the market hall in Royan (engineers: Bernard Lafaille and René Sarger) or the restaurant Xochimilco (engineer: Felix Candela). All those shells are based on geometrical principles, but are highly efficient. With a thickness of 8 centimetres and a span of 52.4 meters, the market hall has a slenderness comparable to the most audacious designs by Heinz Isler, which are compression only structures under self-weight. Solutions optimised for buckling or non-symmetrical load cases tend to introduce crease. The crease introduce more curvature and each sector behaves like an arch with high bending stiffness. This explains the introduction of creases for objectives that require high bending stiffness, like buckling or non-symmetrical loads. This solution is however less efficient than pure shell action for symmetrical loads, so that the no 'optimal' solution outperforms the others on all optimisation criteria.

Comparison of NURBS and Marionette

The comparative study for 6 families of optimisation problems shows that the problems parametrised with the marionette mesh regularly outperforms the NURBS model. In 22 out of 30 comparisons, the optimisation finds a better solution with the marionette method. In six comparative optimisation families, the marionette design space has the best optimum five times. The difference between the two design space is statistically significant, so that the marionette design space can be considered to be of high quality. Multi-criteria optimisation should provide more detailed answers about this statement.

6.4.4 Multi-criteria optimisation

In the followings, we show results of multi-criteria optimisation for both NURBS and marionette framework for shells with $\frac{t}{L} = \frac{1}{1000}$. The considered objectives are the two displacements and the linear buckling load. We display the absolute values, so we recall that displacement is minimised, whereas linear buckling load is maximised.

Figure 6.29 represents the Pareto front found after 50 iterations of the evolutionary algorithm for a population size of 200. Since there are three objectives, the objective space cannot be simply represented in two dimensions. We show thus three projections of the design space. It is noticed that there are three clusters of optima, represented in different colours. Each of these cluster dominates the others on one of the projections. For example, the black cluster dominates the others in the δ_0/δ_1 map, the blue one dominates the others in the p_{cr}/δ_0 map and the orange one dominates in the p_{cr}/δ_1 map. The clusters have a high dispersion along the δ_0 components (they are elongated in this direction). This means that by increasing slightly the displacements under symmetrical loads, one can improve significantly other performance metrics of a structure. For example, one can double the buckling capacity compared to the structure that minimising δ_0 with marginal loss of stiffness. Such trade-off should be considered carefully by engineers.

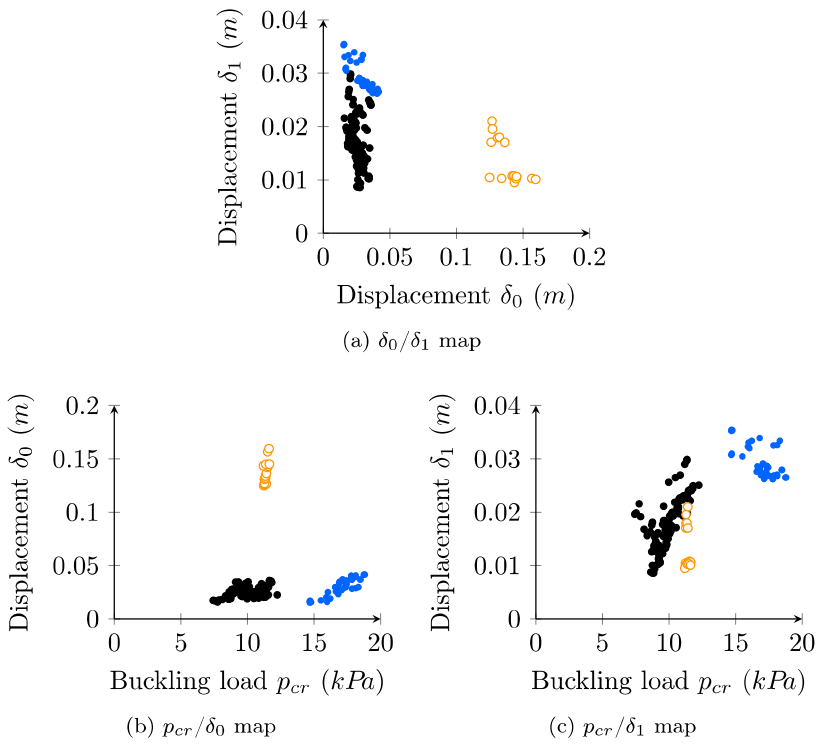

(a) δ_0/δ_1 map

(b) p_{cr}/δ_0 map

(c) p_{cr}/δ_1 map

Figure 6.29 – Pareto front for three objectives for the marionette design space for the shell with $t/L = 1/1000$. Three clusters, in three different colours can be identified.

Results of multi-criteria optimisation for the NURBS design space can be found in Figure 6.30. The fiftieth generation (with a population size of 200) is shown. Unlike the marionette design space, no cluster can be identified. Some similarities arise however. Consider for instance Figure 6.30b: shells with a low displacement also have a relatively low buckling load. By choosing a strain energy that equals 120% of the minimum strain energy, one can multiply the linear buckling load of the structure by a factor of 2. Interestingly, it can be seen that the maximal buckling load of the front obtained with the NURBS design space is far below the one found with the marionette design space. The evolutionary algorithm failed to find the cluster that would be equivalent to the blue cluster of Figure 6.29. This is in accordance with the difference found between marionette and NURBS models in the single-valued buckling optimisation. Performances on other metrics are less visible, but the vast majority of the Pareto front of the Marionette space dominate the Pareto front of the NURBS model. The difference observed in single-valued optimisation must therefore not only be attributed to the peculiarities of the single-valued optimisation. They reveal a difference of quality between the NURBS and marionette design space, namely here the better performance of the marionette design space, that we attribute to the enrichment of the description of one elevation.

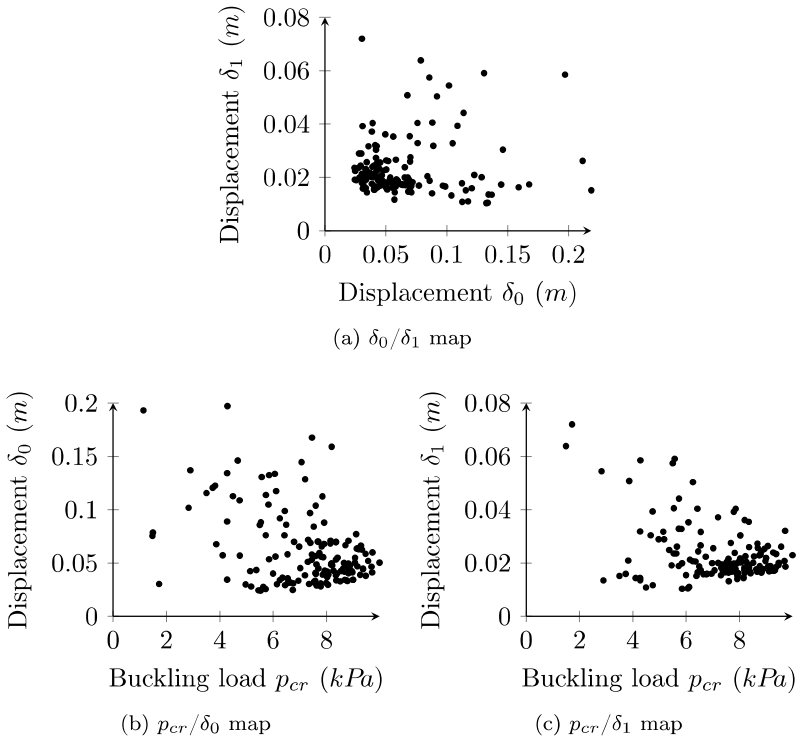

(a) δ_0/δ_1 map

(b) p_{cr}/δ_0 map

(c) p_{cr}/δ_1 map

Figure 6.30 – Pareto front for three objectives for the NURBS design space for the shell with $t/L = 1/1000$.

6.5 Discussion and guidelines

6.5.1 Sensitivity to initialisation

The optimisation of the shells on three supports demonstrates that optimisation can significantly improve the performance of a structure. The optimisation procedures lead to significant changes of the parameters (and thus the visual appearance of shells) and of the performance metrics. For example, the strain energy can be divided by a factor of 70 after optimisation. The linear buckling load can also be multiplied by more than 20 without significant change of mass. This drastic improvement of the mechanical behaviour shows that the initialisation is far from being optimal: this could be expected, since the marionette and NURBS patches have a very low gaussian curvature. The dome structure on contrary was initialised with a good design: the optimisation improved this design, but the change is not as significant.

The difference of behaviour of optimisation algorithms with the shells with free-edges compared to the closed dome can be interpreted by two factors. First, the non-optimality of the initialisation implies that the optimisation algorithms will look for solutions 'far away' (in the parameter space) from the initial input, so that they might get stuck in local optima. This was expected in our study and motivated our choice of initialisation. An initialisation with a strong negative gaussian curvature at the free-edge would have unlikely yielded optima with vanishing curvature at the free-edge. Second, the design of shells with free-edges is much more challenging than the design of domes, since many strategies can be employed to stiffen a free-edge. This difficulty was already observed by Bletzinger and Ramm.

6.5.2 Relevance of the marionette technique in structural optimisation

The marionette method provides a rich design space for fabrication-aware shape generation. The performance of optimisation algorithms is comparable to the one of NURBS, and when single objective functions are considered, the Marionette method often outperforms NURBS in our study. This might seem counter-intuitive, as the latter one offer a wider design space and should feature better global

optima. However, it also has many undesirable configurations. For example, consider the first case-study of a dome. The NURBS model has one additional degree of freedom, it can be seen easily that the additional mode corresponds to the deformation of one elevation. The additional shape parameter of the NURBS model can be seen in Figure 6.31. The intuition of an engineer is that this mode is not the most relevant for structural modelling. Increasing the number of degrees of freedom (for example by taking 4×4 control points for the in-plane parametrisation), would not create interesting modes of deformation for the NURBS model.

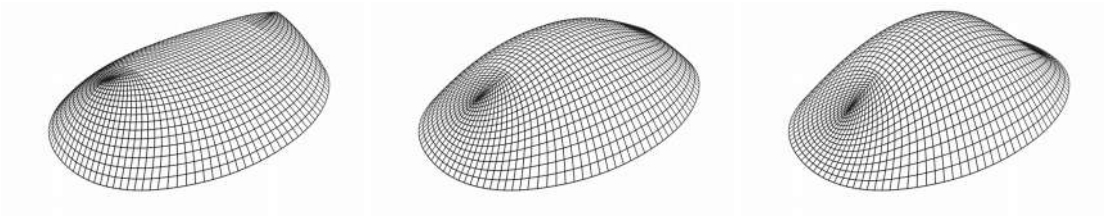

Figure 6.31 – The shape parameter specific to the NURBS model.

We should however be careful with sweeping generalisations. The problems studied in this chapter, which are classical problems in shape optimisation of shell structures, were properly parametrised by following examples in existing literature. As an example, the decomposition in six different patches is necessary for the appropriate modelling of the shell on three supports. The case-studies, although based on a fair amount of optimisation runs, did not investigate the influence of mesh topology on the results. Choosing appropriate parametrisations and mesh singularities is important for NURBS-based optimisation, but it is even more important for the marionette method.

6.5.3 Proper parametrisation

It appears that some features, like the curvature of free-edges affect drastically the structural behaviour of shell structures. By aligning the mesh with the free-edge, it is possible to control this value with only one parameter, and eases the local exploration of the design space. Moreover, free edges are often visible and the alignment of the panels layout with it can be considered more æsthetically pleasing.

The present study considered two variations on the boundary conditions. The shell on three supports considered a bounding region for the boundaries so that the shape of the boundary could change during optimisation, whereas the ellipsoidal dome has fixed boundaries. The second example is obviously more constrained, and since marionette meshes have less degrees of freedom than regular meshes, we should make a comment on the topic of imposed boundaries. Treating linear hard constraints (like vertex position) with the marionette method can be done by Singular Value Decomposition. As discussed in Chapter 5, the resulting vector space can be null if too many constraints are imposed. This is not the case of the ellipsoidal dome. One of the most delicate aspects is thus the handling of straight boundaries. If the mesh is aligned with it, this constrains highly the shape generation, as the marionette mesh is locally a cylinder. Therefore, it is necessary to have quad meshes which are not aligned with straight boundaries if one wants double curvature at the supports. This difficulty was already highlighted in [245].

6.5.4 A possible improvement: the optimisation of gridshells

Structural parametrisation of gridshells

The marionette technique and NURBS are methods that create surfaces with a specified parametrisation. The optimisation problem treated in the present chapter considered shells with isotropic material, so that only the parameter 'shape' is significant. The parametrisation itself becomes an important design parameter when constructing discrete structures, like gridshells. In such cases, the structure has a certain anisotropy depending on the orientation of the members. The parametrisation of the structure influences thus the distribution of stiffness. The question of parameterisation of gridshell structures is extremely important, as it impacts their bearing capacity and the fabrication. [267] optimised the parameterisation of gridshell structures in order to minimise their deflection under different load cases. It is however more

interesting to take both shape and parametrisation into account. The next logical step to follow is to study the relevance of the marionette meshes for the optimisation of gridshells.

The full potential of the method could be harnessed if different mesh toplogies could be compared. An algorithm for automatic quadrangulation of domains with prescribed points on boundaries was proposed by [178] and applied to the creation of quadrangulations based on sketches [244]. The possibilities offered by such methods seem very promising, as they could allow for interactive modifications of the mesh topologies and possibly automated generation of different design spaces. [191] introduced a strategy to explore all the possible quadrangulations of a surface. However, the aforementioned methods consider meshes with boundaries aligned, which can be too restrictive in the general context of architectural design.

To better understand the potential of topology changes, consider Figure 6.32. Five mesh topologies are chosen to mesh the interior of an ellipse, which recalls the problem studied in Section 6.3. The thick lines correspond to boundaries of NURBS patches. The colors of the thick lines depend on the two-colourability of the topology. The three meshes at the bottom correspond to classical solutions in architectural design. The two solutions on the left recall *scale-trans surfaces* discussed in [98], the solution on the right recalls surfaces of translation. It has no singularity, but as a result, irregular panels are bound to appear at the boundary.

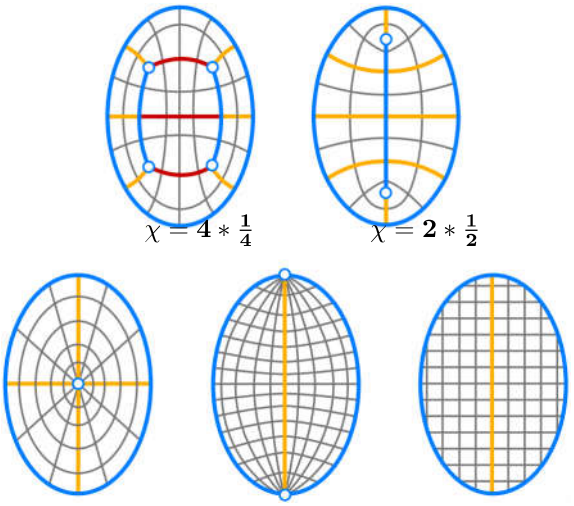

Figure 6.32 – Mesh of the interior of an ellipse: white dots denote singularities.

The two configurations on top of Figure 6.32 are less common in architectural application. The introduction of several singularities makes the size of the facets more uniform, and avoid the problem of concentration of structural elements in one point, which occurs inevitably when poles are introduced. Figure 6.33 shows how one can obtain new topologies by merging singularities. This could be the basis of a new mesh grammar for shape and topology optimisation of gridshell structures. Combined with the marionette technique, one could achieve economical solutions satisfying fabrication constraints and of high efficiency.

6.6 Summary of intellectual contribution

This chapter assessed the potential of a modelling technique taking into account fabrication constraints for structural optimisation. The analysis of the degrees of freedom offered by this method shows that if used as a classical CAD tool, marionette meshes diminish slightly the size of the design space offered by NURBS patches. However, the designer can choose arbitrary shape functions and separate the description of vertical and horizontal components of the shape. In total, fifty comparative optimisation problems have been considered. It corresponds to more than 100,000 function calls. The performance of the marionette mesh is confirmed, as it outperforms NURBS in a majority of cases. Viewing the space of marionette

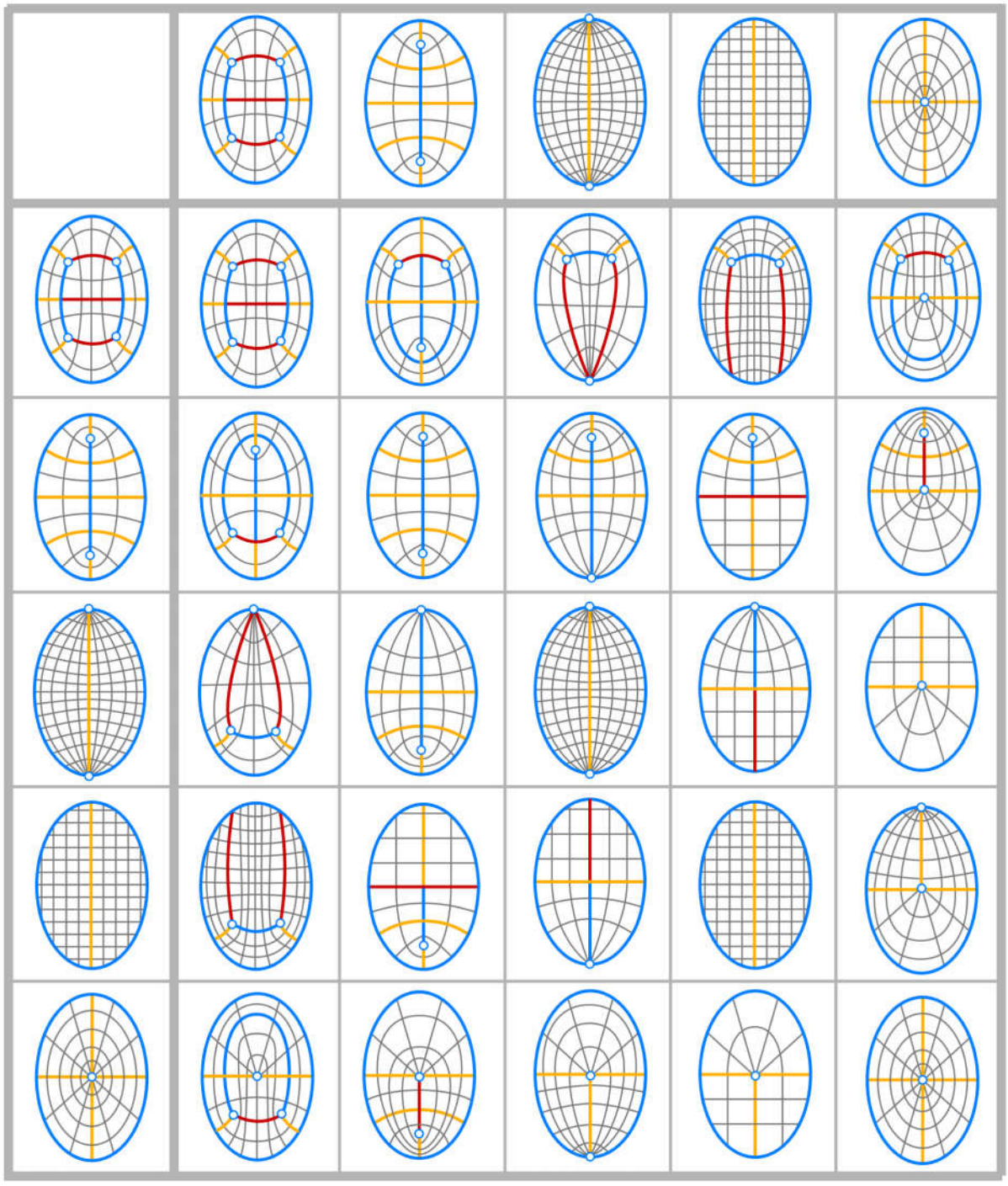

Figure 6.33 – An overview of several mesh topologies obtained by combination of simplicial meshes: 15 different design are proposed, creating as many design spaces.

meshes as a vector space, we can imagine a vertex-based optimisation with a set of linear constraints, so that finite-element parametrisation could be used with marionette meshes as well.

The separation of the parametrisation of the plane view and of the elevation finds motivation in the theory of thin shells. We see indeed a relation between this point of view and the one taken by PUCHER: by separating the vertical and horizontal components of the stresses, one notices that vertical equilibrium (and form) can be derived from horizontal equilibrium (with the choice of a proper stress function), see for example [264]. It is indeed a well-known fact that horizontal equilibrium of thin shells under vertical loads is found by integration of an AIRY stress function, whereas vertical equilibrium is found by solving a more complex non-linear differential equation. Enriching the description of the elevation in marionette meshes will hence provide more possibilities to find a good geometry.

The case-study shows that geometrically linear or purely equilibrium-based thinking is not necessarily the best solution for thin shells. We notice indeed that the minimisation of the strain energy or of the maximal tensile stress can yield structures with low buckling capacity. On the Pareto fronts generated in our multi-objective optimisation, increasing of a few percent the strain energy of a shell can indeed improve significantly its buckling capacity. For highly optimised shells, the effect of non-linearities should be considered with care. Ekkehard RAMM called thin shell the *Prima Donna* of structures. It carries load efficiently through membrane action, so that extreme slenderness can be achieved. It is however sensitive to imperfections and instabilities, so that catastrophic failures might occur [206].

Like all CAD-based optimisation techniques, the optimised shape has the same topological features as the initial shape. The biggest challenge left is to provide guidance on the topology to chose. We did not provide new tool or algorithm for that purpose but we identified existing methods that can be combined with the marionette technique to generate different parametric design spaces of surfaces covered with planar facets. These tools could be used for the design of particular structural systems. As a preliminary step in this direction, the next chapter proposes a systematic study of two non-standard structural systems where the form is generated with the marionette method.

Chapter 7

Application to innovative structural systems

This chapter proposes to study the design of non-standard structural systems within a fabrication-aware design space. We showed previously that semi-regular or non-smooth patterns can be generated easily with the Marionette technique. The potential of gridshells meshed with patterns constituted of triangles and hexagons, also known as *kagome pattern* and generalisation of folded plate structures are investigated.

7.1 Problem statement

7.1.1 Statement

The marionette technique proposed in Chapter 5 is an intuitive method of complex shape generation, which has a high potential for the parametrisation of structural optimisation problems. The method provides indeed the end-user with a rich fabrication-aware design space. Chapter 6 proposed the exploration of this design space in the context of shape optimisation of shell structures. The marionette method is revealed to be an efficient way to parametrise structural design problems, but remains restricted to conventional systems.

In Chapter 5, we discussed non-standard applications of the marionette method, beyond quadrilateral meshes and beyond smoothly parametrised surfaces. The method is indeed not limited to quadrilateral meshes, and the smoothness of the projection and elevation curves has no influence on the solution of the marionette problem. The aim of this chapter is thus to propose an assessment of the marionette method for the generation of non-conventional structural systems. This approach can be compared to the one of Candela or Dischinger, who evaluated the mechanical behaviour of the shapes they built with analytical formulæ.

In the followings, we consider two structural systems illustrated in Figure 7.1 for which the marionette method can be applied: gridshells with a Kagome (tri-hex) mesh and folded plate structures. These two types of structures can be considered as discrete shells, and as such, they are sensitive to buckling and instabilities, although the Kagome grid shown in Figure 7.1 is designed with respect to bending due to its shape and boundary conditions. This chapter studies specifically the relevance of non-standard configurations generated with the marionette meshes, especially with respect to mechanical criteria, like stiffness or buckling capacity.

First, a specific literature review on the design and analysis of gridshells and folded plate structures is presented. The general methodology for shape generation and structural analysis is then detailed in the second section. The performance of kagome gridshells and folded plate structures are then assessed in the third and fourth section. The fifth section discusses the potential of the geometrically-constrained methods developed in this dissertation.

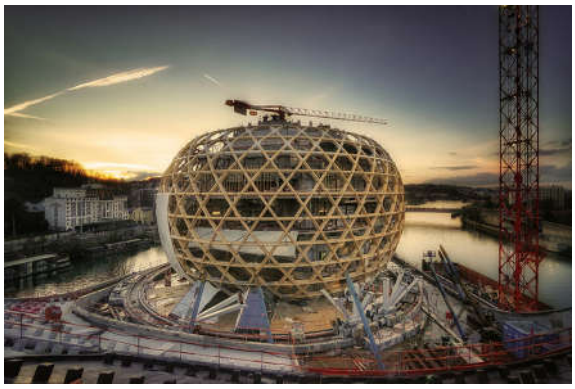

(a) Cité Musicale (arch: Shigeru Ban, picture: Nicolas Gromond)

(b) Wooden folded plate structure (picture: IBOIS)

Figure 7.1 – Two structural systems studied in the Chapter: Kagome gridshell (left) and folded plate structure right).

7.1.2 Research questions

Fabricators face an increasing demand of non-standard structural systems, illustrated by some of the recent realisation of Shigeru Ban. While there is a rich literature on the analysis of commonly built structural systems, the designers are often left with few guidelines for innovative structural configurations. This chapter merges fabrication considerations (planarity of facets) with an evaluation of the structural behaviour of such configurations. The main contributions of this chapter are:

- A comparative study on the stability of Kagome and quadrangular gridshells;
- Propositions for corrugation strategies of folded plate structures;
- A comparative assessment of the structural performance of the two proposed corrugation strategies;
- Design guidelines for Kagome gridshells and folded plate structures.

In the following, we present the methodology employed in this chapter.

7.2 Methodology

7.2.1 Parametric study

The aim of this chapter is to provide engineers and architects with basic knowledge on some innovative structural systems during conceptual stages of design. We propose thus a parametric study taking into account global shape parameters: rise-over-span ratio, grid density (for gridshells), rate of corrugation (for folded plate structures), etc. The nature of the parameters depends on the structural systems, for this reason different parameters are introduced for gridshells (in Section 7.3.5) and for folded plate structures (in Section 7.4.6). Most of the parameters introduced, like rise-over-span and grid density, have an influence on the visual aspect of the structure. Figure 7.2 shows an example of parameters used in the study on kagome gridshells.

The parametric studies performed in this chapter aim at proposing a comparative assessment between a standard structural system and a non-standard system. The comparison with technological solutions that are well-documented on a large number of models (more than 800 models were constructed in this chapter) provides the designers with references and lead to an evaluation of the potential offered by kagome gridshells and folded plate structures. Based on the obtained results, we emphasize on the their interpretation with simplified models in order to extrapolate the performances of kagome gridshells and folded plate structures to other geometries or load cases. Figure 7.3 represents the methodology employed in this chapter.

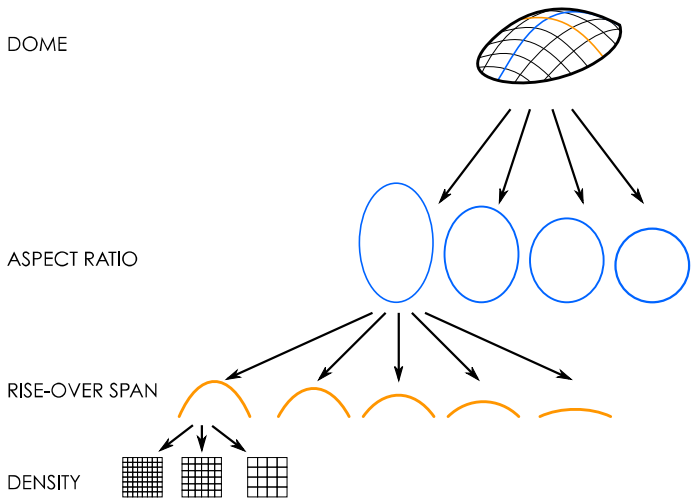

Figure 7.2 – An example of parametric study.

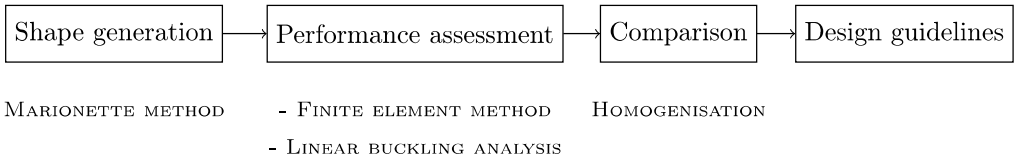

Figure 7.3 – Framework for performance assessment.

7.2.2 Shape modelling with the marionette method

This chapter illustrates the possibilities offered by the marionette method for structural design. The shapes are thus generated with the marionette technique. The plane view is parametrised by NURBS patches, and the elevation are controlled with NURBS curves. In our study on folded plate structures, specific rules are applied for the corrugation in order to generate non-smooth surfaces. These rules can be considered as local perturbations, but the overall shape parametrisation is done with NURBS patches. The methodology for shape generation is illustrated in Figure 7.4.

In order to compare with previous literature on gridshells, we restricted the shapes of gridshell structures to surfaces of translation. The literature on the structural analysis of free-form folded-plate structures being more limited, we set emphasis on the formal possibilities of the marionette technique and studied more complex shapes.

7.2.3 Structural analysis

Structural analysis is at the core of the methodology employed in this chapter, as we want to establish guidelines for the conceptual design of non-standard structural systems. The analysis software used is Karamba, a plug-in integrated with parametric CAD tools Rhinoceros™ and Grasshopper™ [205, 204]. This software enables to perform structural analysis within a 3D-modelling environment, which considerably eases the design process for structural engineers.

Finite element modelling

We use the finite element method, which finds an approximate solution of the weak form of a PDE problem. In mechanics, the weak form is found with the formulation of the principle of virtual work. It can be demonstrated that the solution of the finite element problem converges towards the solution of the weak form with mesh refinement [22]. We discuss here the choice of elements as well as the choice of

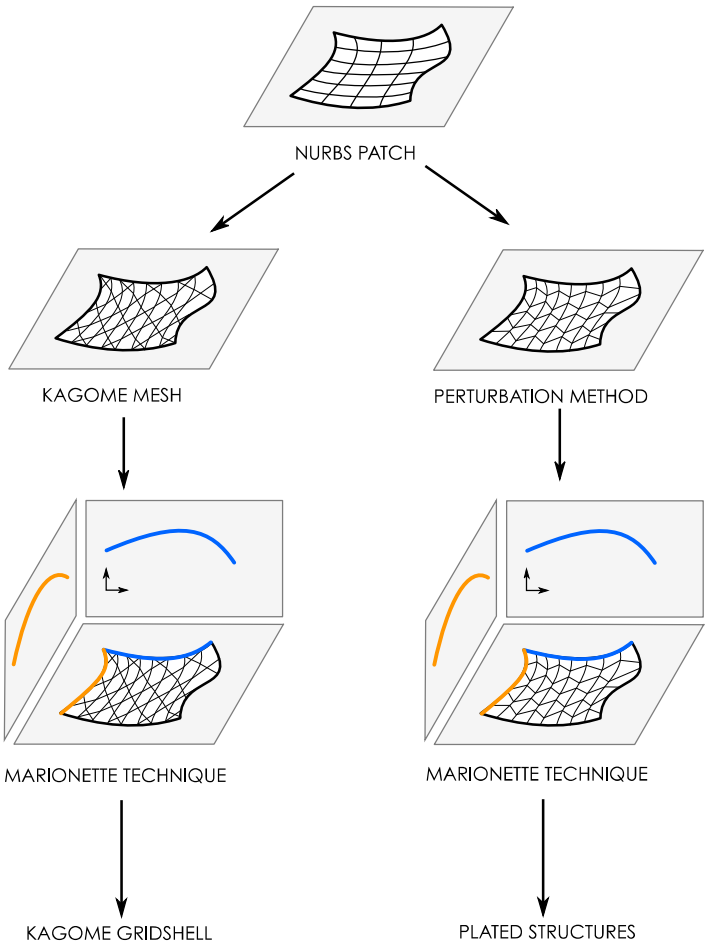

Figure 7.4 – Methodology for the generation of non-standard structural configurations.

subdivisions.

Gridshells The gridshells are modelled with beam elements with three elements per member. The subdivision allows to capture eventual localised buckling modes, which can arise in gridshells.

Folded plate structures Mechanical attachment is a key aspect in the structural response of folded plate structures. Therefore, we discuss the modelling of connections between plates, which is illustrated in Figure 7.5. Each plate is slightly shrunk and subdivided, and springs are introduced between the duplicated nodes. The local z axis of each spring is aligned with the edge boundary (orange arrow in Figure 7.5). In that way the force $\mathbf{F_z}$ corresponds to in-plane shear, $\mathbf{F_y}$ corresponds to out-of-plane shear. The links restrict translations, and allow rotations along y and z axis. Rotations are restricted along the x axis.

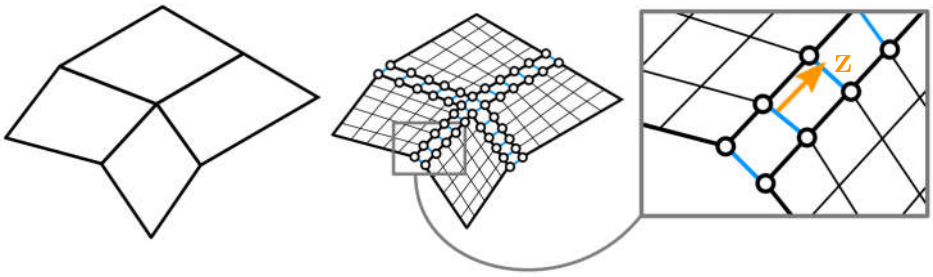

Figure 7.5 – Model of structural attachment: initial geometry (left), shrunk plates with subdivision (middle) and links between the duplicated nodes (right).

The linkage between the plates is made with spring elements. The spring axial and shear stiffness are not a parameter of our study, but could be taken into account depending on the type of connection used. Our study considers springs that act as rigid links for the translational degrees of freedom. Figure 7.6a shows the influence of the axial and shear stiffness on the overall displacement of a plated structure under a uniform live load. It is noticed than when increasing the axial and shear stiffness of the spring, the maximal displacement converges to a certain value. The springs act then as rigid links. The spring stiffness was thus set accordingly to this convergence graph at $10^7 N/m$.

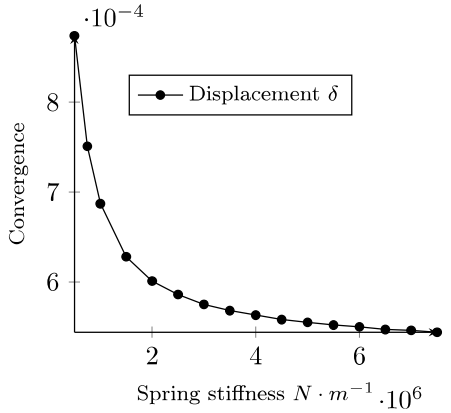

(a) Influence of spring stiffness on displacements

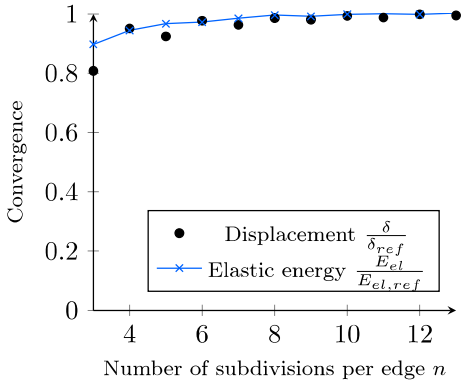

(b) Influence of mesh refinement on convergence

Figure 7.6 – Numerical studies on the convergence of the Finite Element model

Folded plate structures are modelled with the TRIC element [9], a linear triangular element. The convergence of the finite element model with mesh refinement is studied with a plated shell. Figure

7.6b shows the convergence of elastic energy and maximal displacement with respect to the number of subdivisions along each edge n. The total number of elements varies with the square of N. Displacement and energy are compared to a reference value, set for 15 subdivisions of each edge, which corresponds to $79,000$ elements. The graph shows that convergence of the model is quickly reached. The convergence of elastic energy and displacements is above 95% for 6 subdivisions per edge. We choose this refinement value in the following, as it is a good compromise between convergence and computational efficiency.

Buckling analysis

This chapter implements geometric non-linear analysis on structures with imperfections, but also considers linear buckling analysis. The stiffness matrix of a structure can be written as the sum of $\mathbf{K}_E$ the elastic stiffness (independent of the applied load $\mathbf{P}$) and of $\mathbf{K}_G$ the geometric stiffness (which decreases here with $\mathbf{P}$). The linear buckling analysis makes the assumption that the coefficients of $\mathbf{K}_G$ vary linearly with the amplitude of $\mathbf{P}$ and finds thus couples of buckling factor and displacement vector $(\lambda, \mathbf{\Phi})$ so that:

$$(\mathbf{K}_E + \lambda \mathbf{K}_G) \cdot \mathbf{\Phi} = \mathbf{0} \tag{7.1}$$

The non-linear buckling problem becomes therefore the eigenvalue problem shown in equation (7.1), the lowest eigenvalue λ_1 giving an estimate of the buckling capacity of the structures. The linearisation hypothesis is in fact a Taylor development, and it is valid if the displacements before buckling are small. In structures subject to large deformations, like gridshells, the linear buckling analysis can overestimate largely the real buckling capacity. In detailed design, fully non-linear analysis is thus required to assess the bearing capacity of gridshells, but the linear buckling analysis can be quickly estimated and can be helpful in conceptual design stage [152].

7.3 Stability of Kagome gridshells

Results on the stability of Kagome gridshells are presented in this section. First, the specific geometries and parameters used in this study are defined. Then, we present the results of the parametric study on the linearised buckling loads of Kagome gridshells.

7.3.1 Previous work on the mechanics of single-layered gridshells

Grid shells are structures composed of beam elements, but that act as continuous shells. They are usually covered with a transparent envelope. Their design must consider fabrication constraints, like the planarity of facets, but also structural performance. In Chapter 5, we presented two innovative methods to cover kagome gridshells with planar facets. This section presents existing literature on the analysis of gridshells. The techniques presented are usually applied to triangular and quadrilateral meshes. So far, there is no study on the structural performance of kagome gridshell.

Due to their high slenderness, gridshells are usually designed with respect to buckling. The structural behaviour of gridshells is usually governed by non-linear effects, most noticeably buckling [49]. Four buckling configurations can be observed in gridshells:

- Global buckling in the manner of a shell;
- Member buckling;
- Snap-through of one node;
- In-plane rotation of one node.

Some design recommendations, often emphasizing simple shapes, like spherical cupolas have been published. Gioncu published a state of the art on the buckling of reticulated structures in 1995 [96]. A report produced by the Working Group of the International Association for Shells and Spatial Structures (IASS) in 2005 completes this review with analytical and numerical results, demonstrating the important advances made in that field [124]. A novel issue is to be published in 2016. A design guide for the stability

of reticulated shells with a thorough literature review is proposed in [90], showing a great mastery of this topic.

These guidelines identify two approaches to evaluate the structural behaviour of a grid structure: homogenisation methods and numerical experiments. The following section establishes a parametric numerical study, and uses previous work on homogenisation of grid structures to comment the numerical results.

Homogenisation and equivalent shell thickness

Homogenisation techniques aim to formulate an equivalent continuous behaviour of a heterogeneous structure with a cell repeated periodically. These methods use the superposition principle and usually work well for structures with a linear behaviour [138]. They have been successfully used for planar grids [140], but a rigorous extension to gridshells is difficult because of the loss of periodicity, due to the variations of curvature. A discussion on this topic is proposed by Gioncu and Balut [97].

The advantage of equivalent thickness model is that they provide structural engineers with simpler formulæ and can be of practical interest for conceptual structural design. Some attempts to provide equivalent shell thickness have been used in previous studies [48, 267, 152, 141]. However, these models do not allow for the modelling of localised buckling and the study of the influence of imperfections for shell structures remains tedious for non-trivial shapes. Nowadays, the ever-growing computational power makes the use of finite element modelling and non-linear analysis ubiquitous in practice, and numerical simulations are often preferred to homogenisation formulæ.

Numerical experiments

Numerical methods are used for the practical design of gridshells, because they allow for integration of complex issues, like material non-linearities or geometrical imperfections. Some guidelines for the analysis of reticulated domes have been proposed by Kato *et al.* [125, 126]: these studies introduced geometrical imperfections and semi-rigid nodes. Bulenda and Knippers [49] performed parametric studies on domes and barrels vaults and evaluated the influence of imperfections on the stability of gridshells. A more complete study using finite element analysis to evaluate local node stiffness of patented connections has been performed by Huang *et al.* [115]. Bruno *et al.* assessed the influence of nodal imperfection and of Eigenmode Imperfection Method (EIM) more recently [47]. Malek *et al.* [152] performed numerical investigations on the buckling of spherical cap domes and considered geometrical values, like grid spacing, or height over span ratio, as parameters. This approach lead to recommendations for the design of gridshells with triangular or quadrangular layout.

Other studies have evaluated the influence of residual stresses in elastic gridshells [141, 169]. A more complete analysis was performed on the elastic gridshell built for the Soliday's festival in Paris, considering accidental ruin of some members [248]. These studies show that high bending stresses due to the form-finding process of elastic gridshells have little influence on the buckling capacity of domes. Such procedures could be extended to steel structures, in order to assess the influence of other residual stress fields on the stability of gridshells.

Imperfections

There are many differences between the ideal numerical shell models and the built structures. These differences, or imperfections can be of different nature: loads, geometry, material, residual stresses in the members. Thin shells are known to be sensitive to imperfections [132]. These parameters are often set as a global geometrical imperfections. Gioncu and Balut also point out that geometrical imperfection tend to govern over material non-linearities for large span structures [97].

Typically, the difference between the built geometry and the computed model is of a few centimeters at most [131]. It is therefore necessary to introduce a norm, in order to asses realistic imperfections. In the following, the norm $\|\cdot\|_\infty$ defined as the maximal displacement is used. Bulenda and Knippers propose a higher bound of $L/500$ for the imperfection with the infinity norm [49]. Based on data on the precision requirements for built project [225], Malek *et al.* studied an imperfection of 3mm [152]. For the

design of the roof of the Great Court at the British Museum, a nor of $L/200$ was chosen for imperfections [233].

The choice of the shape function is discussed in Section 7.3.6. The first buckling mode is recommended by design codes, and was used for example for the design of the roof of the British Museum and the Palacio de Comunicaciones [233, 225]. However, different studies show that other imperfections shapes should be considered, as they result in a bigger reduction of the buckling capacity of gridshells. Examples of such shapes can be found in [49] with the use of dynamic eigenmodes, and a discussion on the choice of appropriate imperfections is proposed in [47]. It has to be noticed that there is no closed-form solution on the worst imperfection possible, some studies even demonstrated that higher order eigenmodes can have a more critical effect on the reduction of buckling capacity [269]. The purpose of the following study being to compare relative performance between Kagome grid pattern and quadrilateral pattern, we will consider the imperfections most commonly used in current practice.

Summary of the literature review

The design of gridshells is governed by their ultimate limit state. Catastrophic failures of steel roofs led to a significant research effort on the stability of reticulated shells. In practice, triangulated gridshells are commonly built because they guarantee in-plane shear stiffness and a shell-like behaviour. The vast majority of the research, either based on numerical experiments or homogenisation approaches, focuses thus on triangulated gridshells. The elegance and efficiency of cable-braced quadrangular gridshells proposed by the office Schlaich Bergermann und Partner also led to a consequent amount of studies. Nevertheless, other structural systems can be preferred over those two solutions because of architectural or manufacturing constraints. For example, quadrangular gridshells with rigid connections have been built recently. Studies on the mechanical performance of non-standard patterns are more rare. One of the few investigations on 'exotic' patterns can be found in [153].

7.3.2 Specific research question

The existing literature on the analysis of gridshells is mainly restricted to triangular grids, quadrangular grids with cable bracing and rigid quadrangular grids. No systematic study on the performances of the kagome grid pattern has been carried out, so that the relevance of this pattern for applications to gridshells is not evaluated. Besides, the possibility to cover kagome grids with planar facets with the methods proposed in this dissertation make them economically viable alternatives to rigid quadrilateral grids. Kagome and quad grid pattern have the same node valence, which indicates similarities:

- they rely on in-plane bending stiffness of the connections;
- they have the same possibilities in terms of torsion-free offsets;
- they have a similar node complexity;
- they can be covered with planar faces using conjugate curves networks;

From these remarks, it can be concluded that kagome and quadrilateral gridshells without cable bracing belong to the same technological design space. Therefore, the assessment of the structural behaviour of kagome gridshells would be particularly meaningful if compared to the one of rigid quadrilateral gridshells.

7.3.3 Basic properties of Kagome lattices

First, we introduce some specific considerations about the geometry of the Kagome grid pattern generated in our study. They tend to have a uniform member length. We propose simple calculations to estimate the number of connections or member length per unit area for a planar Kagome lattice made out of regular hexagons and triangles.

Description of the pattern

The regular Kagome pattern is made out of regular hexagons and triangles. The pattern is periodic, and can thus be described by the study of a unit-cell shown in Figure 7.7. In this image, all the edges have the same length l, the dimensions of the unit cell are easily found based on properties of equilateral triangles.

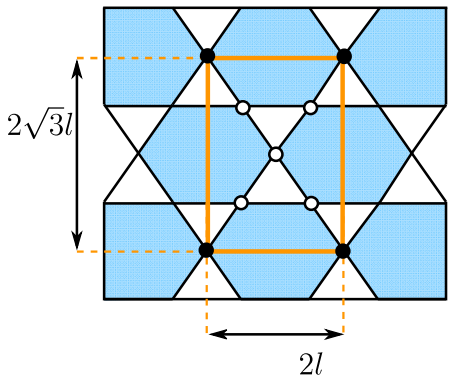

Figure 7.7 – A basic cell of a Kagome lattice.

The pattern is compared to a square pattern, where the unit cell is obviously a square with edge length l.

Structural density

We compute now the edge length per unit area. In the unit cell, we count 10 edges and 4 half edges. The edge length per unit area L_A is thus:

$$L_A = \frac{\left(10 + 4 \cdot \frac{1}{2}\right) \cdot l}{2\sqrt{3}l \cdot 2l} = \frac{\sqrt{3}}{l} \tag{7.2}$$

We can compare this value with the edge length per unit area for the square pattern, where $L_A = \frac{2}{l}$. For a same edge length, the ratio of member lengths is thus equals to $\frac{\sqrt{3}}{2}$. This gives the estimation for the mass ratio of equation (7.11).

7.3.4 Number of connections

The number of nodes per unit area is an important question, as the cost of connections highly impacts the cost of gridshells. For the unit cell depicted in Figure 7.7, there are 5 nodes that belong only to the cell (in white), whereas 4 nodes belong to 4 adjacent cells (in black). The number of connections per unit area is thus:

$$N_{nodes} = \frac{5 + 4 \cdot \frac{1}{4}}{2\sqrt{3}l \cdot 2l} = \frac{\sqrt{3}}{2l^2} \tag{7.3}$$

For a square grid, the number of nodes per unit area is simply $\frac{1}{l^2}$. The ratio of these two values is thus equals to $\frac{\sqrt{3}}{2}$, which gives an estimate for the ratio used in equation (7.25).

7.3.5 Numerical experiment and choice of the parameters

Two typical free-form structures are barrel-vaults and domes. Theses shapes are easily generated using translation or scale-trans surfaces surfaces, which have the advantage of generating planar quadrilateral facets. A method to convert such meshes to planar Kagome meshes is described in 5.4.4.

The dome is a surface of translation defined with two parabolæ.

$$z\left(x,y\right)=\frac{4h}{L^2}\left(y-L\right)\cdot y+\frac{4H}{d^2}\left(x-\frac{d}{2}\right)\left(x+\frac{d}{2}\right) \tag{7.4}$$

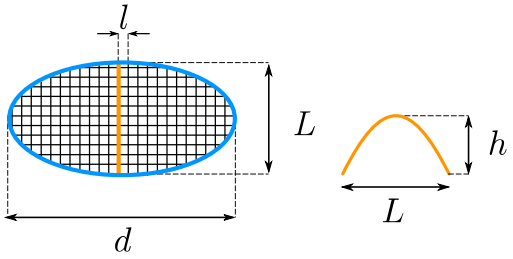

Figure 7.8 – Geometrical parameters describing the dome.

The barrel vault is a scale-trans surface. The curves on the ground are sine curves, and the elevation is a parabola. We write $f\left(x\right)=d\sin\frac{2\pi x}{L_1}$, the equation of the surface follows:

$$z\left(x,y\right)=\frac{4h\left(1-\frac{2\cdot f(x)}{L}\right)}{L^2}\left(y-f\left(x\right)\right)\left(y-L+f\left(x\right)\right) \tag{7.5}$$

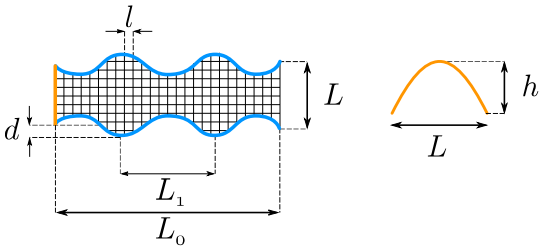

Figure 7.9 – Geometrical parameters describing the barrel vault.

The geometrical parameters describing the two models are displayed in Figures 7.8 and 7.9. The number of geometrical parameters is quite important, we decrease their numbers by introducing non-dimensional parameters. The physical meaning of these ratios is explained and detailed below. The main span L of the structures is set to 30 meters. Three ratios Π_1, Π_2 and Π_3 correspond to geometrical parameters. The two ratios Π_4 and Π_5 are the performance metrics studied in this section.

Aspect ratio

The geometry has a main span L and another characteristic length d. The first ratio is called *aspect ratio* and is defined by equation (7.6). For the domes, the ratio Π_1 correspond to the ratio of curvatures, whereas for the barell vault, higher values of Π_1 correspond to higher gaussian curvature (the case $\Pi_1=0$ is a cylinder).

$$\Pi_1=\frac{d}{L} \tag{7.6}$$

Notice that different aspect ratios could be constructed from the barrel vault. For the simplicity of the demonstration, it was decided to set the ratio L_0/L to 4 and the ratio L_1/L_0 to 2.5. These values are similar to the configuration of the gridshell roof covering the museum of Downland [106].

Rise-over-span ratio

The name is self-explanatory: the second non-dimensional parameter is the ratio of the characteristic height h with respect to the main span L. Common formulæ indicate that structural performance should increase with this number.

$$\Pi_2 = \frac{h}{L} \tag{7.7}$$

Structural density ratio

We consider here the grids to have a mean member length of l. The comparison of this number to the main span, as done in equation (7.8) gives indications on the grid coarseness.

$$\Pi_3 = \frac{l}{L} \tag{7.8}$$

Buckling ratio

The last parameter compares the buckling pressure p_{cr} found by linear buckling analysis to the member bending stiffness EI/L^4. The number described by equation (7.9) is the value that is compared between Kagome and quadrilateral meshes. The ratio I/L^4 being kept constant in this study, the buckling ratio will be a measure of the stiffness due to the form and mesh topology independently of the section properties.

$$\Pi_4 = \frac{p_{cr} L^4}{EI} \tag{7.9}$$

Notice that only the quadratic moment of inertia I is considered. A comparable non-dimensional number could be constructed with the span L, the axial stiffness EA and the critical pressure p_{cr}. However, it is a well-known fact that member shortening has more impact on very shallow structures which won't be considered in our study.

Structural efficiency

We introduce finally a variable, later called *structural efficiency*, in order to compare the performance of Kagome and quadrilateral grid pattern. The parameter is defined as:

$$\Pi_5 = \frac{p_{cr}.A}{m \cdot g} \tag{7.10}$$

where A is the horizontal surface covered, and m the mass of the structure. The number defined by equation (7.10) compares the total resultant of vertical forces to the resultant of gravity forces. It must be noticed that for a same structural density, *i.e.* individual member length, the total length of members differs between the Kagome and quadrilateral grid. For a square grid with edge length l, the total beam length per unit area is $\frac{2}{l}$. For a Kagome grid made of regular hexagons and triangles and edge length l, the total beam length per unit area is $\frac{\sqrt{3}}{l}$. From this simple case, an estimation of the ratio of the masses is given by:

$$\frac{m_{Kagome}}{m_{Quad}} \sim \frac{\sqrt{3}}{2} \simeq 86\% \tag{7.11}$$

In other terms, for a same structural density, the Kagome grid is slightly lighter than the quadrilateral grid. This difference justifies the fact to look more closely at the structural efficiency, and not only at the buckling load.

Table 7.1 sums up the range of variations of each parameter. The range of parameters is chosen to fit existing designs: for example the rise-over-span ratio remain in general superior to 0.1 to avoid high bending stresses or snap-through. The structural density are chosen so that the minimal member length is 1.253, a reasonable value compared to built projects. Each set of geometrical parameters generates a geometry for a quadrilateral and a Kagome grid. Two load cases are considered, as discussed in Section 7.3.6. The parametric study proposed in this Section consists thus of 500 linear buckling analysis and several fully non-linear analysis for the study on imperfections sensitivity.

	Π_1	Π_2	Π_3
Barrel Vault	$[0, 0.025, 0.05, 0.075, 0.1, 0.125, 0.15]$	$[0.1, 0.2, 0.3, 0.4, 0.5]$	$[\frac{1}{24}, \frac{1}{16}, \frac{1}{12}]$
Dome	$[1, 1.33, 1.67, 2]$	$[0.1, 0.2, 0.3, 0.4, 0.5]$	$[\frac{1}{32}, \frac{1}{24}, \frac{1}{16}]$

Table 7.1 – Variations of the parameters in the present study.

7.3.6 Material, loads and boundary conditions

The material used is steel, and we restrict our study to a linear elastic material law. Detailed studies with plasticity have been made previously and are reviewed in [124]. These studies are necessary to evaluate with high fidelity the post-buckling behaviour of gridshells, at the cost of high computational cost. In the first steps of the design process, engineers need to perform many analysis, often with simplified assumptions and a linearised buckling load is already a good indicator of the structural performance. It was already chosen as design criterion in [152] and [169]. The modelling hypothesis follow:

- the supports are pin joints with full translational restraint;
- the joints are assumed to be fully rigid;
- in the barrel vault, the arches are simply supported[1];
- distributed loads are replaced by concentrated loads at connections.

The boundary conditions chosen for the arch were set so as to restraint translations. Generally speaking, the stiffness of the free-edge is of high importance in the design of gridshells. An arch is generally stiffer than the inner part of the gridshell. The stiffness of the arches could be a parameter of this study, but this should be considered as a specific design question that is not influenced by the structural pattern. Several solutions are indeed possible to stabilise a free-edge, like an increase of the cross-section (Bulenda and Knippers propose to multiply the bending stiffness by 30) or the introduction of a spoke-wheel bracing in the manner of russian engineer Vladimir Shukhov [226].

The members are made of circular hollow section, with a wall thickness of 10mm and a diameter of 200mm for the dome and the barrel vault. With these geometries, there is no difference between I_y, I_z, and torsional buckling of members is not possible, which simplifies the parametric study. Two load cases are considered: a uniform projected vertical load of $1kPa$ and a non-symmetrical load of $1kPa$ applied following the normal of the surfaces with the pattern of Figure 7.10.

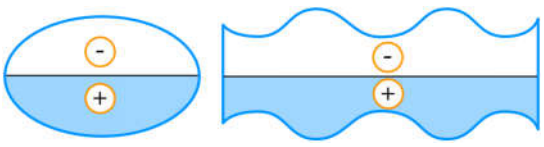

Figure 7.10 – Areas of positive and negative pressure for the non-symmetrical load case, top view of Figure 7.8.

Current literature focuses more on uniform symmetrical load cases [152]. Koiter has shown than spherical caps are subject to geometrical imperfections for such load case, but not for concentrated load. Therefore, it is meaningful to consider this kind of load case in our sensitivity analysis. Furthermore, non-symmetrical load cases are known to be more critical than symmetrical ones for buckling and often govern the sizing of gridshells. The asymmetrical load case is thus also considered in order to provide

[1] It is a well known-fact that free-edge are weak points of gridshells, and that buckling would be localised on the free-edge. Bulenda and Knippers observed that multiplying the stiffness of the free-edge by 30 to 40 is sufficient to avoid such problem. Note that there are many ways to stiffen an edge (large cross-section at the free-edge, negatively curved edge, spoke-wheel system, etc.).

guidance on situations closer to the engineering practice. The chosen asymmetrical load represents here a wind load, which usually features areas of positive and negative pressure. Wind loads computed from the Eurocode can usually be decomposed between a symmetrical and asymmetrical component. Since we already study a symmetrical load case, we focus only on the non-symmetrical component of this load.

Imperfection sensitivity

This section focuses on the influence of imperfection on Kagome gridshells. Similar study could be conducted on folded plate structures. The tested geometry is a dome supported on a circular plan ($\Pi_1 = 1$, $\Pi_2 = 0.2$, $\Pi_3 = 1/32$), and subject to a uniform vertical load. Figure 7.11 shows different plots of linear buckling load p_{cr} normalised by the linear buckling load of the structure without imperfection $p_{cr,0}$ computed with different imperfection amplitudes for the infinity norm. The Kagome pattern is more sensitive to imperfections than the quadrangular pattern. For the amplitude of $L/500$, the reduction of the linearised buckling load is approximately 10%.

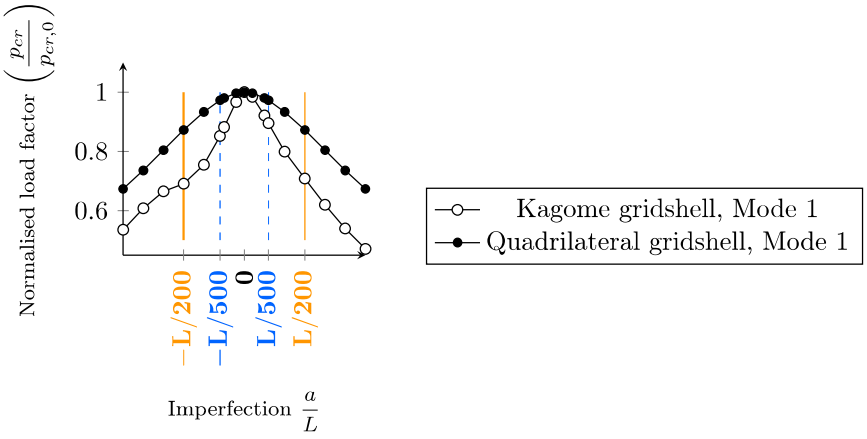

Figure 7.11 – Influence of imperfection scale on the linear buckling load.

A second order analysis is thus performed on both perfect and imperfect geometry to evaluate more precisely the influence of imperfections. The load/displacement diagrams for the Kagome and quadrilateral gridshells obtained are displayed in Figure 7.12a and 7.12b respectively. The four horizontal lines represent the linearised buckling loads. Three imperfection amplitudes are considered: the first one is a small imperfection (1/1500) and can be compared to the one used by Malek *et al.* [152], the second corresponds to the (1/500), as proposed by Bulenda and Knippers [49], the third one is of ($L/200$) as recommended in EC3 [85].

The structures with imperfections do not reach their linearised buckling loads, contrary to perfect structures. The shapes of the load/displacement graphs are also smoother than the ones of the gridshells without imperfection. Consider for example the imperfect geometry with a norm of $15cm$ ($L/200$): the structure behaves in a fully non-linear manner and it is hard to distinguish a linear domain. This indicates that the linearised buckling load is not suited for structures with high imperfection norm, as high stresses are at stake before buckling. Considering the imperfection amplitude of $L/500$ proposed by Bulenda and Knippers [49], we notice that the bearing capacity of the imperfect structure decreases by approximately 15%. With the norm proposed by Malek *et al.* [152], the loss of bearing capacity with imperfections is negligible for the considered geometry.

The qualitative behaviour of Kagome gridshells with respect to imperfections is similar to what has been analysed in previous research [49, 152], and Figure 7.12a and 7.12b are indeed similar. In the treated example, the decrease of bearing capacity with respect to imperfection (with the first buckling mode) is however less important than in previous literature, for example [49] who considered cable braced quadrilateral gridshells. It can however be compared to the decrease observed in a previous study for quadrilateral gridshells [152]. The explanation given by Malek *et al.* is that quadrilateral (and Kagome) gridshells rely on in-plane bending stiffness of the members to withstand loads, whereas triangulated

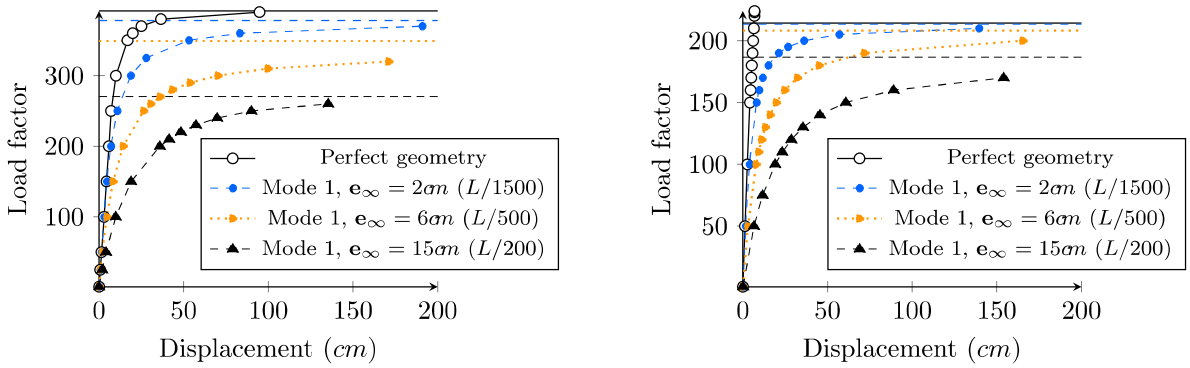

(a) Kagome grid pattern

(b) Quadrilateral grid pattern

Figure 7.12 – Load/displacement diagram for domes with different grid topologies and different amplitudes of imperfection.

gridshells can transfer out-of-plane loads with axial forces in the members. Small imperfection can therefore introduce bending moments in triangular gridshells and change their load transfer mechanism, from axial forces to axial and bending combined.

To go further, we propose to study the load where the displacement reaches the service limit state. The displacement is found with a second order analysis. We set $\delta_{SLS} = \frac{L}{200}$ and compare the influence of imperfection for quad and Kagome gridshells. Figure 7.13 shows the critical non-dimensional service load defined as $\frac{p_{SLS}L^4}{EI}$. Kagome grids remain stiffer regardless of the imperfection. This additional criterion shows also that the imperfection does not change the relative performance of Kagome and quadrilateral grids for simple performance metrics used in preliminary design.

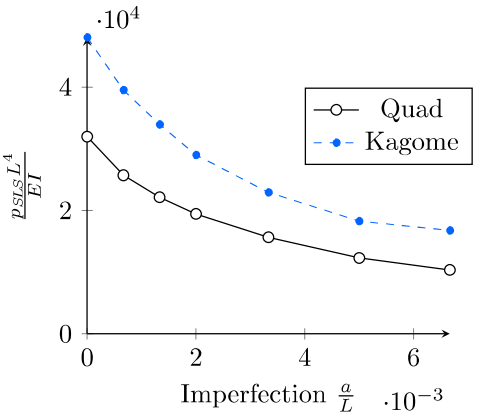

Figure 7.13 – Non-dimensional SLS load for Kagome and Quad gridshells

This section discussed the influence of imperfection on the structural performance of gridshells. The study of sensitivity to imperfection suggests that Kagome and quadrilateral gridshells without cable-bracing have qualitatively similar behaviours for linear buckling analysis. Even if classical approaches, like Eigenmode imperfection, illustrate the limitations of linear buckling analysis for detailed stages of design, we propose in the following to compare the bearing capacity of Kagome and quadrilateral gridshells by studying the linearised buckling load without imperfections, because this performance indicator is commonly used in conceptual design stages. In detailed design, geometrical and material non-linear analysis are required to assess the structural response of gridshells with full accuracy.

7.3.7 Buckling of barrel vaults

Linear buckling analyses were performed on barrel vaults with different geometrical configurations under symmetrical loading, and the results are shown in Figure 7.15 in a non-dimensional form. In Figure 7.15a, $\Pi_1 = 0$ and there is no corrugation, while in Figure 7.15b $\Pi_1 = 0.15$ and the shape is ondulating like the one shown in Figure 7.14. We notice that the corrugation is significantly improving the structural behaviour. The case $\Pi_1 = 0.15$ has a buckling load almost four times higher than the cylinder (case $\Pi_1 = 0$). The best design is shown in Figure 7.14.

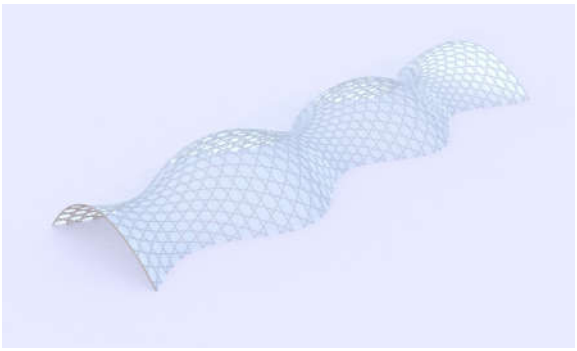

Figure 7.14 – Optimal barrel vault: $\Pi_1 = 0.15$, $\Pi_2 = 0.3$, $\Pi_3 = \frac{1}{24}$.

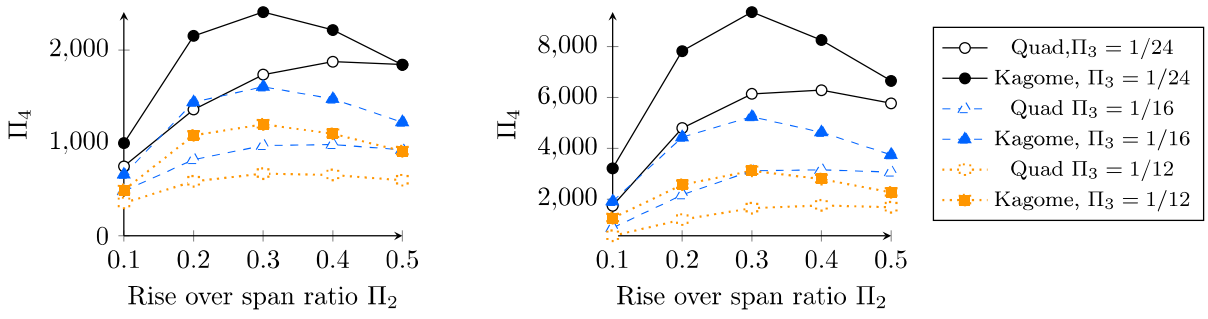

(a) Cylinder: $\Pi_1 = \frac{d}{L} = 0$

(b) Corrugated barrel vault: $\Pi_1 = \frac{d}{L} = 0.15$

Figure 7.15 – Comparison of the buckling capacity of Kagome and quadrangular grids for the barrel vault geometry.

It appears that, in general, Kagome grids have a higher buckling load. In order to quantify this assertion, we introduce the number r, later called *ratio of efficiency*, defined by equation (7.12). The same parameters values are chosen identical for both grids. A ratio superior to 1 indicates that the Kagome gridshell is more efficient than the quadrilateral gridshell.

$$r\left(\Pi_1, \Pi_2, \Pi_3\right) = \frac{\Pi_{5,Kagome}\left(\Pi_1, \Pi_2, \Pi_3\right)}{\Pi_{5,Quad}\left(\Pi_1, \Pi_2, \Pi_3\right)} \tag{7.12}$$

In the following, Π_1, Π_2 and Pi_3 have been varied and results are shown in Figure 7.16. We have chosen to represent the buckling load in terms of Π_1 and to compare the best design of both structures defined by equation (7.12). This ratio remains above 1.5, with a peak at 2.6. The most efficient designs

correspond to moderate rise-over-span ratio ($\Pi_2 = 0.3$) and a dense grid.

$$\begin{cases} r_{min}\left(\Pi_1\right) = & \min\limits_{\Pi_2,\Pi_3} r\left(\Pi_1,\Pi_2,\Pi_3\right) \\ r_{max}\left(\Pi_1\right) = & \max\limits_{\Pi_2,\Pi_3} r\left(\Pi_1,\Pi_2,\Pi_3\right) \\ r_{best}\left(\Pi_1\right) = & \dfrac{\max\limits_{\Pi_2,\Pi_3} \Pi_{5,Kagome}\left(\Pi_1,\Pi_2,\Pi_3\right)}{\max\limits_{\Pi_2,\Pi_3} \Pi_{5,Quad}\left(\Pi_1,\Pi_2,\Pi_3\right)} \end{cases} \tag{7.13}$$

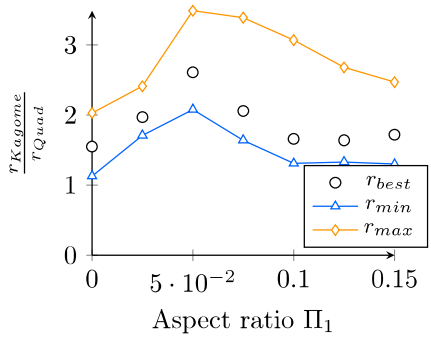

Figure 7.16 – Comparison of the best designs for different values of Π_1.

7.3.8 Barrel vaults under non-symmetrical loads

Non-symmetrical loads were then considered with the distribution shown in Figure 7.10. The behaviour of the structure is then dominated by bending and becomes very different for both structures. Consider Figure 7.17: the quadrilateral grid has a higher buckling load, but the buckling occurs for a high level of displacements, superior to 20% of the span. Of course, the ruin of members will occurs before the structure buckles and the results on linear buckling analysis are subject to caution for the quadrilateral grid in this case. This is a general situation: under non-symmetrical loads, quad gridshells are considerably softer than Kagome gridshells. For the studied example, the Kagome grid is 5 times stiffer. Using the same SLS criterion than previously ($\frac{L}{200}$), the Kagome grid clearly outperforms the quadrilateral grid. Considering the large displacements of the quadrilateral gridshells under non-symmetrical loads, it did not seem relevant to display the results on linear buckling analysis for this load case.

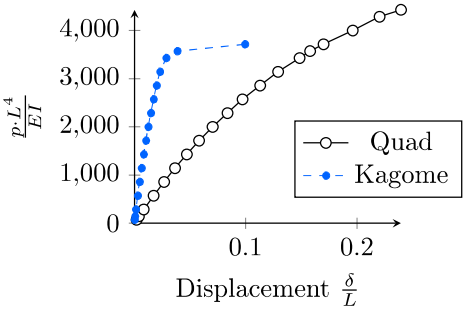

Figure 7.17 – Load-displacement for a non-symmetrical load $\left(\Pi_1 = 0.075, \Pi_2 = 0.3, \Pi_3 = \frac{1}{24}\right)$

7.3.9 Buckling of domes

The same parametric study is then reproduced for the dome geometry. Figure 7.18 shows the non-dimensional buckling loads computed for the symmetrical load case. Kagome and quad grids have a

similar behaviour: the buckling load is a decreasing function of Π_3. For slender domes (smaller values of Π_2), increasing the height also increases the buckling load, but a maximum is reached when Π_2 is approximately 0.3. The optimal value of Π_2 depends on the cross-section used. The buckling becomes then more localised, and a change of the shape has lower impact on the buckling.

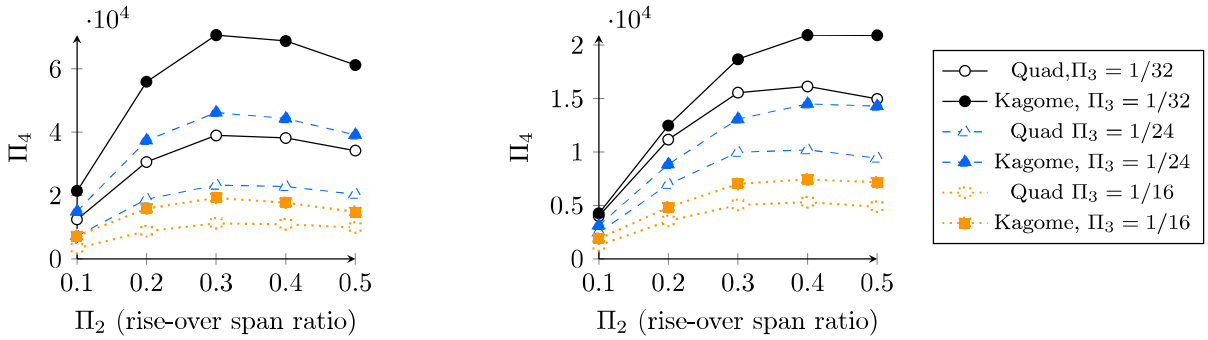

(a) $\Pi_1 = \frac{d}{L} = 1$ (b) $\Pi_1 = \frac{d}{L} = 2$

Figure 7.18 – Comparison of the buckling capacity of Kagome and quadrangular gridshells for the dome geometry.

Figure 7.19a shows then r_{min}, r_{max} and r_{best} for different values of Π_1. It is noticed that the Kagome gridshell is more efficient than the quadrilateral gridshell in the sense of equation 7.12 and this for all the configuration considered in the present study. The gain in structural efficiency is very important, especially for domes with a moderate aspect ratio, when the shell is the most efficient. It can be concluded that Kagome gridshells are more efficient than quadrilateral gridshells when considering linear buckling analysis. The most interesting geometrical configurations (moderate rise-over-span, and small aspect-ratio) are also the ones where the relative performances of the two meshes typologies differ the most. The efficiency can be doubled in those cases.

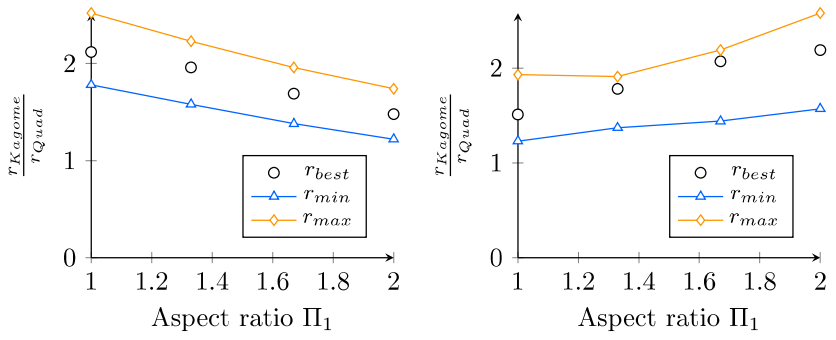

(a) Symmetrical load (b) Non-symmetrical load

Figure 7.19 – Comparison of the structural performance of domes.

Finally, Figure 7.19b compares the performance of Kagome and quadrilateral lattices for nonsymmetrical load cases. The Kagome lattice remains more efficient in all cases, with a minimum gain in structural efficiency of 23%. The tendency is inverted compared to the symmetrical load cases: Kagome grids are more efficient when the ratio Π_2 is higher.

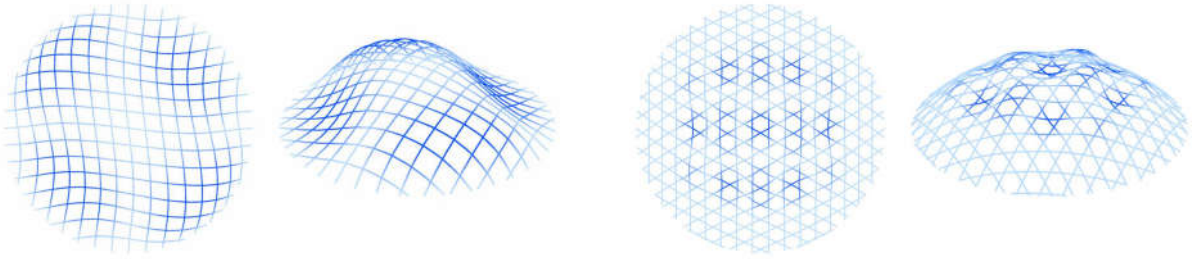

(a) First mode, $\Pi_4 = 889$ (b) First mode, $\Pi_4 = 6885$

Figure 7.20 – Comparison of the first buckling modes for quadrilateral meshes and Kagome meshes.

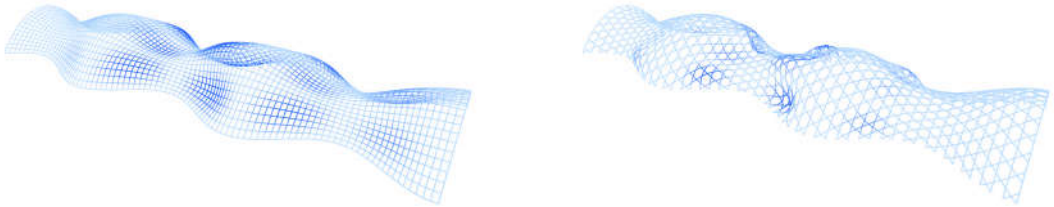

(a) First mode, $\Pi_4 = 6145$ (b) First mode, $\Pi_4 = 9361$

Figure 7.21 – Comparison of buckling modes on the most performant barrel vaults in our study.

7.3.10 Discussion

Shape of buckled domes

A more detailed look at the parametric study shows that the nature of buckling modes differs between Kagome and quadrilateral gridshells. Figure 7.20 illustrates the first buckling modes for two domes with the same member length, both for quadrilateral and Kagome meshes. On these images, darker colours indicate larger displacements. Each dark spot corresponds to an 'anti-node' on the buckled shape. Counting these spots, it can be noticed that the number of anti-nodes is higher in the Kagome lattice, and that the wavelength is shorter. This difference has been observed for coarse and fine grids.

This difference illustrates the fact that Kagome lattices have a higher in-plane shear stiffness than quadrangular meshes. Their higher buckling capacity can be explained by the fact that they activate buckling modes with shorter wavelength. This remark also holds for barrel vaults. Figure 7.21 shows the same kind of phenomenon for the buckling modes of the most efficient designs of barrel vaults of our study. There is the same number of anti-nodes in Figure 7.21a and 7.21b, but the anti-nodes are more concentrated in the Kagome lattice.

Influence of mesh refinement

The results of the previous section indicate that refining of meshes improves the critical buckling load of gridshells. We show a more detailed analysis of this statement by studying a dome with $\Pi_1 = 1.33$. The convergence of the structural efficiency with respect to the number of cells is interpreted with homogenisation principles and analytical formulæ from [140] and [58] and detailed in 7.3.10

Consider a unit cell with characteristic length l (defined in Figure 7.8 and 7.9). If one builds an equivalent shell, it is meaningful to consider that the bending and axial stiffness $\mathcal{D}$ and $\mathcal{A}$ depend linearly on $1/l$ (doubling the number of beams would double the bending stiffness). This is found in homogenised

models by Lebée and Sab for flat thick quadrangular beams layouts [140].

$$\begin{cases} \mathcal{D} = & \dfrac{EI}{l} \\ \mathcal{A} = & \dfrac{EA}{l} \end{cases} \tag{7.14}$$

The buckling load of an isotropic spherical shell under uniform pressure p_{cr} is given by following the formula, found for example in [249] or [58]:

$$p_{cr} = \frac{2\sqrt{\mathcal{A}\mathcal{D}}}{R^2} \tag{7.15}$$

By combining equations (7.14) and (7.15), the critical buckling load of an equivalent isotropic shell depends thus linearly on the number of cells. It is well-known that homogenised models describe accurately the actual model when the number of cells is large enough. Having these considerations in mind, we should expect the ratio Π_5 to be constant for sufficiently small values of Π_3, because the mass m varies linearly with $1/l$ and so does the homogenized buckling load. Figure 7.22a shows the variations of the structural efficiency with respect to Π_3. It appears that Π_5 tends to a constant when $\frac{1}{\Pi_3}$ increases. The convergence is reached for $\frac{1}{\Pi_3} \simeq 25$. This value is linked with the chosen cross-section, here 200mm pipes. The slenderness of the members at $\frac{1}{\Pi_3} \simeq 25$ is of 5, which is higher than what is found in built projects.

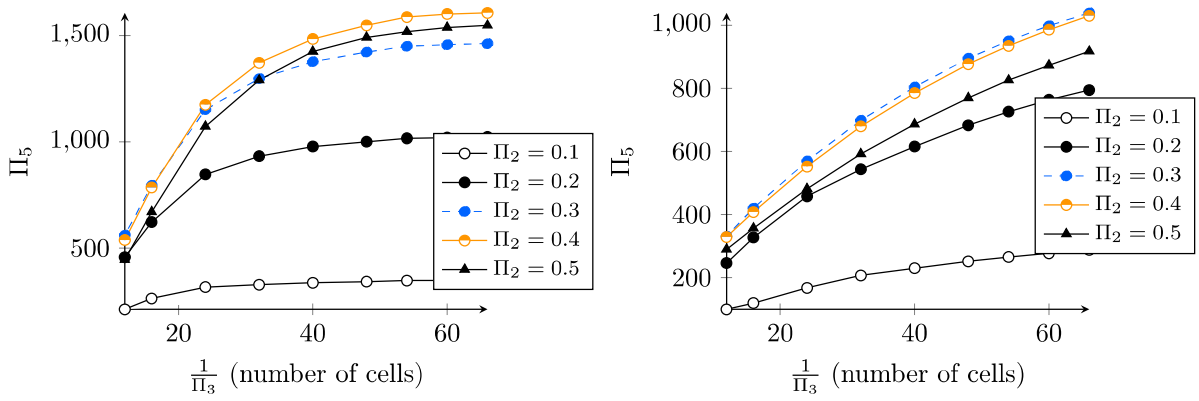

(a) Kagome grid pattern

(b) Quadrilateral grid pattern

Figure 7.22 – Structural efficiency for different grid refinements ($\Pi_1 = 1.33$).

The convergence of the structural efficiency to a constant indicates that Kagome grids tend to behave like isotropic shells. On the contrary, the efficiency of the quadrilateral grid does not converge to a constant when the grid is refined. To better understand this, consider that the buckling capacity of orthotropic shells depends on the in-plane shear stiffness. An example of analytical formula is given for shells of revolution by *Crawford* [58]. Still referring to the results of Lebée and Sab [140], we give an estimate of the in-plane shear stiffness G_{xy} for quadrangular grids (we make the assumption that the beams are Euler-Bernoulli beams):

$$G_{xy} = \frac{EI}{l^3} \tag{7.16}$$

This term clearly increases faster than the bending stiffness when the unit-cell becomes smaller. This non-linearity explains why the graph of Figure 7.22b increases with the number of cells $\frac{1}{\Pi_3}$ without reaching a plateau. The convergence study is thus a good indicator of the fact that Kagome lattices are isotropic, whereas quadrilateral grids are orthotropic.

Homogenisation approach and equivalent buckling loads

To go further, we adapt the formula of an anisotropic spherical cap of radius R under uniform pressure found by Crawford [58] to a quadrangular gridshell with equivalent properties derived from [140]. The problem treated by Crawford considers that the shell is isotropic with principal axis along parallel and meridians. The geometry is different from the domes studied in this Section, but it one of the only analytical formulæ available in the literature for orthotropic shells. We take count of the fact that our problem deals with circular hollow sections to simplify $I_y = I_z = I$.

Equivalent shell stiffness of a quadrangular gridshell Let us construct the equivalent axial and bending stiffness tensors from the homogenisation. From [140], we have:

$$\begin{cases} A_{xx} = A_{yy} = \mathcal{A} = \dfrac{ES}{l} \\ G_{xy} = \left(\dfrac{l}{G\mathcal{S}} + \dfrac{l^3}{12EI} \right)^{-1} \\ \nu_x = 0 \\ \nu_y = 0 \end{cases} \tag{7.17}$$

and

$$\begin{cases} D_{xx} = D_{yy} = \mathcal{D} = \dfrac{EI}{l} \\ D_{xy} = \dfrac{GJ}{l} \end{cases} \tag{7.18}$$

The grid relies only on bending of elements for the in-plane shear stiffness, and on beam torsion for the torsional stiffness of the equivalent shell. All terms depend linearly on $\frac{1}{l}$ (equivalently the number of cells) except the in-plane shear stiffness, which depends on $\frac{1}{l^3}$.

Buckling of orthotropic spherical cap under uniform pressure We derive now the theoretical buckling load of an anisotropic shell from the work of Crawford [58]. The equations simplify greatly when $D_{xx} = D_{yy}$ and $A_{xx} = A_{yy}$. Crawford introduces the quantities D_3, G_3 and Ψ defined by:

$$\begin{cases} D_3 = \nu_x \cdot D_y + D_{xy} \\ G_3 = \dfrac{2G_{xy}}{1 - \nu_x\nu_y - \left(2\nu_y \frac{G_{xy}}{A_{yy}}\right)} \\ \Psi = \dfrac{\mathcal{A}\left(1 - \nu_x^2\right)}{\mathcal{D}R} \end{cases} \tag{7.19}$$

With these notations, the buckling load of the isotropic spherical shell is:

$$p_{cr} = \frac{4\mathcal{D}\sqrt{\Psi}}{R} \tag{7.20}$$

Crawford computes then the ultimate buckling load of the anisotropic shell $\overline{p_{cr}}$ given by:

$$\overline{p_{cr}} = \begin{cases} p_{cr} & \text{if} \quad \dfrac{D_3}{\mathcal{D}} \geq \dfrac{\mathcal{A}}{G_3} \\ p_{cr} \left(\dfrac{1 + \frac{D_3}{\mathcal{D}}}{1 + \frac{\mathcal{A}}{G_3}} \right)^{\frac{1}{2}} & \text{if} \quad \dfrac{D_3}{\mathcal{D}} < \dfrac{\mathcal{A}}{G_3} \end{cases} \tag{7.21}$$

In the case of gridshells, the second inequality is verified, and using equations (7.17) and (7.18), we obtain:

$$\overline{p_{cr}} = \frac{4\sqrt{\mathcal{A}\mathcal{D}}}{R^2} \sqrt{\frac{1 + \frac{D_{xy}}{\mathcal{D}}}{1 + \frac{\mathcal{A}}{2G_{xy}}}} \tag{7.22}$$

So that finally:

$$\overline{p_{cr}} = \frac{4E\sqrt{SI}}{lR^2}\sqrt{\frac{1+\frac{GJ}{EI}}{1+ES\left(\frac{1}{2GS}+\frac{l^2}{24EI}\right)}} \tag{7.23}$$

The first term corresponds to the buckling capacity of an isotropic shell, it is proportional to $\frac{1}{l}$. The second term (under the square root) varies non-linearly with $\frac{1}{l}$ because of the terms in l^2, which come from the equivalent in-plane shear stiffness. The limit of structural efficiency for a high number of cells is given by equation (7.24), as l tends towards 0. We write ρ the volumic mass of steel (the mass per unit of a quad grid being $\frac{2\rho}{l}$) and get:

$$\Pi_5^* = \lim_{N\to\infty}\Pi_5 = \frac{2E\sqrt{SI}}{\rho R^2}\sqrt{\frac{1+\frac{GJ}{EI}}{1+\frac{ES}{2GS}}} \tag{7.24}$$

Figure 7.23 shows the application of equation (7.23) with the cross-section used in our parametric study and $\Pi_1 = 1$, which is the closest configuration to a spherical cap. The limit of the structural efficiency Π_5^* is also shown. It is noticed that the orthotropic shell converges slowly towards the limit, which explains why our convergence study does not show a plateau for the quadrilateral gridshell.

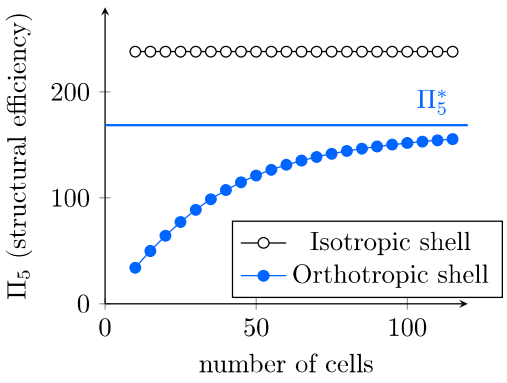

Figure 7.23 – Influence of grid refinements on the structural efficiency with a homogenised model

Design guidelines for Kagome lattices

Structural engineers can improve the efficiency of their designs by using different strategies. We discuss here some of these. In our study, the shape is an important factor of performance: changing a rise-over-span ratio from 10% to 20% doubles the structural efficiency. The optimal rise-over-span ratio is around 30%. For larger values, the gridshells become subject to localised buckling, and overall curvature of the shape does not provide any help. The change of geometry does not bring significant changes in the cost of fabrication of the elements, as our method guarantees meshing with flat panels.

Increasing the structural density also increases the structural performance of quadrilateral and Kagome lattices. For Kagome lattices, this strategy has a limit, as the structural efficiency tends to a constant when the number of cells tends to infinity. Even for very high structural density, this phenomenon does not occur for the quadrilateral lattices studied in this Section. This strategy has however a practical limitation, as the number of connections increases when increasing the density of the grid. Connections are very expensive and often govern the cost of the structure in gridshells. Denser grids are also costly, and the benefit in structural performance might be tempered by an increased construction cost.

We note here that the conversion rule chosen implies that, for a same value of Π_3, Kagome grids have less vertices (and thus connections) than quadrilateral grids. Writing N_{Kagome} and N_{Quad} the number of nodes, we have following simple relation proven in 7.3.3:

$$\frac{N_{\text{Kagome}}}{N_{\text{Quad}}} = \frac{\sqrt{3}}{2} \simeq 86\% \tag{7.25}$$

Therefore, the Kagome grids of the present study are structurally more efficient than quadrilateral grids for gridshells designed with a linear buckling criterion, and their cost of connections is also significantly lower.

7.4 Structural explorations with folded plate structures

7.4.1 Structural morphogenesis of folded plate structures

What is a folded plate structure?

So-called folded plate structures have been used for decades (see a patented example in [11]). These structures consist of rigid plate elements connected along the edges. Figure 7.24 displays an early example of folded plate structure in FRP by Renzo Piano: the structure was meant to be disassembled element by element, the structural attachment between the edges is visible on the right hand side.

Figure 7.24 – An example of folded plate structures: Sulfur Extraction Facility (arch.: Renzo Piano, retrieved from compositesandarchitecture.com)

Recently, numerical fabrication methods and more complex shape generation principles for folded plate structures extended their possibilities. Two of the main concerns of designers are structural efficiency and fabrication cost. The planarity of the plates is thus of particular importance in the structural morphology of folded plate structures. The following section proposes the use of a unifying framework for the generation of corrugated plated shell structures covered with planar quadrilaterals. The generated design space is thus constituted of constructible shapes: some illustrations of their formal possibilities are shown in Figure 7.25. The corrugation strategies introduced in this chapter leave potential for structural optimisation.

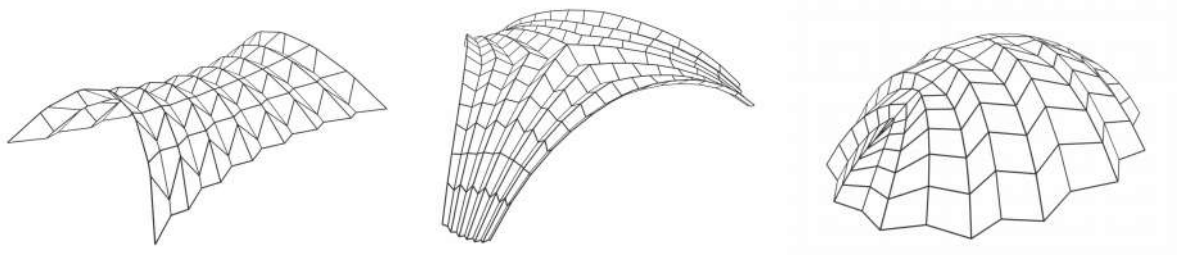

Figure 7.25 – Several designs generated with the method presented in this chapter, all facets are planar quadrilaterals. Two corrugation strategies are introduced in this chapter: the alternate translation (used in the left and middle) and the row translation strategy (used in the right).

In the followings of this Section, we sum up existing approaches for the morphogenesis of folded plate structures, and assess current knowledge on their structural behaviour.

Origami

Connections between plated structures and origami were made by Buri and Weinand [50], as origami naturally generate creases, which can be interesting for the structural behaviour of plated structures. Origami is also an active field of study and can be of interest for builders, as rigid origami are covered with planar facets and simplify manufacturing. The topic of folded structures for architecture has been studied extensively, a review of this topic is proposed by Lebée [137], and some examples apply to folded plate structures. For example, Tachi generalised the form-finding of the Miura-Ori folding pattern with planar quadrilateral and proposed a design for a barrel vault [243], other applications were proposed in [95]. Recent examples of folded plate structures include planar quadrilateral meshes generated with a principle using two curves [50, 210]. Notice that some rigid origami are rigorously described by the means of discrete differential geometry. For example, Schief *et al.* studied the egg-box pattern and its foldability, naming the resulting meshes *discrete Voss surface* [218].

Hexagonal pattern

It is a well-known fact that trivalent plates generally form a stable plated system. For example, origami requires a folding pattern which is two colorable, and folding of a trivalent system requires bending or twisting at least one plate [137]. Several built examples use this stability property, like the TRADA Pavilion [105] and a pavilion built for the Landesgartenschau. While the latter building is a success, Knippers and Li reveal potential pitfalls when covering a shape with planar hexagons [143]. Meshing with planar hexagons implies indeed following lines of curvatures, and the hexagons tend to align with Dupin's indicatrix. In negative curvature area, the panels take a bow tie shape. This implies poor nesting and large wastes generated. Acute angles resulting from the bow-tie shape can also be problematic in terms of construction. Beside, hexagonal meshing does not guarantee stability in any situation, especially in areas with zero gaussian curvature [143]. Unlike quadrilateral patterns, hexagonal patterns cannot be creased and therefore do not benefit from a high structural depth.

Structural performance

Creased structures are often considered to be highly efficient. In a study on cylindrical corrugated shell, Buri and Weinand claim that *'the higher the amplitude, the stronger the resistance of the folded plate structure'* [50]. This statement is well documented in the case of flat geometries or arches [154], which were studied by Buri and Weinand. Indeed, creases introduce an equivalent inertia larger than the inertia of the single elements. In structures subject to biaxial stresses, the influence of creases is however not so obvious as it decreases the axial stiffness in the transverse direction.

A study comparing the performance of different patterns for folded plate structures applied to a cylindrical shell was proposed in [100]. It demonstrates that the Miura Ori pattern is subject to much higher deflection than patterns based on trapezoids or the Yoshimura pattern. The choice of an appropriate corrugation strategy is therefore crucial, but the lack of a unifying framework makes the comparison of solutions difficult. Other case studies on wooden plated structures have been made and successful demonstrators were built in recent years [50, 241, 100], but the difficulty to parametrise a design space of feasible solutions with planar quadrilateral facets has limited the generality of these studies.

A multi-objective exploration of a design space of folded plate structures was performed with genetic algorithms in [79, 256]. The proposed design space was however restricted to spherical shapes or to triangular meshes, which are less stable than hexagonal or quadrilateral patterns.

7.4.2 Specific research question

General corrugation strategy

Folded plate structures are rarely applied in the context of free-form structures. This scarceness can be explained by two factors: the complexity of the shape generation procedure and the lack of understanding of doubly-curved creases in the context of civil engineering. The modelling strategies offered to the designers often generate a restricted design space and are peculiar to certain mesh topologies. As an example, an origami folding pattern has to be two-colourable, which makes the modelling of some

topologies impossible. The objective of the next section is to introduce a general framework for the modelling of plated structures covered with planar panels. The proposed method is not restricted to origami, and unifies some of the previous design strategies described in [241]. The corrugation strategy can also be extended to non-standard patterns, like the kagome pattern.

Structural assessment of folded plate structures

Folded plate structures are usually applied to cylindrical shapes, were the crease can be understood as a way to increase the bending stiffness of the shell. In doubly-curved shapes, creases increase the bending stiffness in the crease direction, but decrease the axial stiffness in the transverse direction. These competing effects have rarely been evaluated in free-form structures, and the comparison of different creasing strategies has only been performed on simple examples.

7.4.3 Corrugation strategy

In the second study, we propose here an innovative method to generate free-form folded plate structures. We use the marionette framework, introduced in Chapter 5, and propose two corrugation strategies based on perturbation of the in-plane view. Recall that the marionette technique solves a hyperbolic equation, and that the smoothness of the final shape depends on initial boundary conditions. Therefore, introducing non-smooth in-plane parametrisations yields non-smooth free-form meshes.

Row-Translation Strategy

In [241], the Miura Ori strategy corresponds to the approximation of a cylinder by a Miura Ori pattern. The solution is made of rhombi. In Figure 7.26, a simple way to generate a network of parallelograms from a square grid is proposed. Starting from a reference mesh, the method consists in assigning a displacement to each row of the planar view and then to apply the marionette technique to the transformed planar view.

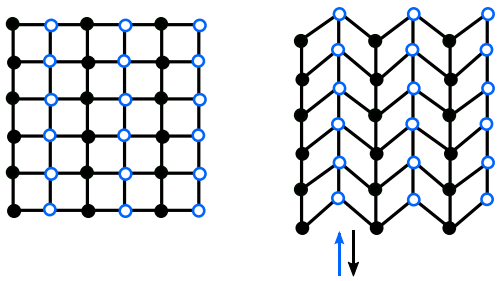

Figure 7.26 – RT strategy for the generation of 'Miura Ori' (herringbone) pattern.

Two parameters are identified to control the corrugation:

- The in-plane corrugation length l, corresponding to the amplitude of the displacement for each row, represented in Figure 7.26;
- The corrugation of the elevation δ, corresponding to the amplitude of the corrugation for one elevation curve.

In the general case, this strategy does not yield foldable pattern. We thus denote it as row-translation (RT) strategy instead of Miura-Ori strategy, which makes explicitly reference to origami and foldable structures.

Alternate-Translation strategy

In [241], a pattern of trapezoids is made on a cylindrical shape. The pattern is generated by local modification of a triangular pattern, but it could be generated directly with a method illustrated in Figure 7.27: the points of the quadrilateral pattern are alternatively translated in two opposite directions.

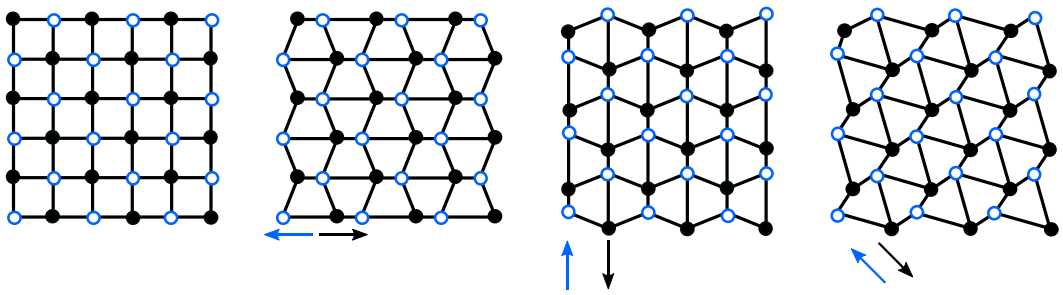

Figure 7.27 – AT Strategy for the generation of 'trapezoid' pattern.

Unlike the Miura-Ori pattern, the elevation curves remain smooth, which leaves two parameters:

- The in-plane crease amplitude l;
- The crease direction, which corresponds to the angle θ made by the translation with the edges of the initial mesh.

By reference to the other proposed strategy, we call this strategy the alternate-translation (AT) strategy.

Controlling complex geometry with NURBS modelling

The geometrical rules underlying creasing strategies make the parametrisation of the design space very light. The marionette method can be used with planar NURBS patches, so that the translations are not specified with respect to absolute values, but to the local coordinate axis of the patches $\mathbf{t_u}$ and $\mathbf{t_v}$. For a general NURBS patch, the translation vector defined is given by:

$$\mathbf{T}(u,v) = l \cdot (\cos\theta \mathbf{t_u} + \sin\theta \mathbf{t_v}) \tag{7.26}$$

The choice of the amplitude can be made with respect to mechanical considerations. Current literature on folded-plate structures makes references on an equivalent structural height to withstand bending. The profile of crease amplitude can also be derived from the bending moment diagram in an equivalent shell.

7.4.4 Definition of the geometry

This section implements the marionette method to generate a design space of folded plate structures covered with planar facets. The two studied geometries are represented in Figure 7.28: they are both derived from a network with two singularities of type 'lemon'. One is a dome without opening, and the other one is obtained by the removal of one sector of the mesh. The two singularities in the closed dome allow for alignment of the mesh on the boundaries, which is meaningful when using creasing strategies. They also illustrate the formal potential of the marionette technique, which allows for the modelling of complex topologies, as shown also in Figure 7.25. The two models are expected to behave differently, as free-edges are known to be a critical issue in thin shell design. The plane view is parametrised with NURBS patches, but is not a parameter of our study. The corrugation strategies introduced in this article are compared. Figure 7.29 represents two plane views of the corrugated domes generated with the AT and RT strategies. Coloured lines correspond to lines with an elevation prescribed with the marionette technique. The initial configuration has an axis of symmetry represented as a thick black line in Figure 6: we choose here to preserve the symmetry. We also point out that the mesh has two singularities and cannot be coloured like a chequerboard (it is not 2-colourable). The two proposed strategies always work with 2-colourable meshes but require adjustments in other cases. The mirroring operation performed here is thus also motivated by topological considerations.

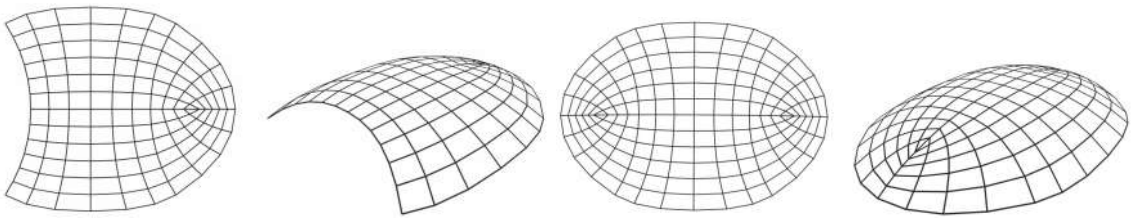

Figure 7.28 – The two configuration studied: a closed dome and a dome with a free edge

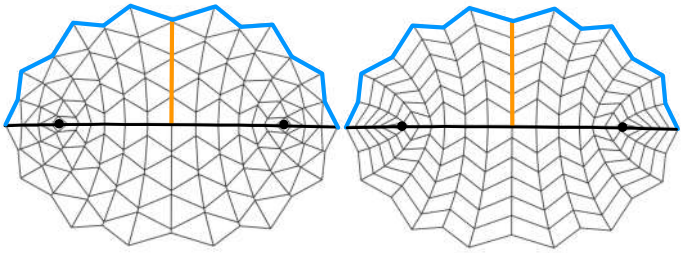

Figure 7.29 – The two corrugation strategies applied to the planar view: AT (left) and RT (right), black dots indicate the two singularities.

7.4.5 Loads, materials, boundary conditions

The material chosen has a Young's modulus of 10.5 GPa. It is no more than a scaling factor when linearised buckling or linear analysis are considered. The boundary conditions are set as pin joints along the edges and translations are fully restrained. In shell design, the governing load case is often a non-symmetrical one (like snow or wind loads for example), as it activates bending moments in the structure. Therefore, we consider a vertical pressure applied on one half of the structure as depicted in Figure 7.30.

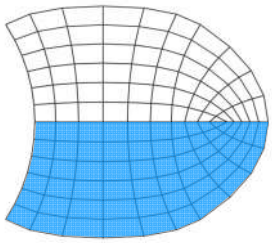

Figure 7.30 – Load distribution: the vertical load is applied to the blue area only.

The study considers the two corrugation strategies introduced in this section. Two mechanical connexions between plates are considered: hinges or moment connections.

7.4.6 Non-dimensional analysis

The structural behaviour of folded plate structures is assessed with two performance metrics: the maximal displacement δ under a given load p and the linearised buckling load p_{cr}. These indicators are useful in conceptual design stages. The detailed design of plated structures requires full non-linear calculations with geometrical imperfections and possibly elasto-plastic design, in the manner of gridshell structures.

Like in many classical works, we present the results with non-dimensional parameters. It has the advantage of reducing the number of parameters thanks to the application of Buckingham Π-Theorem. The geometries described here can be characterised by a span L, a height h and a thickness t. We add

the amplitude l of the in-plane corrugation vector $\mathbf{T}(u, v)$ defined by equation (7.26). The mesh has $n \times m$ subdivisions. The material is characterised by its Young modulus E and Poisson's ratio ν (more parameters can arise when considering orthotropic materials). There are thus seven physical variables, and two units. We can construct five dimensionless parameters that define uniquely the problem.

The first one is the rise-over-span ratio, which is typically between 15% and 40% for gridshells [226]. We chose two values for this ratio: 15% and 35%.

$$\Pi_1 = \frac{h}{L} \tag{7.27}$$

The second is the corrugation ratio, which indicates the level of corrugation in the surface. It can take values between 0 and 0.5.

$$\Pi_2 = \frac{nl}{L} \tag{7.28}$$

As an example, Figure 7.31 shows four ellipsoidal shapes with varying corrugation ratios, all other parameters being equal. The overall shape is unchanged, but local crumbling is added, creating large ribs. The geometries displayed in Figure 7.31 are studied in Section 7.4.7.

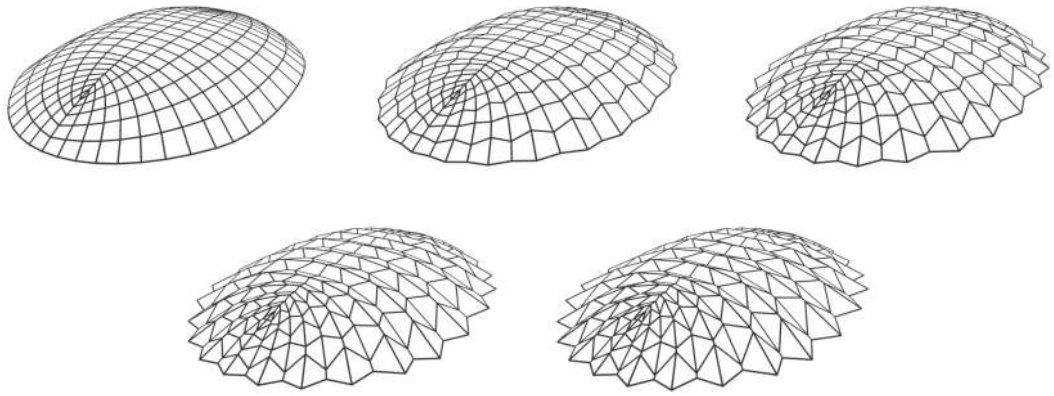

Figure 7.31 – Domes generated with AT strategy, with different corrugation ratios (from left to right and top to bottom:$\Pi_2 = 0, 0.1, 0.2, 0.3, 0.4$)

The third ratio is the slenderness, typically below 1% for applications in high-performance shells.

$$\Pi_3 = \frac{t}{L} \tag{7.29}$$

Higher values of Π_3 correspond to higher bending stiffness, relatively to the axial stiffness. Indeed, writing $\mathcal{D}$ and $\mathcal{A}$ the bending and axial stiffness of the plate, the quantity introduced in equation (7.29) can be described by:

$$\Pi_3 \propto \sqrt{\frac{\mathcal{D}}{\mathcal{A}L^2}} \tag{7.30}$$

The next two ratios correspond to non-dimensional buckling load and displacement. They are the performance metric studied in the next section.

$$\Pi_4 = \frac{p_{cr}L^3}{Et3} \tag{7.31}$$

$$\Pi_5 = \frac{\delta E t^2}{pL^3} \tag{7.32}$$

The results are not normalised with respect to the mass, like usually done in studies on structural efficiency [154, 165]. The mass of the corrugated structures varies indeed by less than 1%, so that Π_4 and Π_5 can be considered as reliable indicators of structural efficiency. In the following, we set the span L and the Young's modulus E as constants. The other parameters can be varied.

7.4.7 Dome buckling

AT Strategy

The results of the linearised buckling calculation for a closed ellipsoidal dome are displayed in Figure 7.32. The parameter studied is the corrugation factor and the performance metric represented is the linear buckling load. Low values of Π_2 indicate smooth geometry and values of Π_2 close to 0.5 indicate highly creased structures (see Figure 7.31). Plates with rigid connections have a substantially higher bearing capacity than hinged plates for geometries without corrugations. Their bearing capacity is however less affected by corrugation: the critical buckling load increases by approximately 30% for rigidly connected shells, and up to a factor 10 for hinged plates. The bearing capacity increases with the rise-over-span ratio. The structure with $h/L = 0.35$ have a linear buckling load two times larger than structures with $h/L = 0.15$.

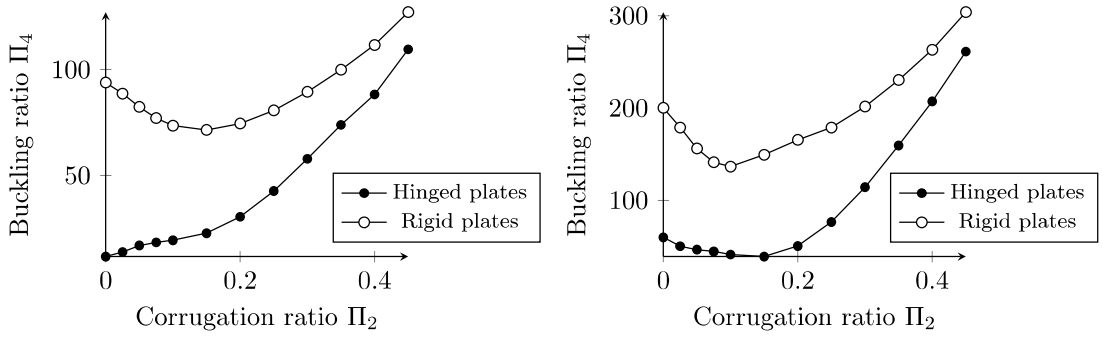

(a) $h/L = 0.15$ (b) $h/L = 0.35$

Figure 7.32 – Buckling load vs. corrugation factor ($t/L = 1\%$, AT strategy)

Low levels of corrugation appear to decrease the bearing capacity of structures with rigid connections, with a minimum reached for $\Pi_2 = 0.15$. For higher values of Π_2, the corrugation increases the structural performance. The effect of corrugation could thus be interpreted as a geometrical imperfection applied to slender structures, like gridshells [165, 49, 169]. Figure 7.33 shows that the ratio of the critical buckling loads $p_{cr,rigid}/p_{cr,hinged}$ decreases with the corrugation amplitude. This tendency shows that the corrugation creates a geometrical interlocking of the plates, which has a rigidifying action. It can be noticed that the ratio $p_{cr,rigid}/p_{cr,hinged}$ decreases with the rise-over span ratio for low corrugation levels (small values of Π_2). For example, for $h/l = 0.15$ this ratio can go up to 8, whereas it is not larger than 4 for $h/l = 0.15$. This can be explained by the fact that shallow structures rely almost only on bending: the influence of the bending rigidity of the links between plates governs then the structural response.

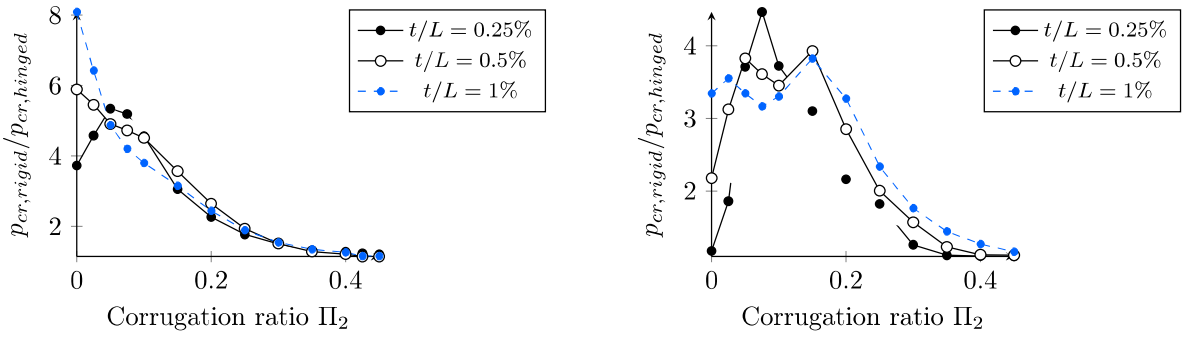

(a) $h/L = 0.15$ (b) $h/L = 0.35$

Figure 7.33 – Ratio of the linearised buckling loads for the rigid and hinged plates configurations (AT strategy)

The results on maximal displacements indicate that structures with small corrugations are less rigid than the reference geometry. Figure 7.34 shows the non-dimensional displacement in function of the corrugation factor. Past a certain corrugation factor (with Π_2 from 0.1 to 0.2), the displacements decrease with corrugation. The stiffest configuration remains the initial one in our study: if only maximal displacement is considered, the interest of crease is therefore non-existent for the considered case study. Recall that corrugation of creased structures increases the bending stiffness in one direction, but decreases the axial stiffness transverse to that direction. We can interpret the curve as follows: first, the axial stiffness diminishes in the transverse direction with small corrugations, but is not compensated by the increase of the bending stiffness. For sufficiently high corrugations, the stress distribution becomes mainly uni-axial and the bending stiffness introduced by the creases governs the structural response. It should be noted however that high corrugation (superior to 0.2) diminishes differences between hinged and rigid connections, as illustrated in Figure 7.35.

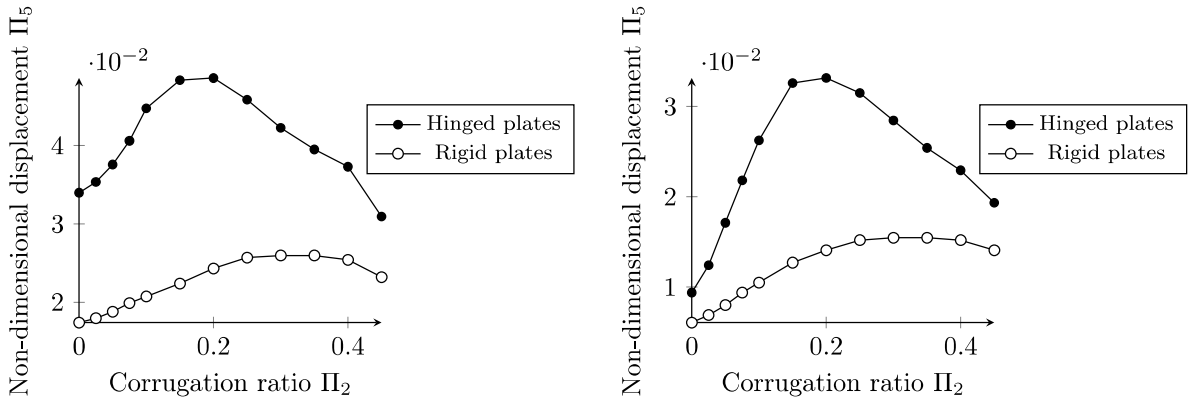

(a) $h/L = 0.15$ (b) $h/L = 0.35$

Figure 7.34 – Non-dimensional displacement vs. corrugation factor ($t/L = 1\%$, AT strategy)

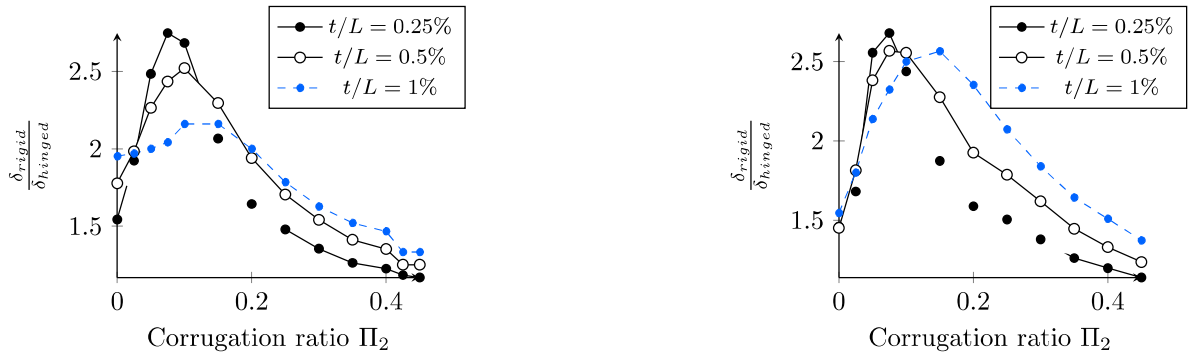

(a) $h/L = 0.15$ (b) $h/L = 0.35$

Figure 7.35 – Ratio of the maximal displacements for hinged and rigid plates (AT strategy)

RT Strategy

Plated structures meshed with the RT strategy behave differently from the ones meshed with the AT strategy. Hinged plates are indeed substantially less efficient than rigid plates for any level of corrugation, as shown in Figure 7.36. In some cases, the corrugation even decreases systematically the buckling capacity of folded plate structures. The rigid plates reach the same buckling load as with the AT strategy

for high corrugations. Plates with hinged connections have however a lower buckling load. This would advocate for the choice of the AT strategy, but the RT strategy yields displacements lower by 50%. Consider for example Figure 7.37a: the lowest non-dimensional displacement obtained for the hinged plates is of 0.021 (for $\Pi_2 = 0.45$), which is lower than the minimum reached for the AT strategy shown in Figure 7.34 (minimum non-dimensional displacement of 0.031). The choice of the most appropriate corrugation strategy is thus a matter of multi-criteria optimisation. The detailed analysis of the governing design criterion is needed to determine the most interesting corrugation strategy.

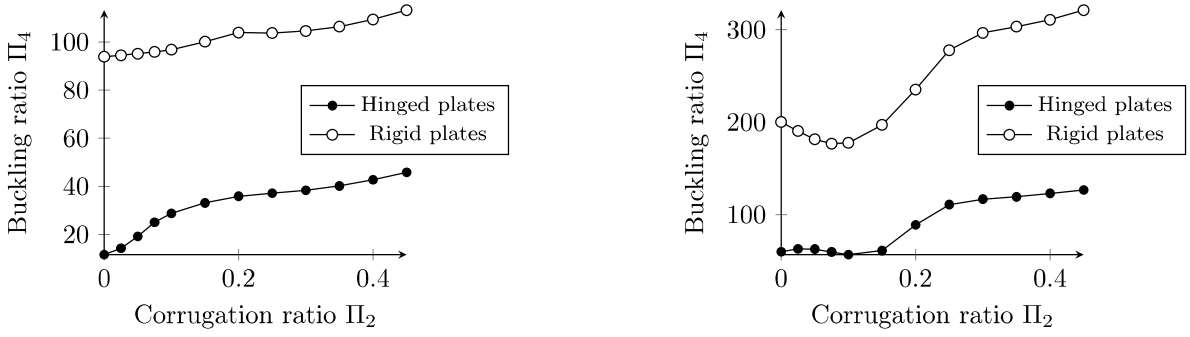

(a) $h/L = 0.15$ (b) $h/L = 0.35$

Figure 7.36 – Buckling load vs. corrugation factor ($t/L = 1\%$, RT strategy)

Figure 7.38 represents the ratio between maximal displacements of folded plate structures with hinges or moment connections. This ratio increases for low levels of corrugations, and decreases after a peak reached approximately for $\Pi_2 = 0.2$. Folded plate structures with rigid links remain at least 40% stiffer than folded plate structures with hinges. It can be concluded that for the RT strategy, the bending stiffness of the links is critical and should be considered with special attention by the designers.

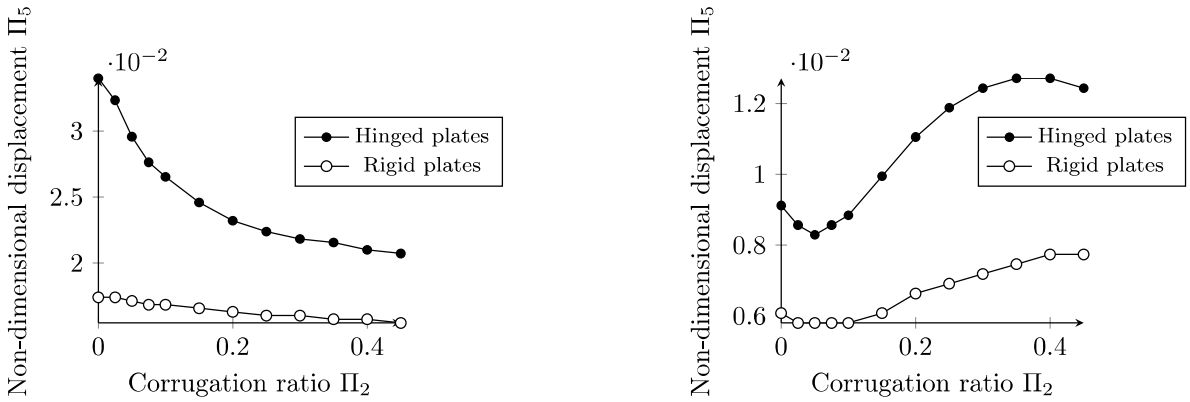

(a) $h/L = 0.15$ (b) $h/L = 0.35$

Figure 7.37 – Non-dimensional displacement vs. corrugation factor ($t/L = 1\%$, RT strategy)

7.4.8 Dome with free-edge

AT Strategy

Consider now the same elliptical dome where an opening has been created, such as shown in Figure 7.28. The resulting free-edge changes the structural response of the shell under non-symmetrical loads. Unlike the closed dome, the corrugation improves significantly the bearing capacity of both hinged and

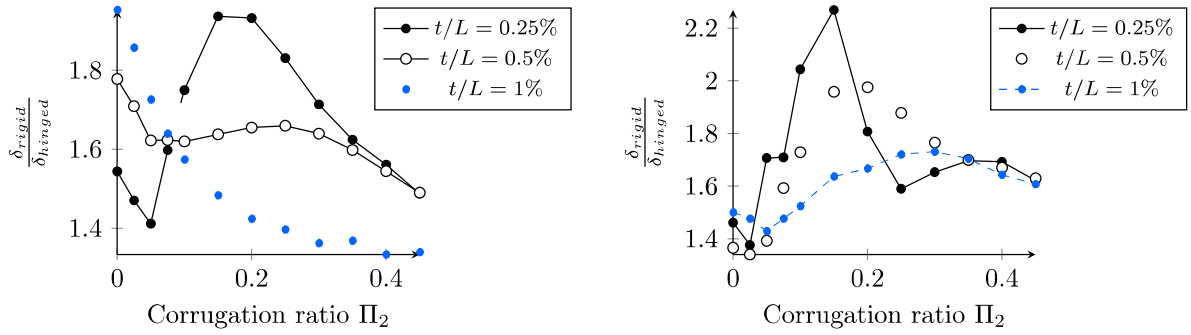

(a) $h/L = 0.15$ (b) $h/L = 0.35$

Figure 7.38 – Ratio of the maximal displacements for hinged and rigid plates (RT strategy)

rigid structures, as shown in Figure 7.39a and 7.39b. Compared to the reference geometry, the critical buckling load is multiplied by up to 4.

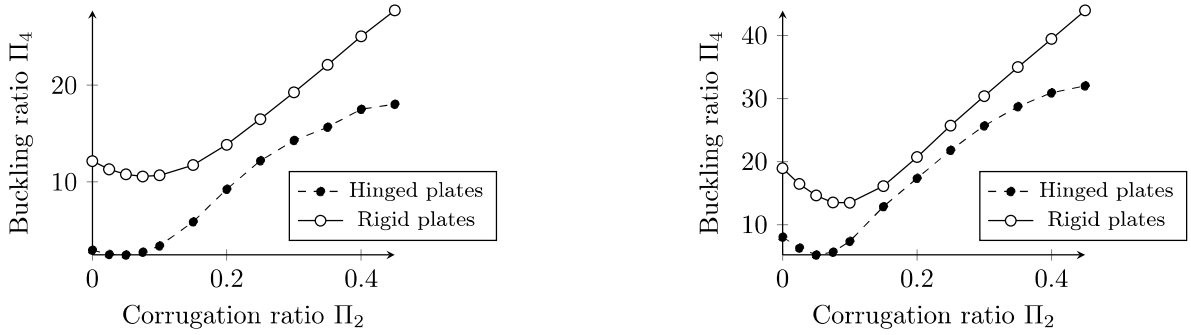

(a) $h/L = 0.15$ (b) $h/L = 0.35$

Figure 7.39 – Buckling load vs. corrugation factor ($t/L = 1\%$, AT strategy)

Figure 7.40 shows the ratio $p_{cr,rigid}/p_{cr,hinged}$ with respect to the corrugation factor. The ratio converges quickly to a value around 1.3. The curve features a plateau for corrugation factors superior to 0.2, which is not observed for the RT strategy on Figure 7.43.

RT Strategy

The RT and AT strategy yields similar results for the linear buckling analysis. The bearing capacity of plated structures is improved by corrugation, as shown in Figure 7.42.

Figure 7.43 displays the ratio $p_{cr,rigid}/p_{cr,hinged}$ in function of the corrugation ratio. For low corrugation levels, plates with rigid attachment have a much higher linear buckling load, but the ratio $p_{cr,rigid}/p_{cr,hinged}$ decreases down to 1.4 for high corrugations. The difference between hinged plates and rigid plates is therefore still important, although the convergence shows that the corrugation decreases the sensitivity to the stiffness of the mechanical attachment between plates.

The main difference between the AT and RT strategy concerns the influence of the corrugation on the maximal displacements. Figure 7.44 shows that the ratio Π_5 decreases less for the RT strategy than for the AT strategy: there is no local minimum for the curves shown in Figure 7.44. The corrugated structures can be up to 2 times stiffer than the non-corrugated ones, which still validates the use of corrugation for shells with free edges

(a) $h/L = 0.15$ (b) $h/L = 0.35$

Figure 7.40 – Ratio of the linearised buckling loads for the rigid and hinged plates configurations

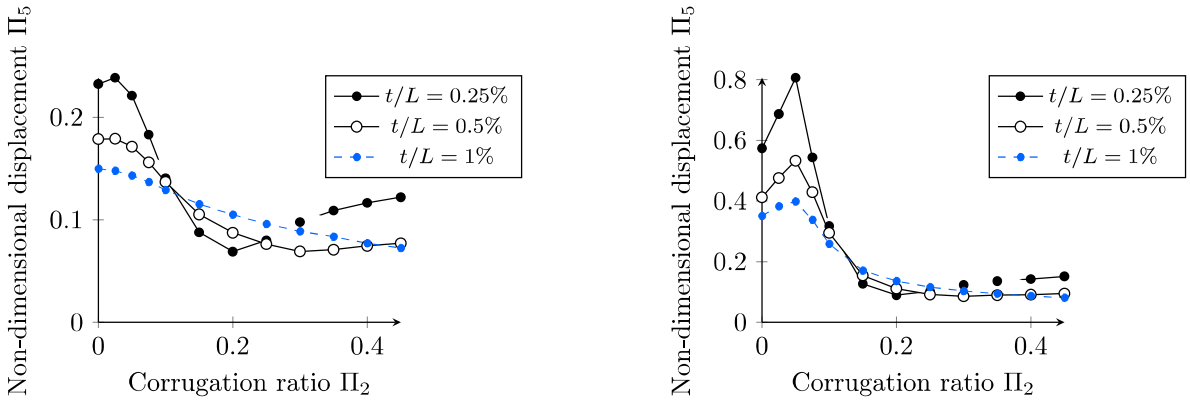

(a) Rigid plates (b) Hinged plates

Figure 7.41 – Non-dimensional displacements vs. corrugation ratio ($h/L = 0.15$), AT strategy

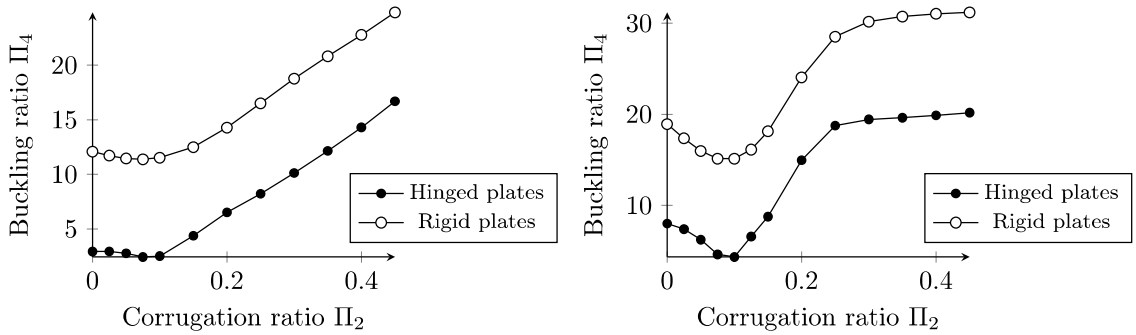

(a) $h/L = 0.15$ (b) $h/L = 0.35$

Figure 7.42 – Buckling load vs. corrugation factor ($t/L = 1\%$, RT strategy)

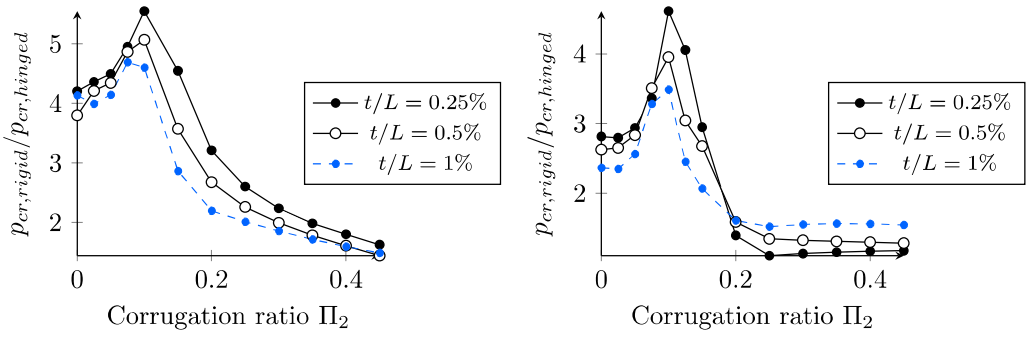

(a) $h/L = 0.15$ (b) $h/L = 0.35$

Figure 7.43 – Ratio of the linearised buckling loads for the rigid and hinged plates configurations

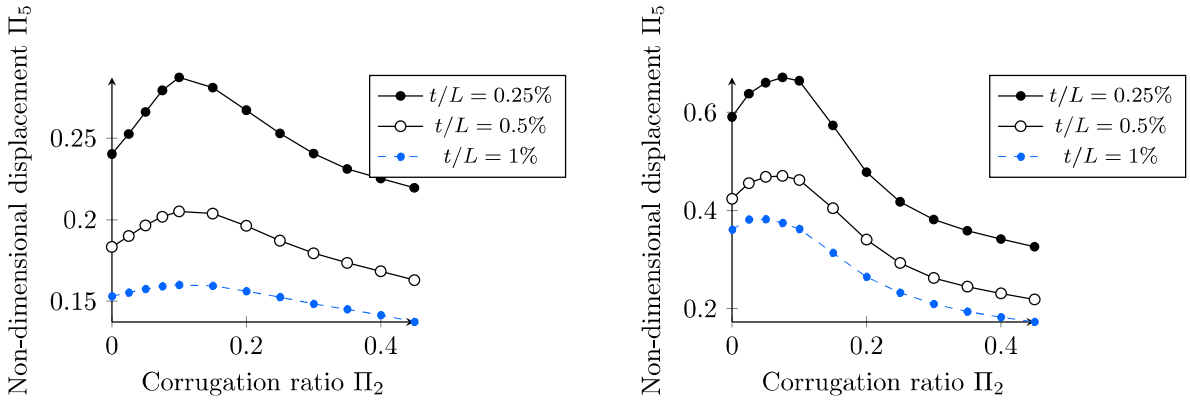

(a) Plates with rigid links (b) Hinged plates

Figure 7.44 – Non-dimensional displacements vs. corrugation ratio ($h/L = 0.15$), RT strategy

7.4.9 Discussion

Comparison of the two strategies

The present parametric study considered two different performance metrics: displacement and linear buckling load. In order to compare the two corrugation strategies, the Pareto optima were computed. Structural engineers aim at minimizing the displacements and at maximizing the linear buckling load. Figures 7.45a and 7.45b show some of the data generated in our study. The optimum of both values is generally not reached for the same values of parameters. In Figures 7.45a and 7.45b, elements belonging to the Pareto frontier are those were no element could be found in the top left quadrant.

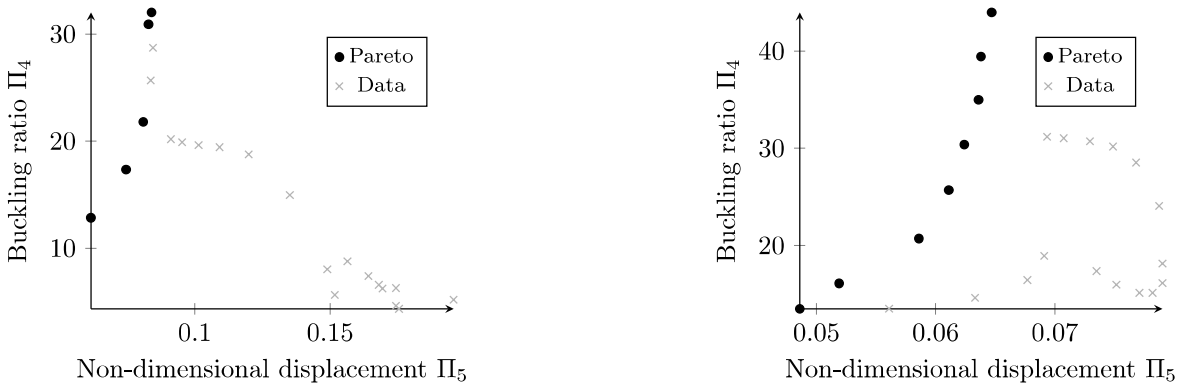

(a) Hinged plates

(b) Rigidly linked plates

Figure 7.45 – Pareto frontier for the open dome, $t/L = 1\%$, AT strategy

In Figures 7.45a and 7.45b, Pareto optimal design are generated with the AT strategy. This is a general observation for the shell with a free edge. For moderate corrugations, the AT strategy also yields significantly stiffer structures (by a factor 3 approximately). It was already observed in [241] on one specific arch design for a symmetrical load. As already discussed in Section 7.4.7, the closed dome configurations have Pareto optima in both the AT and RT design space. The AT strategy increases significantly the linear buckling load while the RT strategy improves the structural stiffness. The parametric study is thus less concluding for the closed domes, as the optimal strategy depends on the weighting of the two factors.

Design guidelines for folded plate structures

Creased structures offer a design space that has not yet revealed its full potential. The numerical exploration of the space of feasible design is eased with our simple strategies that require few parameters. The computational cost for a systematic study on the influence of corrugation remains however high, as mesh refinements are inevitable and lead to large models. The case studies performed in this section allow us to provide some guidelines for future design explorations with plated shell structures.

First, the numerical study demonstrates that plated structures are highly sensitive to imperfections. A small change in the initial geometry can greatly modify the buckling capacity of plated shells, especially for non-corrugated shapes. As corrugation increases, the structure transitions from shell behaviour to arch behaviour. Indeed, curved corrugated structures loose stiffness in the transverse direction, as illustrated in [185]. The structural performance of plated shells with moderate values of corrugation is thus poor, since it does not benefit of two-way stress distribution or large equivalent bending stiffness.

Second, it appears that creased plated shells are efficient for structures with a uniaxial stress state. For example, barrel vaults are subject mainly to uniaxial stresses, and the corrugation improves significantly the structural behaviour. On the contrary, creasing does not seem to necessarily be a meaningful strategy when the smooth structures rely on biaxial stress state. In those cases, the geometry forces the loads to follow the ridges and valleys of the corrugation, turning a biaxial stress state into a uniaxial one. In our case study on domes, corrugated structures are less rigid than non-corrugated ones. Therefore, creasing

strategies should be used in priority for structures with a privileged spanning direction. Examples of such structures include barrel vaults, toric shapes like stadia, shells with free edges or shells on punctual supports.

Third, it is noticed that the rotational stiffness between plates influences the overall structural behaviour, especially for low levels of corrugation. Configurations with fully connected plates are more rigid, but are more difficult to fabricate. Our strategy introduces configurations that are not foldable, and guarantees the stability of structures even with hinges between plates.

Finally, the objective functions associated to the performance metrics used in this chapter are not convex. Furthermore, the data generated in this study considered mainly the influence of corrugation on the structural performances of plated shell structures. This advocates for the use of global optimisation algorithms for the structural optimisation of plated shell structures and validates the approach used in [256, 79].

7.5 On the potential of geometrically-constrained approach

7.5.1 Gridshells with semi-regular patterns

This chapter proposed Irregular, but beautiful patterns can also be used for steel gridshells [6]. For these irregular meshes it is harder to get an intuition of the design space, and in those case it is meaningful to use a more general approach than the marionette mesh. Still prescribing the planar view, the problem of facet planarity is linear and it is possible to compute the space of solutions with a singular value decomposition (SVD): this problem has been studied in [192].

7.5.2 Folded plate structures with non-standard patterns

This work focused on quadrilateral meshes, as it is commonly used for folded plate structures. The marionette method can however be generalized to other patterns, as illustrated in Chapter 5 [166].

Patterns mixing valence four or three, like the Cairo tiling could be of interest in future work. The valence three would provide stability for hinged plates whereas the valence four makes the pattern more flexible than hexagonal pattern. A post rationalisation technique for the modelling of semi-regular meshes with planar facets has been proposed in [118]. The method requires however good initial input, for example when the mesh layout follows the lines of curvature of the surface or conjugate curve network. The marionette technique and other bottom-up design strategies, like the ones introduced in Chapters 3 and 4 should be investigated to provide such parametrisations.

7.5.3 Towards double-layer shells: free-form sandwich panels

Creased patterns and origami have a potential beyond folded plate structures. Sandwich panels based on the Miura Ori folding pattern like the one depicted in Figure 7.46 were considered from the 1960's. In those applications, the folding pattern is used for the core of the sandwich panel and guarantees out-of-plane shear stiffness, whereas the skins assure the bending stiffness. Since the deflections of thin plates are mainly governed by their bending rigidity, the materials used for the core and skins can be different: typically the skins are made out of a 'noble' material, like aluminium, and the core can be made out of lower grade, cheaper material. The behaviour of sandwich panels with the Miura Ori pattern is described in [136, 139], which demonstrates that the shear stiffness of such panels is superior to the one of honeycomb sandwich panels.

Despite their remarkable structural properties, sanwich panels with origami have not been applied to doubly-curved structures. This can be understood by the difficulties encountered in the connection between the core and the skins which arises for flat panels and is expected to be even greater with curved structures. While this remark holds for small-scale sandwich panels found in the aeronautics industry, the construction of doubly-curved structures at the scale of a building can be revisited with the marionette technique. Keeping the topology of the Miura-Ori sandwich panels, we can write a new problem depicted in Figure 7.47. The geometrical restrictions to impose follow:

- Assure the planarity of the panels constituting the core;

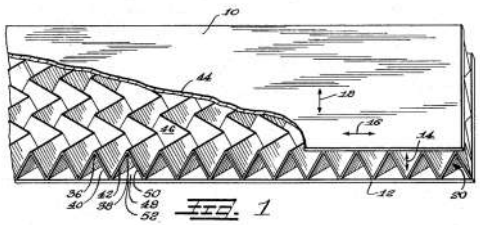

Figure 7.46 – Sandwich panel based on the Miura Ori pattern [207]

- Assure the planarity of the panels constituting the upper layer (skin);
- Assure the planarity of the panels constituting the lower layer (skin);
- Assure proper compatibility between core and upper skin;
- Assure proper compatibility between core and lower skin;

Each of this items corresponds to the computation of a vector space of solutions with the marionette method. The compatibility conditions are equivalent to the intersection of the three vector spaces. The marionette method could be helpful to compute such vector spaces of solutions and assess the formal potential of doubly-curved sandwich panels, like discussed in Chapter 5.

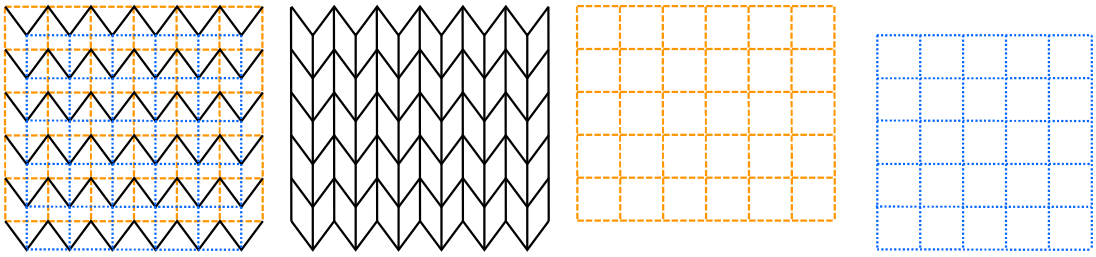

Figure 7.47 – From left to right: connectivity of a sandwich panel, core, upper layer, lower layer.

This possibility requires to be implemented and will be studied in future work. A proposition has been done recently for timber sandwich panels based on a honeycomb pattern covering a simple cylindrical shape. However, sandwich panels usually feature different materials for the core and skins: the core provides shear rigidity, whereas the skin withstand the bending loads: the mechanical requirements on the skin are thus much more demanding. Finally, the choice of appropriate material and subsequent structural connexions need to be studied with care, and such considerations exceed the scope of this discussion. The marionette technique provides however a promising way to generate technologically-feasible curved sandwich panels at the scale of a building.

7.6 Summary of intellectual contribution

In this Chapter, we proposed the evaluation of the potential of the marionette technique for the design of non-conventional structural systems. The study reveals the interest of bottom-up strategies for fabrication-aware design. The very existence of this study demonstrates indeed that the tools developed in this dissertation allow the designer to explore numerous variations. More than 800 geometries covered with planar facets were generated and evaluated without the need of post-rationalisation. To the best of our knowledge, this investigation is the broadest structural exploration of a fabrication-aware design space performed together with the study of Chapter 6.

The results of the comparative studies performed in this chapter lead to an assessment of some innovative structural systems. Kagome gridshells are revealed to be more efficient than quadrangular gridshells

for two simple design criteria: linear buckling and maximal displacement. The difference between the two systems is explained by the isotropy and higher in-plane shear stiffness of the kagome gridshell. A simplified homogenised linear buckling load is derived and illustrates the importance of the in-plane shear stiffness. Quadrangular and kagome gridshells share many technological similarities: the study presented in this chapter suggests that kagome gridshells could be a viable alternative to rigid quadrangular gridshells used nowadays. More detailed calculations, using material and geometrical nonlinearities should be performed in order to confirm this statement. The comparison of kagome gridshells to triangular gridshells could also be made, but they have different complexity due to different node valence. In this case, the mechanical behaviour is not the only factor of choice, and the node complexity should be taken into account in order to compare the cost of triangular and kagome gridshells.

Two creasing strategies were then proposed to generate folded plate structures with planar quadrangular facets. The marionette framework unifies previous design approaches based on origami or restricted to tessellations of the sphere. The comparison of the two methods demonstrates that creasing is not necessarily a meaningful strategy. Low levels of corrugations can be interpreted as geometrical imperfections that lower the stiffness and buckling capacity. Creases are useful mainly on structures that have a free-edge, which is an observation that was made in previous research.

Finally, we discussed possible explorations with the geometrically-constrained methods proposed in this dissertation. Other structural systems could be explored, like doubly-curved sandwich structures. The range of applications of the marionette technique is large, since it is not restricted a specific pattern. This chapter did not propose an exhaustive investigation of the topic, due to the many possibilities offered by the marionette method. A more complete cartography of the possibilities offered by different patterns and methods (like generalised cyclidic nets), both in terms of design freedom and in terms of mechanical performances could be made and provide guidance to structural engineers and architects.

Chapter 8

Conclusion and perspectives

8.1 Intellectual contribution on structural morphology

In his paper *'New challenges for the structural morphology group'*, BORGART identified three research questions to guide the research on structural morphology:

- Do we need computational design tools, black boxes or a greater understanding?
- Do form finding and optimization methods result in a required result and constructable design?
- Do complex geometry structures need new structural typologies?

A posteriori, we believe that this dissertation remarkably echoes these three question and therefore we will use them to analysis its main contributions.

8.1.1 New tools for understanding complex geometries

Architects and engineers need to construct a mental representation of the design space. This requires an understanding of complex notions. Being able to put a name on a shape or a structural element is an important part of this thought process. Each word embeds a collection of notions that are implicitly shared by architects and engineers. For example, the words 'arch' of 'cable' refer to shapes (parabola), but also to a mechanical behaviour (compression or tension forces). In the second part of this dissertation, we refer to the vocabulary of analytical shapes, which is not commonly done with computational techniques. The designers can rediscover well-known shapes and generate them with interesting fabrication properties.

In Chapters 3, 4 and 5, modelling methods referring to the cultural background of architects and engineers have been proposed. Starting from simple transformations, namely discrete Combescure transformations and Möbius transformations, we demonstrated in Chapters 3 and 4 that it is possible to generate doubly-curved shapes intuitively from a few control curves. More precisely, Chapter 3 introduced isogonal moulding surfaces, a family of shapes with high node congruence. The role of Combescure transformations and of the integral of gaussian curvature of the surfaces for their generation has been illustrated. The approximation of Monge surfaces by surfaces of revolution was also proposed and guaranteed repetition of nodes, members and panels with a design freedom comparable to scale-trans surfaces. In Chapter 4 we then used the geometry of circles to generate shapes parametrised by their lines of curvature. We have shown that it is possible to expand the family of canal surfaces easily by combining Combescure and Möbius transformations. We also proposed the generalisation of cyclidic nets to non-smooth surfaces with doubly-curved creases and to complex topologies. We hence provided a framework for doubly-curved creases, a structural typoogy that had fruitful applications in thin shell design, but which were left apart by computational methods so far.

Chapter 5 revisited descriptive geometry to generate shapes covered with planar facets. The resulting shape generation method is called *marionette technique*. It refers specifically to a vocabulary understood by all architects and engineers. Its principle is very simple and can be hand-drawn. In that sense, we believe that the marionette technique is a computational design tool that helps the designer to build

an intimate understanding of construction constraints.The computational tools available to the designer with our methods are primitives using two or three curves or tools resembling Bézier surfaces. This recalls shape generation tools used previously, which should thus be of intuitive use.

8.1.2 Rationality in structural optimisation

The second research question deals with fabrication of mechanically optimal design. It is clear that classical structural optimisation does not deal with construction constraints, so that the results have a limited practical interest. For Borgart, *'The result [of structural optimisation or form-finding] is an unusable design tool, which is the reason they are not widely used in practice at current. The possible solution would be to incorporate the fabrication aspects (production and assemblage) as variables or constraints into the form finding process (design tool).'* There are other reasons that explain why optimisation is not more used in practice, but this dissertation has addressed the question of construction rationality in structural optimisation.

The marionette technique was adapted to provide a CAD-based parametrisation of the design space. A benchmark compared the relative performances of NURBS and marionette parametrisation for structural optimisation. The study illustrated the potential of the marionette method, for which the structural optimisation is at least as efficient as for NURBS models. The resulting structures are all constructible at a reasonable cost, since they integrate construction constraints. This application is a step made by optimisation towards the engineering practice.

8.1.3 Innovative structural typologies

This dissertation was not meant to be limited to one structural system, but rather to provide new methods to generate innovative structural configurations. Chapter 7 studied two non-standard structural systems: gridshell based on the kagome grid pattern and folded plate structures. The relevance of the two systems has been assessed with comparative parametric studies. The kagome grid pattern was demonstrated to be comparable to quadrilateral gridshells in terms of complexity of fabrication, but it has a higher stiffness and buckling capacity. Two methods for the generation of planar kagome meshes have been proposed in Chapter 5: the first one is a conversion from PQ-mesh, and the second is based on the marionette technique. The marionette method has also been used to generate non-smooth plated structures. Their interest lies within the fact that they do not derive from origami, and have an intrinsic geometrical stiffness. New creasing strategies have been proposed and their performance have been evaluated for quadrilateral meshes. These strategies could be extended to other patterns.

The potential offered by the marionette technique and by generalised cyclidic nets has yet to be fully explored. Non-smooth shapes can also arise from generalised cyclidic nets, so that the study performed in Chapter 6 could be applied to this framework as well. The mastering of discrete offsets (for example the fast computation of Combescure transform used for super-canal surface) makes also the construction of double layer structures possible, so that many opportunities for new structural typologies may arise from the tools proposed for geometrical modelling.

8.2 Possible developments

The methodology proposed in this dissertation has led to different applications. To pursue Borgart's idea, we propose different research axes that derive from the findings of this dissertation.

- Can we find an unifying framework for form-finding and fabrication-aware design?
- Do we need mesh-based or surface-based modelling tools?
- How can we take new technologies of fabrication into account?
- How do we make the findings of structural morphology accessible to our community?

8.2.1 Fabrication-aware form-finding

This dissertation proposed different methods for geometrically-constrained mesh generation. An investigation of the structural performance of some structures generated with the marionette technique demonstrated that this framework can yield mechanically efficient solutions. The tools used to assess the possibilities of the marionette technique were structural optimisation and the systematic exploration of parametric design spaces. So far, the possibilities to combine our methods with mechanical form-finding have not been evaluated.

There is nonetheless a great potential for a combined form-finding approach merging mechanics and geometry, especially with the Marionette technique. We have seen that the Marionette technique takes the point of view of affine geometry and finds a vector space of solution for the facet planarity constraint. This space of solutions could be computed using Singular Value Decomposition. We have seen in the literature review that the force-density method also solves a linear system of equations, and that linear constraints can be taken into account, again with the aid of SVD. Another example of applications of linear algebra to form-finding problems is the study of tensegrity structures: the existence of kinematics can also be determined by SVD [190]. Therefore, linear algebra and efficient SVD computation could give a unifying framework for facet planarity and computation of equilibrium.

8.2.2 Isogeometric analysis with the marionette technique

In Chapter 6, we proposed to use the marionette technique to parametrise structural optimisation problems and evaluated the relevance of this proposition. The computation were based on classical finite element analysis. We believe that there is a potential to use isogeometric analysis for the evaluation of thin shell structures, in the manner of [257]. This implies the computation of NURBS or T-splines parametrised by conjugate curve networks. The problem can be written as an optimisation problem with non-linear constraints and can be linearised with the point of view using planar projections. Progress in this direction could bridge the gap between discrete and smooth geometry as well as improving computation time for structural analysis.

8.2.3 New technologies in the construction industry

Motro's force-form diagram considers technology as one of the five aspects of structural morphology. The late 1990's and the early 2000's have seen the democratisation of numerically controlled production tools in architecture. Moving away from a paradigm of standardisation, these tools allow for more flexibility in the fabrication process. This shift of the industry will bring new possibilities and new complications. The possibilities of 3D printing or robotic fabrication are often seen as game changers in the construction industry, but their limitations are not necessarily well understood. Those new technologies bring new sets of constraints, which means new shapes and new design spaces. In order to better understand the limitations and potential of new technologies, future research should aim at formalising the new fabrication constraints and identify geometrical invariants, like the one used in this work.

8.2.4 Propagation methods and innovative structural systems

Propagation methods correspond generally to Cauchy-type problems. They result in intuitive tools for surface generation, with a perfect control of two boundaries. The control of the two other boundaries is however more difficult. The example of marionette meshes shows for example that loops need special conditions in order to be properly closed. We made a connection between this problem and the periodicity of a solution in a Cauchy-type problem. In the marionette formalism, this condition is linear, and thus easily expressed or interpreted. The exploration of other propagation algorithms will need to be supported on a better understanding of periodicity conditions for hyperbolic equations.

Some constructions constraints naturally yield hyperbolic equations. For example, elastic gridshells are usually built with a constant-length grid pattern, which is called Tchebychev net. It is possible to adapt the methods proposed in this dissertation for the generation of gridshells covered with PQ-mesh or developable strips [72]. We believe that many other structural systems, like reciprocal frames, could benefit from such methods.

8.2.5 Shape grammar for free-form architecture

The literature review demonstrated that structural morphogenesis relies historically on the composition of complex shapes. The present dissertation focused on new generating principles for doubly curved shapes with constructional rationality, leaving the question of shape composition largely unexplored. Automated methods for shape composition have been famously employed in architecture, and applications of grammar have been proposed to structures in [176]. Such methods are necessary to unleash the possibilities of fabrication-aware design.

8.2.6 Teaching of architectural geometry

Geometry is often thought as the common language between architects and structural engineers. The way we teach geometry to architecture and engineering students defines the vocabulary that would be available to young practitioners, and their ability to communicate with each others. We believe that providing intuitive tools for the understanding of complex geometrical concepts could benefit to both architects and engineers. Geometry is indeed not limited to computation, but is an element of language used to establish a dialogue between people from different backgrounds.

Our literature review has demonstrated a strong interest in computational techniques applied to architectural geometry: this kind of approach is extremely relevant for research purpose, but it does not construct a common ground for the understanding of geometry. Simple notions, like Möbius transformations or marionette meshes could however provide simplified frameworks for the teaching of geometry. Perhaps the biggest room for exploration for the geometrical methods proposed in this dissertation lies within the education of future builders with playful and intuitive tools.

8.3 Conclusion

Shepherd advocated for a renewal of geometrical modelling tools, stating that *'It is time for a Tabula Rasa in terms of how software is used to design complex geometry structures'*[231]. We believe that radical changes must be made in the way we model free-form architecture but proposed a different approach.

Previous work on structural morphogenesis are often thought as universal solutions, like surfaces of subdivision, Pascalian forms, or mesh optimisation methods. Rather than proposing one unique framework that would span between all possible technological applications for free-form structures (glazed structures, concrete shells, elastic gridshells, tensile or pneumatic structures, vaults, and structural systems to be invented), we propose different modelling frameworks suited for particular technological applications. Each set of technological constraints is analysed and provides the user with a tailor-made design space: there is indeed no reason to use the same tool to model a concrete shell, a reciprocal frame, a GFRP gridshell or a tensile structure. Each technology has its own peculiarities, so that it is meaningful to navigate through different design spaces following the material and technological constraints.

The applications of the shape generation methods proposed in this dissertation still encounter practical limitation, like the implementation of boolean operations or automation of non-standard pattern generation. In comparison, NURBS benefited from decades of research and development, so that they are fully operational. An effort should thus be made to bridge this gap.

During the course of the present work, several pavilions using some of the notions developed in this dissertation have been built. The tools and methods proposed here would be meaningless if not applied to built projects. We should remember that architectural geometry and structural morphology should be considered applied sciences. Beyond equations, we have yet to find meaningful applications of the theories developed in laboratories by mathematicians, too often for mathematicians. The biggest challenge for the research in architectural geometry remains to be intelligible by the many, to foster creativity and to confront itself with reality .

Bibliography

[1] Journal of the international association for shell and spatial structures, 1993. 2.1.3

[2] Final report summary - ARC (Architectural Freeform Structures from Single-Curved Panels), 2014. 2.3.2

[3] P. Adam. Sur les surfaces isothermiques à lignes de courbure planes dans un système ou dans les deux systèmes. *Annales scientifiques de l'E.N.S.*, 10:319–358, 1893. 4.1.2

[4] S. Adriaenssens and M. Barnes. Tensegrity spline beam and grid shell structures. *Engineering structures*, 23(1):29–36, 2001. 2.4.1

[5] S. Adriaenssens, M. Barnes, and C. Williams. A new analytic and numerical basis for the form-finding and analysis of spline and gridshell structures. 1999. 2.4.1

[6] S. Adriaenssens, L. Ney, E. Bodarwe, and C. Williams. Finding the form of an irregular meshed steel and glass shell based on construction constraints. *Journal of Architectural Engineering*, 18(3):206–213, 2012. 2.1.4, 5.1.2, 7.5.1

[7] S. Alinhac. *Hyperbolic partial differential equations*. Springer Science & Business Media, 2009. 5.1.5, 5.1.5

[8] S. Allen and D. Dutta. Supercyclides and blending. *Computer Aided Geometric Design*, 14(7):637 – 651, 1997. 4.2

[9] J. Argyris, L. Tenek, and L. Olofsson. TRIC: a simple but sophisticated 3-node triangular element based on 6 rigid-body and 12 straining modes for fast computational simulations of arbitrary isotropic and laminated composite shells. *Computer Methods in Applied Mechanics and Engineering*, 145(1-2):11–85, jun 1997. 7.2.3

[10] J. S. Arora. Guide to structural optimization. In *Advances in Structural Optimization*. ASCE, 1997. 6.1.1

[11] K. Arpad. Folded plate structures and components therefor, Jan. 26 1971. US Patent 3,557,501. 7.4.1

[12] M. Ashby. Multi-objective optimization in material design and selection. *Acta materialia*, 48(1):359–369, 2000. 2.4.2

[13] D. Attali, J.-D. Boissonnat, and H. Edelsbrunner. Stability and computation of medial axes-a state-of-the-art report. In *Mathematical foundations of scientific visualization, computer graphics, and massive data exploration*, pages 109–125. Springer, 2009. 2.2.2

[14] J. Bader and E. Zitzler. Hype: An algorithm for fast hypervolume-based many-objective optimization. *Evolutionary computation*, 19(1):45–76, 2011. 6.2.6

[15] M. Bagneris. *Contribution à la conception et à la réalisation des morphologies non-standard: les formes pascaliennes comme outil*. PhD thesis, Université Montpellier 2, 2009. (document), 1.2.3, 2.1, 2.1.3, 2.2.5

[16] M. Bagneris, R. Motro, B. Maurin, and N. Pauli. Structural Morphology issues in Conceptual Design of Double Curved Systems. *International Journal of Space Structures*, 23(2):79—-87, 2008. 2.1.1, 2.1.3

[17] W. Baker. Keynote lecture. 2015. 2.1.3

[18] N. Baldassini. Glass and geometry. In *Glass Processing days*, 2005. 2.3.3

[19] R. Baldock et al. *Structural optimisation in building design practice: case-studies in topology optimisation of bracing systems.* PhD thesis, University of Cambridge, 2007. 2.4.2

[20] K. Bana, K. Kruppa, R. Kunkli, and M. Hoffmann. KSpheres - an efficient algorithm for joining skinning surfaces. *Computer Aided Geometric Design*, 31(7-8):499–509, oct 2014. 4.2.1

[21] M. R. Barnes. Form finding and analysis of tension structures by dynamic relaxation. *International journal of space structures*, 14(2):89–104, 1999. 2.4.1

[22] K. J. Bathe. *Finite Element Procedures.* 2006. 1, 7.2.3

[23] L. L. Beghini, A. Beghini, N. Katz, W. F. Baker, and G. H. Paulino. Connecting architecture and engineering through structural topology optimization. *Engineering Structures*, 59:716–726, 2014. 2.4.2

[24] P. Bézier. Définition numérique des courbes et surfaces i. *Automatisme*, 11(12):625–632, 1966. 1.3.3

[25] D. P. Billlington. *The Tower and the Bridge: the new art of structural engineering.* Princeton University Press, 1985. 2.2.1, 2.4.1, 4.1.3

[26] M. Bizzarri, M. Lávička, and J. Vršek. Canal surfaces with rational contour curves and blends bypassing the obstacles. *Computer-Aided Design*, 64:55–67, jul 2015. 4.3.2

[27] J. Blassel and A. Pfadler. La gare de strasbourg. *Construction métallique*, 45(1):15–36, 2008. 2.3.3

[28] K.-U. Bletzinger and E. Ramm. Form finding of shells by structural optimization. *Engineering with computers*, 9(1):27–35, 1993. 2.4.2, 6.1.3, 6.2.3

[29] K.-U. Bletzinger and E. Ramm. A general finite element approach to the form finding of tensile structures by the updated reference strategy. *International Journal of Space Structures*, 14(2):131–145, 1999. 2.4.1

[30] K.-U. Bletzinger and E. Ramm. Structural optimization and form finding of light weight structures. *Computers & Structures*, 79(22):2053–2062, 2001. 2.4.2

[31] K.-U. Bletzinger, R. Wüchner, F. Daoud, and N. Camprubí. Computational methods for form finding and optimization of shells and membranes. *Computer Methods in Applied Mechanics and Engineering*, 194(30):3438–3452, 2005. 2.4.2

[32] P. Block and J. Ochsendorf. Thrust network analysis: A new methodology for three-dimensional equilibrium. *Journal of the International Association for Shell and Spatial Structures*, 48:167–173, 2007. 2.4.1

[33] P. Bo, Y. Liu, C. Tu, C. Zhang, and W. Wang. Surface fitting with cyclide splines. *Computer Aided Geometric Design*, 43:2–15, 2016. 2.3.4, 4.2.1, 4.4.4

[34] P. Bo and J. Wallner. Circular Arc Structures. *ACM Transactions on Graphics (TOG)*, 30(4):101, 2011. 3.1.1, 3.1.3, 3.5.1, 4.1.3

[35] A. Bobenko. Surfaces from Circles. In *Discrete Differential Geometry*, volume 38, pages 3–35. Springer, 2008. 2.3.4, 4.1.1, 5.1.5

[36] A. Bobenko and E. Huhnen-Venedey. Curvature line parametrized surfaces and orthogonal coordinate systems: discretization with Dupin cyclides. *Geometriae Dedicata*, 159(1):207–237, 2012. 2.3.4, 4.1.2, 4.2.1, 4.3.2, 4.4.1

[37] A. Bobenko, D. Matthes, and Y. B. Suris. Discrete and smooth orthogonal systems: C^∞-approximation. *International Mathematics Research Notices*, 45:2415–2459, 2003. 2.3.4, 4.1.1

[38] A. Bobenko and P. Schröder. Discrete Willmore Flow. In *Proceedings of the third Eurographics symposium on Geometry processing*, page 101. Eurographics Association, 2005. 4.2.5, 4.4.4

[39] A. Bobenko and B. A. Springborn. Minimal surfaces from circle patterns : Geometry from combinatorics. *Annals of Mathematics*, 164:231–264, 2006. 2.3.4, 4.6

[40] A. Bobenko and Y. Suris. *Discrete differential geometry. Integrable Structure.* American Mathematical Society, 2008. 1.4.1, 2.3.2, 2.3.3

[41] A. I. Bobenko, H. Pottmann, and J. Wallner. A curvature theory for discrete surfaces based on mesh parallelity. *Mathematische Annalen*, 348(1):1–24, 2010. 2.3.4

[42] A. Borgart. New challenges for the structural morphology group. *Journal of the International Association for Shell and Spatial Structures*, 51(3):183–189, 2010. 2.4.4, 2.5.1

[43] M. Botsch, L. Kobbelt, M. Pauly, P. Alliez, and B. Lévy. *Polygon mesh processing.* CRC press, 2010. 3.5.1

[44] S. Bouaziz, M. Deuss, Y. Schwartzburg, T. Weise, and M. Pauly. Shape-Up: Shaping Discrete Geometry with Projections. *Computer Graphics Forum*, 31(5):1657–1667, Aug. 2012. 2.3.3

[45] L. Bouhaya, O. Baverel, and J.-F. Caron. Optimization of gridshell bar orientation using a simplified genetic approach. *Structural and Multidisciplinary Optimization*, 50(5):839–848, 2014. 3.1.1

[46] V. Braibant and C. Fleury. Shape optimal design using b-splines. *Computer Methods in Applied Mechanics and Engineering*, 44(3):247–267, 1984. (document), 6.1.1, 6.1

[47] L. Bruno, M. Sassone, and F. Venuti. Effects of the Equivalent Geometric Nodal Imperfections on the stability of single layer grid shells. *Engineering Structures*, 112:184–199, apr 2016. 7.3.1, 7.3.1

[48] K. P. Buchert. *Split Rigidity Theory of Plates, Shells & Stability.* Columbia, 1985. 7.3.1

[49] T. Bulenda and J. Knippers. Stability of grid shells. *Computers & Structures*, 79(12):1161–1174, 2001. 7.3.1, 7.3.1, 7.3.1, 7.3.6, 7.3.6, 7.4.7

[50] H. Buri and Y. Weinand. ORIGAMI-Folded Plate Structures, Architecture. In *10th World Conference on Timber Engineering*, pages 2–5, 2008. 7.4.1, 7.4.1

[51] F. Candela. Structural applications of hyperbolic paraboloidical shells. In *Journal Proceedings*, volume 51, pages 397–416, 1955. 2.2.3

[52] F. Candela. General formulas for membrane stresses in hyperbolic paraboloidical shells. In *Journal Proceedings*, volume 57, pages 353–372, 1960. 2.2.3

[53] E. Catmull and J. Clark. Recursively generated B-spline surfaces on arbitrary topological meshes. *Computer-Aided Design*, 10(6):350 – 355, 1978. 4.5.1

[54] A. Choisy. *L'art de bâtir chez les Byzantins.* Librairie de la Societé Anonyme de Publications Périodiques, 1883. 2.2.1

[55] R. P. Clune. *Algorithm selection in structural optimization.* PhD thesis, Massachusetts Institute of Technology, 2013. 2.4.2, 6.2.5, 6.3.3

[56] D. Cohen-Steiner, P. Alliez, and M. Desbrun. Variational Shape Approximation. *ACM Transactions on Graphics (TOG)*, 23(3):905–914, 2004. 3.5.1

[57] M. Cook, A. Palmer, and J. Sischka. Sage music centre, gateshead-design and construction of the roof structure. *Structural Engineer*, 84(10):23, 2006. 3.3.3

[58] R. F. Crawford and D. B. Schwartz. General instability and optimum design of grid- stiffened spherical domes. *AIAA Journal*, 3(3):511—-515, may 1965. 7.3.10, 7.3.10, 7.3.10, 7.3.10, 7.3.10

[59] L. Cremona. *Le figure reciproche nella statica grafica.* U. Hoepli, 1879. 2.4.1

[60] C. Cui, H. Ohmori, and M. Sasaki. Computational morphogenesis of 3d structures by extended eso method. *Journal of the International Association for Shell and Spatial Structures*, 44(1):51–61, 2003. 2.4.2

[61] B. Cutler and E. Whiting. Constrained planar remeshing for architecture. In *Proceedings of Graphics Interface 2007*, pages 11–18. ACM, 2007. 2.3.3

[62] G. Darboux. *Leçons sur la théorie générale des surfaces et les applications géométriques du calcul infinitésimal.* 1915. 3.3, 4.4.1

[63] P. De Casteljau. Courbes à pôles. *National Industrial Property Institute (France)*, 1959. 1.3.3

[64] B. Deng, S. Bouaziz, M. Deuss, A. Kaspar, Y. Schwartzburg, and M. Pauly. Interactive design exploration for constrained meshes. *Computer-Aided Design*, 61:13–23, Apr. 2015. 2.3.3

[65] B. Deng, S. Bouaziz, M. Deuss, J. Zhang, Y. Schwartzburg, and M. Pauly. Exploring local modifications for constrained meshes. *Computer Graphics Forum*, 32(2 PART1), 2013. 2.3.3, 5.4.3

[66] B. Descamps, R. Filomeno Coelho, L. Ney, and P. Bouillard. Multicriteria optimization of lightweight bridge structures with a constrained force density method. *Computers & Structures*, 89(3-4):277–284, Feb. 2011. 2.4.3

[67] M. Dimcic. *Structural optimization of grid shells based on genetic algorithms.* PhD thesis, University of Stuttgart, ITKE, 2011. 2.4.1

[68] F. Dischinger. Die rotationsschalen mit unsymmetrischer form und belastung. *Bauingenieur*, 16:374, 1935. 2.2.1

[69] C. Douthe. *Etude de structures élancées précontraintes en matériaux composites, application à la conception des gridshells.* PhD thesis, Ecole des Ponts ParisTech, 2007. 2.4.4

[70] C. Douthe and O. Baverel. Design of nexorades or reciprocal frame systems with the dynamic relaxation method. *Computers & Structures*, 87(21-22):1296–1307, Nov. 2009. 2.4.1, 4.1.1

[71] C. Douthe, J. Caron, and O. Baverel. Gridshell structures in glass fibre reinforced polymers. *Construction and Building Materials*, 24(9):1580–1589, Sept. 2010. 2.4.1

[72] C. Douthe, R. Mesnil, H. Orts, and O. Baverel. Isoradial meshes: covering elastic gridshells with planar facets. *Automation in Construction*, 2016. 4.2.5, 8.2.4

[73] D. Dutta, R. Martin, and M. Pratt. Cyclides in surface and solid modeling. *IEEE Computer Graphics and Applications*, 13(1):53–59, Jan. 1993. 4, 4.1.3, 4.4.1

[74] G. A. E. and Z. W. *Theoretical Elasticity.* Oxford University Press, second edition, 1968. 2.4.1

[75] P. Eigenraam. *Flexible mould for production of double-curved concrete elements.* PhD thesis, TU Delft, Delft University of Technology, 2013. 2.3.3

[76] M. Eigensatz, M. Deuss, and M. Kilian. Case Studies in Cost-Optimized Paneling of Architectural Freeform Surfaces. In *Advances in Architectural Geometry.* 2010. (document), 2.1, 3.1.1

[77] G. Elber and M.-S. Kim. The Bisector Surface of Rational Space Curves Bisector Surface of Rational Space Curves. *ACM Transactions on Graphics*, 19(6), 1996. 4.3.2

[78] B. Espion. Pioneering hypar thin shell concrete roofs in the 1930s. *Beton-und Stahlbetonbau*, 111(3):159–165, 2016. 2.2.3

[79] A. Falk and P. Von Buelow. Form exploration of folded plate timber structures based on performance criteria. Hemming Group Ltd., 2011. 7.4.1, 7.4.9

[80] R.-q. Feng and J.-m. Ge. Shape optimization method of free-form cable-braced grid shells based on the translational surfaces technique. *International Journal of Steel Structures*, 13(3):435–444, 2013. 6.1.2

[81] D. E. Finkel. Direct optimization algorithm user guide. 2003. 6.2.5

[82] M. Firl. *Optimal shape design of shell structures.* PhD thesis, Universität München, 2010. 6.1.2

[83] M. Firl and K.-U. Bletzinger. Shape optimization of thin walled structures governed by geometrically nonlinear mechanics. *Computer Methods in Applied Mechanics and Engineering*, 237-240:107–117, Sept. 2012. 2.4.2, 2.4.2

[84] M. Firl, R. Wüchner, and K.-U. Bletzinger. Regularization of shape optimization problems using fe-based parametrization. *Structural and Multidisciplinary Optimization*, 47(4):507–521, 2013. 2.4.2, 6.1.1

[85] E. C. for Standardization. En1993-1-6:2007 eurocode 3: design of steel structures - part 1-6:Strength and stability of shell structures, 2007. 7.3.6

[86] A. Francavilla, C. Ramakrishnan, and O. Zienkiewicz. Optimization of shape to minimize stress concentration. *The Journal of Strain Analysis for Engineering Design*, 10(2):63–70, 1975. 6.1.1

[87] C.-W. Fu, C.-F. Lai, Y. He, and D. Cohen-Or. K-set tilable surfaces. *ACM Transactions on Graphics*, 29:1, 2010. 3.1.1

[88] S. Fujita and M. Ohsaki. Shape optimization of free-form shells using invariants of parametric surface. *International Journal of Space Structures*, 25(3):143–157, 2010. 6.1.2

[89] J. F. Gabriel. *Beyond the Cube: the architecture of Space Frames and Polyhedra.* John Wiley & Sons, 1997. 3.1.1

[90] T. V. Galambos. *Guide to stability design criteria for metal structures.* John Wiley & Sons, 1998. 7.3.1

[91] L. Garnier, S. Foufou, and M. Neveu. Conversion d'un carreau de Bézier rationnel biquadratique en un carreau de cyclide de Dupin quartique. *TSI. Technique et science informatiques*, 25(6):709–734, 2006. 4.1.2

[92] S. Gaß and F. Otto. Experiments, form-force-mass 5. information of the institute for lightweight structures (il) university of stuttgart nr. 25, 1975. 2.2.2

[93] D. Gebreiter. *Structuring Free-Form Building Envelopes.* PhD thesis, University of Bath, 2012. 1.3.3

[94] E. Ghys. Mr2850589 (review) 53a05. *Enseign. Math.(2)*, 57(1-2):165–208, 2011. 3.1.1

[95] F. Gioia, D. Dureisseix, R. Motro, and B. Maurin. Design and analysis of a foldable/unfoldable corrugated architectural curved envelop. *Journal of Mechanical Design*, 134(3):031003, 2012. 7.4.1

[96] V. Gioncu. Buckling of reticulated shells: State of the art. *International Journal of Space Structures*, 10(1), 1995. 2.4.2, 7.3.1

[97] V. Gioncu and N. Balut. instability Behaviour of Single Layer Reticulated Shells. *International Journal of Space Structures*, 7(4):243–252, 1992. 7.3.1, 7.3.1

[98] J. Glymph, D. Shelden, C. Ceccato, J. Mussel, and H. Schober. A parametric strategy for free-form glass structures using quadrilateral planar facets. *Automation in Construction*, 13(2):187–202, Mar. 2004. 2.2.4, 4.1.1, 4.2.5, 5.3.2, 6.5.4

[99] L. Gründig, L. Ekert, and E. Moncrieff. Geodesic and Semi-Geodesic Line Algorithms for Cutting Pattern Generation of Architectural Textile Structures. *Proceedings of the Asia-Pacific Conference on Shell and Spatial Structures, Beijing.*, 1996. 3.3.1

[100] B. Hahn. Analyse und beschreibung eines räumlichen tragwerks aus massivholzplatten. Technical report, 2009. 7.4.1

[101] S. Haker, S. Angenent, A. Tannenbaum, R. Kikinis, G. Sapiro, and M. Halle. Conformal surface parameterization for texture mapping. *IEEE Transactions on Visualization and Computer Graphics*, 6(2):181–189, 2000. 2.3.4

[102] M. Haldimann, A. Luible, and M. Overend. *Structural use of glass*, volume 10. Iabse, 2008. 2.3.3

[103] E. Happold and W. Liddell. Timber lattice roof for the Mannheim Bundesgartenschau. *The structural engineer*, 53(3):99–135, 1975. 2.4.1, 2.4.2

[104] J. Harding. Dimensionality reduction for parametric design exploration. In M. K. Sigrid Adriaenssens, Fabio Gramazio, editor, *Advances in Architectural Geometry*. 2016. 2.1.1

[105] J. Harding and H. Lewis. The TRADA Pavilion - A Timber Plate Funicular Shell. In *2013 IASS Annual Symposium: Beyond the Limits of Man*, page 5. 2013. 2.3.3, 7.4.1

[106] R. Harris, J. Romer, O. Kelly, and S. Johnson. Design and construction of the downland gridshell. *Building Research & Information*, 31(6):427–454, 2003. 7.3.5

[107] E. L. Hernández, S. Sechelmann, T. Rörig, and C. Gengnagel. Topology optimisation of regular and irregular elastic gridshells by means of a non-linear variational method. In *Advances in Architectural Geometry 2012*, pages 147–160. Springer, 2013. 2.4.4

[108] D. Hilbert and S. Cohn-Vossen. *Geometry and the Imagination*, volume 87. American Mathematical Soc., 1999. 1.4.1

[109] T. Hoffmann. *On Local Deformations of Planar Quad-Meshes*, pages 167–169. Springer Berlin Heidelberg, Berlin, Heidelberg, 2010. 2.3.3

[110] A. Holgate. *The art of structural engineering: the work of Jörg Schlaich and his team.* Edition Axel Menges, 1997. 2.2.4, 3.1.1

[111] R. Hooke. A description of helioscopes, and some other instruments. *Royal Society, London*, 1675. 2.4.1

[112] M. Huard, M. Eigensatz, and P. Bompas. Planar panelization with extreme repetition. In *Advances in Architectural Geometry 2014*, pages 259–279. Springer, 2015. 3.1.1

[113] S. Huerta Fernández. *The geometry and construction of Byzantine vaults: the fundamental contribution of Auguste Choisy.* Instituto Juan de Herrera, 2009. 2.2.1

[114] A. Hussein. Sandworks / sand tectonic prototype. In *ACADIA 2105: Computational Ecologies: Design in the Anthropocene - Proceedings of the 35th Annual Conference of the Association for Computer Aided Design in Architecture (ACADIA)*, October 2015. (document), 2.2.2, 2.4

[115] K. J. Hwang, J. Knippers, and S. W. Park. Influence of Various Types Node Connectors on the Buckling Loads of Grid Shells. In *Proceedings of the International Association for Shell and Spatial Structures (IASS) Symposium 2009 Evolution and Trends in Design, Analysis and Construction of Shell and Spatial Structures*, number October, pages 1841–1852, 2009. 3.1.2, 7.3.1

[116] H. Isler. Generating shell shapes by physical experiments. *Bulletin of the International Association for Shell and Spatial Structures*, 34(1):53–63, 1993. 2.4.1

[117] A. Javary. *Traité de géométrie descriptive*. Delagrave, 1881. 5.1.2

[118] C. Jiang, C. Tang, A. Vaxman, P. Wonka, and H. Pottmann. Polyhedral patterns. *ACM Transactions on Graphics (TOG)*, 34(6):172, 2015. 2.3.3, 7.5.2

[119] S. G. Johnson. The nlopt nonlinear-optimization package, 2015. Accessed: 2016-02-11. 6.2.5

[120] D. R. Jones, C. D. Perttunen, and B. E. Stuckman. Lipschitzian optimization without the lipschitz constant. *Journal of Optimization Theory and Applications*, 79(1):157–181, 1993. **??**, 6.2.5

[121] P. Joshi and C. H. Séquin. Energy Minimizers for Curvature-Based Surface Functionals. *Computer-Aided Design and Applications,*, 4(5):607–617, 2007. 4.4.4

[122] P. Kaelo and M. Ali. Some variants of the controlled random search algorithm for global optimization. *Journal of optimization theory and applications*, 130(2):253–264, 2006. **??**, 6.2.5

[123] A. Kaspar and B. Deng. Realtime Deformation of Constrained Meshes Using GPU. In *Symposium on GPU Computing and Applications*, 2013. 2.3.3

[124] S. Kato, M. Fujimoto, and T. Ogawa. Buckling load of steel single-layered reticulated domes of circular plan. *Journal of the International Association for Shell and Spatial Structures*, 46(147):41–63, 2005. 7.3.1, 7.3.6

[125] S. Kato, I. Mutoh, and M. Shomura. Collapse of semi-rigidly jointed reticulated domes with initial geometric imperfections. *Journal of Constructional Steel Research*, 48(2-3):145–168, nov 1998. 7.3.1

[126] S. Kato, T. Yamashita, S. Nakazawa, Y.-b. Kim, and A. Fujibayashi. Analysis based evaluation for buckling loads of two-way elliptic paraboloidal single layer lattice domes. *Journal of Constructional Steel Research*, 63(9):1219–1227, sep 2007. 7.3.1

[127] J. Kiendl, K.-U. Bletzinger, J. Linhard, and R. Wüchner. Isogeometric shell analysis with kirchhoff–love elements. *Computer Methods in Applied Mechanics and Engineering*, 198(49):3902–3914, 2009. 2

[128] M. Kilian, S. Flöry, Z. Chen, A. Sheffer, and H. Pottmann. Developable Surfaces with Curved Creases. In *Advances in Architectural Geometry*, pages 33–36, 2008. 4.1.3

[129] F. Klein. Vergleichende Betrachtungen über neuere geometrische Forschungen. *Mathematische Annalen*, 43(1):63–100, mar 1893. 5.2.4

[130] J. Knippers, J. Cremers, M. Gabler, and J. Lienhard. Construction manual for polymers+ membranes. *Institut für internationale Architektur-Dokumentation, München*, 2011. 2.3.3

[131] J. Knippers and T. Helbig. Recent Developments in the Design of Glazed Grid Shells. *International Journal of Space Structures*, 24(5):111–126, 2009. 2.3.4, 3.1.2, 7.3.1

[132] W. T. Koiter. The stability of elastic equilibrium. Technical report, Air Force Flight Dynamics Laboratory, 1977. 2.4.2, 7.3.1

[133] K. Kondo, A. Oguri, and J. Sasaki. Osaka maritime museum, japan. *Concrete*, 36(7):12–13, 2002. 3.5.2

[134] N. Kotelnikova-Weiler. *Optimisation mécanique et énergétique d'enveloppes en matériaux composites pour les bâtiments*. PhD thesis, Université Paris-Est, 2012. 1.1.2, 1.2a

[135] R. Krasauskas. Circular Meshes, cyclide splines and geometric algebra. In *Algebraic geometry in the sciences*, Oslo, 2011. 4.4.3, 4.4.3, 4.4.3

[136] A. Lebée. *Homogénéisation de plaques périodiques épaisses, application aux panneaux sandwichs à âme pliable en chevrons.* PhD thesis, Université Paris-Est, 2011. 7.5.3

[137] A. Lebée. From Folds to Structures , a Review. *International Journal of Space Structures*, 30(2):55–74, 2015. 5.3.1, 7.4.1, 7.4.1

[138] A. Lebée and K. Sab. A Bending-Gradient model for thick plates. Part I: Theory. *International Journal of Solids and Structures*, 48(20):2878–2888, oct 2011. 7.3.1

[139] A. Lebée and K. Sab. Homogenization of thick periodic plates: Application of the bending-gradient plate theory to a folded core sandwich panel. *International Journal of Solids and Structures*, 49(19):2778–2792, 2012. 7.5.3

[140] A. Lebée and K. Sab. Homogenization of a space frame as a thick plate: Application of the Bending-Gradient theory to a beam lattice. *Computers & Structures*, 127:88–101, oct 2013. 7.3.1, 7.3.10, 7.3.10, 7.3.10, 7.3.10

[141] B. Lefevre, C. Douthe, and O. Baverel. Buckling of elastic gridshells. *Journal of the International Association for Shell and Spatial Structures*, 56(3):153–171, 2015. 3.1.1, 7.3.1, 7.3.1

[142] C. Leroy. *Traité de stéréotomie, comprenant les applications de la géométrie descriptive à la théorie des ombres, la perspective linéaire la gnomonique, la coupe des pierres et la charpente, avec un atlas composé de 74 planches in folio.* Mallet-Bachelier, 1857. (document), 2.3.1, 2.9

[143] J.-M. Li and J. Knippers. Segmental timber plate shell for the landesgartenschau exhibition hall in schwäbisch gmünd - the application of finger joints in plate structures. *International Journal of Space Structures*, 30(2):123–139, 2015. 2.3.3, 7.4.1

[144] Y. Li, Y. Liu, and W. Wang. Planar hexagonal meshing for architecture. *IEEE Transactions on Visualization and Computer Graphics*, 21(1):95–106, Jan 2015. 2.3.3

[145] I. Liddell. Frei otto and the development of gridshells. *Case Studies in Structural Engineering*, 4:39 – 49, 2015. 2.4.1

[146] K. Linkwitz and H. Schek. A new method of analysis of prestressed cable networks and its use on the roofs of the olympic game facilities at munich. In *9th Congress of IABSE*, 1972. 2.4.1

[147] Y. Liu and W. Wang. On Vertex Offsets of Polyhedral Surfaces. In *Proceeding of Advances in Architectural Geometry*, pages 61–64, 2008. 2.3.4, 4.4.2

[148] Y. Liu, W. Wang, H. Pottmann, J. Wallner, and Y. Yong-Liang. Geometric Modeling with Conical Meshes and Developable Surfaces. *ACM Trans. Graphics*, 25(3):681—-689, 2006. 2.3.1, 2.3.3, 2.3.3, 2.3.3, 2.3.3, 2.3.4, 3.3.1, 4.1.1, 5.1.5

[149] Y. Liu, W. Xu, J. Wang, L. Zhu, B. Guo, F. Chen, and G. Wang. General planar quadrilateral mesh design using conjugate direction field. *ACM Trans. Graph.*, 30(6):140:1–140:10, Dec. 2011. 2.3.3

[150] L. Lombard, J. Lalande, and F. Consigny. Algorithmic optimization of the cross-section distribution across a steel framework structure. In *Advances in Architectural Geometry 2014*, pages 243–257. Springer, 2015. 2.4.2

[151] W. Ma. Subdivision surfaces for cad - an overview. *Computer-Aided Design*, 37(7):693 – 709, 2005. 4.5.1

[152] S. Malek, T. Wierzbicki, and J. Ochsendorf. Buckling of spherical cap gridshells: A numerical and analytical study revisiting the concept of the equivalent continuum. *Engineering Structures*, 75:288–298, sep 2014. 7.2.3, 7.3.1, 7.3.1, 7.3.1, 7.3.6, 7.3.6, 7.3.6, 7.3.6

[153] S. Malek and C. Williams. Structural Implications of using Cairo Tiling and Hexagons in Grid-shells. In *Proceedings of the International Association for Shell and Spatial Structures (IASS), 2013, Beyond the Limits of Man*, pages 3–6, 2013. 7.3.1

[154] S. R. Malek. *The effect of geometry and topology on the mechanics of grid shells.* PhD thesis, Massachusetts Institute of Technology, 2012. 7.4.1, 7.4.6

[155] R. Mark and D. Billington. Structural imperative and the origin of new form. *Technology and culture*, 30(2):300–329, 1989. 2.2.1

[156] R. Mark and P. Hutchinson. On the structure of the roman pantheon. *The Art Bulletin*, 68(1):24–34, 1986. 2.2.1

[157] R. T. Marler and J. S. Arora. Survey of multi-objective optimization methods for engineering. *Structural and multidisciplinary optimization*, 26(6):369–395, 2004. 2.4.3

[158] B. Marrey. *Nicolas Esquillan: un ingénieur d'entreprise.* Broché, 1992. 4.1.3

[159] R. Martin, J. De Pont, and T. J. Sharrock. Cyclide surfaces in computer aided design. *The mathematics of surfaces*, pages 253–268, 1986. 2.3.4, 2.3.4

[160] B. Maurin and R. Motro. The surface stress density method as a form-finding tool for tensile membranes. *Engineering structures*, 20(8):712–719, 1998. 2.4.1

[161] B. Maurin and R. Motro. Concrete shells form-finding with surface stress density method. *Journal of Structural Engineering*, 130(6):961–968, 2004. 2.4.1

[162] J. C. Maxwell. I.-on reciprocal figures, frames, and diagrams of forces. *Transactions of the Royal Society of Edinburgh*, 26(01):1–40, 1870. 2.4.1

[163] D. McLean. A method of Generating Surfaces as a Composite of Cyclide Patches. *The Computer Journal*, 28(4):433–438, Apr. 1985. 4.1.3

[164] R. Mesnil, C. Douthe, O. Baverel, and B. Léger. Möbius Geometry and Cyclidic Nets : A Framework for Complex Shape Generation. In *Proceedings of the IASS, Future Visions*, 2015. 4.5.1

[165] R. Mesnil, C. Douthe, O. Baverel, and B. Léger. Linear buckling of quadrangular and Kagome grids: a comparative assessment. *Engineering Structures*, 2016. 7.4.6, 7.4.7

[166] R. Mesnil, C. Douthe, O. Baverel, and B. Léger. Marionette mesh: from descriptive geometry to fabrication-aware design. In *Advances in Architectural Geometry*, 2016. 7.5.2

[167] R. Mesnil, C. Douthe, O. Baverel, and B. Léger. Marionette Mesh: modeling free-form architecture with planar facets. *International Journal of Space Structures*, 2016 (submitted). 4.1.1, 4.1.1, 4.3.1

[168] R. Mesnil, C. Douthe, O. Baverel, B. Léger, and J.-F. Caron. Isogonal moulding surfaces: a family of shapes for high node congruence in free-form structures. *Automation in Construction*, 59:38–47, 2015. 3.2.1, 4.1.3, 4.3.2, 4.5.1, 5.2.4, 5.2.5

[169] R. Mesnil, J. Ochsendorf, and C. Douthe. Stability of pseudo-funicular elastic grid shells. *International Journal of Space Structures*, 30(1):27–36, 2015. 7.3.1, 7.3.6, 7.4.7

[170] M. Miki, T. Igarashi, and P. Block. Parametric Self-supporting Surfaces via Direct Computation of Airy Stress Functions. *ACM Transaction on Graphics*, 34(4), 2015. 5.1.2

[171] G. Monge. Des courbes à double courbure. *Journal de l'École Polytechnique*, 2:345–363. 2.3.1

[172] G. Monge. *Géométrie descriptive.* Baudouin, 1798. 5.1.2

[173] G. Monge. *Application de l'analyse à la géométrie, à l'usage de l'Ecole impériale polytechnique.* 1807. 3.3, 3.3.1, 3.3.1

[174] R. Motro and B. Maurin. Bernard Laffaille and Nicolas Esquillan, Two French Pioneers. In *IASS-IABSE Symposium: Taller, Longer, Lighter*, 2011. 4.1.3

[175] R. Motro, C. Silvestri, B. Maurin, and B. Dresp-Langley. Visual perception and free-form structure: From image parameters to perceptual cues for optimal design. *Journal of the International Association for Shell and Spatial Structures*, 48(156):23–28, 2007. 2.1.1

[176] C. Mueller. *Computational exploration of the structural design space.* PhD thesis, Massachusetts Institute of Technology, 2014. (document), 1.3.1, 1.7, 2.4.2, 8.2.5

[177] C. T. Mueller and J. A. Ochsendorf. Combining structural performance and designer preferences in evolutionary design space exploration. *Automation in Construction*, 52:70–82, 2015. 2.4.2

[178] A. Nasri, M. Sabin, and Z. Yasseen. Filling N-sided regions by quad meshes for subdivision surfaces. *Computer Graphics Forum*, 28(6):1644–1658, 2009. 6.5.4

[179] A. Nealen, T. Igarashi, O. Sorkine, and M. Alexa. Laplacian mesh optimization. In *Proceedings of the 4th international conference on Computer graphics and interactive techniques in Australasia and Southeast Asia*, pages 381–389. ACM, 2006. 2.3.3

[180] J. Nocedal and S. Wright. *Numerical Optimization.* Springer Science & Business Media, 2006. 2.4.2, 3.5.1, 4.4.4, 5.3.2, 5.3.3

[181] H. Nooshin. Algebraic representation and processing of structural configurations. *International Journal of Computer and Structures*, pages 119–130, 1975. 2.1.2

[182] H. Nooshin. A technique for surface generation. In *IASS Symposium, Stuttgart, Germany*, 1996. 2.1.2

[183] H. Nooshin. Formex formulation of freeform structural surfaces. *Asian journal of civil engineering (Building and Housing)*, 8(4):459–469, 2007. 2.1.2

[184] H. Nooshin, P. Disney, and C. Yamamoto. Formian: The programming language of formex algebra. *University of Surrey Publication*, 1993. 2.1.2

[185] A. D. Norman, K. A. Seffen, and S. D. Guest. Morphing of curved corrugated shells. *International Journal of Solids and Structures*, 46:1624–1633, 2009. 7.4.9

[186] V. V. Novozhilov. *The theory of thin shells.* P. Noordhoff, 1959. 6.2.4

[187] H. Ohmori. Computational morphogenesis its current state and possibility for the future. *International Journal of Space Structures*, 25(2):75–82, 2010. 2.4.2

[188] R. Otter and A. Day. Tidal flow computation. 1960. 2.4.1

[189] F. Otto, R. Trostel, and F. K. Schleyer. *Tensile structures; design, structure, and calculati on of buildings of cables, nets, and membranes.* The MIT Press, 1973. 2.4.1

[190] S. Pellegrino. Structural computations with the singular value decomposition of the equilibrium matrix. *International Journal of Solids and Structures*, 30(21):3025 – 3035, 1993. 8.2.1

[191] C.-H. Peng, M. Barton, C. Jiang, and P. Wonka. Exploring Quadrangulations. *ACM Transactions on Graphics (TOG)*, 33(1):1–12, 2014. 6.5.4

[192] R. Poranne, R. Chen, and C. Gotsman. On linear spaces of polyhedral meshes. *IEEE Transactions on Visualization and Computer Graphics*, 21(5):652–662, May 2015. 2.3.3, 7.5.1

[193] R. Poranne, E. Ovreiu, and C. Gotsman. Interactive planarization and optimization of 3d meshes. In *Computer Graphics Forum*, volume 32, pages 152–163. Wiley Online Library, 2013. 2.3.3

[194] H. Pottmann, A. Asperl, M. Hofer, and A. Kilian. *Architectural Geometry.* Bentley Institute Press, 2007. 3.3.1, 5.2.4

[195] H. Pottmann, M. Eigensatz, A. Vaxman, and J. Wallner. Architectural geometry. *Computers & graphics*, 47:145–164, 2015. 2.3.4

[196] H. Pottmann, P. Grohs, and B. Blachitz. Edge offset meshes in Laguerre geometry. *Advances in Computational Mathematics*, 33:45–73, 2010. 2.3.4, 4.1.1

[197] H. Pottmann, C. Jiang, M. Höbinger, J. Wang, P. Bompas, and J. Wallner. Cell packing structures. *Computer-Aided Design*, 60:70–83, mar 2015. 2.3.4, 2.3.4

[198] H. Pottmann, Y. Liu, J. Wallner, A. Bobenko, and W. Wang. Geometry of multi-layer freeform structures for architecture. *ACM Transactions on Graphics*, 26(3):65, July 2007. 2.3.4, 2.3.4, 3.1.3, 3.2.2, 3.5.2, 4.1.1, 4.1.1, 4.1.1, 4.1.2

[199] H. Pottmann, A. Schiftner, P. Bo, H. Schmiedhofer, W. Wang, N. Baldassini, and J. Wallner. Freeform surfaces from single curved panels. *ACM Transactions on Graphics*, 27(3):1, Aug. 2008. 2.3.4

[200] H. Pottmann and J. Wallner. The focal geometry of circular and conical meshes. *Advances in Computational Mathematics*, 29(August):249–268, 2006. 2.3.4, 2.3.4, 4.1.1

[201] M. J. Powell. A direct search optimization method that models the objective and constraint functions by linear interpolation. In *Advances in optimization and numerical analysis*, pages 51–67. Springer, 1994. **??**, 6.2.5

[202] M. J. Powell. A view of algorithms for optimization without derivatives. *Mathematics Today-Bulletin of the Institute of Mathematics and its Applications*, 43(5):170–174, 2007. 6.2.5, 6.2.5

[203] M. J. Powell. The bobyqa algorithm for bound constrained optimization without derivatives. *Cambridge NA Report NA2009/06, University of Cambridge, Cambridge*, 2009. **??**, 6.2.5

[204] C. Preisinger. Linking Structure and Parametric Geometry. *Architectural Design*, 83(2):110–113, mar 2013. 7.2.3

[205] C. Preisinger and M. Heimrath. Karamba - A Toolkit for Parametric Structural Design. *Structural Engineering International*, 24(2):217–221, May 2014. 7.2.3

[206] E. Ramm and W. A. Wall. Shell structures - a sensitive interrelation between physics and numerics. *International journal for numerical methods in engineering*, 60(1):381–427, 2004. 6.6

[207] G. Rapp. Sandwich-type structural element, Dec. 6 1960. US Patent 2,963,128. (document), 7.46

[208] R. Richter, J. E. Kyprianidis, B. Springborn, and M. Alexa. Constrained modelling of 3-valent meshes using a hyperbolic deformation metric. In *Computer Graphics Forum*. Wiley Online Library, 2016. 3.1.1

[209] M. Rippmann, L. Lachauer, and P. Block. Interactive Vault Design. *International Journal of Space Structures*, 27(4):219–230, 2012. 5.1.2

[210] C. Robeller, A. Stitic, P. Mayencourt, and Y. Weinand. Interlocking folded plate: Integrated mechanical attachment for structural wood panels. In *Advances in Architectural Geometry 2014*, pages 281–294. Springer, 2015. 5.3.1, 7.4.1

[211] C. Rogers and W. K. Schief. On the equilibrium of shell membranes under normal loading. Hidden integrability. *Proceedings of the Royal Society of London A: Mathematical, Physical and Engineering Sciences*, 459:2449–2462, 2003. 4.2.3

[212] T. Rörig, S. Sechelmann, A. Kycia, and M. Fleischmann. Surface panelization using periodic conformal maps. In *Advances in Architectural Geometry 2014*, pages 199–214. Springer, 2015. 2.3.4

[213] T. H. Rowan. *Functional stability analysis of numerical algorithms*. PhD thesis, University of Texas at Austin, 1990. **??**, 6.2.5

[214] J. Sakarovitch. *Epures d'architecture: De la coupe des pierres a la géométrie descriptive XVI-XIX siècles*, volume 21. Springer Science & Business Media, 1998. 2.1.1

[215] J. Sakarovitch. Gaspard Monge Founder of 'Constructive Geometry'. In *Proceedings of the Third International Congress on Construction History*, Cottbus, 2009. 2.3.1, 2.3.1, 5

[216] H.-J. Schek. The force density method for form finding and computation of general networks. *Computer methods in applied mechanics and engineering*, 3(1):115–134, 1974. 2.4.1, 2.4.1

[217] F. Scheurer. Materialising complexity. *Architectural Design*, 80(4):86–93, 2010. 2.3.4

[218] W. K. Schief, A. Bobenko, and T. Hoffmann. On the Integrability of Infinitesimal and Finite Deformations of Polyhedral Surfaces. 38:67–93, 2008. 7.4.1

[219] W. K. Schief and B. G. Konopelchenko. On the unification of classical and novel integrable surfaces. I. Differential geometry. *Proceedings of the Royal Society A: Mathematical, Physical and Engineering Sciences*, 459(2029):67–84, jan 2003. 4.2.3

[220] A. Schiftner and J. Balzer. Statics-sensitive layout of planar quadrilateral meshes. *Advances in Architectural Geometry 2010*, pages 221–236, 2010. 2.4.4

[221] A. Schiftner, M. Höbinger, J. Wallner, and H. Pottmann. Packing circles and spheres on surfaces. *ACM Transactions on Graphics (TOG)*, 28(5):139, 2009. 2.3.4

[222] J. Schlaich and R. Bergermann. *Leicht und Weit: Jörg Schlaich-Rudolf Bergermann*. Prestel, 2003. 2.4

[223] J. Schlaich and H. Schober. Freeform glass roofs. In *Metropolis & Beyond, Proceedings of the 2005 Structures Congress and the 2005 Forensic Engineering Symposium*. 2.2.4, 2.3.3

[224] J. Schlaich and H. Schober. Glass Roof for the Hippo Zoo at Berlin. *Structural Engineering International*, 7(4):252–254, 1997. 2.2.4, 2.3.3

[225] M. Schlaich, U. Burkhardt, L. Irisarri, and J. Goñi. Palacio de comunicaciones-a single layer glass grid shell over the courtyard of the future town hall of madrid. In *Symposium of the International Association for Shell and Spatial Structures (50th. 2009. Valencia).*, 2010. 1.2.1, 7.3.1

[226] H. Schober. *Transparent shells - form topology structure*. Ernst & Sohn, 2016. 1.1.3, 2.2.3, 2.2.4, 2.4.4, 3.1.1, 3.1.2, 3.3.3, 3.5.2, 7.3.6, 7.4.6

[227] P. Séjourné. *Grandes Voûtes Tome 1 - voûtes inarticulées*. Bourges, imprimerie edition, 1913. 4

[228] G. Senatore and D. Piker. Interactive real-time physics. *Computer-Aided Design*, 61:32–41, Apr. 2015. 4.1.1

[229] C. H. Séquin. CAD Tools for Aesthetic Engineering. *Computer-Aided Design*, 37(7):737–750, 2005. 4.4.4

[230] D. Shelden. *Digital surface representation and the constructability of Gehry's architecture*. PhD thesis, Massachusetts Institute of Technology, 2002. 1.3.2

[231] P. Shepherd and P. Richens. The case for subdivision surfaces in building design. *Journal of the International Association for Shell and Spatial Structures*, 53(4):237–245, 2012. 1.3.3, 8.3

[232] M. Singh and S. Schaefer. Triangle surfaces with discrete equivalence classes. In *ACM Transactions on Graphics (TOG)*, volume 29, page 46. ACM, 2010. 3.1.1

[233] J. Sischka. *Engineering the construction of the great court roof for the British Museum*, chapter 21, pages 199–207. Thomas Telford, 2000. 7.3.1

[234] X. Song, M. Aigner, F. Chen, and B. Jüttler. Journal of Computational and Applied Circular spline fitting using an evolution process. *Journal of Computational and Applied Mathematics*, 231(1):423–433, 2009. 3.5.1, 3.5.1

[235] J. M. Songel. *A conversation with Frei Otto.* Princeton Architectural Press, 2010. 2.4.1

[236] Z. Soyuçok. Infinitesimal deformations of surfaces and the stress distribution on some membranes under constant inner pressure. *International Journal of Engineering Science*, 34(9):993–1004, jul 1996. 4.2.3

[237] Y. Srinivas and D. Dutta. Intuitive procedure for constructing geometrically complex objects using cyclides. *Computer-Aided Design*, 26(4):327–335, apr 1994. 4.2.1

[238] E. Stavropoulou, M. Hojjat, and K.-U. Bletzinger. In-plane mesh regularization for node-based shape optimization problems. *Computer Methods in Applied Mechanics and Engineering*, 275:39–54, jun 2014. 2.4.2

[239] S. Stephan, K. Knebel, and J. Sanchez-Alvarez. Reticulated Structures On Free-Form Surfaces. *Stahlbau*, 73:562–572, 2004. 3.1.2

[240] G. N. Stiny. Computing with form and meaning in architecture. *Journal of Architectural Education*, 39(1):7–19, 1985. 2.2.6

[241] A. Stitic and Y. Weinand. Timber folded plate structures–topological and structural considerations. *International Journal of Space Structures*, 30(2):169–177, 2015. 7.4.1, 7.4.2, 7.4.3, 7.4.3, 7.4.9

[242] M. Stolpe. Truss optimization with discrete design variables: a critical review. *Structural and Multidisciplinary Optimization*, 53(2):349–374, 2016. 2.4.2

[243] T. Tachi. Freeform rigid-foldable structure using bidirectionally flat-foldable planar quadrilateral mesh. *Advances in architectural geometry 2010*, pages 87–102, 2010. 7.4.1

[244] K. Takayama, D. Panozzo, A. Sorkine-Hornung, and O. Sorkine-Hornung. Sketch-Based Generation and Editing of Quad Meshes. *ACM Transactions on Graphics*, 32(4):97, 2013. 5.1.6, 6.5.4

[245] C. Tang, X. Sun, A. Gomes, J. Wallner, and H. Pottmann. Form-finding with polyhedral meshes made simple. *ACM Trans. Graphics*, 33(4), 2014. 2.3.3, 2.4.4, 6.5.3

[246] Y. Tanno, H. Kozuka, and M. Nakai. Odate dome, japan. In *IASS Symposium 2001: International Symposium on Theory, Design and Realization of Shell and Spatial Structures, Nagoya, Japan, 9-13 Oct. 2001*, pages 372–373, 2001. 3.3.3

[247] M. Tarini, E. Puppo, D. Panozzo, N. Pietroni, and P. Cignoni. Simple Quad Domains for Field Aligned Mesh Parametrization. *ACM Transactions on Graphics*, 30(6):142, 2011. 5.1.6

[248] F. Tayeb, J.-F. Caron, O. Baverel, and L. Du Peloux. Stability and robustness of a 300 m2 composite gridshell structure. *Construction and Building Materials*, 49:926–938, 2013. 4.5.1, 7.3.1

[249] S. Timoshenko and J. Gere. *Theory of elastic stability.* McGraw-Hill, New York, 1961. 4.2.3, 7.3.10

[250] C. Troche. Planar hexagonal meshes by tangent plane intersection. *Advances in architectural geometry*, 1:57–60, 2008. 2.3.3

[251] T. Van Mele, M. Rippmann, L. Lachauer, and P. Block. Geometry-based understanding of structures. *Journal of the International Association for Shell and Spatial Structures*, 53:285–295, 2012. 2.4.1

[252] A. Vaxman. Modeling polyhedral meshes with affine maps. *Computer Graphics Forum*, 31(5):1647–1656, 2012. 2.3.3

[253] A. Vaxman. A projective framework for polyhedral mesh modelling. *Computer Graphics Forum*, 33(8):121–131, 2014. 2.3.3

[254] A. Vaxman, C. Müeller, and O. Weber. Conformal mes deformations with Möbius transformations. *ACM Transactions on Graphics (TOG)*, 2015. 2.3.3

[255] D. Veenendaal, M. West, and P. Block. History and overview of fabric formwork: using fabrics for concrete casting. *Structural Concrete*, 12(3):164–177, 2011. 2.3.3

[256] P. von Buelow, A. Falk, and M. Turrin. Optimization of structural form using a genetic algorithm to search associative parametric geometry. In *Proceedings of the International Conference on Structures Architecture (ICSA 2010)*, 2010. 7.4.1, 7.4.9

[257] W. A. Wall, M. A. Frenzel, and C. Cyron. Isogeometric structural shape optimization. *Computer methods in applied mechanics and engineering*, 197(33):2976–2988, 2008. 8.2.2

[258] J. Wallner and H. Pottmann. Geometric Computing for Freeform Architecture. *Journal of Mathematics in Industry*, 1(1):4, 2011. 1.2.2, 1.6b

[259] J. Wang, C. Jiang, P. Bompas, J. Wallner, and H. Pottmann. Discrete line congruences for shading and lighting. In *Computer Graphics Forum*, volume 32, pages 53–62. Wiley Online Library, 2013. 1.1.2, 1.2b

[260] W. Wang and Y. Liu. *A Note on Planar Hexagonal Meshes*, pages 221–233. Springer New York, New York, NY, 2010. 2.3.3, 2.3.4

[261] W. Wang, Y. Liu, D. Yan, B. Chan, R. Ling, and F. Sun. HKU CS Tech Report TR-2008-13 Hexagonal Meshes with Planar Faces. *Dept. of CS, HKU, Tech. Rep*, 2008. 2.3.3, 4.1.1, 4.1.2

[262] W. Wang, J. Wallner, and Y. Liu. An angle criterion for conical mesh vertices. *Geometry Pre-Print*, 157:1–10, 2006. 2.3.4, 3.3.2, 3.5.2

[263] T. Wester. Structural Morphology, a New Challenge in Engineering and Architecture. In *IASS International Symposium on Shell and Spatial Structures*. 2.1

[264] C. Williams. Appendix b: differential geometry and shell theory. In S. Adriaenssens, P. Block, D. Veenendaal, and C. Williams, editors, *Shell Structures for Architecture*. Routledge, 2014. 6.6

[265] C. J. Williams. The definition of curved geometry for widespan structures. 2000. 2.4.1

[266] C. J. Williams. Patterns on a surface: The reconciliation of the circle and the square. *Nexus Network Journal*, 13(2):281–295, 2011. 2.4.1

[267] P. Winslow, S. Pellegrino, and S. B. Sharma. Multi-objective optimization of free-form grid structures. *Structural and Multidisciplinary Optimization*, 40:257–269, 2010. 6.5.4, 7.3.1

[268] T. Winterstetter, M. Alkan, R. Berger, M. Watanabe, A. Toth, and W. Sobek. Engineering complex geometries - the heydar aliyev centre in baku. *Steel Construction*, 8(1):65–71, 2015. 2.3.3

[269] S. Yamada, A. Takeuchi, Y. Tada, and K. Tsutsumi. Imperfection-sensitive overall buckling of single-layer lattice domes. *Journal of Engineering Mechanics*, 2(April):382–386, 2001. 7.3.1

[270] D. Yang, B. Guo, C. Chong, and C. Liu. Modeling and structural behavior of cable-stiffened single-layer latticed domes of hexagonal meshes. *Journal of Constructional Steel Research*, 114:237–246, 2015. 6.1.2

[271] Y.-L. Yang, Y.-J. Yang, H. Pottmann, and N. J. Mitra. Shape Space Exploration of Constrained Meshes. *ACM Trans. Graphics*, 30:124, 2011. 2.3.3

[272] M. Zadravec, A. Schiftner, and J. Wallner. Designing quad-dominant meshes with planar faces. In *Computer Graphics Forum*, volume 29, pages 1671–1679. Wiley Online Library, 2010. 2.3.3

[273] H. Zimmer, M. Campen, R. Herkrath, and L. Kobbelt. Variational tangent plane intersection for planar polygonal meshing. In *Advances in Architectural Geometry 2012*, pages 319–332. Springer, 2013. 2.3.3

[274] H. Zimmer, F. Lafarge, P. Alliez, and L. Kobbelt. Zometool Shape Approximation. In *Geometric Modeling and Processing*, Singapore, Singapore, June 2014. 3.1.1

[275] S. Zube and R. Krasauskas. Representation of Dupin cyclides using quaternions. *Graphical Models*, 82:110–122, nov 2015. 4.4.4

Relevant publications by the author

R. Mesnil, C. Douthe, O. Baverel and B. Léger. Buckling of quadrangular and Kagome gridshells: a comparative assessment. *Engineering Structures*, 132(3):337-348, 2017.

R. Mesnil, C. Douthe, O. Baverel, B. Léger, and J.-F. Caron. Structural morphology and performance of plated shell structures with planar quadrilateral facets. *Journal of the IASS*, 58(1):7-22, 2017.

R. Mesnil, C. Douthe, O. Baverel and B. Léger. Generalised cyclidic nets for the modeling of complex shapes in architecture. *International Journal of Architectural Computing*, 2017 (accepted).

R. Mesnil, C. Douthe, O. Baverel and B. Léger. Marionette meshes: modelling free-form architecture with planar facets. *International Journal Of Space Structures*, 2017.

R. Mesnil, C. Douthe, O. Baverel, B. Léger. Marionette mesh: from descriptive geometry to fabrication-aware design. *Advances in Architectural Geometry 2016*, 2016.

R. Mesnil, C. Douthe, O. Baverel, B. Léger, and J.-F. Caron. Isogonal moulding surfaces: a family of shapes for high node congruence in free-form structures. *Automation in Construction*, 59:38-47, 2015.

R. Mesnil, C. Douthe, O. Baverel, B. Léger. Structural exploration of a fabrication-aware design space with Marionettes Meshes. *Proceedings of the IASS Annual Symposium 2016 - Spatial Structures in the 21st Century*, 2015.

R. Mesnil, C. Douthe, O. Baverel, B. Léger. Möbius Geometry and Cyclidic Nets: A Framework for Complex Shape Generation. *Proceedings of the IASS, Future Visions*, 2015.

R. Mesnil, Y. Santerre, C. Douthe, O. Baverel, B. Léger. Generating high node congruence with Monge's surfaces. *Proceedings of the IASS, Future Visions*, 2015.

R. Mesnil, C. Douthe, O. Baverel, B. Léger. Isogonal moulding surfaces: towards a new shape grammar for high node congruence in free-form structures *CIGOS*, 2015.